

# D3.1



## Beacon - Bentonite Mechanical Evolution

Description of the constitutive models available at the start of the project.

Conceptual bases, mathematical description and capabilities and shortcomings.

### DELIVERABLE (D3.1)

Author: Antonio Gens

Reporting period: 01/06/17 – 30/11/18

Date of issue of this report: **24/11/18**

Start date of project: **01/07/17**

Duration: 48 Months

This project receives funding from the Euratom research and training programme 2014-2018 under grant agreement No 745 942

#### Dissemination Level

<b>PU</b>	Public	X
<b>RE</b>	Restricted to a group specified by the partners of the Beacon project	
<b>CO</b>	Confidential, only for partners of the Beacon project	

**DISTRIBUTION LIST**

Name	Number of copies	Comments
Athanasios Petridis (EC) Christophe Davies (EC)  Beacon partners		

## Abstract

This Deliverable presents the constitutive models available at the start of the project for the different modelling teams involved in Work Package 3. They will be used in the validation exercises performed in Work Package 5. This set of constitutive models presented constitute the baseline situation on which future modifications will be undertaken. A number of key features of bentonite behaviour (mechanical and hydraulic) have been identified providing benchmarks for model assessment.

Nine teams have presented constitutive hydromechanical models that are summarised in this Deliverable, focusing on the most characteristic features of their formulation. The scope of the constitutive models presented is very wide, providing, already at the start of the project, a large diversity of approaches and formulations that will allow the assessment of their relative capacity to model satisfactorily the mechanical behaviour of the bentonite.

The capabilities of the models in relation to the set of key bentonite behaviour features are collected in summary Tables. Most of those features can be qualitatively simulated by the current state of development of most of the models. Those capabilities will be however re-assessed in the light of the results of the validation tests.

It is concluded that the current set of mechanical constitutive models constitute, in any case, a very good starting platform to undertake the modelling activities envisaged in the project.



## Content

<b>1. Introduction</b> .....	5
<b>2. Work Package 3: general overview</b> .....	7
<b>3. Constitutive models</b> .....	10
3.1 Bundesanstalt fuer Geowissenschaften und Rohstoffe (BGR), DE .....	10
3.2 Charles University (CU), CZ (in collaboration with CTU) .....	12
3.3 Clay Technology (Clay Tech), SE .....	15
3.4 Ecole Polytechnique Federale de Lausanne (EPFL), CH .....	17
3.5 Imperial College, London (ICL), UK .....	20
3.6 Quintessa, UK .....	23
3.7 Teknologian tutkimuskeskus, (VTT), FI .....	26
3.8 Universitat Politècnica de Catalunya (UPC), ES .....	28
3.9 Université de Liège (ULg), BE .....	32
<b>4. Concluding Remarks</b> .....	35
<b>Appendix 1. Instructions and suggestions for reports from modelling teams</b> .	36

# 1 Introduction

The dismantling of a number of large-scale in situ tests performed in several Underground Research Laboratories (URLs) have revealed that barriers and seals may not exhibit complete homogenization even at the end of the transient period when they already have become saturated. Dry density gradients persist at the end of some of the experiments. Engineered barrier and seals often use bentonite as the sole component or, if mixed with other materials, bentonite is often the prime component.

Final heterogeneity may be a consequence of initial heterogeneities set up during installation. There are different sources of heterogeneity that affect different scales. At large scale, heterogeneity may arise from the combination of blocks and granular bentonite in the same design, from the unavoidable technological voids or from the spaces between blocks that remain after installation. The use of granular bentonite or the employment of mixtures of different kinds (e.g. pellets-powder, sand/bentonite) provide another source of heterogeneity this time at the mesoscale. Even at the microscale there is significant heterogeneity, for instance in compacted bentonite where the microstructure consists of an arrangement of aggregates leaving relative large pores between them.

However, heterogeneity but may also develop from an initially homogenous system due to the complex thermo-hydro-mechanical interactions that take place during the transient phase. Other sources of heterogeneity is the potential of erosion, piping, dissolution and/or colloid formation that may arise in barriers and seals installed in crystalline rock.

It is recognized that the mechanical behaviour of the bentonite underlies much of the evolution and final state of the barriers and seals. However, so far the mechanical of the bentonite has received relatively little attention compared with its thermo-hydraulic behaviour. Relatively simple models have been employed to simulate its stress-strain-strength characteristics. The mechanical behaviour of bentonite is however complex exhibiting features such as irreversibility and stress-path dependence. The main objective of the Beacon project is to develop and test the tools necessary for the assessment of the mechanical evolution of the installed bentonite barrier and the resulting performance of the barrier. Figure 1-1 shows the overall organization of the project in a number of Work Packages and the relationship between them.

Work Package 3 plays a central role in the structure of the project as it is devoted to the development of the constitutive models for describing the hydromechanical behaviour of the bentonite in an appropriate manner. It is recognized that current models face limitations in their predictive capabilities and significant advances are required. The models must prove their predictive capabilities, reliability and robustness and they should preferably be grounded on a good understanding of the phenomena involved. To this end, they will be validated using a several laboratory and field-scale tests. This is reflected in the direct relationship between Work Package 3 and Work Package 5 devoted to testing, verification and validation of the models developed (see Figure 1-1).

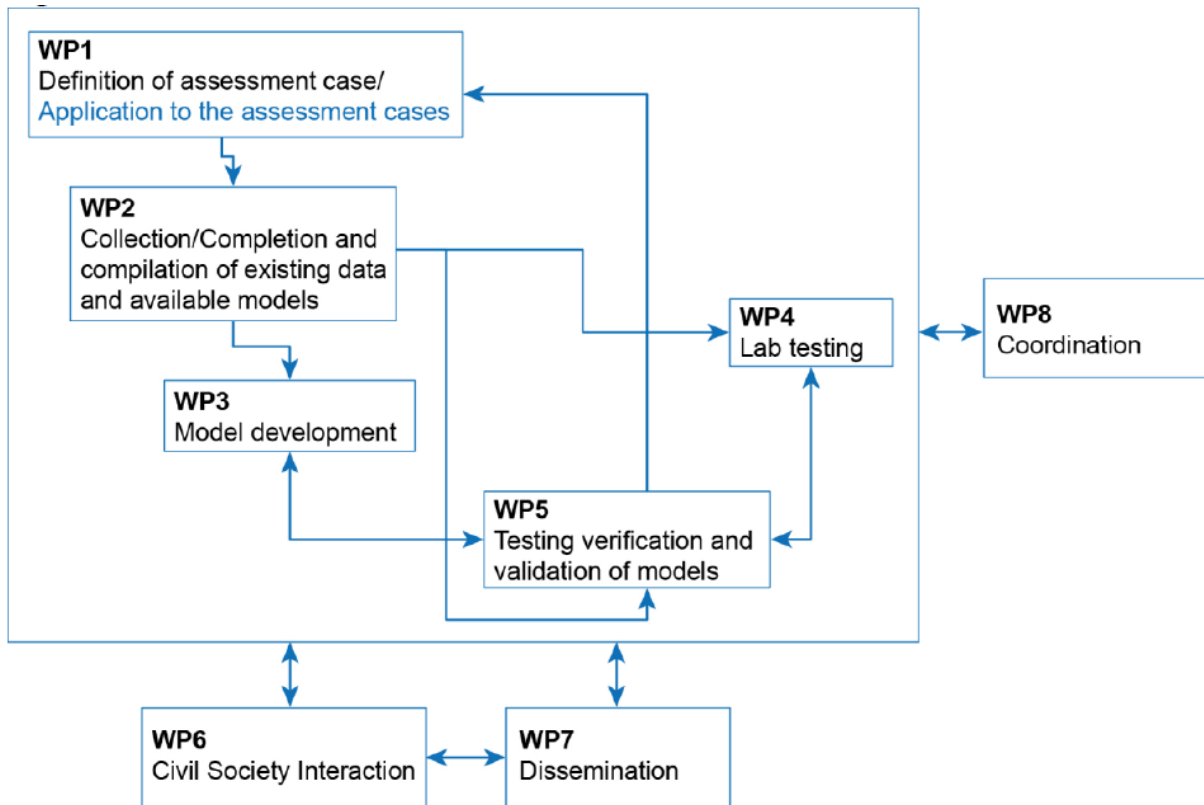


**Figure 1-1.** Structure of the Beacon project in terms of Work Packages. The arrow indicate one-way or two-ways relationships between Work Packages. The central location of Work Package 3 is apparent in the diagram.

The objective of this report is to present the constitutive models available at the start of the project. They constitute the starting point for future developments to be reported in subsequent Deliverables. Chapter 2 presents an overview of Work Package 3 whereas Chapter 3 contains a brief summary of the hydromechanical constitutive laws described in the initial teams' reports together with a first assessment of their capabilities in relation with key aspects of bentonite mechanical behaviour. Finally, some concluding remarks are offered in Chapter 4. The individual teams' reports constitute a set of Annexes to this Deliverable.

## 2 Work Package 3: general overview

As indicated above, the main role of Work Package 3 is the development of constitutive model for the description of the mechanical behaviour of bentonite or bentonite-based mixtures with the aim of introducing them into numerical tools capable of analysing boundary value problems of engineering significance. Ideally, those constitutive models should consider the following cases:

- Saturated and unsaturated materials
- Compacted bentonite (Blocks) and granular bentonite (e.g. pellet-based)
- Isothermal and non-isothermal conditions

although it is recognised that not all models will necessarily have this comprehensive level of generality.

The development of constitutive models have been carried out by the following teams:

- Bundesanstalt fuer Geowissenschaften und Rohstoffe (BGR), DE
- Charles University (CU), CZ (in collaboration with CTU)
- Clay Technology (ClayTech), SE
- Ecole Polytechnique federale de Lausanne (EPFL), CH
- Imperial College, London (ICL), UK
- Quintessa (Quintessa), UK
- Teknologian tutkimuskeskus, (VTT), FI
- Universitat Politècnica de Catalunya (UPC), ES
- Université de Liège (ULg), BE

VTT was not included in the initial proposal for Work Package 3 but it has joined the activities of the Work Package in collaboration with the Universidad Castilla – la Mancha (UCLM, a third party of Beacon).

The reports of those participants with the description of the hydromechanical constitutive model are listed as Annexes A to I

Other organization participate in of Work Package 3:

- Centro de Investigaciones Energeticas, Medioambientales y Tecnologicas (CIEMAT), ES
- Czech Technical University (CTU), CZ
- Gesellschaft fur Anlagen und Reaktorsicherheit (GRS). DE
- Karlsruher Institut fuer Technologie (KIT), DE
- Lietuvos Energetikos Institutas (LEI), LT
- Posiva (POSIVA), FI

---

(D3.1) – Description of the constitutive models available at the start of the project. Conceptual bases, mathematical description and capabilities and shortcomings.

Dissemination level: PU

Date of issue of this report: **21/11/18**

GRS and LEI have also submitted reports (Annexes J and K, respectively) but no description of mechanical constitutive models at this stage.

In January 2018, there was a joint scientific meeting of Work Packages 3 and 5 where the initial state of development of the constitutive models was presented and discussed. The teams were asked to deliver reports of the initial state of the constitutive laws providing information on:

- Background (physical, mathematical...)
- Basic hypotheses and scope (hydraulic, thermal, chemical...)
- Mathematical description
- Theoretical framework (plasticity, hypoplasticity...)
- Equations
- Input parameters and their sources

as well as an indication of their qualitative and quantitative performance.

To facilitate a more common assessment of the models, the teams were asked explicitly what were the model capabilities concerning a number of features of behaviour:

1. Dependence of swelling strain on applied stress and on dry density
2. Irreversibility of strains in wetting/drying cycles
3. Behaviour during swelling stress test. Dependence of swelling pressure on dry density
4. Stress path dependence from an unsaturated to a saturated state
5. Stress path dependence from a saturated to an unsaturated state
6. Dependence of strains developed in a temperature cycle (increase/decrease) on OCR (or stress)

The first five items correspond to an isothermal formulation whereas the sixth one requires the incorporation of temperature effects. The features selected for this purpose are those that are deemed, in principle, most relevant to explain the evolution of engineered barriers and seals during the transient phase. In addition, each team was asked to fill the Table in Figure 2-1 as a summary of the initial state of their constitutive models. The full specifications for the reports provided to the participants are presented in Appendix 1 of this Deliverable.

Table 1. Features Table

Name of the constitutive law:			
Behaviour feature	YES	NO	Remarks
<b>Mechanical behaviour</b>			
Dependence of swelling strain on applied stress (at the same dry density) (Figure 1)			
Dependence of swelling stress on dry density (at the same stress) (Figure 1)			
Irreversibility of strains in wetting/drying cycles (Figure 2)			
Dependence of swelling pressure on dry density (Figure 4)			
Stress path dependence from an unsaturated to a saturated state (Figure 5)			
Stress path dependence from a saturated to an unsaturated state (Figure 6)			
Double structure/porosity considered?			
Are temperature effects considered in the model?			
Dependence of strains developed in a temperature cycle (increase/decrease) on OCR (or stress) (Figure 7)			
<b>Hydraulic behaviour (retention curve)</b>			
Hysteresis			
Dependence on void ratio			
Double structure/porosity considered?			

*Figure 2-1. Summary Table of the capabilities of the constitutive models*

(D3.1) – Description of the constitutive models available at the start of the project. Conceptual bases, mathematical description and capabilities and shortcomings.

Dissemination level: PU

Date of issue of this report: **21/11/18**

### 3 Constitutive models

This section contains a summary of the main features of the constitutive models available to the teams involved in the Work Package. The full description is provided in the corresponding Annexes A to I. The qualitative performance of the models is summarised by reference to the Tables (Figure 2-1) supplied by each team. It should be noted that the fact that a model is capable to simulate a particular feature in its initial formulation does not imply that the model results are automatically satisfactory; this can only be evaluated in the validation exercises against experimental observations. The Table simply provides an overview of the basic capabilities of the model in relation to what have been considered key features of behaviour.

#### 3.1 Bundesanstalt fuer Geowissenschaften und Rohstoffe (BGR), DE

The report by BGR focuses on the description of the coupled THM formulation implemented in Open Geo Sys (OSG) code. The mechanical model implemented in the code is linear elasticity and it is formulated in terms of effective stresses that incorporate Biot’s coefficient. To account for the expansive behaviour of the bentonite, a linear swelling model extension is included where a linear relationship between swelling stress and water saturation is postulated.

The model is tested under a variety of conditions: no confinement (Figure 3-1) fully confined and under various confining stresses. No checks on the key features of Figure 2-1 are provided in the report.

Table 3-1 provides a summary of the current capabilities of the model with some relevant comments.

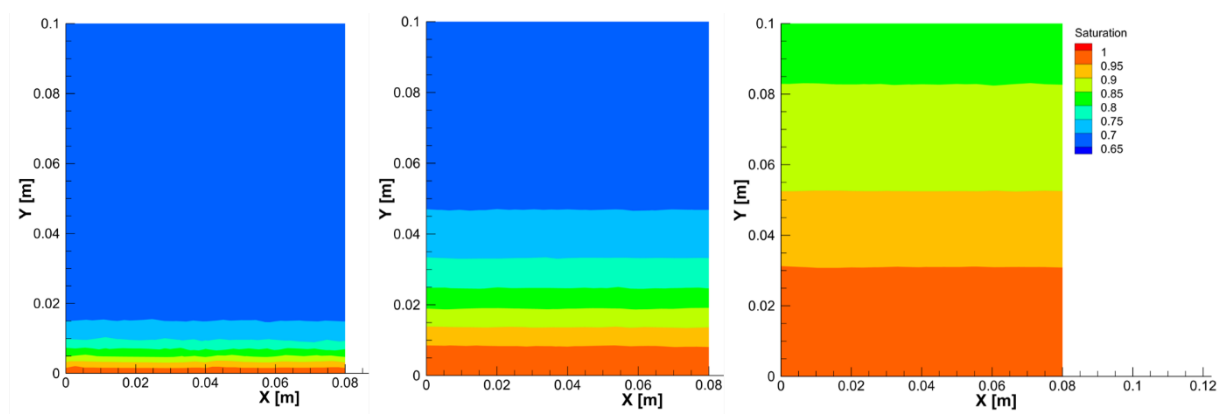


**Figure 3-2.** Progress of hydration under no confining conditions

**Table 3-1** Summary Table of the current capabilities of the BGR OpenGeoSys-5 model

Name of the constitutive law:		Linear-elasticity with linear swelling	
Behaviour feature	YES	NO	Remarks
<b>Mechanical behaviour</b>			
Dependence of swelling strain on applied stress (at the same dry density) (Figure1)	x		Strains are dependent on overburden pressure
Dependence of swelling stress on dry density (at the same stress) (Figure 1)	x		Maximum swelling pressure is implicitly dependent on dry density and is a user-defined constant. The evolution is dependent on the saturation.
Irreversibility of strains in wetting/drying cycles (Figure 2)		x	Due to linear elasticity, strains are reversible
Dependence of swelling pressure on dry density (Figure 4)		x	User-specified and constant for the whole simulation
Stress path dependence from an unsaturated to a saturated state (Figure 5)		x	
Stress path dependence from a saturated to an unsaturated state (Figure 6)		x	
Double structure/porosity considered?		x	
Are temperature effects considered in the model?	x		Thermally dependent parameters fluid parameters, vapour diffusion and thermal expansion of all phases.
Dependence of strains developed in a temperature cycle (increase/decrease) on OCR (or stress) (Figure 7)	x		Thermal expansion is incorporated in the mechanical model for non-isothermal hydromechanical processes
<b>Hydraulic behaviour (retention curve)</b>			
Hysteresis		x	
Dependence on void ratio		x	
Double structure/porosity considered?		x	

### 3.2 Charles University (CU), CZ (in collaboration with CTU)

The CU model is a double structure formulation developed within the framework of hypoplasticity. Figure 3-2 presents a schematic representation of the double structure concept whereas Figure 3-3 represents the double-structure coupling concept that underlies the model.

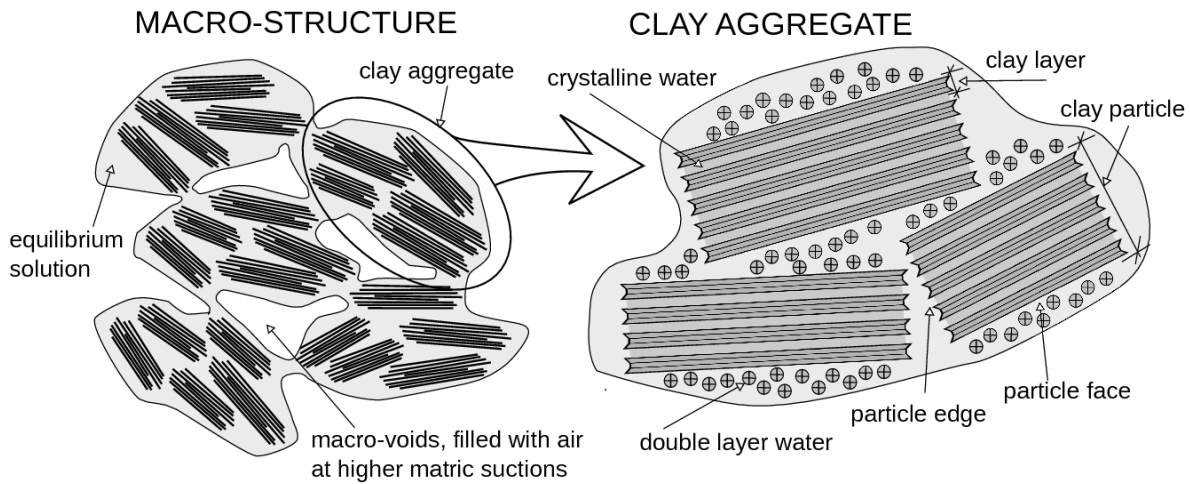


**Figure 3-2.** Schematic representation of the double structure concept

Characteristic features of the model:

- Hypoplastic formulation of the mechanical part of the model with Overconsolidation Ratio, OCR (or void ratio) as a key state variable
- Hysteretic formulation of the hydraulic water retention model for the macrostructure (Figure 3-4)
- A non isothermal extension has been included

Table 3-2 provides a summary of the capabilities of the model. It is the only model that currently satisfies all the requirements set up in the summary Table.

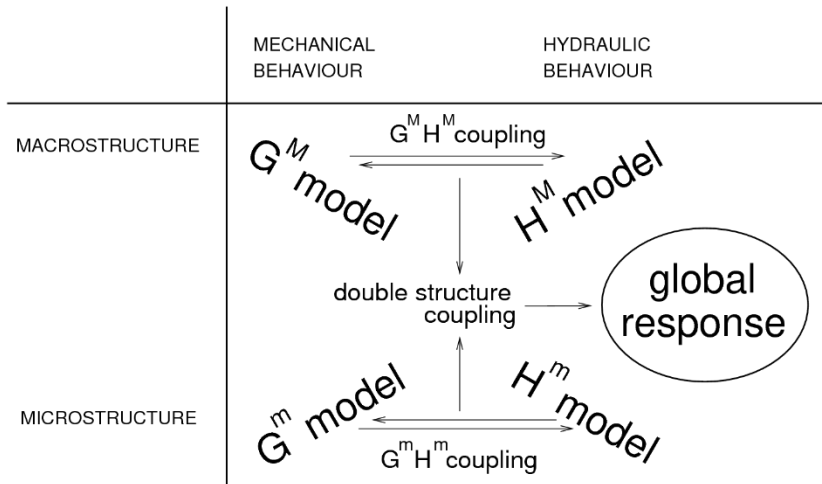


**Figure 3-3.** Schematic representation of the double structure coupling concept

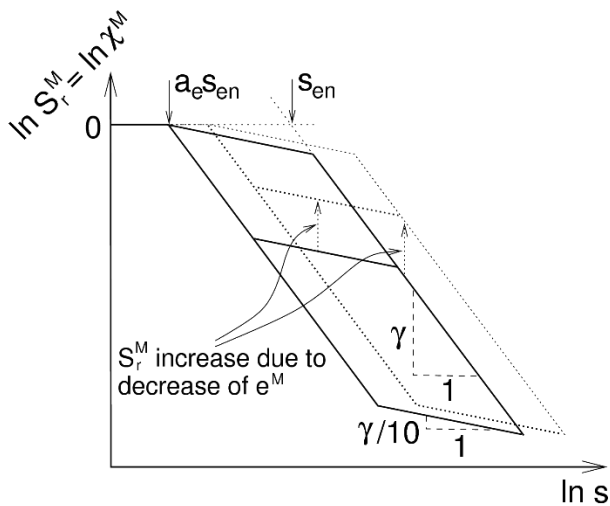


**Figure 3-4.** Hysteretic formulation of the water retention model for the macrostructure.

*Table 3-2 Summary Table of the current capabilities of the CU hypoplastic model*

Name of the constitutive law:		Hypoplasticity for Expansive Soils	
Behaviour feature	YES	NO	Remarks
<b>Mechanical behaviour</b>			
Dependence of swelling strain on applied stress (at the same dry density)	YES		
Dependence of swelling strains on dry density (at the same stress)	YES		
Irreversibility of strains in wetting/drying cycles	YES		
Dependence of swelling pressure on dry density	YES		
Stress path dependence from an unsaturated to a saturated state	YES		
Stress path dependence from a saturated to an unsaturated state	YES		
Double structure/porosity considered?	YES		
Are temperature effects considered in the model?	YES		
Dependence of strains developed in a temperature cycle (increase/decrease) on OCR (or stress)	YES		
<b>Hydraulic behaviour (retention curve)</b>			
Hysteresis	YES		
Dependence on void ratio	YES		
Double structure/porosity considered.	YES		

### 3.3 Clay Technology (Clay Tech), SE

The model developed is called the Hysteresis Based Material (HBM) model. In contrast to most other models, in the current state of development is applicable to saturated conditions only. It will therefore require extension to unsaturated conditions. In fact, the Clay Tech document already includes a suggestion on how this extension can be undertaken, albeit limited to isotropic conditions (i.e. no deviatoric stresses). In any case, it is envisaged that the fully developed model will include water-unsaturated and non-isotropic conditions

It is also characteristic of this model that it is based on an expression of the chemical potential of the clay water and its pressure dependence. This is then generalised to include hysteresis and to account for the bentonite strength. It is assumed that the clay potential for a specific void ratio can exist in the space limited by two bounding functions. The basic approach is illustrated in Figure 3-5.

The constitutive model incorporates non-isothermal conditions but only through the thermal expansion of water. Although thermal expansion is influenced by void ratio and applied stress, it is likely that a more general formulation may be eventually required.

Table 3-3 provides a summary of the current capabilities of the model with some relevant comments.

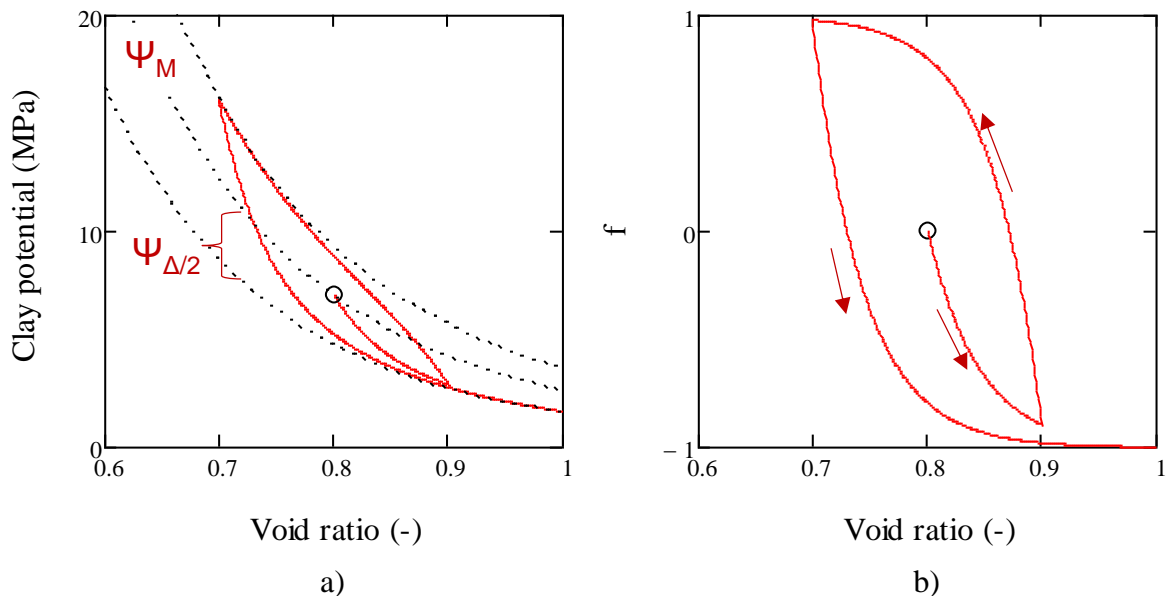


**Figure 3-5.** a) Hysteretic evolution of clay potential bounded by two limiting functions. b) Hysteretic evolution of the path variable,  $f$ .

*Table 3-3 Summary Table of the current capabilities of the Clay Tech HBM model*

Name of the constitutive law:		Hysteresis Based Material model		
Behaviour feature	YES	NO	Remarks	
<b>Mechanical behaviour</b>				
Dependence of swelling strain on applied stress (at the same dry density)	x		Only wetting direction has been defined	
Dependence of swelling strains on dry density (at the same stress)	x		Only wetting direction has been defined	
Irreversibility of strains in wetting/drying cycles	x		Assumed for saturated conditions	
Dependence of swelling pressure on dry density	x		Swelling pressure curve is equivalent to the clay potential as zero suction.	
Stress path dependence from an unsaturated to a saturated state	-	-	Has not been analysed	
Stress path dependence from a saturated to an unsaturated state		x	Saturated conditions assumed	
Double structure/porosity considered?	x		For unsaturated conditions	
Are temperature effects considered in the model?	x		First and foremost through the thermal expansion of water.	
Dependence of strains developed in a temperature cycle (increase/decrease) on OCR (or stress)	x		Thermal expansion influenced by the void ratio and load. Only temperature increase tested.	
<b>Hydraulic behaviour (retention curve)</b>				
Hysteresis	x		Inherent from the HBM model	
Dependence on void ratio	x		Inherent from the HBM model	
Double structure/porosity considered?	x		Micro pores water-filled and macro pores gas-filled	

### 3.4 Ecole Polytechnique federale de Lausanne (EPFL), CH

ACMEG is the model put forward by the EPFL team. It is a quite general constitutive model, based on elasto-plasticity, for saturated and unsaturated soils and for both isothermal and non-isothermal conditions. It belongs to the currents stage of evolution of a suite if models that have progressively incorporated new phenomena and new capabilities, as illustrated in the following Table.

Version	Modelled processes	Reference
ACMEG-S	Unsaturated states	Nuth (2009)
ACMEG-DC	Dessication cracks	Péron (2008)
ACMEG-2S	Aggregated soils in unsaturated conditions	Koliji (2008)
ACMEG-TS	Non-isothermal unsaturated conditions	François & Laloui (2008)
ACMEG-B	Biologically induced calcite precipitation	Fauriel & Laloui (2012)
ACMEG-C	Osmotic effects	Witteveen et al. (2013)

The version ACMEG-TS will be used in the project as being the most suitable one of the material and analyses envisaged.

In contrast to other models, a single structure formulation is adopted. Irreversible features are incorporated without the need of a double porosity interaction. However, the team expects that model extensions aiming to deal with pellet-based materials may need to take explicitly into account the double porosity in the mechanical model.

The model uses Bishop’s effective stress definition ensuring a direct dependence of the mechanical response on the hydraulic state. However, a refined expression for effective stress may be developed considering the different suction components. The increase in apparent preconsolidation pressure with capillary suction and temperature is taken into account, defining a generalised loading collapse curve (Figure 3-6). The mechanical model is complemented with a water retention model that accounts for hysteresis and the mechanical and temperature effects on the hydraulic behaviour (Figure 3-7). This provides a two-way coupling between mechanics and hydraulics.

Table 3-4 contains the current assessment of the model features and capabilities.

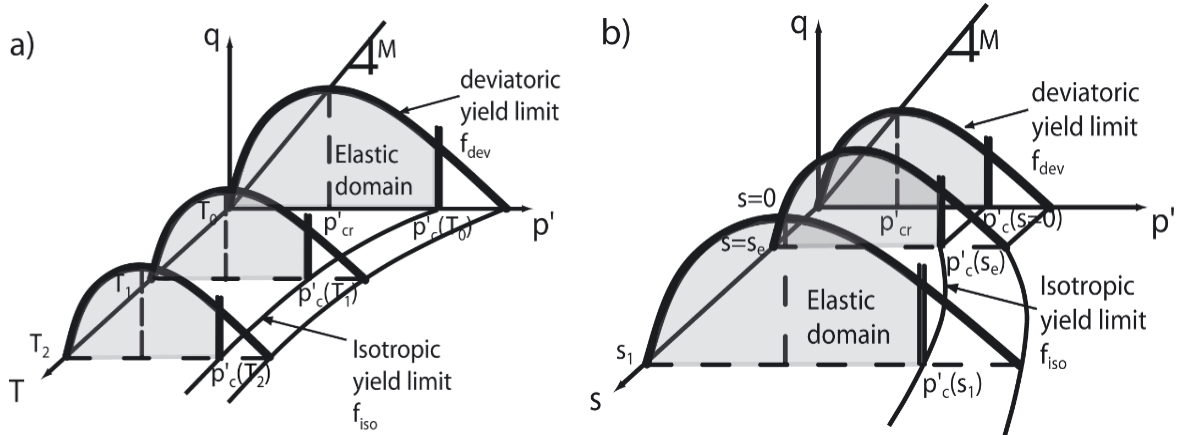


**Figure 3-6.** Evolution of the yield surface with a) suction, b) temperature

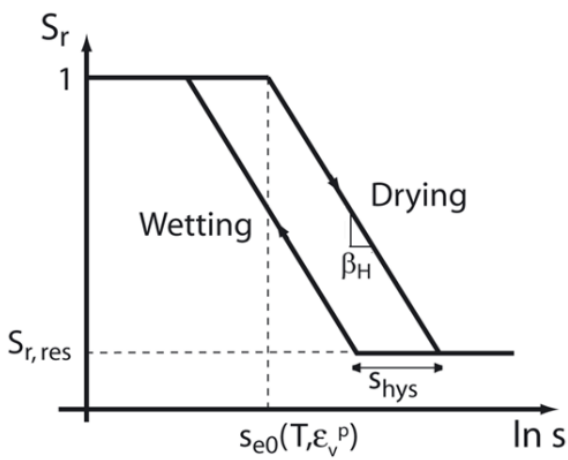


**Figure 3-7.** Hysteretic water retention model

*Table 3-4 Summary Table of the current capabilities of EPFL's ACMEG-TS model*

Name of the constitutive ACMEG-TS law:			
Behaviour feature	YES	NO	Remarks
<b>Mechanical behaviour</b>			
Dependence of swelling strain on applied stress (at the same dry density)	X		As expected: the higher the stress, the lower the swelling
Dependence of swelling <b>strains</b> on dry density (at the same stress)	X		The higher the dry density (preconsolidation stress), the higher the swelling stress
Irreversibility of strains in wetting/drying cycles	X	X	Irreversible behaviour but final cumulated shrinkage.
Dependence of swelling pressure on dry density	X		Well captured
Stress path dependence from an unsaturated to a saturated state	X		
Stress path dependence from a saturated to an unsaturated state	X		
Double structure/porosity considered?		X	
Are temperature effects considered in the model?	X		Both elastic (thermal expansion/compression) and plastic (thermal collapse) effects are considered
Dependence of strains developed in a temperature cycle (increase/decrease) on OCR (or stress)	X		Low OCRs induce thermal collapse upon heating
<b>Hydraulic behaviour (retention curve)</b>			
Hysteresis	X		
Dependence on void ratio	X		
Double structure/porosity considered?		X	

### 3.5 Imperial College, London (ICL), UK

The Imperial College – Double Structure model (IC DSM) is a development of an existing and tried IC SSM (Imperial College Single Structure Model). They are defined in the framework of elasto-plasticity. They share a number of features with the Barcelona Expansive Model (BExM) and the Barcelona Basic Model (BBM) but there also many significant differences. Figure 3-8 depicts the conceptual double-structure scheme assumed in the model.

Some significant developments of this model are:

- The incorporation of the air entry suction in the definition of stress variables
- The use of a more general and flexible shape for the definition of yield surface (Figure 3-9)
- Adoption of non-associated plasticity
- Modified variation of  $\lambda$  with suction (Figure 3-10)
- The adoption of Matsuoka-Nakai shape for the deviatoric plane.

The hydraulic model only considers a single structure and displays hysteresis and void ratio dependence. The model has been developed for isothermal conditions.

Current features and capabilities of the model are summarised in Table 3-5.

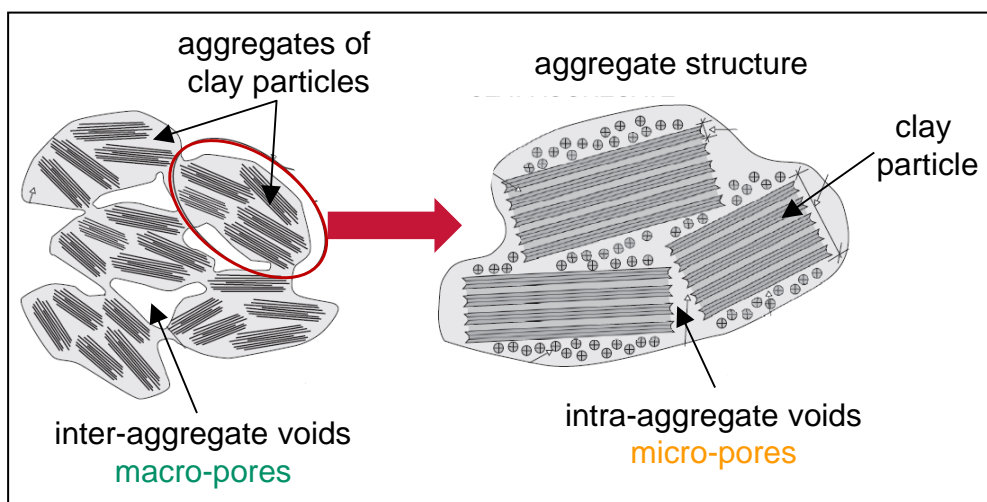


**Figure 3-8.** Conceptual illustration of a double porosity structure

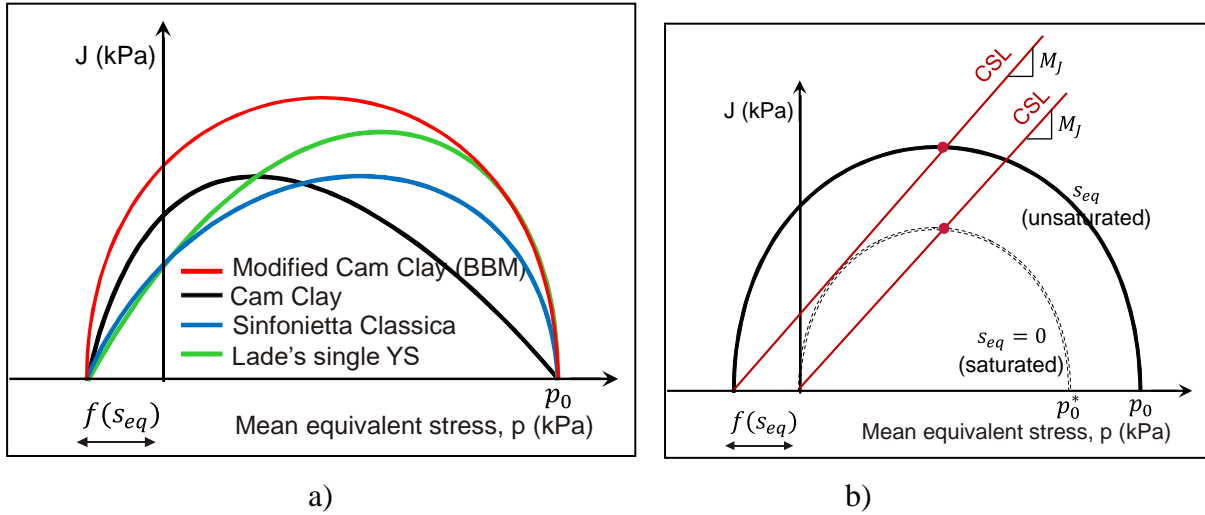


**Figure 3.9.** a) Possibilities of the yield surface formulation, b) Plastic potential

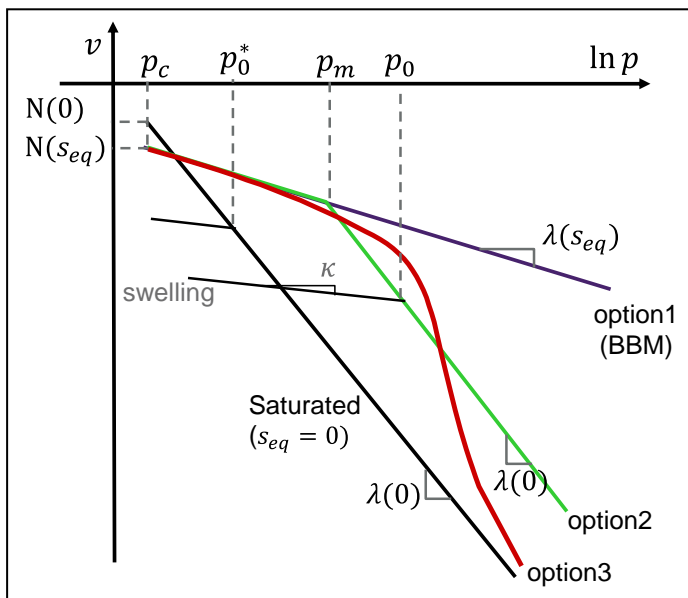


**Figure 3-10.** Variation of  $\lambda$  in the isotropic plane

*Table 3-5 Summary Table of the current capabilities of ICL's IC DSM Model*

Name of the constitutive law:		IC DSM	
Behaviour feature	YES	NO	Remarks
<b>Mechanical behaviour</b>			
Dependence of swelling strain on applied stress (at the same dry density)	x		
Dependence of swelling strains on dry density (at the same stress)	x		
Irreversibility of strains in wetting/drying cycles	x		
Dependence of swelling pressure on dry density	x	x	The swelling pressure predicted for the loose sample seems high. We need to investigate this further.
Stress path dependence from an unsaturated to a saturated state	x		
Stress path dependence from a saturated to an unsaturated state	x		
Double structure/porosity considered?	x		
Are temperature effects considered in the model?		x	Not in the present formulation.
Dependence of strains developed in a temperature cycle (increase/decrease) on OCR (or stress)		x	No temperature effects are considered.
<b>Hydraulic behaviour (retention curve)</b>			
Hysteresis	x		
Dependence on void ratio	x		
Double structure/porosity considered?		x	

### 3.6 Quintessa, UK

The model developed by Quintessa is called the Internal Limit Model (ILM). It alludes to a rather different process of constitutive model formulation based on an interesting empirical observation: the fact that three important relationships:

- The swelling pressure of the bentonite versus dry density; (Figure 3-11)
- Suction versus water content; (Figure 3-12)
- Void ratio versus vertical stress for loading and unloading (oedometer tests). (Figure 3-13)

can be described by a single exponential equation of the form

$$p = p_0 * \exp\left(\frac{-e}{\lambda}\right)$$

where the definition of  $p$  depends on the relationship being considered.

The curves corresponding to those relationships constitute Internal Limit Curves. They suggest that for a given dry density of the bentonite there is a limiting stress that the material can support be that stress due to swelling, compaction or suction. In addition, it is assumed that suction is related to the difference between free swelling suction and stress.

The full formulation of the model as a fully couple thermo-hydro mechanical model incorporates the Modified Cam Clay model to account for plastic deformation. It should be noted that the plastic and swelling strains are computed separately; the latter is based on the change of water content. Thermal strains are incorporated via a simple thermal expansion model. The model assumes a single porosity and no hydraulic hysteresis is considered.

Current capabilities of the model are summarised in Table 3-6.

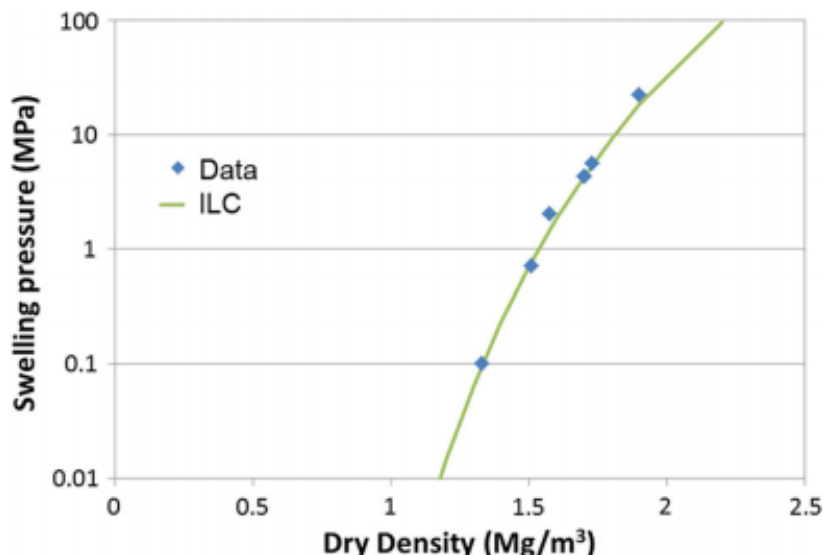


**Figure 3-11.** Internal limit curve for swelling pressure-dry density

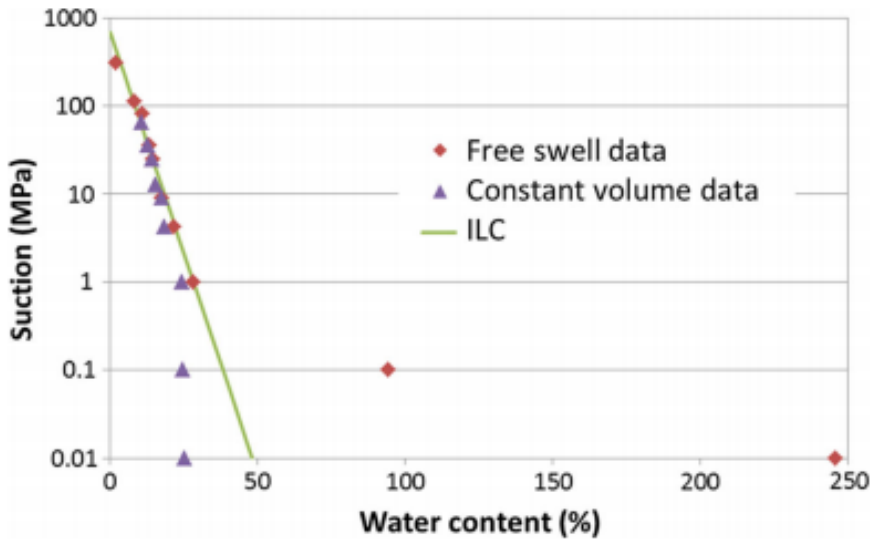


Figure 3-12. Internal limit curve for suction-water content

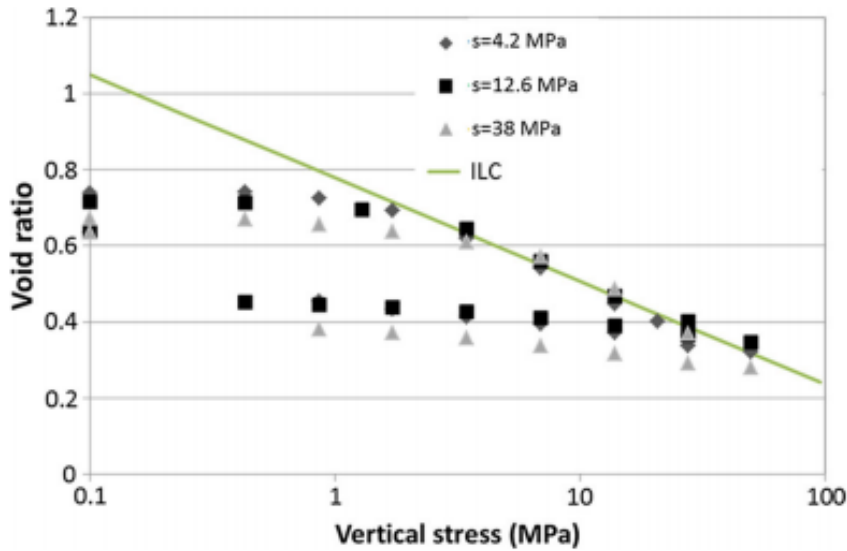


Figure 3-13. Internal limit curve for void ratio – vertical stress

**Table 3-6** Summary Table of the current capabilities of Quintessa's ILM model

Name of the constitutive law: Internal Limit Model (ILM)			
Behaviour feature	YES	NO	Remarks
<b>Mechanical behaviour</b>			
Dependence of swelling strain on applied stress (at the same dry density) (Figure1)	✓		
Dependence of swelling stress on dry density (at the same stress) (Figure 1)	✓		
Irreversibility of strains in wetting/drying cycles (Figure 2)	✓		
Dependence of swelling pressure on dry density (Figure 4)	✓		
Stress path dependence from an unsaturated to a saturated state (Figure 5)	✓		
Stress path dependence from a saturated to an unsaturated state (Figure 6)	✓		
Double structure/porosity considered?		X	
Are temperature effects considered in the model?	✓		
Dependence of strains developed in a temperature cycle (increase/decrease) on OCR (or stress) (Figure 7)	✓		
<b>Hydraulic behaviour (retention curve)</b>			
Hysteresis		X	
Dependence on void ratio	✓		
Double structure/porosity considered?		X	

### 3.7 Teknologian tutkimuskeskus, (VTT), FI

The report by VTT focuses on the general THM formulation but a few details are provided regarding the mechanical constitutive model that it is being developed in conjunction with the Universidad de Castilla – La Mancha (UCLM).

The adopted elastoplastic mechanical model uses a double structure assumption (Figure 3-14). The two constitutive mechanical models Barcelona Basic Model (BBM), and the Barcelona Expansive Model (BExM) are adopted as modelling frameworks for the macro- and the microstructure and the coupling between them in confined conditions. The formulation of the BBM and BExM has been modified to allow for anisotropy in the stress-strain relationship. In addition, the model has been extended using a state surface approach that accounts for chemo-mechanical coupling and for free-swelling processes.

The current capabilities of the model are presented in Table 3.7, although no supporting model results are supplied in the accompanying report.

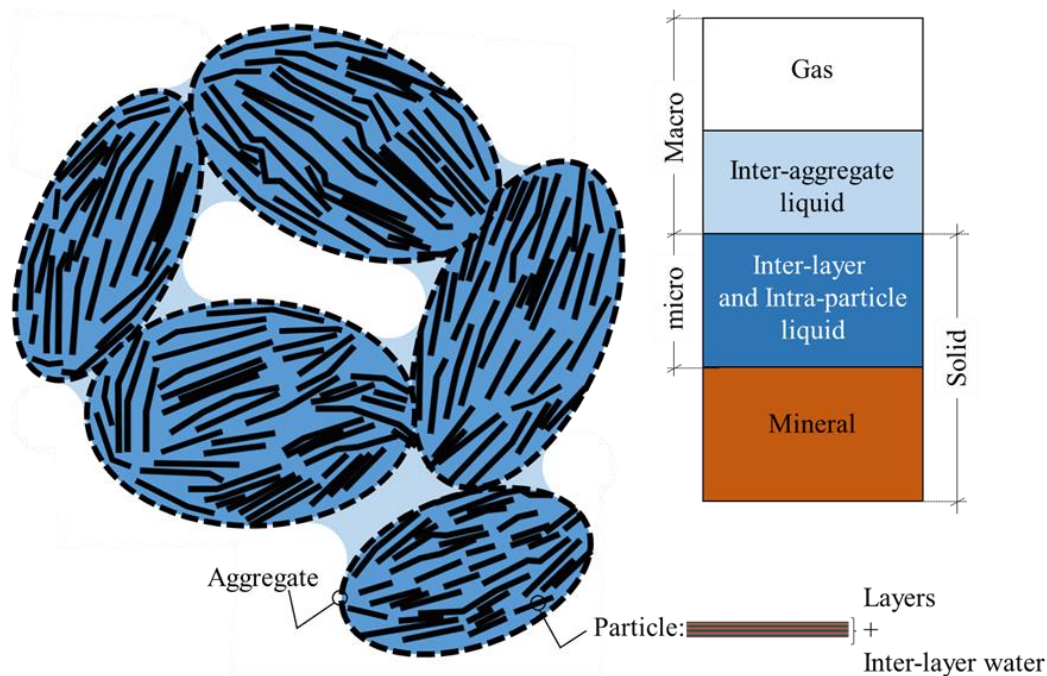


*Figure 3-14. Conceptual scheme of the double structure material*

*Table 3-7 Summary Table of the double structure elastoplastic model by VTT-UCLM*

Name of the constitutive law:			
Behaviour feature	YES	NO	Remarks
<b>Mechanical behaviour</b>			
Dependence of swelling strain on applied stress (at the same dry density)	x		Through the dependency of microwater chemical potential on pressure component of the stress and the water exchange term
Dependence of swelling strains on dry density (at the same stress) (	x		Through the dependency of microwater chemical potential on pressure component of the stress and the water exchange term
Irreversibility of strains in wetting/drying cycles		x	no suction increase/decrease yield surfaces, but possibly plastic strains with the implemented yield surfaces
Dependence of swelling pressure on dry density	x		Through the dependency of microwater chemical potential on pressure component of the stress and the water exchange term
Stress path dependence from an unsaturated to a saturated state			Possibly, depends on the simulation setup (no specific mechanisms determined for this behaviour, though)
Stress path dependence from a saturated to an unsaturated state			Possibly, depends on the simulation setup (no specific mechanisms determined for this behaviour, though)
Double structure/porosity considered?	x		
Are temperature effects considered in the model?	x		Thermal expansion
Dependence of strains developed in a temperature cycle (increase/decrease) on OCR (or stress)		x	
<b>Hydraulic behaviour (retention curve)</b>			
Hysteresis		x	
Dependence on void ratio	x		
Double structure/porosity considered?	x		

### 3.8 Universitat Politècnica de Catalunya (UPC), ES

The model presented by UPC is an improved version of the Barcelona Expansive Model (BExM) based on elasto-plasticity and a double structure formulation (Figure 3-15). The interaction between the two structure levels is expressed by means of interaction functions (Figure 3-16). Only isothermal conditions are considered.

The following enhancements have been incorporated:

- A more consistent definition of porosity and volume fractions
- The microstructure may be unsaturated
- A consistent relationship for the elastic parameters of microstructure and macrostructure
- No hydraulic equilibrium between microstructure and macrostructure
- A linear relationship for the water exchanges between microstructure and macrostructure
- A more physically based definition of the interaction functions.

The current capabilities of the model are indicated in Table 3-8

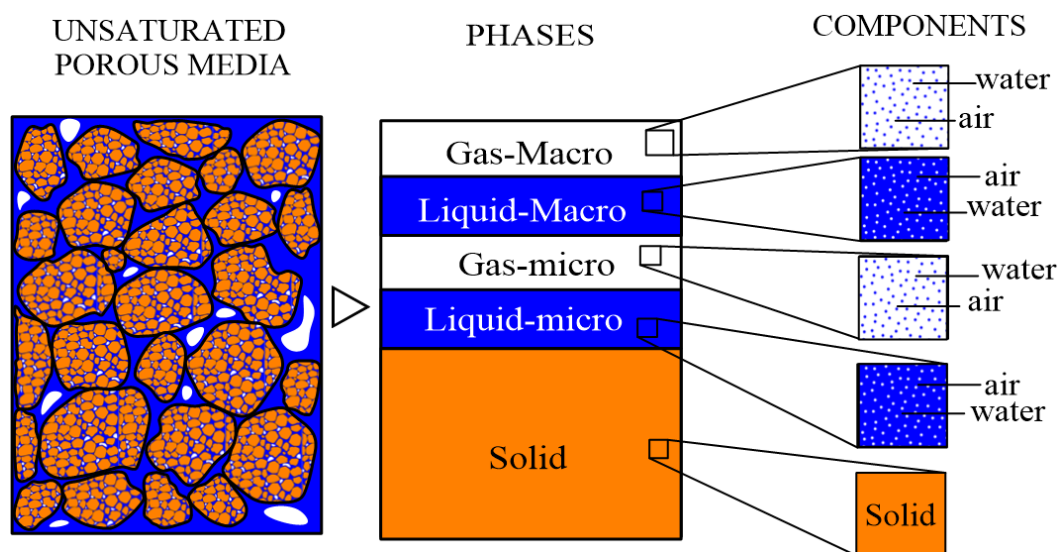


*Figure 3-15. Conceptual scheme of the double structure material*

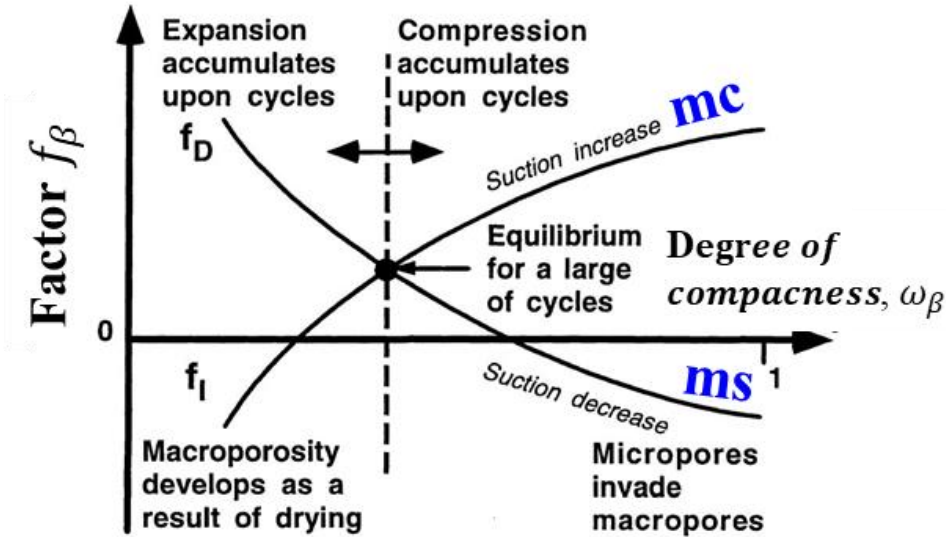


Figure 3-16. Interaction functions indicating the physical phenomena involved

**Table 3-8 Summary Table of the enhanced BExM of UPC**

Name of the constitutive law: <b>Double Structure Model</b>			
Behaviour feature	YES	NO	Remarks
<b>Mechanical behaviour</b>			
Dependence of swelling strain on applied stress (at the same dry density) ( <b>Fel! Hittar inte referenskölla.</b> )	X		The location of the stress state respect to the LC curve generates this dependence. See Section <b>Fel! Hittar inte referenskölla.</b>
Dependence of swelling stress on dry density (at the same stress)	---	---	The analysis performed at section <b>Fel! Hittar inte referenskölla.</b> does not reflect this dependence in a single element test. The imposition of the stress state avoids the evolution of swelling stress. The better way to check this dependency is through swelling pressure test (Section <b>Fel! Hittar inte referenskölla.</b> )
Irreversibility of strains in wetting/drying cycles ( <b>Fel! Hittar inte referenskölla.</b> )	X		The irreversible strains are generated in wetting/drying paths that cross the LC curve. See Section <b>Fel! Hittar inte referenskölla.</b>
Dependence of swelling pressure on dry density ( <b>Fel! Hittar inte referenskölla.</b> )	X		At the same initial conditions, stress state and suction, different values of the isotropic yield stress for saturated conditions $P_o^*$ (dry density) generate different kinetics and final values of swelling pressure. See Section <b>Fel! Hittar inte referenskölla.</b>
Stress path dependence from an unsaturated to a saturated state	X		This feature comes from the hydro-mechanical (HM) constitutive formulation. Numerical testing requires an additional effort related to the numerical implementation. The transition of saturated to unsaturated (or vice versa) is not trivial issue with the net stress as stress variable.
Stress path dependence from a saturated to an unsaturated state	X		
Double structure/porosity considered?	X		The expansive clay is considered as a multiphase porous media composed by the arrangement of clay aggregates and micro- and macro-pores
Are temperature effects considered in the model?		X	The formulation presented here is Hydro-Mechanical (HM). This team is working (in parallel way) on the Thermo-Hydro-Mechanical (THM) coupling.

Dependence of strains developed in a temperature cycle (increase/decrease) on OCR (or stress)		X	---
<b>Hydraulic behaviour (retention curve)</b>			
Hysteresis		X	---
Dependence on void ratio		X	Ongoing work.
Double structure/porosity considered?	X		Macro- and micro-structural levels are associated to different water retention curve (WRC). The evolution of these WRC depends on the successful development of the above feature.

### 3.9 Université de Liège (ULg), BE

The model developed by the Université de Liège differs from other models in the fact that a double porosity is adopted for the hydraulic component of the model whereas a single structure model is used for the mechanical component. Only isothermal conditions are addressed.

Water storage and hydration mechanisms are considered in a double structure framework assuming a bimodal pore distribution that may evolve under hydration to single mode one. The basic parameter in the hydraulic formulation is the water ratio  $e_w$  that is considered distributed in the two levels of porosity. It thus incorporates the effect of void ratio on water retention.

For the mechanical behaviour, the model uses the elastoplastic Barcelona Basic Model (BBM) (Figure 3-17). The model has been implemented in the computer code LAGAMINE. However, the elastic stiffness for suction changes has been modified, through a limit degree of saturation, to take into account that bentonite-based materials are capable to sustain high value of suction without desaturating due to their high air-entry value (Figure 3-18).

Table 3-9 presents a summary of the current capabilities of the model.

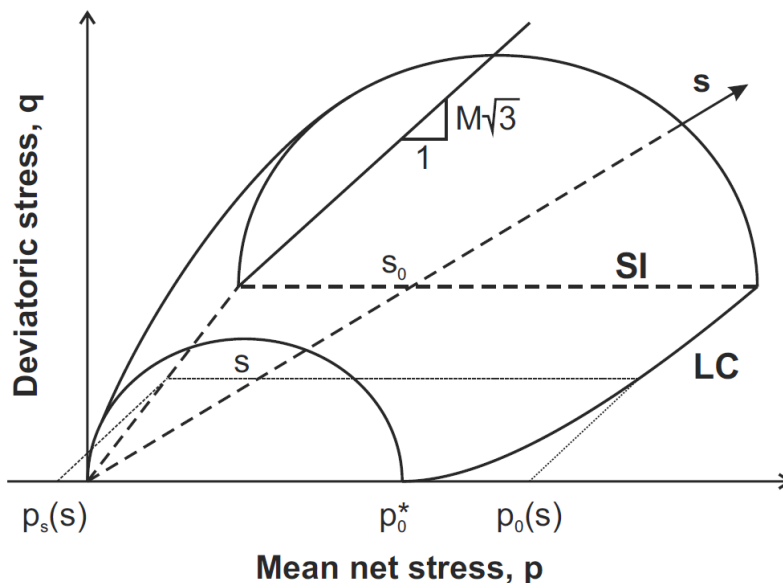


**Figure 3-17.** Yield function of the Barcelona Basic Model

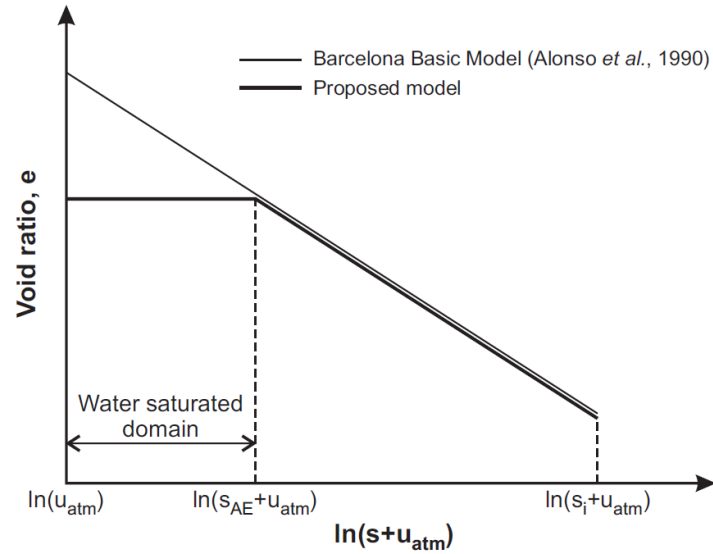


**Figure 3-18.** Evolution of void ratio along a wetting path under constant mean net stress. Barcelona Basic Model and proposed model

*Table 3-9 Summary Table of the ULg model*

Name of the constitutive law:			
Behaviour feature	YES	NO	Remarks
<b>Mechanical behaviour</b>			
Dependence of swelling strain on applied stress (at the same dry density) (Figure1)	✓		
Dependence of swelling strains on dry density (at the same stress) (Figure 1)	✓		
Irreversibility of strains in wetting/drying cycles (Figure 2)	✓		
Dependence of swelling pressure on dry density (Figure 4)	✓		
Stress path dependence from an unsaturated to a saturated state (Figure 5)	✓		
Stress path dependence from a saturated to an unsaturated state (Figure 6)			Not treated
Double structure/porosity considered?		X	
Are temperature effects considered in the model?		X	
Dependence of strains developed in a temperature cycle (increase/decrease) on OCR (or stress) (Figure 7)		X	
<b>Hydraulic behaviour (retention curve)</b>			
Hysteresis	✓		
Dependence on void ratio	✓		
Double structure/porosity considered?	✓		

## 4 Concluding remarks

The present Deliverable has presented an account of the mechanical constitutive models available at the start of the project based on the reports submitted by the different teams that constitute Annexes to this document.

The scope of the constitutive models presented is very wide, providing, already at the start of the project, a large diversity of approaches and formulations that will allow the assessment of their relative capacity to model satisfactorily the mechanical behaviour of the bentonite through the validation exercises performed within Work Package 5.

In spite of this diversity, most of the models are developed within the framework of elasto-plasticity although, naturally, the details of the formulation differ significantly from one model to another. There is nevertheless a model (by CU) that is based on the hypoplasticity framework. In addition two models (ClayTech, Quintessa) take relevant empirical observations as a starting point allowing the development of the models from the bottom up, in contrast to the more usual approach.

A very common conceptual assumption for many models is the adoption of a double structure (or double porosity approach) for the formulation of the mechanical, and, to a lesser extent, the hydraulic components of the model. This is probably prompted (at least partially) by the anticipation that it will be necessary to simulate the behaviour of pellet-based materials where the double structure is readily apparent. This inevitably adds a significant additional complexity to the formulation and the application of the models including the need to determine additional model parameters.

A number of the models may account for non-isothermal conditions (e.g, Clay Tech, CU, VTT, EPFL, Quintessa) often through the addition of a thermal expansion term. In contrast, the ACMEG model of EPFL integrates the thermal part component of the model in a coupled way with the rest of the formulation. It is unclear at present what level of complexity will be required for the thermal component of the model to deal appropriately with non-isothermal situations.

The models have been preliminary assessed in relation to a number of bentonite behaviour features that are considered key to simulate properly the behaviour of the bentonite, especially in relation to the evolution of heterogeneity in a variety of HM and THM settings. It is interesting to note that most of those features can be already qualitatively simulated by the current state of development of most of the models. This, of course, does not mean that the models will not require additional modifications depending on the results of the validation exercises. It may be concluded, however, that the current set of mechanical constitutive models constitute a very good and promising starting platform to undertake the modelling activities envisaged in the project.

## Appendix 1

### INSTRUCTIONS AND SUGGESTIONS FOR REPORTS FROM MODELLING TEAMS

#### 1. Introduction

According to the planning of the Beacon project, Deliverable 3.1 has to be submitted by month 9 from the start of the test. The subject of Deliverable 3.1 is “Description of the constitutive models available at the start of the project. Conceptual bases, mathematical description and model capabilities and shortcomings”. To compile this Deliverable, it is necessary for the individual modelling teams to provide reports describing the current state of their constitutive models. Those reports will be added to the Deliverable as Appendices and they will be synthesised in the main body of the document.

This note contains a number of instructions and suggestions for developing the individual reports. It is recognized that different models are in quite dissimilar stages of development. Therefore, the instructions and suggestions presented herein should be applied with considerable flexibility in accordance to the particular requirements and constraints of each team.

#### 2. Table of contents

It is suggested that the Table of contents of the individual reports is structured as follows:

- Introduction
- Background (physical, mathematical...)
- Basic hypotheses and scope (hydraulic, thermal, chemical...)
- Mathematical description
  - Theoretical framework (plasticity, hypoplasticity...)
  - Equations
- Input parameters and their sources
- Performance (qualitative, quantitative...)
- Conclusions

#### 2. Qualitative features of the constitutive model

An important part of the presentation of the constitutive models is the description of some key qualitative features. In this way, the capabilities and limitations of each constitutive model can be more readily assessed. Below a number of features to be considered are suggested. They are not specific tests cases, this is why they are not precisely specified and the teams are free to explore these issues in the way they find more suitable. Naturally, one way is to run the constitutive model on the suggested stress paths (as single element tests) using credible input parameters for the model but other means can also be used. Again, there is no need at the present time for the teams to consider all cases below.

### 2.1 Dependence of swelling strain on applied stress and on dry density

The stress paths to be followed to check this potential dependence are simply a number of swelling tests at different stresses where suction is reduced from some initial value down to zero (Figure 1). Those paths can be followed assuming different initial dry densities.

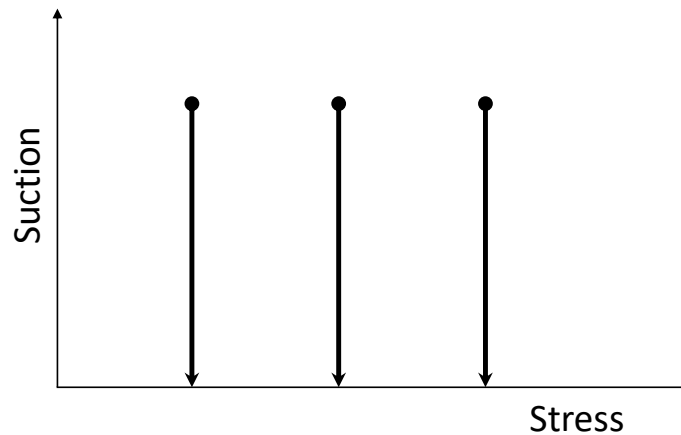


Figure 1. Swelling tests at constant stress. Stress may be vertical total stress (in oedometer tests) or mean total stress (in isotropic loading tests)

### 2.2 Irreversibility of strains in wetting/drying cycles

The stress paths to be followed in this case involve a suction reduction to zero and a subsequent increase of suction to the initial value (Figure 2). In this way, it can be checked whether the strains recover at the end of the cycle or whether irreversible strains are produced instead.

### 2.3 Behaviour during swelling stress test. Dependence of swelling pressure on dry density.

A swelling stress test involves the reduction of suction from an initial value down to zero while maintaining the volume of the specimen constant throughout. Now total stress is not controlled but it evolves during the test (Figure 3). The stress value at the end of the test is called the swelling pressure. It would be interesting to observe the type of stress paths obtained for a particular model.

Swelling pressure is strongly dependent on dry density (Figure 4). The dependence of swelling pressure on dry density is an important feature that should be checked.

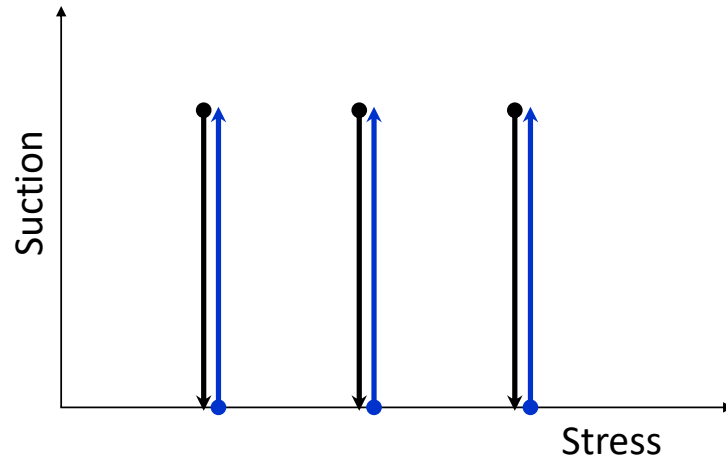


Figure 2. Swelling/drying tests at constant stress. Stress may be vertical total stress (in oedometer tests) or mean total stress (in isotropic loading tests)

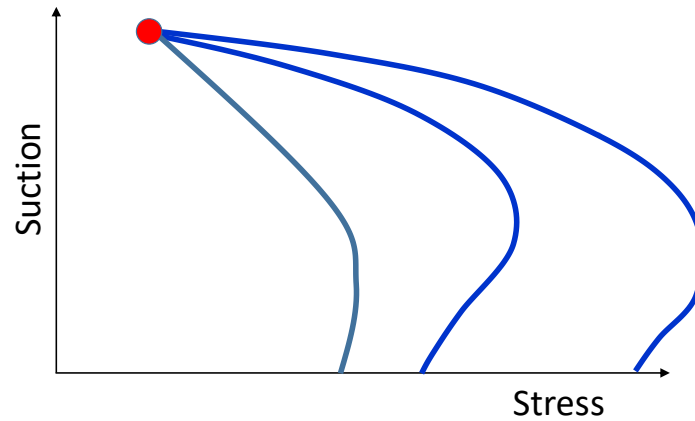


Figure 3. Suction-stress paths in swelling pressure tests. Stress may be vertical total stress (in oedometer tests) or mean total stress (in isotropic loading tests)

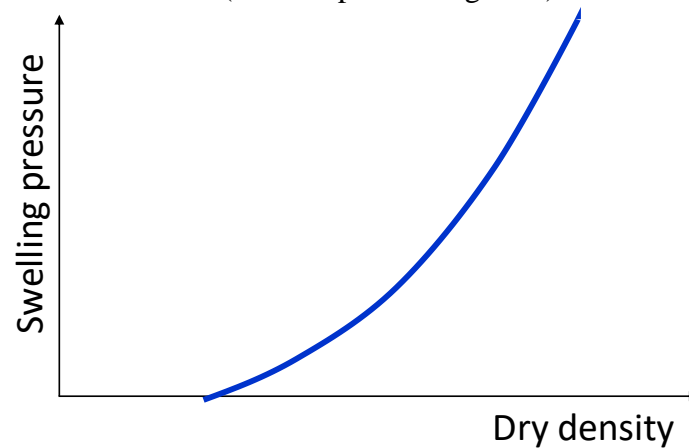


Figure 4. Possible dependence of swelling pressure on dry density

*2.4 Stress path dependence from an unsaturated to a saturated state*

Stress path dependency can be checked by simulating different stress paths starting at the same initial value of suction and stress and finishing at a final common value of stress and zero suction. Three paths are suggested (Figure 5):

- Reduction of suction to zero followed by an increase of stress (red path).
- Increase of stress under constant suction followed by reduction of suction to zero (brown path).
- Swelling pressure test followed by a stress reduction to the final value (blue path).

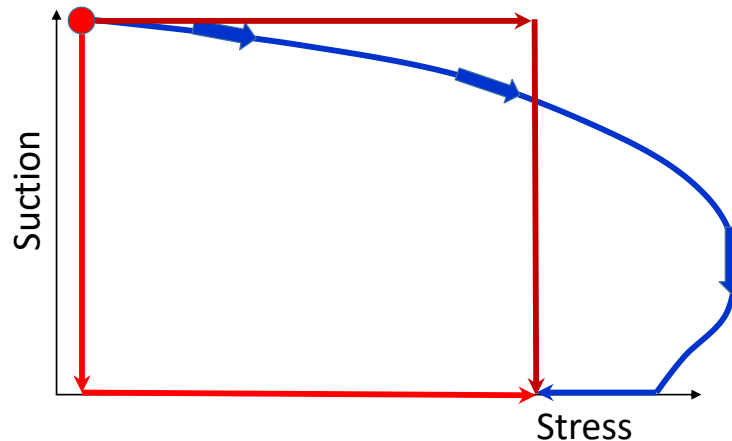


Figure 5. Suggested suction-stress paths to check stress path dependency from an unsaturated to a saturated state. Stress may be vertical total stress (in oedometer tests) or mean total stress (in isotropic loading tests)

### 2.5 Stress path dependence from a saturated to an unsaturated state

Stress path dependency can be checked by simulating different stress paths starting at the same initial value stress and zero suction and finishing at a final common value of stress suction. Two paths are suggested (Figure 6):

- Increase of suction followed by an increase of stress at constant suction (red path).
- Increase of stress under zero suction followed by an increase of suction (brown path).

### 2.6 Dependence of strains developed in a temperature cycle (increase/decrease) on OCR (or stress)

For the constitutive models that incorporate a thermal component, it is interesting to check the strains that develop during a cycle of increase/reduction of temperature and its dependence on OCR (overconsolidation ratio) or applied stress (Figure 7). Saturated conditions should be considered but it may also be of interest to observe this behaviour under different values of suction.

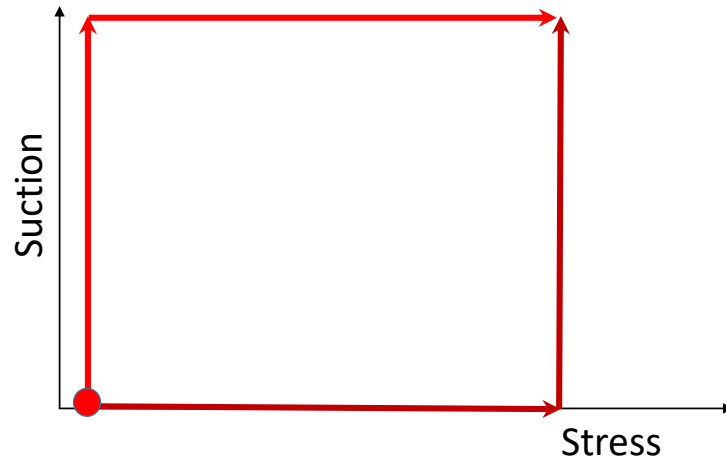


Figure 6. Suggested suction-stress paths to check stress path dependency from a saturated to an unsaturated state. Stress may be vertical total stress (in oedometer tests) or mean total stress (in isotropic loading tests)

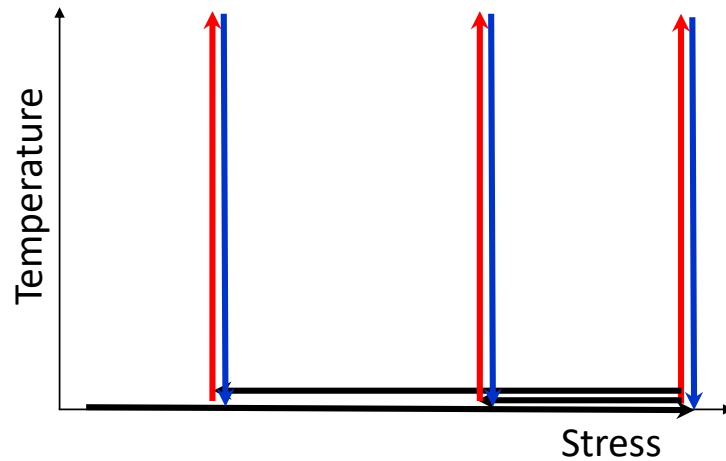


Figure 7. Temperature (increase/decrease) cycle at different stresses. Stress may be vertical total stress (in oedometer tests) or mean total stress (in isotropic loading tests)

### 3. Features Table

The teams should try to fill, as much as possible the attached Table 1 according to the features exhibited by their models. Recognizing that sometimes a straight YES/NO answer is not possible, a remarks box has been included in the Table. The completed Tables should provide a fast way to assess the capabilities and limitations of the constitutive models at the present stage of development.

Table 1. Features Table

Name of the constitutive law:			
Behaviour feature	YES	NO	Remarks
<b>Mechanical behaviour</b>			
Dependence of swelling strain on applied stress (at the same dry density) (Figure1)			
Dependence of swelling stress on dry density (at the same stress) (Figure 1)			
Irreversibility of strains in wetting/drying cycles (Figure 2)			
Dependence of swelling pressure on dry density (Figure 4)			
Stress path dependence from an unsaturated to a saturated state (Figure 5)			
Stress path dependence from a saturated to an unsaturated state (Figure 6)			
Double structure/porosity considered?			
Are temperature effects considered in the model?			
Dependence of strains developed in a temperature cycle (increase/decrease) on OCR (or stress) (Figure 7)			
<b>Hydraulic behaviour (retention curve)</b>			
Hysteresis			
Dependence on void ratio			
Double structure/porosity considered?			



#### **4. Final Remarks**

It is envisaged that the individual reports will have a length of about 15-25 pages but the teams should use their judgement to go outside these limits (in any direction) if necessary. Please, use the Beacon Deliverable template for format.

If at all possible, the documents should be written using Word.

Reports should be sent to [antonio.gens@upc.edu](mailto:antonio.gens@upc.edu) by **February 28th, 2018**.

#### **Acknowledgements**

This project receives funding from the Euratom research and training programme 2014-2018 under grant agreement No 745942.

# D3.1



## Description Of The Current State Of Constitutive Models

### DELIVERABLE (D3.1)

## ANNEX A

Author(s): **Vinay Kumar, Annika Schäfers, Hua Shao**

Reporting period: 01/06/17 – 30/11/18

Start date of project: **01/06/17**

Duration: 48 Months

This project receives funding from the Euratom research and training programme 2014-2018 under grant agreement No 745 942		
<b>Dissemination Level</b>		
<b>PU</b>	Public	X
<b>RE</b>	Restricted to a group specified by the partners of the Beacon project	
<b>CO</b>	Confidential, only for partners of the Beacon project	



**REVIEW**

<b>Name</b>	<b>Internal/Project/External</b>	<b>Comments</b>

**DISTRIBUTION LIST**

<b>Name</b>	<b>Number of copies</b>	<b>Comments</b>
Athanasios Petridis (EC) Christophe Davies (EC)  Beacon partners		

## **Abstract**

The current state of a limited selection of constitutive models implemented in OpenGeoSys are explained using simulations of simplified coupled hydro-mechanical models under various boundary conditions. The necessary theoretical background is explained and the simulation results are compiled.

## Content

<b>2</b>	<b>Introduction</b> .....	<b>5</b>
<b>3</b>	<b>Basic hypothesis and scope</b> .....	<b>5</b>
3.1	Thermal Processes (T) .....	5
3.2	Hydraulic Processes (H) .....	6
3.3	Mechanical model: M Process.....	9
<b>4</b>	<b>Coupled Models</b> .....	<b>9</b>
<b>5</b>	<b>Input parameters and sources</b> .....	<b>11</b>
<b>6</b>	<b>Performance: Qualitative and Quantitative</b> .....	<b>11</b>
6.1	Base Test Case: Water saturation in an uniaxially unconstrained domain .....	12
6.2	Saturation in a constrained domain.....	15
6.3	Saturation in a domain under confining stresses .....	16
<b>7</b>	<b>Conclusions</b> .....	<b>19</b>
<b>8</b>	<b>Bibliography</b> .....	<b>21</b>
	Figure 1: Capillary pressure – saturation relationship for Bentonite .....	8
	Figure 2: Relative permeability – saturation relationship for Bentonite .....	8
	Figure 3: Model domain used in the test cases, the output is read along the dotted line. ....	12
	Figure 4: Domain geometry along with the FEM discretization. The points in the middle are used to generate output.....	12
	Figure 5: Saturation profiles in the model domain at t=17 hours, 7 days and 73 days .....	13
	Figure 6: Pressure profile along a line in the middle of the domain. ....	13
	Figure 7: Stress profile along a line in the middle of the domain. ....	14
	Figure 8: Vertical displacement along a line in the middle of the domain .....	14
	Figure 9: Temporal evolution of the saturation and the effective stress at two control points in the domain .....	15
	Figure 10: Pressure profile along a line in the middle of the domain. ....	15
	Figure 11: Displacement profile along a line in the middle of the domain.....	16
	Figure 12: Temporal evolution of the saturation and the effective stress at two control points in the domain.....	16
	Figure 13: Vertical stress and displacement profile along a line in the middle of the domain at confining stress 5 MPa. ....	17
	Figure 14: Temporal evolution of the saturation and the effective stress at two control points in the domain at confining stress of 5 MPa.....	17
	Figure 15: Vertical stress and displacement profile along a line in the middle of the domain at confining stress of 10 MPa.....	18
	Figure 16: Temporal evolution of the saturation and the effective stress at two control points in the domain at confining stress of 10 MPa.....	18
	Figure 17: Vertical stress and displacement profile along a line in the middle of the domain at confining stress of 20 MPa.....	19
	Figure 18: Temporal evolution of the saturation and the effective stress at two control points in the domain at confining stress of 20 MPa.....	19

## 1 Introduction

The BGR uses OpenGeoSys (OGS) (Kolditz et al. 2012a) for coupled THM simulations in the framework of nuclear waste disposal. OGS is as a free, multi-platform scientific tool for the simulation of single or coupled processes in porous and fractured media. The models implemented in OGS range from single thermal (T), hydraulic (H), mechanical (M) and chemical (C) processes to complex coupled THMC processes.

## 2 Basic hypothesis and scope

OGS solves the governing equations of THMC processes formulated in the framework of continuum mechanics. For the scope of this project only the THM capabilities of OGS is explained and only the HM capabilities are utilized for model tests. The following forms a non-comprehensive list of processes available in OGS

- Heat transport in a multiphase continua with multiple fluid and solid phases,
- Single and multiphase flow in deformable porous media,
- Mechanical processes involving elasticity, poro- and thermoelasticity, elastoplasticity and viscoelasticity.

At the time of this report, the following capabilities are available in OGS for the simulation of coupled THM processes.

### 2.1 Thermal Processes (T)

The heat transport problem is modelled either with the equation for pure conduction in the case of a solid or a stationary multiphase continuum or with the advection-diffusion equation in a multiphase continuum involving fluid flow. The former is used when the flow velocities are expected to be low, which is relevant to low permeable media encountered in the storage of HAW. The following equation describes the heat transport at steady state under pure conduction.

$$q = -\lambda_{pm} \nabla T \quad (1.1)$$

Where

- $q \left[ \frac{W}{m^2} \right]$ : the heat flux per unit area,
- $\lambda_{pm} \left[ \frac{W}{m K} \right]$ : the thermal conductivity of the porous medium,
- $T [K]$ : the temperature.

Eq. (1.2) is used when the contribution to the heat transport by the flow is comparable to that from thermal diffusion. The following equation gives the conservation law for heat transport under the combined influence of convection and conduction for a medium with one solid phase (superscript “s”) and one or many fluid phases (superscript “ $\alpha$ ”)

$$\left( (1-\phi) \rho^s c_p^s + \sum_{\alpha=l,g} \phi S^\alpha \rho^\alpha c_p^\alpha \right) \frac{\partial T}{\partial t} + \nabla \cdot \left( \sum_{\alpha=l,g,s} \mathbf{q}^{E\alpha} \right) = Q^E \quad (1.2)$$

Where

- $\rho \left[ \frac{kg}{m^3} \right]$ : the density,
- $\phi [-]$ : the porosity,
- $S^\alpha [-]$ : the saturation of the fluid phase  $\alpha$ ,
- $\mathbf{q}^{E\alpha} = \phi \sum_{\alpha=l,g} (c^\alpha \rho^\alpha) T_V - \lambda \nabla T \left[ \frac{W}{m^2} \right]$ : the total advective and diffusive temperature fluxes of all the phases and
- $C_p \left[ \frac{J}{kg K} \right]$ : the specific heat capacity at constant pressure.

Thermal processes will not be considered in the test cases investigated in this report.

## 2.2 Hydraulic Processes (H)

The hydraulic processes are modelled using the variation of the mixture theory viz. the theory of porous media at the continuum scale in a Representative Elementary Volume (REV) (Bear 1988). In the chosen REV the governing equation describing single-phase fluid flow in porous media is given by the Darcy's law

$$\mathbf{q} = -\frac{\mathbf{K}}{\mu} (\nabla p - \rho \mathbf{g}) \quad (1.3)$$

Where

- $\mathbf{K} [m^2]$ : the intrinsic permeability tensor,
- $\mu \left[ \frac{kg}{ms} \right]$ : the dynamic viscosity,
- $\rho \left[ \frac{kg}{m^3} \right]$ : the fluid density,
- $\mathbf{g} \left[ \frac{m}{s^2} \right]$ : the gravitation vector.

- $\nabla p \left[ \frac{Pa}{m} \right]$ : the pressure gradient.

The above law is extended, with the assumption of immiscible fluids, to multiphase flow by the introduction of relative permeability of phase  $\alpha$  as  $k_r^\alpha$  and separate phase pressures  $\nabla p^\alpha$  for the constitutive fluid phases. The extended law is given by

$$q = -\rho^\alpha \frac{\mathbf{K} \cdot k_r^\alpha}{\mu^\alpha} (\nabla p^\alpha - \rho^\alpha \mathbf{g}) \quad (1.4)$$

Introducing the concept of saturation and by defining the saturation  $S^\alpha$  as the measure of the volume of the pore-space occupied by phase  $\alpha$ , the law of conservation of mass is formulated as below

$$\frac{\partial}{\partial t} \left( \sum_{\alpha=l,g} \rho^\alpha S^\alpha \phi \right) + \nabla \cdot (\mathbf{q}^\alpha) = Q^\alpha \quad (1.5)$$

This equation gives the conservation of each component of a phase.  $J^\alpha$  gives the sum of the advective and diffusive fluxes of the liquid phases. The closure conditions for the model are given by defining the capillary pressure  $p_c$  (1.6), the fluid saturations (1.7), the relative permeabilities (1.8) and by relating the capillary pressure and relative permeabilities to the saturation (Figure 1 and Figure 2) by either the Brooks Corey model or the van Genuchten model given by equation (1.9) and (1.10).

$$p^g - p^l = p^c \quad (1.6)$$

$$\sum_{\alpha=l,g} S^\alpha = 1 \quad (1.7)$$

$$\sum_{\alpha=l,g} k_r^\alpha = 1 \quad (1.8)$$

$$S_{\text{eff}} = \frac{S^w - S_r^w}{1 - S_r^w} = \left( 1 + (\xi p_c)^n \right)^{-m}, p_c > 0 \quad (1.9)$$

$$\mathbf{k}_{\text{rel}}(h) = \frac{1 - (\xi h)^{n-2} [1 + (\xi h)^n]^{-m}}{[1 + (\xi h)^n]^{2m}} \quad (1.10)$$

Where  $\xi$ ,  $n$  and  $m$  are the van Genuchten parameters,  $S_r^w$  the residual saturation and  $h$  defined by

$$h = \frac{p^\alpha}{\rho^\alpha g} \quad (1.11)$$

With the above conditions, different formulations of the multiphase flow problem can be derived with different primary variables.

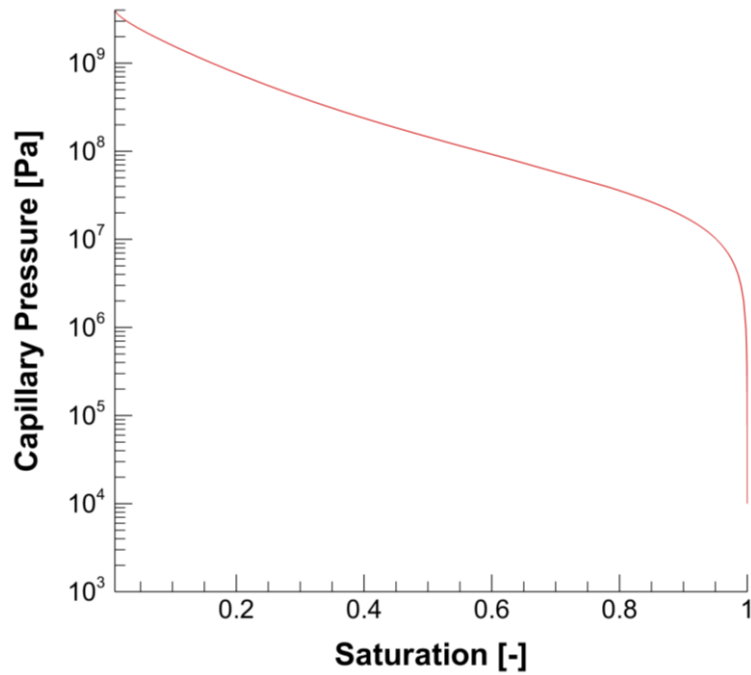


Figure 1: Capillary pressure – saturation relationship for Bentonite (Kolditz et al. 2012b)

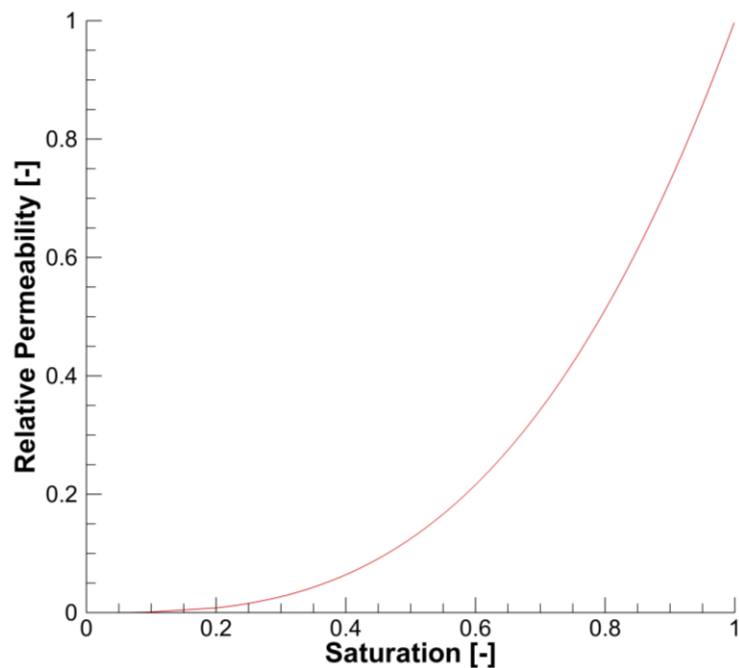


Figure 2: Relative permeability – saturation relationship for Bentonite (Kolditz et al. 2012b)

The above system can be further simplified for the specific case of gas-water flow. Under the assumption that the gas phase is connected to the atmosphere, the gas pressure can be considered to be always at atmospheric pressure and is neglected. In eq. (1.6) the capillary pressure is now equal to the negative of the fluid pressure. The mass balance equation (1.5) for the gas phase is likewise neglected and only the mass balance of the liquid phase is considered.

Compositional effects in a multiphase system arising usually due to non-isothermal conditions are considered only in limited scope. Phase change due to vaporization is considered whereas

condensation is neglected. The mass balance of the gas phase is likewise neglected in (1.5). Only the vapor flux (the flux of water vapor in the gas phase) is considered. A simplified expression for the vapor flux is obtained by approximating the diffusive flux in the gas phase to be dependent on the gradients of pressure and temperature (Rutqvist et al. 2001).

$$\mathbf{q}_{D,w}^g = -D_{pv} \nabla p^l - D_{Tv} \nabla T \quad (1.12)$$

The two new diffusion coefficients  $D_{pv}$  and  $D_{Tv}$  are respective functions of temperature, pressure and physical constants. This model is referred to as the Richard's flow model.

### 2.3 Mechanical model: M Process

The mechanical model used previously to model processes in bentonite is linear elasticity in the form of the generalized Hooke's law which links the components of the stress tensor  $\boldsymbol{\sigma}$  to the components of the strain tensor  $\dot{\boldsymbol{\delta}}$  through the 4<sup>th</sup> order stiffness tensor  $\mathbf{C}$ .

$$\boldsymbol{\sigma} = \mathbf{C} : \dot{\boldsymbol{\delta}} \quad (1.13)$$

Assuming small strains, the vector of deformation is used to calculate the components of the strain tensor with the equation

$$\dot{\boldsymbol{\delta}} = \frac{1}{2} (\nabla \mathbf{u} + \nabla^T \mathbf{u}) \quad (1.14)$$

The stresses calculated from (1.13) is then used in the equation of conservation of momentum of the solid phase

$$\nabla \cdot \boldsymbol{\sigma} + \mathbf{f}_b = \rho \frac{\partial \mathbf{v}}{\partial t} \quad (1.15)$$

Where

- $\boldsymbol{\sigma} \left( \frac{kg}{m s^2} \right)$ : the stress tensor
- $\mathbf{f}_b \left( \frac{kg}{m s^2} \right)$ : the body forces
- $\rho \left( \frac{kg}{m^3} \right)$ : the density of the solid phase and
- $\mathbf{v} \left( \frac{m}{s} \right)$ : the velocity of the solid phase.

If the acceleration of the solid phase is small, the right hand side of (1.15) can be neglected.

## 3 Coupled Models

The previously explained models can be coupled to each other in various ways. The hydro-mechanically (HM) coupled models relevant for the mechanical evolution of bentonite is explained in the following sections under the assumption of isothermal and saturated

conditions. The models can be extended to consider non-isothermal conditions and unsaturated conditions in the context of multiphase flow or Richard's model. A HM coupled model is derived by introducing the concept of effective stress  $\boldsymbol{\sigma}'$  in the mechanical constitutive law which is defined as the difference total stress  $\boldsymbol{\sigma}$  and the pore water pressure  $p$ .

$$\boldsymbol{\sigma}' = \boldsymbol{\sigma} - \alpha_{\text{Biot}} p \mathbf{I} \quad (1.16)$$

The above definition of the effective stress describes how the stresses in the system are distributed not only over the solid skeleton but also over the water phase. The definition includes the Biot's coefficient  $\alpha_{\text{Biot}}$  which is based on the modulus of compression of the porous skeleton  $K$  and that of the grains of the porous system  $K_s$ .

$$\alpha_{\text{Biot}} = 1 - \frac{K}{K_s} \quad (1.17)$$

The poroelastic effective stress (1.16) is used in (1.15) to get the momentum balance of a simplified HM coupled system

$$\nabla \cdot (\boldsymbol{\sigma} - \alpha_{\text{Biot}} p \mathbf{I}) + \rho \mathbf{g} = 0 \quad (1.18)$$

The mass balance can be likewise extended to yield

$$\left( \frac{\phi}{K^w} + \frac{\alpha_{\text{Biot}} - \phi}{K^s} \right) \frac{\partial p}{\partial t} + \nabla \cdot (\mathbf{q}) + \alpha_{\text{Biot}} \nabla \cdot \frac{\partial \mathbf{u}}{\partial t} = 0 \quad (1.19)$$

A THM coupled model for non-isothermal conditions and unsaturated flow is derived by extending the above model with the following additional aspects

- The energy balance equation (1.2),
- The Darcy's law for multiphase flow (1.4),
- Compositional flow by considering the change of water from the liquid phase to water vapor given by the vapor pressure function (1.12)
- The change in vapor density as a function of temperature and saturation.
- Thermal expansion of the solid and fluid phases by introducing the thermal expansion coefficient  $\beta_T$  in the mechanical model (1.16) and mass balance for the fluid phase (1.5) respectively

$$\Delta \varepsilon_T = \beta_T \Delta T \quad (1.20)$$

- The mechanical model can be modified to consider the effect of saturation on the effective stress tensor by introducing the Bishop's coefficient  $\chi$  in (1.16) defined as below

$$\chi = \begin{cases} 0 & S^w < 1 \\ 1 & \text{else} \end{cases} \quad (1.21)$$

## 4 Swelling model for Bentonite

Additionally to the previously mentioned model extensions the swelling of the medium with the uptake of water is available in OGS as a "linear swelling" model. In this empirical model, the increment of the developed swelling stress is linked to the increment of water saturation and a maximum swelling pressure  $\sigma_{\text{max,sw}}$ . This model, given by (1.22) can be included in the

mechanical model.

$$\Delta\sigma_{sw} = -\sigma_{\max,sw} \Delta S^w I \quad (1.22)$$

The extended versions of (1.18) and (1.19) describing non-isothermal compositional flow in a deformable and swelling porous media according to the Richard's model are

$$\nabla \cdot (\boldsymbol{\sigma} - \alpha_{\text{Biot}} \chi p \mathbf{I} - \boldsymbol{\sigma}_{sw} - \mathbf{D} \cdot (\beta_r^s \Delta T)) + \rho \mathbf{g} = 0 \quad (1.23)$$

$$\begin{aligned} \phi \left[ \frac{\rho^w - \rho^v}{\rho_w} \frac{\partial S}{\partial p} \right] \frac{\partial S}{\partial t} + \left( \frac{\phi}{K^w} + \frac{\alpha_{\text{Biot}} - \phi}{K^s} \right) \frac{\partial p}{\partial t} + \nabla \cdot (\mathbf{q}^w + \mathbf{q}^v) / \rho^w + S \alpha_{\text{Biot}} \nabla \cdot \frac{\partial \mathbf{u}}{\partial t} + \\ \phi \frac{1-S}{\rho^w} \left[ \left( h \frac{\partial \rho^{vSat}}{\partial T} + \frac{\rho^v p}{RT^2} \right) \frac{\partial T}{\partial t} + \frac{\rho^v}{\rho^w RT} \frac{\partial S}{\partial t} \right] - (\phi S \beta_r^w + (\alpha - \phi) \beta_r^s) \frac{\partial T}{\partial t} = 0 \end{aligned} \quad (1.24)$$

Where the superscripts  $w, s, v$ , and  $vSat$  refer to water, solid, vapor and saturated vapor respectively.

## 5 Input parameters and sources

To illustrate the capabilities of the model, a few test cases have been simulated with varying boundary condition. The example parameters are chosen from the DECOVALEX-THM task D (Birkholzer et al. 2008) and are also used in Kolditz et al. 2012b. The implemented models in OGS have also been used to simulate Bentonite with other parameter sets (e.g. Wang et al. 2016; Wang et al. 2015) within the framework of a THM modelling task. The parameter set used for in this report is given below

*Table 1: Parameters for Bentonite used in the test cases*

Density	1600	kg/m <sup>3</sup>
Young's Modulus	3.17E+08	Pa
Poisson's Ratio	0.35	-
Saturated Permeability	2.00E-21	m <sup>2</sup>

## 6 Performance: Qualitative and Quantitative

The performance of the models is illustrated below under the assumptions made in section 5. A hypothetical model of dimension 8 cm x 10 cm of pure bentonite is discretized and simulated under different hydraulic and mechanical boundary conditions along the boundaries  $\partial\Gamma_1, \partial\Gamma_2, \partial\Gamma_3$  and  $\partial\Gamma_4$ .

- The lateral boundaries  $\partial\Gamma_2$  and  $\partial\Gamma_4$  have no-flow conditions normal to the boundaries and no deformation in the X direction.
- The bottom boundary  $\partial\Gamma_1$  allows no vertical deformation in the normal direction.
- A constant pressure boundary condition is set up along  $\partial\Gamma_1$  for the hydraulics.
- The top boundary  $\partial\Gamma_3$  has a no deformation condition for the zero-volume change cases and prescribed stress conditions for the cases investigating different confining stresses.

All the test cases are simulated with the Richards flow model for unsaturated flow in linearly elastic porous media under isothermal conditions with a Biot's coefficient of 1.0. The performance of the model under the different conditions is briefly discussed below.

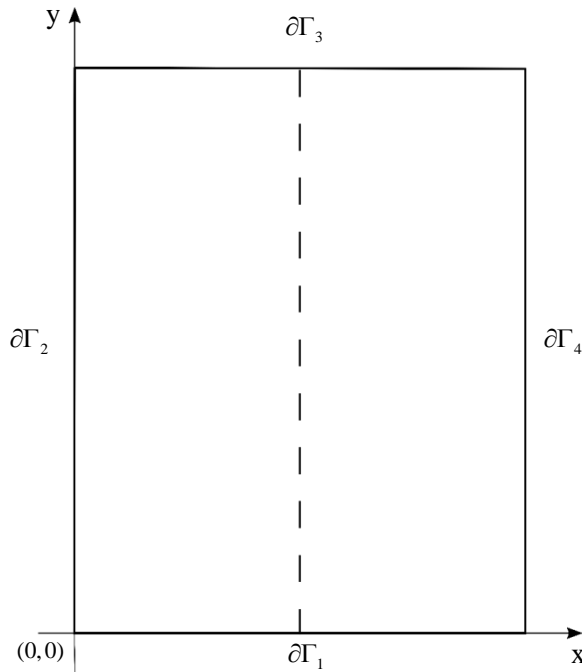


Figure 3: Model domain used in the test cases, the output is read along the dotted line.

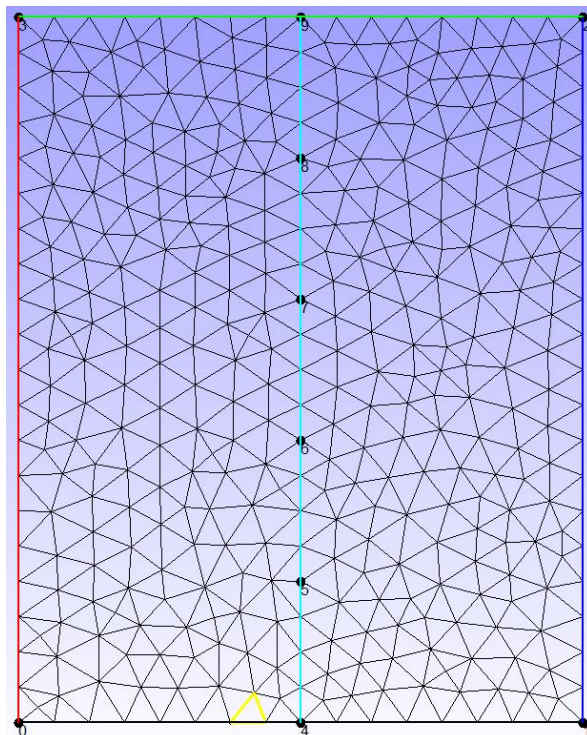


Figure 4: Domain geometry along with the FEM discretization. The points in the middle are used to generate output.

### 6.1 Base Test Case: Water saturation in an uniaxially unconstrained domain

For the base case, the model domain is simulated with the only linear elastic HM coupling

without swelling. In this scenario and in the other test scenarios, water is injected from the bottom at a constant pressure into a partially saturated domain with an initial suction pressure of  $-7E-7$  Pa. The flow of water reduces the suction in the domain to zero with time. The saturation profile is shown in Figure 5 at three instances in time.

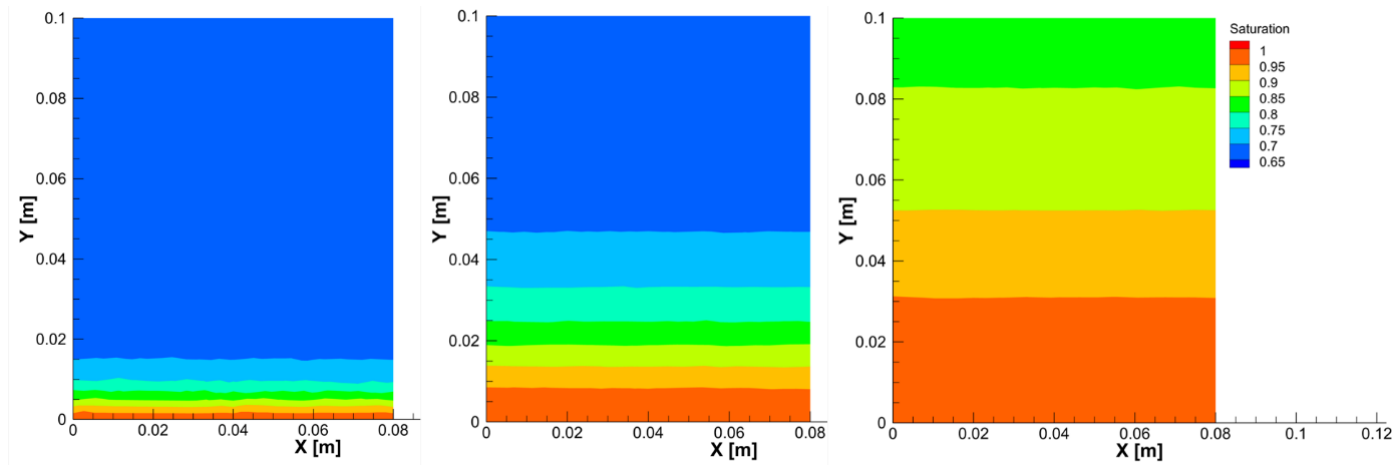


Figure 5: Saturation profiles in the model domain at  $t=17$  hours, 7 days and 73 days.

In Figure 6 the pressure profile, in Figure 7 the vertical stress profile and Figure 8 the vertical displacement profile at three instances in time along a line running through the middle of the domain is shown respectively.

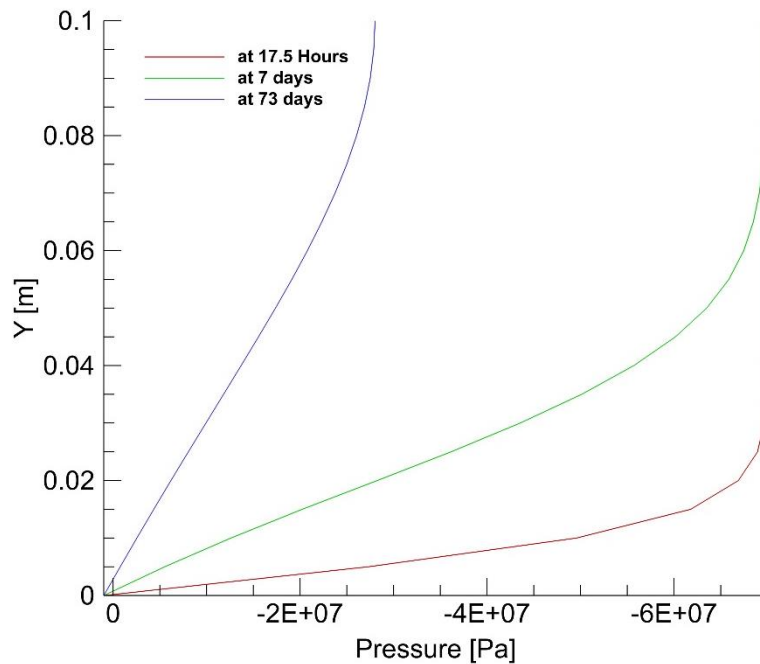
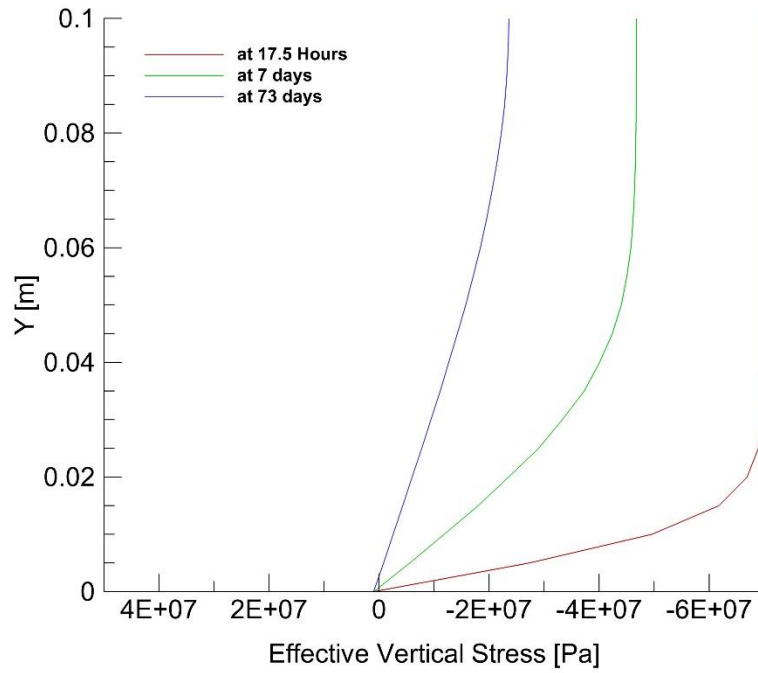
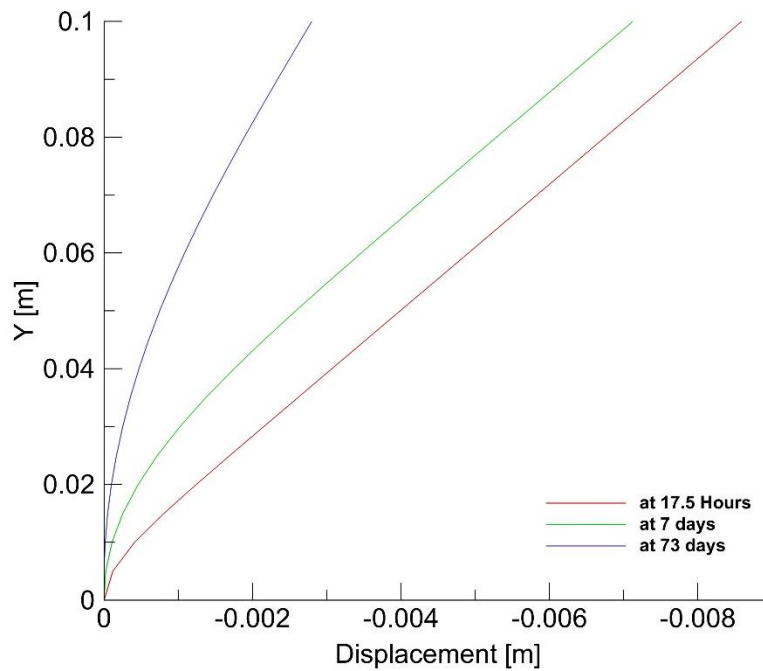


Figure 6: Pressure profile along a line in the middle of the domain.



*Figure 7: Stress profile along a line in the middle of the domain.*



*Figure 8: Vertical displacement along a line in the middle of the domain.*

The development of the effective vertical stress and the saturation with time at  $y = 2$  cm and at  $y = 8$  cm is shown in Figure 9

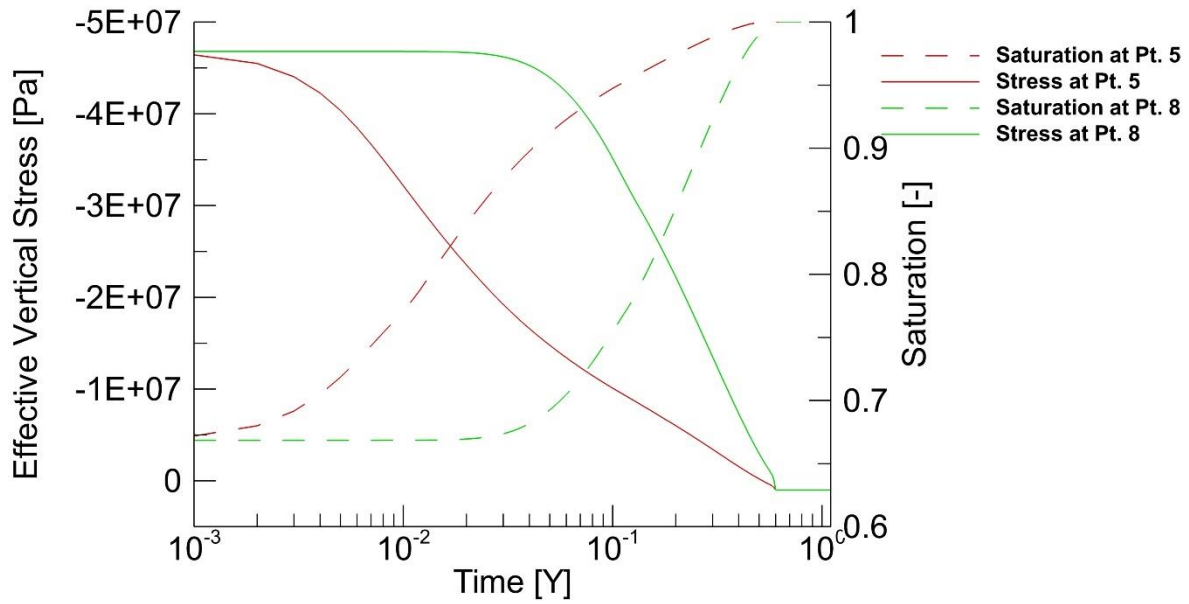


Figure 9: Temporal evolution of the saturation and the effective stress at two control points in the domain.

## 6.2 Saturation in a constrained domain

In this scenario, the saturation is done under constant volume conditions by enforcing a zero-displacement boundary at the top of the domain but allowing for water outflow. The effective vertical stress profile of the domain is shown in Figure 10 and the displacements in the domain is shown in Figure 11.

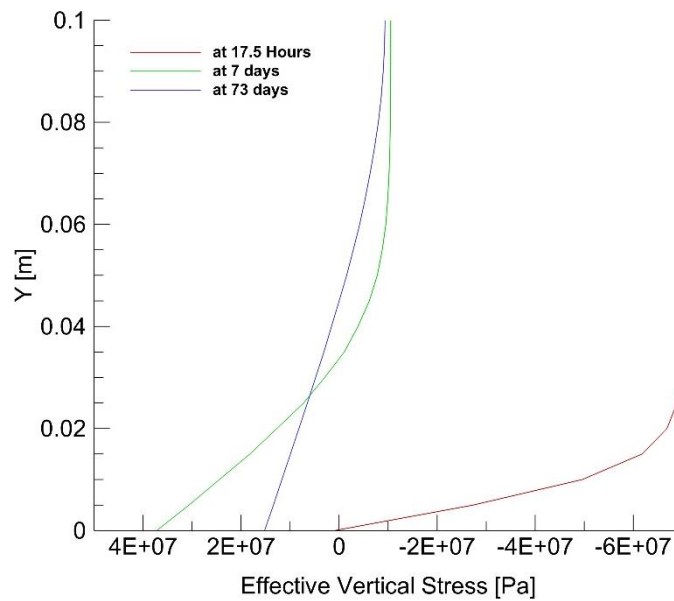


Figure 10: Pressure profile along a line in the middle of the domain.

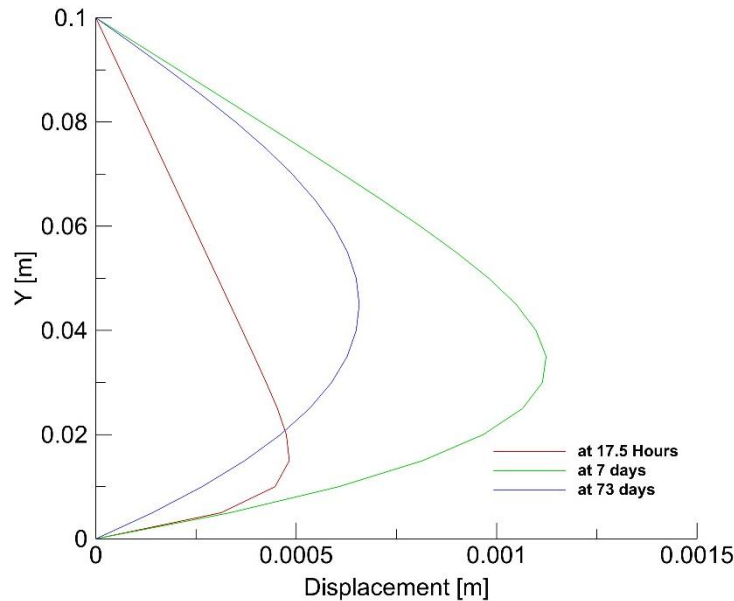


Figure 11: Displacement profile along a line in the middle of the domain.

The temporal development of the stresses at a two points along the center-line of the domain is shown in Figure 12.

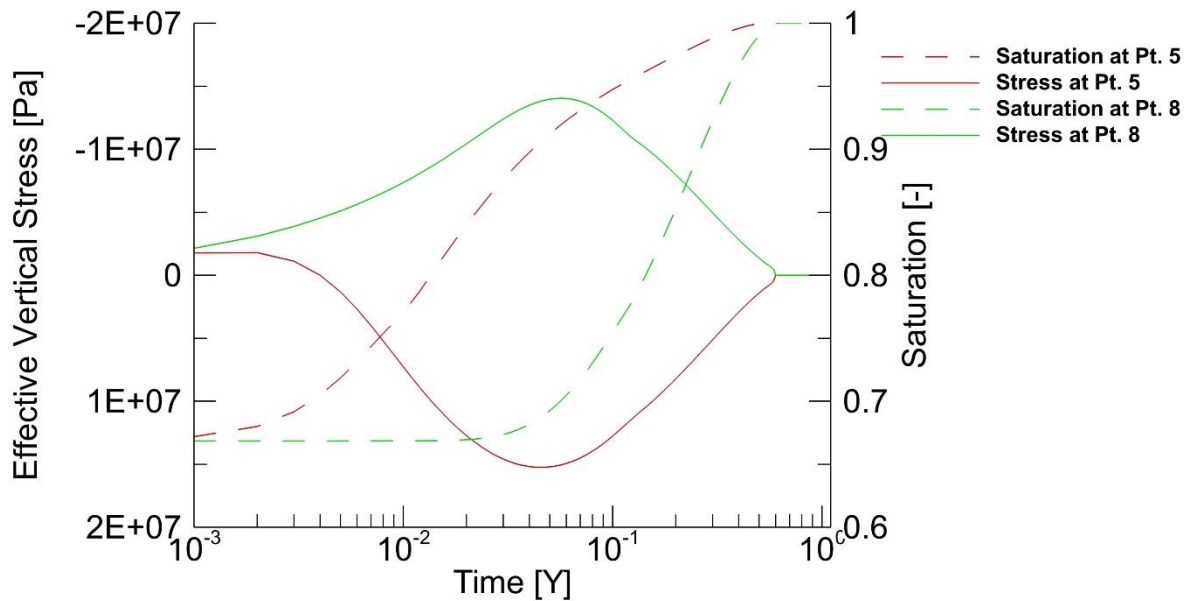


Figure 12: Temporal evolution of the saturation and the effective stress at two control points in the domain.

### 6.3 Saturation in a domain under confining stresses

In the third test, the saturation tests are carried out in a domain under a constant effective confining stresses at the top boundary of 5 MPa, 10 MPa and 20 MPa respectively. The effective vertical stress and displacement profiles are shown in Figure 13, Figure 15 and Figure 17. The temporal development of the saturation and the effective vertical stress at a two points along the center-line of the domain is shown in Figure 14, Figure 16 and Figure 18.

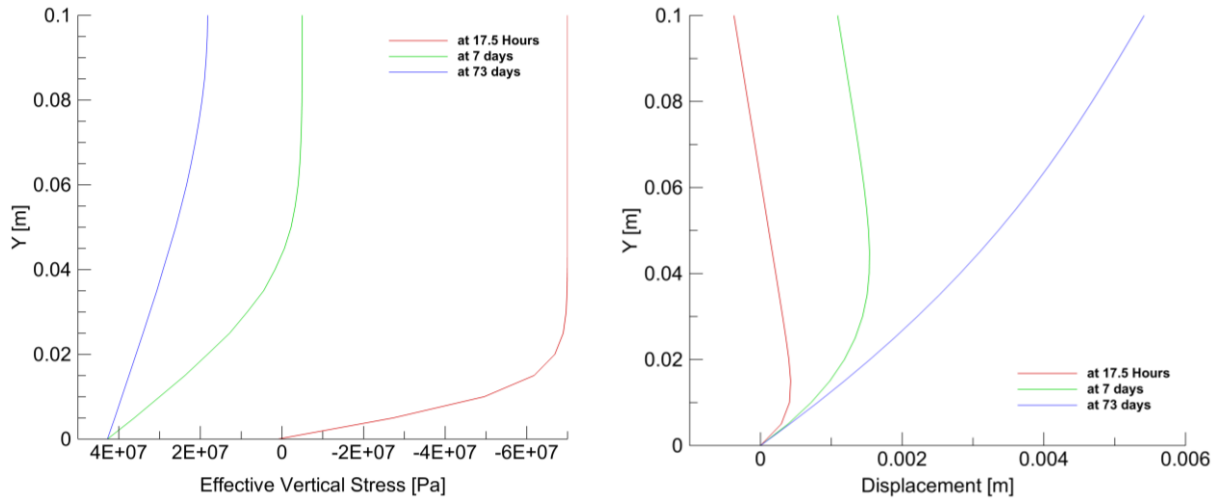


Figure 13: Effective vertical stress and displacement profile along a line in the middle of the domain at confining stress 5 MPa.

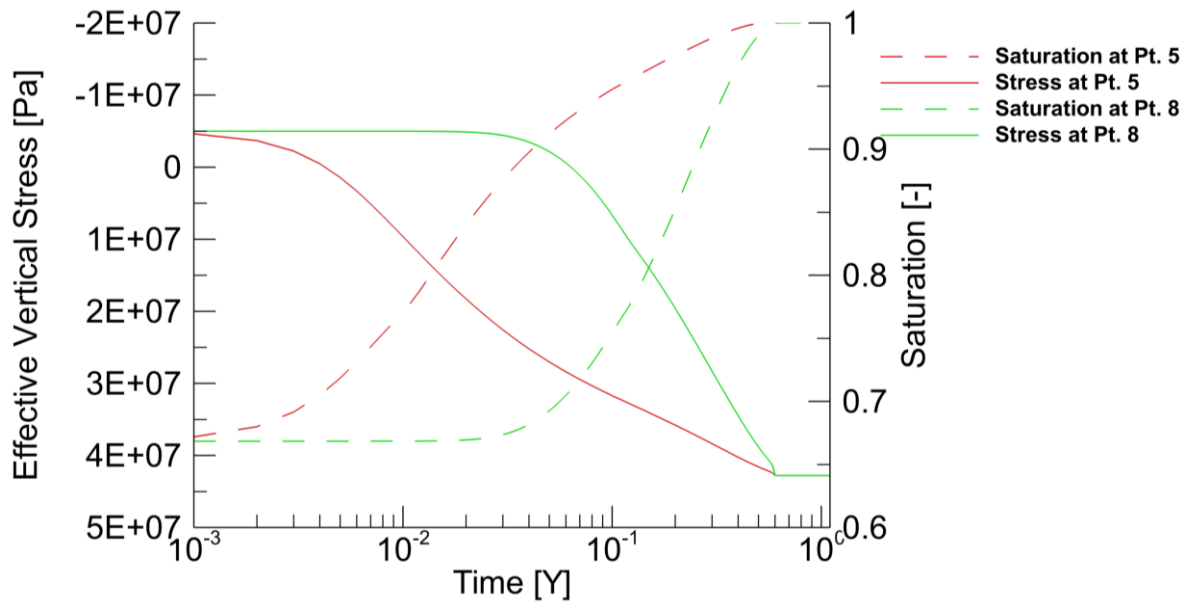


Figure 14: Temporal evolution of the saturation and the effective stress at two control points in the domain at confining stress of 5 MPa.

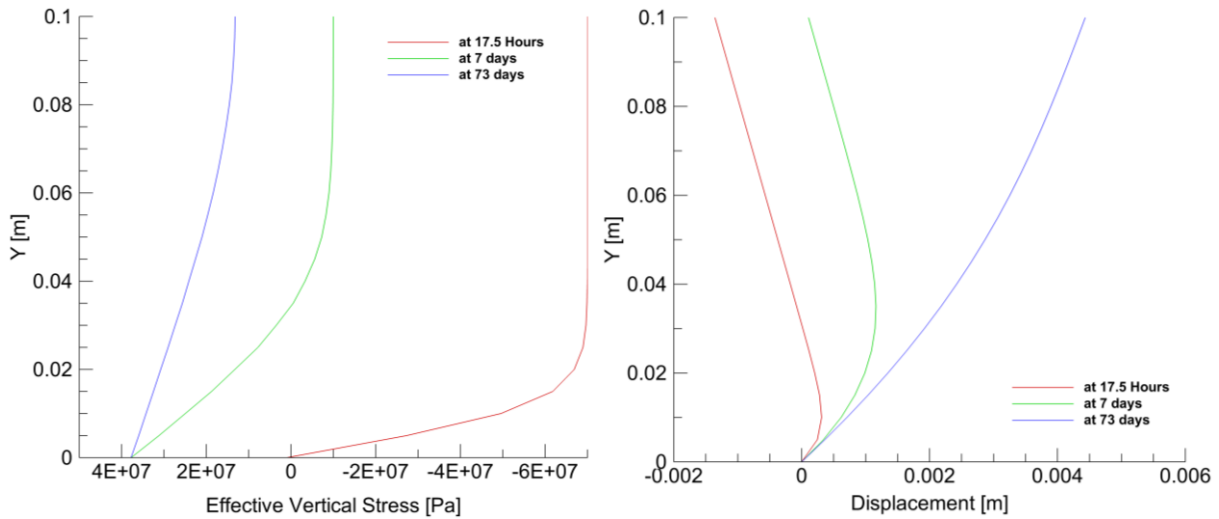


Figure 15: Effective vertical and displacement profile along a line in the middle of the domain at confining stress of 10 MPa.

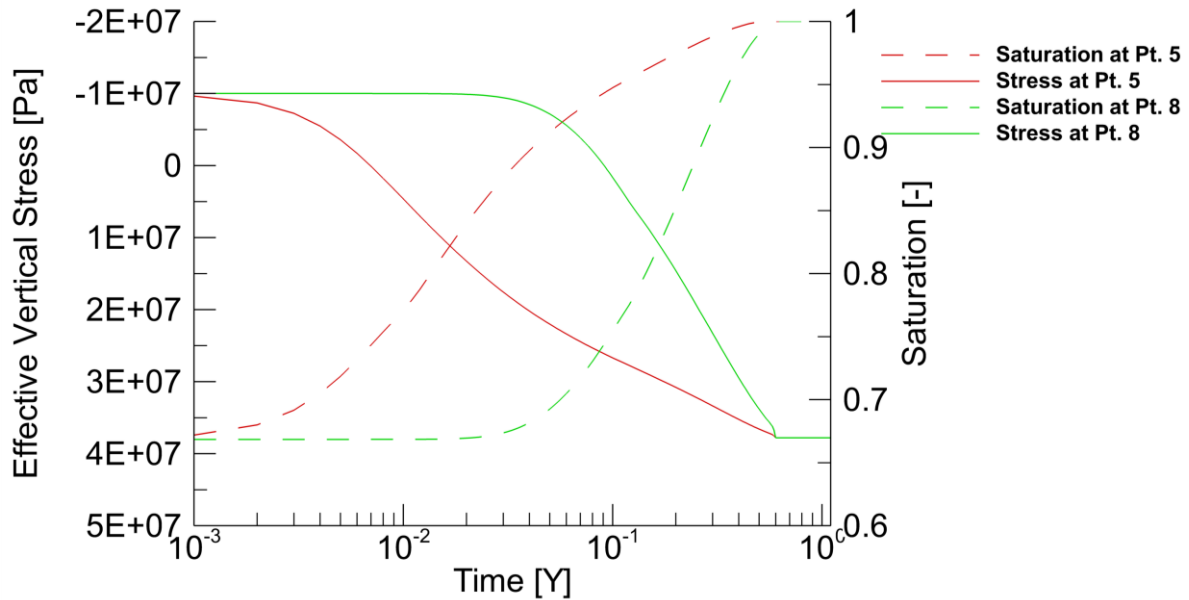


Figure 16: Temporal evolution of the saturation and the effective stress at two control points in the domain at confining stress of 10 MPa.

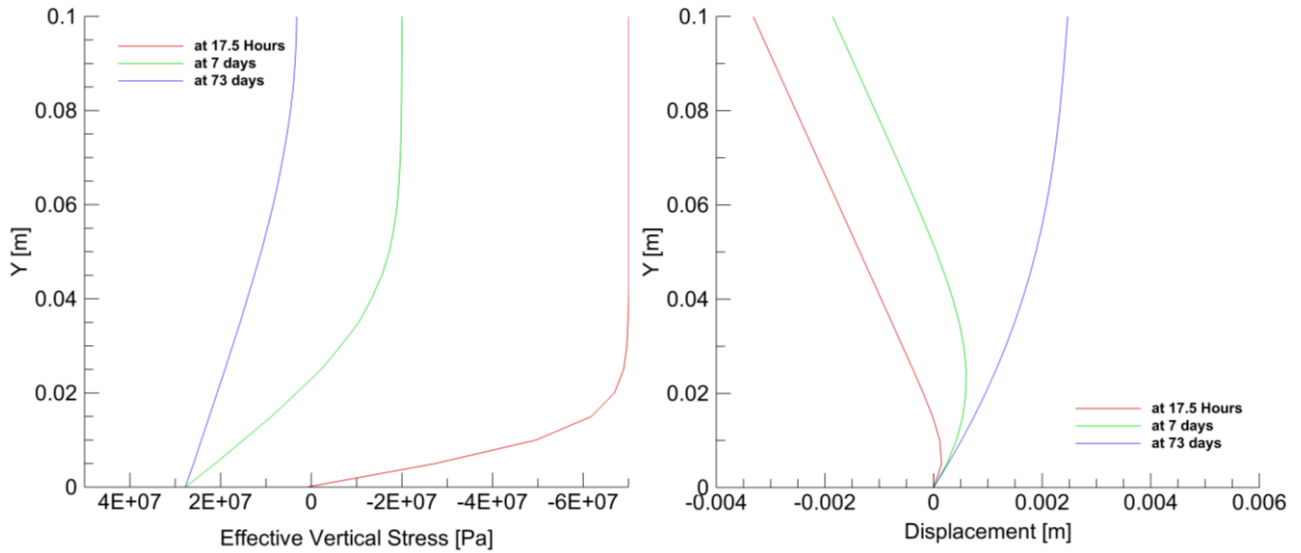


Figure 17: Effective vertical and displacement profile along a line in the middle of the domain at confining stress of 20 MPa.

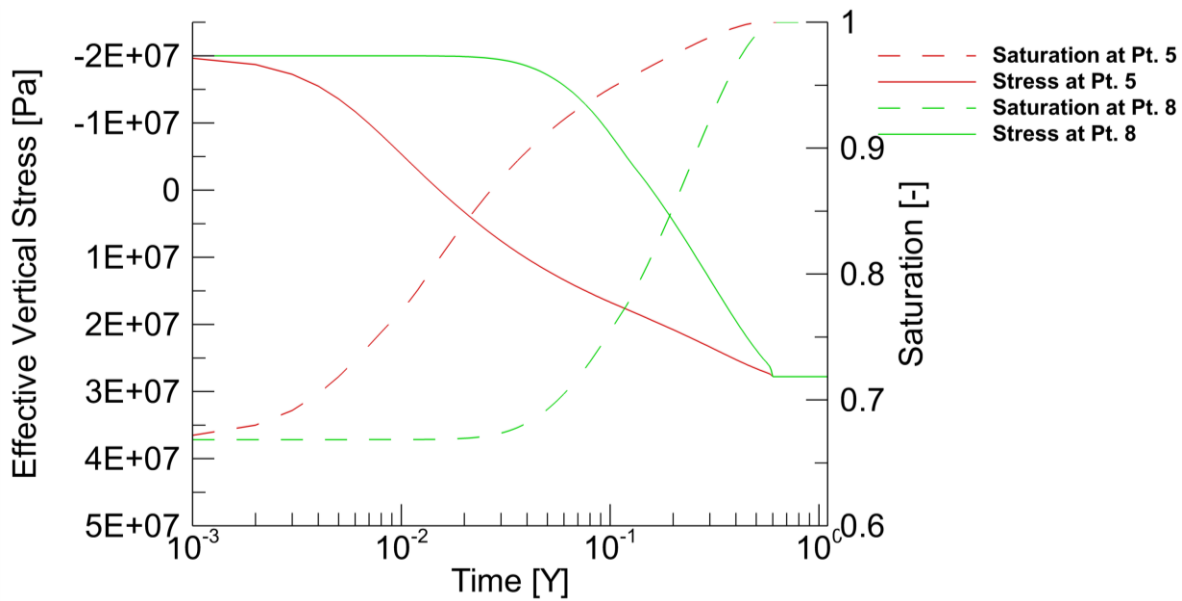


Figure 18: Temporal evolution of the saturation and the effective stress at two control points in the domain at confining stress of 20 MPa.

## 7 Conclusions

The tested models demonstrate the linearly elastic coupled HM model implemented in OGS under various boundary conditions. They demonstrated the influence of water saturation in a domain with an initial high suction pressure and the development of the HM coupled processes along the model domain and in time. The models were tested under no confinement boundary, fully confined boundary and under various confining stresses. The development of stresses and displacement were investigated in all the models.

*Table 2: Features of the linear elastic model with swelling used in OGS*

Name of the constitutive law:		Linear-elasticity with linear swelling	
Behaviour feature	YES	NO	Remarks
<b>Mechanical behaviour</b>			
Dependence of swelling strain on applied stress (at the same dry density) (Figure 1)	x		Strains are dependent on overburden pressure
Dependence of swelling stress on dry density (at the same stress) (Figure 1)	x		Maximum swelling pressure is implicitly dependent on dry density and is a user-defined constant. The evolution is dependent on the saturation.
Irreversibility of strains in wetting/drying cycles (Figure 2)		x	Due to linear elasticity, strains are reversible
Dependence of swelling pressure on dry density (Figure 4)		x	User-specified and constant for the whole simulation
Stress path dependence from an unsaturated to a saturated state (Figure 5)		x	
Stress path dependence from a saturated to an unsaturated state (Figure 6)		x	
Double structure/porosity considered?		x	
Are temperature effects considered in the model?	x		Thermally dependent parameters fluid parameters, vapour diffusion and thermal expansion of all phases.
Dependence of strains developed in a temperature cycle (increase/decrease) on OCR (or stress) (Figure 7)	x		Thermal expansion is incorporated in the mechanical model for non-isothermal hydromechanical processes
<b>Hydraulic behaviour (retention curve)</b>			
Hysteresis		x	
Dependence on void ratio		x	
Double structure/porosity considered?		x	

## 8 Bibliography

Bear, Jacob (1988): Dynamics of fluids in porous media. New York, N.Y: Dover Publications (Dover Books on Physics and Chemistry).

Birkholzer, J.; Rutqvist, Jonny; Sonnenthal, E.; Barr, D. (2008): DECOVALEX-THMC Project. Task D: Long-Term Permeability/Porosity Changes in the EDZ and Near Field due to THM and THC Processes in Volcanic and Crystalline-Bentonite Systems. SKI. Stockholm (45).

Kolditz, O.; Bauer, S.; Bilke, L.; Böttcher, N.; Delfs, J. O.; Fischer, T. et al. (2012a): OpenGeoSys. An open-source initiative for numerical simulation of thermo-hydro-mechanical/chemical (THM/C) processes in porous media. In *Environ Earth Sci* 67 (2), pp. 589–599. DOI: 10.1007/s12665-012-1546-x.

Kolditz, Olaf; Görke, U. J.; Shao, Hua; Wang, Wenqing (Eds.) (2012b): Thermo-hydro-mechanical-chemical processes in fractured porous media. Benchmarks and examples. Berlin, Heidelberg [u.a.]: Springer (Lecture Notes in Computational Science and Engineering, 86).

Rutqvist, J.; Börgesson, L.; Chijimatsu, M.; Kobayashi, A.; Jing, L.; Nguyen, T. S. et al. (2001): Thermohydromechanics of partially saturated geological media. Governing equations and formulation of four finite element models. In *International Journal of Rock Mechanics and Mining Sciences* 38 (1), pp. 105–127. DOI: 10.1016/S1365-1609(00)00068-X.

Wang, Xuerui; Shao, Hua; Hesser, Jürgen; Kolditz, Olaf (2016): Analysis of the THM behaviour in a clay-based engineered barrier system (EBS). Modelling of the HE-E experiment (Mont Terri URL). In *Environ Earth Sci* 75 (20), p. 173. DOI: 10.1007/s12665-016-6116-1.

Wang, Xuerui; Shao, Hua; Wang, Wenqing; Hesser, Jürgen; Kolditz, Olaf (2015): Numerical modeling of heating and hydration experiments on bentonite pellets. In *Engineering Geology* 198, pp. 94–106. DOI: 10.1016/j.enggeo.2015.09.009.



FACULTY OF SCIENCE  
Charles University



# BEACON

Bentonite Mechanical Evolution

## DELIVERABLE (D3.1)

### ANNEX B

#### COUPLED THERMO-HYDRO-MECHANICAL DOUBLE STRUCTURE CONSTITUTIVE MODEL FOR EXPANSIVE SOILS

Authors: doc. RNDr. David Mašín, M.Phil., Ph.D.  
prof. Ing. Jaroslav Kruis, Ph.D.

Institutions: Charles University  
Czech Technical University



## Table of Contents

1	Introduction .....	3
2	Background and basic hypotheses .....	3
3	Mathematical description .....	5
3.1	Theoretical framework .....	5
3.2	Mathematical formulation of the THM model .....	7
4	Input parameters .....	10
5	Performance .....	11
5.1	Dependence of swelling strain on applied stress and on dry density .....	11
5.2	Irreversibility of strains in wetting/drying cycles .....	12
5.3	Behaviour during swelling stress test. Dependence of swelling pressure on dry density. 13	
5.4	Stress path dependence from an unsaturated to a saturated state .....	15
5.5	Stress path dependence from a saturated to an unsaturated state .....	17
5.6	Dependence of strains developed in a temperature cycle (increase/decrease) on OCR (or stress) .....	19
5.7	Features Table .....	21
6	Final Remarks .....	23
7	Acknowledgements .....	23
8	References .....	23
9	Appendix .....	25



## 1 Introduction

In this report, we present a summary of the constitutive model for bentonite used by the Czech teams (Charles University and Czech Technical University) for simulations within the project BEACON. The model is a coupled thermo-hydro-mechanical model based on hypoplasticity principles combined with the concept of double structure.

The model has been developed by Mašín (2017) by a hierarchical enhancement of the earlier model by Mašín (2013), which did not consider the effects of temperature. That model, in turn, was a double structure enhancement of earlier models for unsaturated and saturated soils.

The hierarchical model structure is described in more detail in Sec. 2. Subsequently, in Sec. 3, we introduce hypoplasticity and mathematical formulation of the THM model and Sec. 4 summarises its material parameters. In Sec. 5, we demonstrate predictive performance of the model by comparing predictions with various benchmark experiments, identified as crucial in the report assignment. Whenever possible, comparison is made not only qualitative, but also quantitative by comparing model predictions with experimental data.

## 2 Background and basic hypotheses

The model has been developed using a double-structure framework originally proposed by Gens and Alonso (1992), who introduced the double structure concept, and Alonso et al. (1999), who developed a complete constitutive model. The model is based on the hydro-mechanical double structure hypoplastic model proposed by Mašín (2013), which has been enhanced by the effects of temperature. Background and basic hypotheses of this model is briefly described in this section.

The hypoplastic double-structure model, and double-structure models in general, are based on the assumption supported by various micro-mechanical studies that in expansive soils one can identify two levels of structure: a macrostructure, which represents an assembly of silt-size aggregates of the clay particles, and a microstructure, which represents the internal structure of these aggregates. A conceptual sketch of these two levels of structure is shown in Figure 1.

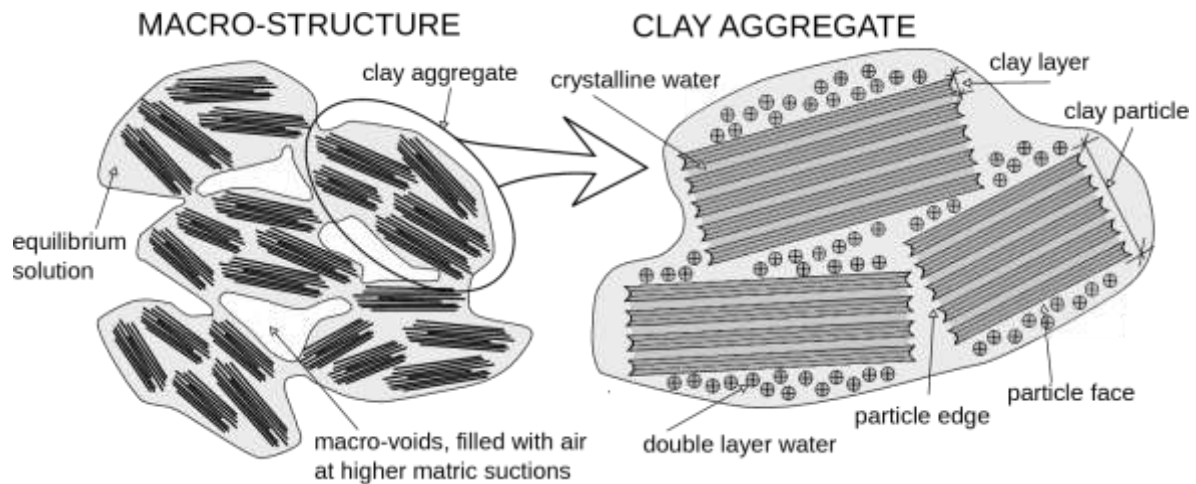


Figure 1: Schematic representation of double structure concept (Mašín, 2013 & 2017).

In Mašín (2013), separate models are considered for the mechanical and hydraulic responses of the microstructure and of the macrostructure. These responses are coupled at each structural level, and the behavior of the two structural levels is linked through the double-structure coupling function. A schematic of the adopted modeling approach is in Figure 2. The individual models are denoted as  $G^M$ ,  $G^m$ ,  $H^M$ , and  $H^m$ , respectively.

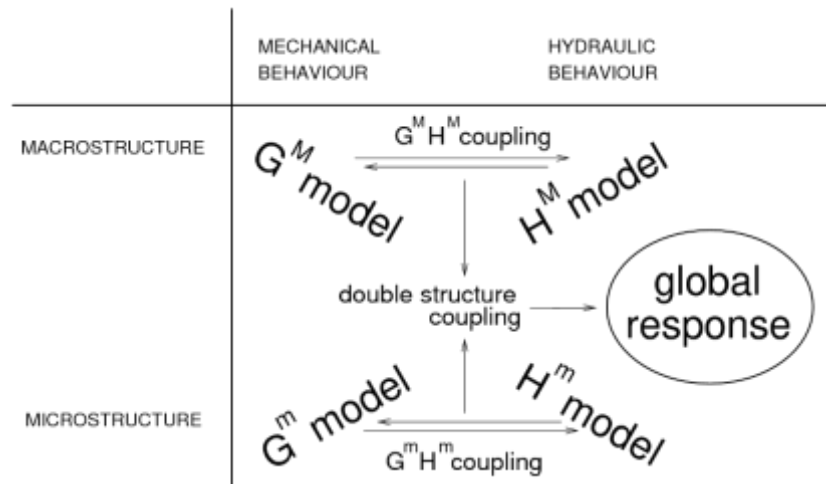


Figure 2: Schematic representation of the double structure coupling concept adopted in the hypoplastic model (Mašín, 2013 & 2017).

In the double-structure model from Mašín (2013), the mechanical behavior of the macrostructure ( $G^M$ ) was described using the model for unsaturated soils developed by Mašín and Khalili (2008), which itself was based on a hypoplastic model for saturated clays from Mašín (2005). The hydraulic response of the macrostructure ( $H^M$ ) was based on the void ratio–dependent water retention model from Mašín (2010). The microstructure has always been considered as fully saturated (simple  $H^m$  model), with its mechanical behavior ( $G^m$ ) reversible volumetric, governed by the Terzaghi effective stress principle (see Mašín and Khalili 2016 for a thorough discussion). The  $G^M H^M$  coupling was accomplished by the dependency of  $H^M$  on volume change and by the dependency of the effective stress on degree of saturation of the macrostructure  $S_r^M$ . The  $G^m H^m$  coupling was introduced through the adoption of the Terzaghi effective stress for the

mechanical behavior of the microstructure. Finally, the double-structure coupling was controlled by a function of relative void ratio, which evolved from the original proposition by Alonso et al. (1999).

The model by Mašín (2017), adopted in BEACON simulations, evolved from the Mašín (2013) by including the thermal component. To accomplish this task, additional thermal dependency has been introduced for water retention curves, volumetric behaviour of microstructure and normal compression behaviour of macrostructure. The final model is a comprehensive model capable of predicting complex THM behaviour of bentonites, as demonstrated in Sec. 5.

### 3 Mathematical description

#### 3.1 Theoretical framework

Hypoplasticity is an approach to non-linear constitutive modelling of geomaterials. In its general form (Gudehus 1996) it may be written as

$$\dot{\boldsymbol{\sigma}} = f_s(\mathcal{L} : \dot{\boldsymbol{\epsilon}} + f_d \mathbf{N} \|\dot{\boldsymbol{\epsilon}}\|) \quad (1)$$

where  $\dot{\boldsymbol{\sigma}}$  and  $\dot{\boldsymbol{\epsilon}}$  represent the objective (Zaremba-Jaumann) stress rate and the Euler stretching tensor respectively,  $\mathcal{L}$  and  $\mathbf{N}$  are fourth- and second-order constitutive tensors, and  $f_s$  and  $f_d$  are two scalar factors. In hypoplasticity, stiffness predicted by the model is controlled by the tensor  $\mathcal{L}$ , while strength (and asymptotic response in general, is governed by a combination of  $\mathcal{L}$  and  $\mathbf{N}$ . Earlier hypoplastic models (such as the model by von Wolffersdorff 1996 and Mašín 2005) did not allow to change the  $\mathcal{L}$  formulation arbitrarily, as any modification of the tensor  $\mathcal{L}$  undesirably influenced the predicted asymptotic states. This hypoplasticity limitation was overcome by Mašín (2012). He developed an approach enabling to specify the asymptotic state boundary surface independently of the tensor  $\mathcal{L}$  and demonstrated it by proposing a simple hypoplastic equivalent of the Modified Cam-clay model. Based this approach, Mašín (2014) developed an advanced hypoplastic model for clays, which is adopted in the the THM model used in this work.

The basic hypoplastic model requires five material parameters  $\varphi_c$ ,  $N$ ,  $\lambda^*$ ,  $\kappa^*$  and  $\nu$ . The parameters have the same physical interpretation as parameters of the Modified Cam clay model, and they are thus easy to calibrate based on standard laboratory experiments. The model parameters  $N$  and  $\lambda^*$  define the position and the slope of the isotropic normal compression line in the  $\ln(1 + e)$  vs.  $\ln(p/p_r)$  plane. The isotropic normal compression line is described using equation

$$\ln(1 + e) = N - \lambda^* \ln\left(\frac{p}{p_r}\right) \quad (2)$$

where  $p_r = 1$  kPa is a reference stress. Parameter  $\kappa^*$  controls the slope of the isotropic unloading line in the same plane and also of the isotropic compression line of overconsolidated soil.  $\varphi_c$  is the critical state friction angle, with identical meaning with any other critical state soil mechanics – based model. Finally, the parameter  $\nu$  controls shear modulus.

Apart from stress, the most important state variable controlling the response of the model is void ratio  $e$ , or, equivalently, overconsolidation ratio  $OCR$ . The  $OCR$  is in hypoplasticity defined as:

$$OCR = \frac{p_e}{p} \quad (3)$$

where  $p_e$  is the Hvorslev equivalent pressure; that is, mean effective stress at the isotropic normal compression line calculated using Eq. (2) at the current void ratio.

The principle of hypoplasticity can best be demonstrated using a simple one-dimensional model. 1D version of hypoplastic model for shear reads:

$$d\tau = Ld\gamma + N|d\gamma| \quad (4)$$

where  $d\tau$  is increment of shear stress (note that compression negative sign convention is adopted),  $|X|$  represents absolute value of  $X$  and  $L$  and  $N$  are two moduli. In hypoplasticity, neither the switch function distinguishing between loading and unloading, as in elasto-plastic model, nor strain decomposition into elastic and plastic parts, are needed. A scalar "modulus"  $N$  may be defined as

$$N = LY \quad (5)$$

with

$$Y = \frac{\tau}{\tau_{yield}} \quad (6)$$

The modulus  $L$  may be specified using a parameter such that  $L = E_n$ . This simple 1D hypoplastic model thus requires two parameters  $\tau_{yield}$  and  $E_n$ . Predictions of this 1D model are shown in Figure 3, where they are compared with predictions of model elasto-plastic.

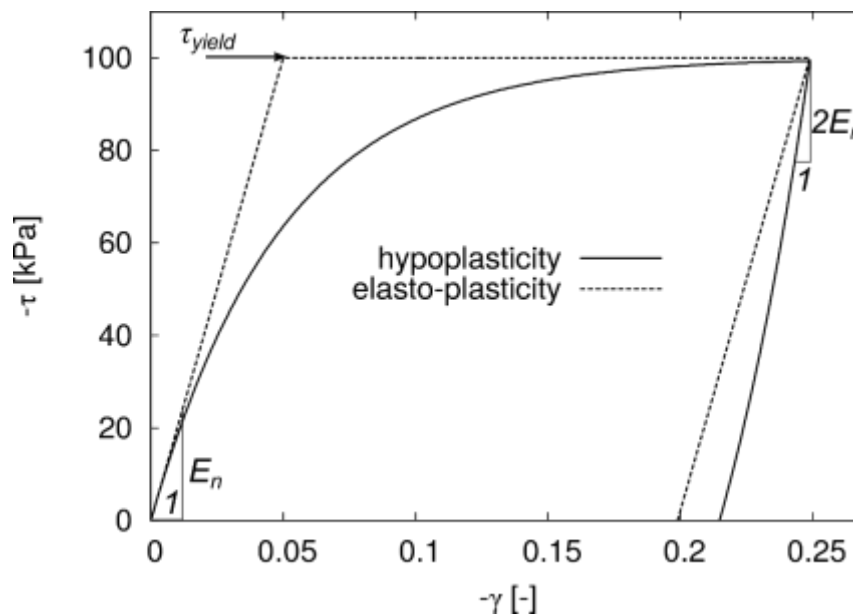


Figure 3: Demonstration of hypoplasticity principles using a simple one-dimensional model.

Let us now consider the Equation (4) and evaluate the stiffness predicted by the hypoplastic model. First of all, the stiffness depends on loading direction (as in elasto-plasticity), thanks to the absolute value appearing in Eq. (4). The following two cases are important for clarifying the model performance:

1. When  $\tau = 0$ ,  $Y$  calculated using Eq. (4) is equal to zero. Therefore,  $N = 0$  and thus

$$d\tau = Ld\gamma \quad (7)$$

$L$  thus specifies the initial modulus for loading from the state  $\tau = 0$ .

2. When  $\tau = \tau_{yield}$ ,  $Y$  is equal to one. Therefore,  $N = L$  and the hypoplastic equation reads

$$d\tau = L(dy + |d\gamma|) \quad (8)$$

In loading,  $d\gamma < 0$  and therefore  $d\tau = 0$ , similar as in elasto-plasticity. During unloading,  $d\gamma > 0$  and hypoplasticity predicts

$$d\tau = 2Ld\gamma \quad (9)$$

It follows from the above that for the special cases of  $\tau = 0$  and  $\tau = \tau_{yield}$  the hypoplastic model predicts similar response as the elasto-plastic model (apart from the unloading modulus at  $\tau = \tau_{yield}$ , which is twice as high as the loading modulus at  $\tau = 0$ ). The most important difference in predictions of the two models is in the intermediate states  $\tau_{yield} < \tau < 0$ . While elasto-plasticity predicts constant stiffness  $E_n$ , hypoplasticity predicts gradual decrease of stiffness, starting from the initial modulus  $E_n$  and ending with the fully plastic state with stiffness equal to zero. The stiffness decrease is caused by the definition of  $Y$ , whose value gradually increases from 0 to 1 and thus forces the modulus  $N$  to vary between zero and  $L$ .

### 3.2 Mathematical formulation of the THM model

The primary equation of the THM hypoplastic model reads

$$\dot{\sigma}^M = f_s[\mathcal{L} : (\dot{\epsilon} - f_m \dot{\epsilon}^m) + f_d \mathbf{N} \|\dot{\epsilon} - f_m \dot{\epsilon}^m\|] + f_u(\mathbf{H}_s + \mathbf{H}_T) \quad (10)$$

For description of the complete mathematical formulation of the model, interested reader is referred to Mašín (2017). Complete model formulation is also given in Appendix of this report. In the following, the main components of Eq. (10) are described:

- Behaviour of *macrostructure* is defined using the hypoplastic approach. Thus, Eq. (10) defines the effective stress rate of macrostructure  $\dot{\sigma}^M$ . It is defined using Bishop equation, in which the factor  $\chi$  is equal to the degree of saturation of macrostructure.

$$\dot{\sigma}^M = \dot{\sigma}^{net} - \mathbf{1} S_r^M \dot{s} \quad (11)$$

where  $\dot{\sigma}^{net}$  is net stress,  $s$  is suction and  $S_r^M$  is degree of saturation of macrostructure defined using a hysteretic macrostructural void ratio-dependent water retention model of Brooks and Corey (1964) type. The water retention model for macrostructure is sketched in Figure 4.

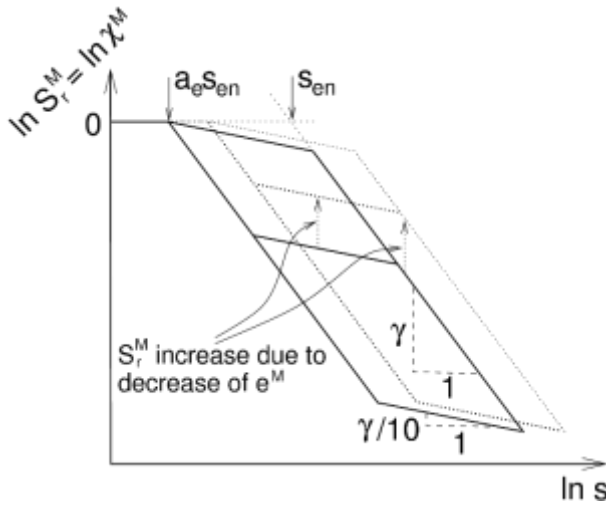


Figure 4: Hysteretic water retention model for macrostructure adopted in hypoplastic THM model for expansive soils.

- Behaviour of *microstructure* is defined using elastic volumetric model, which can be written as

$$\dot{\epsilon}^m = \frac{1}{3} \left( \alpha_s \dot{T} - \frac{\kappa_m}{p^m} \dot{p}^m \right) \quad (12)$$

where  $\epsilon^m$  is microstructural strain,  $\dot{T}$  is temperature rate,  $p^m$  is microstructural mean effective stress and  $\alpha_s$  and  $\kappa_m$  are parameters. Microstructure is always assumed to be fully saturated and its behaviour governed by the Terzaghi effective stress, that is

$$\sigma^m = \sigma^{net} - \mathbf{1}s \quad (13)$$

- The double structure coupling is accomplished through the factor  $f_m$  appearing in Eq. (10). This factor depends on relative density, such that for the most dense state  $f_m = 1$  and for the most loose state  $f_m = 0$ . These values mean that at the loose state microstructural strain does not cause any macrostructural deformation, because microstructural units (aggregates) swell into the macrovoids. Contrary, at the densest possible state macrostructure is basically closed, and any microstructural strain causes equivalent strain macrostructural. The factor  $f_m$  is defined as

$$f_m = 1 - (r_{em})^m \quad (14)$$

where  $m$  is a parameter and  $r_{em}$  is relative void ratio defined as

$$r_{em} = \frac{e - e_d}{e_i - e_d} \quad (16)$$

where  $e_d$  is minimum void ratio (equal to microstructural void ratio) and  $e_i$  is maximum void ratio (equal to the void ratio at the isotropic normal compression line).

- Eq. (10) contains two tensors  $\mathbf{H}_S$  and  $\mathbf{H}_T$  and a scalar factor  $f_u$ . The factors  $\mathbf{H}_S$  and  $\mathbf{H}_T$  are denoted as wetting- and heating-induced collapse factors, calculated to ensure that during wetting and heating of specimen whose state is close to the isotropic normal compression line (NCL), its state remains at NCL and thus wetting- and heating-induced collapse is predicted. The factor  $f_u$  depends on relative density and decreases the effect of  $\mathbf{H}_S$  and  $\mathbf{H}_T$  for higher overconsolidation ratios.
- Last, Eq. (10) contains two scalar factors  $f_s$  and  $f_d$ . These are denoted as barotropy- and pyknotropy factors and they control the effect of stress and void ratio on macrostruc-



tural soil stiffness. They were taken over from the basic hypoplastic model for clays from Mašín (2014).

The complete mathematical formulation of the THM hypoplastic model is in Appendix.

## 4 Input parameters

Model parameters and their description is summarised in Table 1.

Table 1: Model parameters and their description (from Mašín, 2017).

Parameter	Description
$\varphi_c$	Critical state friction angle of macrostructure in a standard soil-mechanics context
$\lambda^*$	Slope of isotropic normal compression line in $\ln(p^M/\rho_v)$ versus $\ln(1+e)$ space
$\kappa^*$	Macrostructural volume strain in $p^M$ unloading
$N$	Position of isotropic normal compression line in $\ln(p^M/\rho_v)$ versus $\ln(1+e)$ space
$\nu$	Stiffness in shear
$n_s$	Dependency of position of isotropic normal compression line on suction
$l_s$	Dependency of slope of isotropic normal compression line on suction
$n_T$	Dependency of position of isotropic normal compression line on temperature
$l_T$	Dependency of slope of isotropic normal compression line on temperature
$m$	(1) Control of $f_w$ and thus dependency of wetting/heating-induced compaction on distance from state boundary surface; (2) control of double-structure coupling function and thus response to wetting-drying and heating-cooling cycles (Mašín 2013b)
$\alpha_s$	Dependency of microstructural volume strains on temperature
$\kappa_m$	Dependency of microstructural volume strains on $p^m$
$e_0^m$	Reference microstructural void ratio for reference temperature $T_r$ , reference suction $s_r$ , and zero total stress
$c_{th}$	Value of $f_m$ for compression
$s_{e0}$	Air-entry value of suction for reference macrostructural void ratio $e_0^M$
$a$	Dependency of macrostructural air-entry value of suction on temperature
$b$	Dependency of macrostructural air-entry value of suction on temperature
$a_e$	Ratio of air entry and air expulsion values of suction for macrostructure water retention model
$s_r$	Reference suction for $e^m$
$e_0^M$	Reference macrostructural void ratio for air-entry value of suction of macrostructure
$T_r$	Reference temperature

## 5 Performance

### 5.1 Dependence of swelling strain on applied stress and on dry density

Specification: The stress paths to be followed to check this potential dependence are simply a number of swelling tests at different stresses where suction is reduced from some initial value down to zero (Figure 5). Those paths can be followed assuming different initial dry densities.

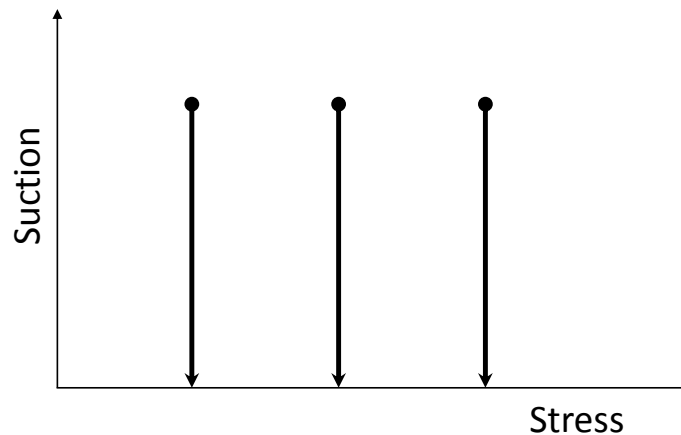


Figure 5: Swelling tests at constant stress. Stress may be vertical total stress (in oedometer tests) or mean total stress (in isotropic loading tests)

Model Performance: Model performance for these tests is demonstrated in Figure 6, showing simulations of oedometric wetting-drying tests at various initial densities and vertical loads. This figure is taken over from Mašín (2013) and represents the behaviour of compacted Boom clay (data by Romero 1999). The model predicts increase of swelling strains with decrease of vertical load and increase of swelling potential with increasing relative density. For very loose samples, wetting-induced compaction is predicted instead of swelling.

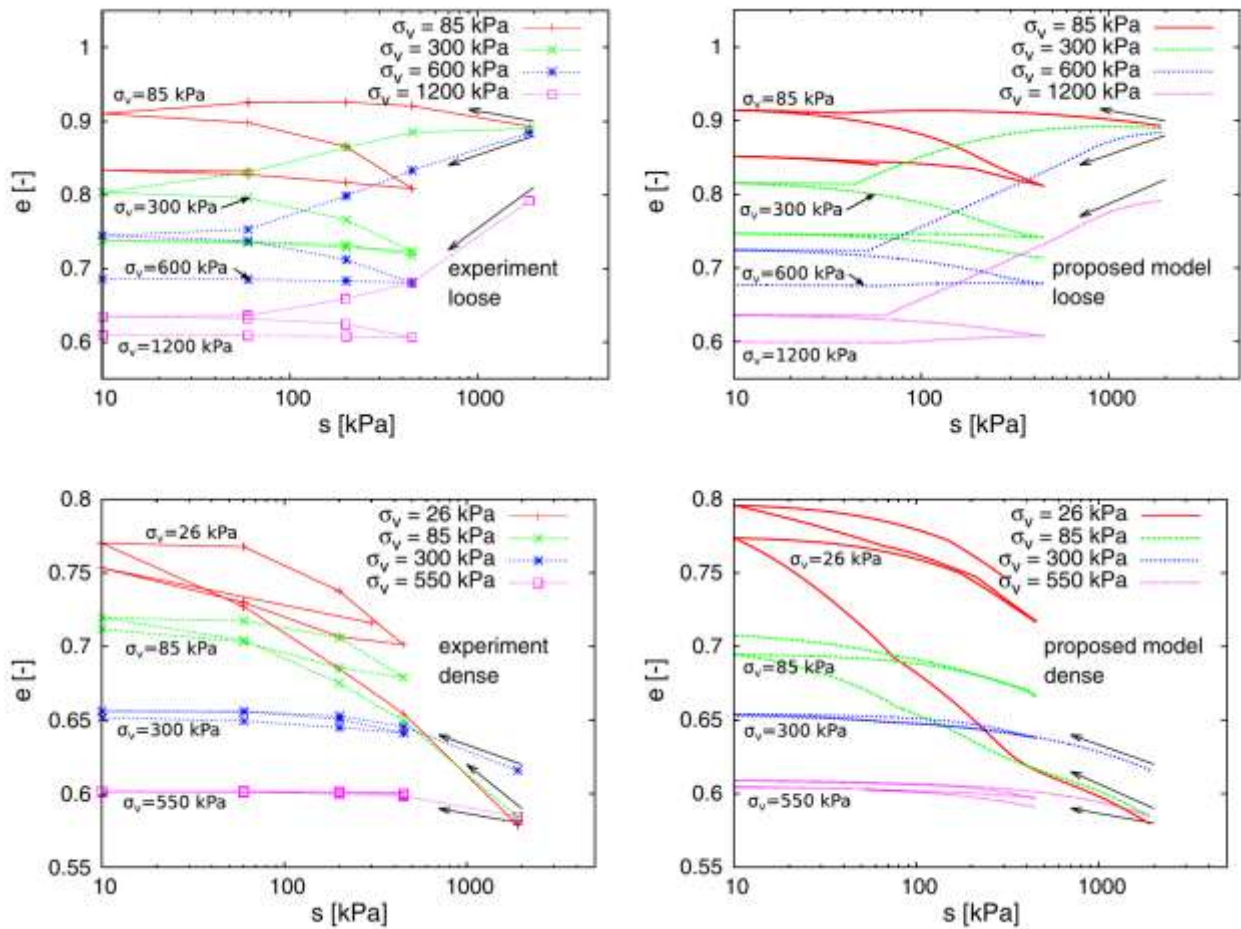


Figure 6: Simulations of oedometric wetting-drying tests at various initial densities and vertical loads. Model performance compared with experimental data on Boom clay (Romero 1999). Figure from Mašin (2013).

## 5.2 Irreversibility of strains in wetting/drying cycles

Specification: The stress paths to be followed in this case involve a suction reduction to zero and a subsequent increase of suction to the initial value (Figure 7). In this way, it can be checked whether the strains recover at the end of the cycle or whether irreversible strains are produced instead.

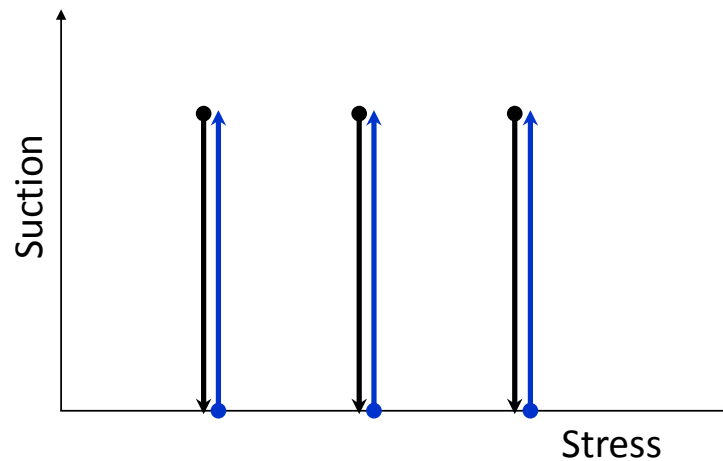


Figure 7: Swelling/drying tests at constant stress. Stress may be vertical total stress (in oedometer tests) or mean total stress (in isotropic loading tests)

Model Performance: Actually, the suction increase paths after wetting are also shown in Figure 6. Clearly, irreversible strains are generated at the end of the wetting-drying cycle. The amount of irreversible strains depends on state (relative density and stress). Figure 6 shows more than one wetting-drying cycle. It is clear that in subsequent cycles the response is more reversible than in the first cycle.

### 5.3 Behaviour during swelling stress test. Dependence of swelling pressure on dry density.

Specification: A swelling stress test involves the reduction of suction from an initial value down to zero while maintaining the volume of the specimen constant throughout. Now total stress is not controlled but it evolves during the test (Figure 8). The stress value at the end of the test is called the swelling pressure. It would be interesting to observe the type of stress paths obtained for a particular model.

Swelling pressure is strongly dependent on dry density (Figure 9). The dependence of swelling pressure on dry density is an important feature that should be checked.

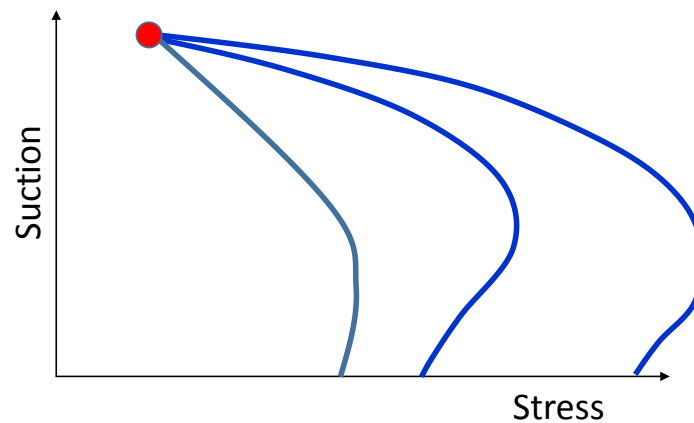


Figure 8: Suction-stress paths in swelling pressure tests. Stress may be vertical total stress (in oedometer tests) or mean total stress (in isotropic loading tests)

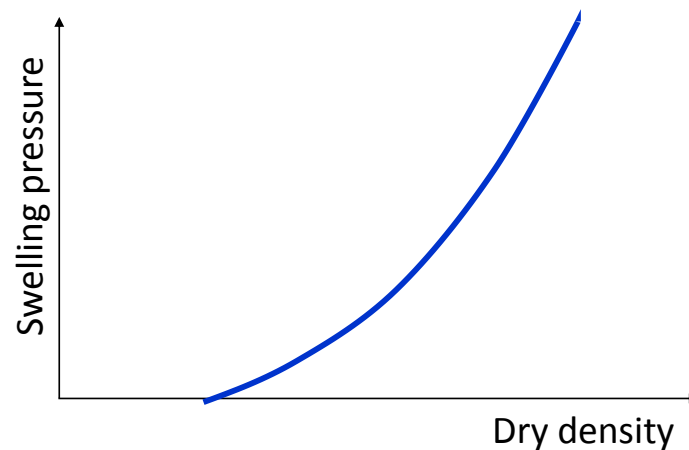


Figure 9: Possible dependence of swelling pressure on dry density

**Model Performance:** Swelling pressure (axial and radial) evolution in constant volume wetting of  $K_0$ -compacted specimens of Boom clay is in Figure 10. The figure is taken from Mašín (2013), experimental data by Romero (1999). Due to anisotropy created during  $K_0$ -compaction, horizontal and vertical stresses are different. Stress paths observed in experiments are quite well reproduced, the model however produces a kink in the stress evolution at suctions of about 80 kPa. This kink is not due to the mechanical model, which is non-linear thanks to its hypoplastic formulation, but due to bi-linear hysteretic water retention model based on Brooks and Corey (1964) formulation.

Dependency of swelling pressure on the initial dry density is shown in Figure 11 representing the data on Czech B75 bentonite (data by Hausmannová, 2017). Swelling pressures are very well reproduced.

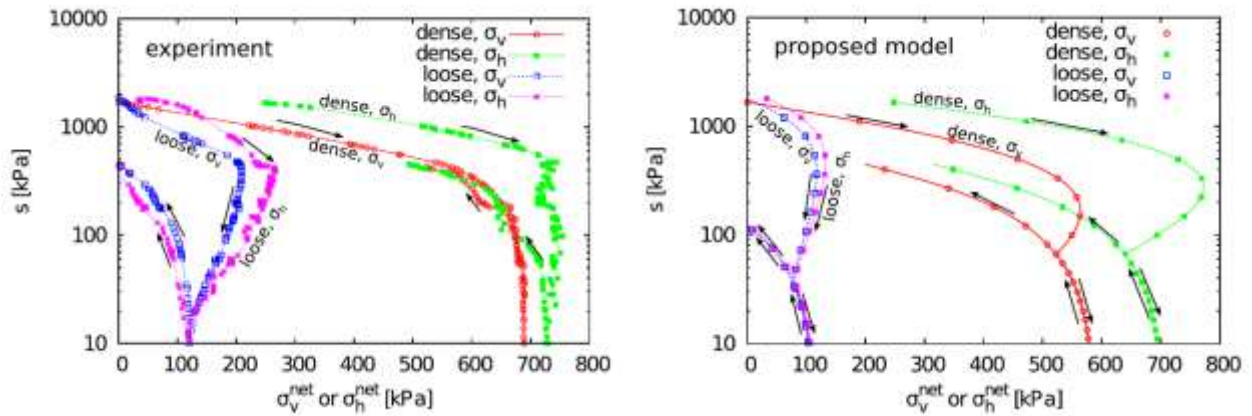


Figure 10: Evolution of vertical and horizontal stress in  $K_0$ -compacted specimens of Boom clay during constant volume wetting-drying test. Experimental data by Romero (1999), figure from Mašín (2013).

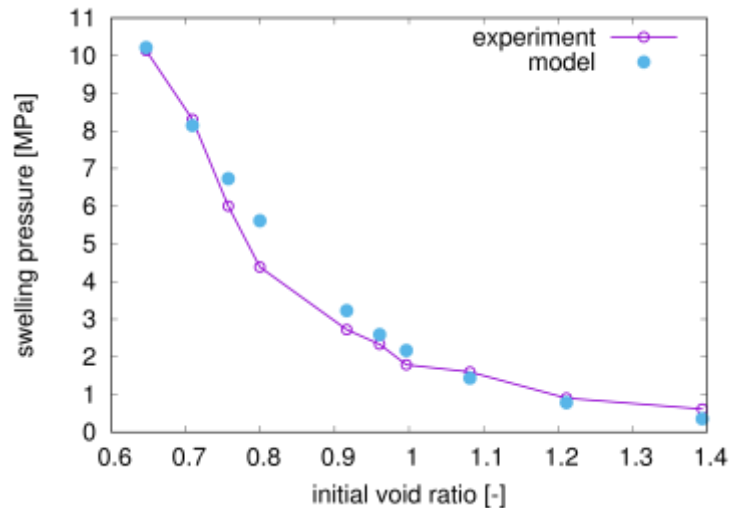


Figure 11: Predictions of the dependency of swelling pressures on the initial void ratio (dry density). Experimental data on B75 bentonite by Hausmannová (2017).

#### 5.4 Stress path dependence from an unsaturated to a saturated state

Specification: Stress path dependency can be checked by simulating different stress paths starting at the same initial value of suction and stress and finishing at a final common value of stress and zero suction. Three paths are suggested (Figure 12):

- Reduction of suction to zero followed by an increase of stress (red path).
- Increase of stress under constant suction followed by reduction of suction to zero (brown path).
- Swelling pressure test followed by a stress reduction to the final value (blue path).

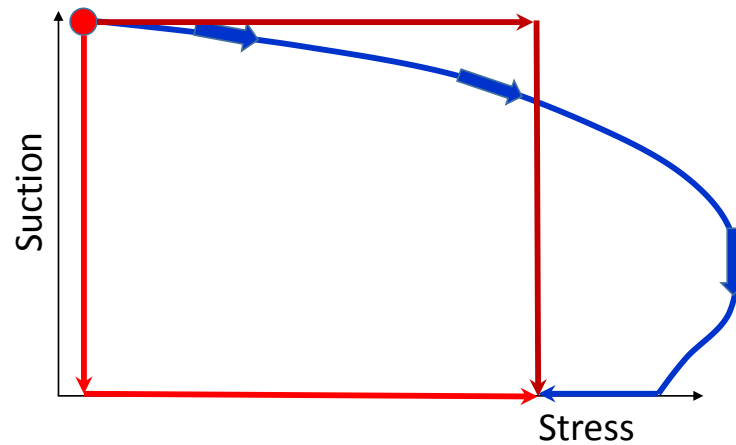
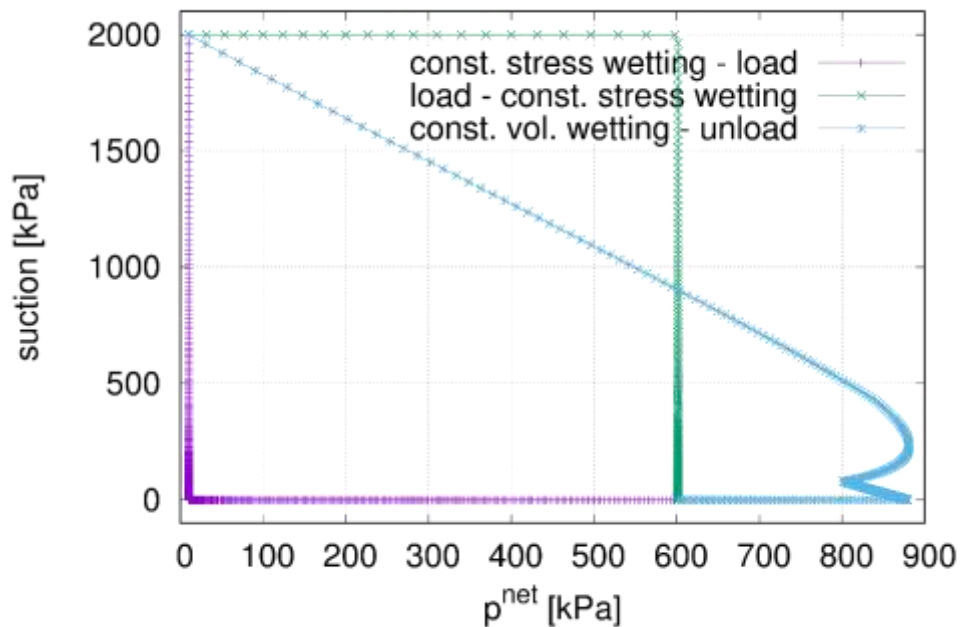


Figure 12: Suggested suction-stress paths to check stress path dependency from an unsaturated to a saturated state. Stress may be vertical total stress (in oedometer tests) or mean total stress (in isotropic loading tests)

Model Performance: Simulations of the prescribed experiments are in Figure 13. Clearly, the model predicts suction - stress path dependency: the final volumetric strain depends on the path taken. Maximum swelling is exhibited by the sample swelling without load, followed by the sample, which is swelling after initial loading. Finally, smallest strains (but still expansive) exhibit sample which was wetted under constant volume and then unloaded to the target stress.



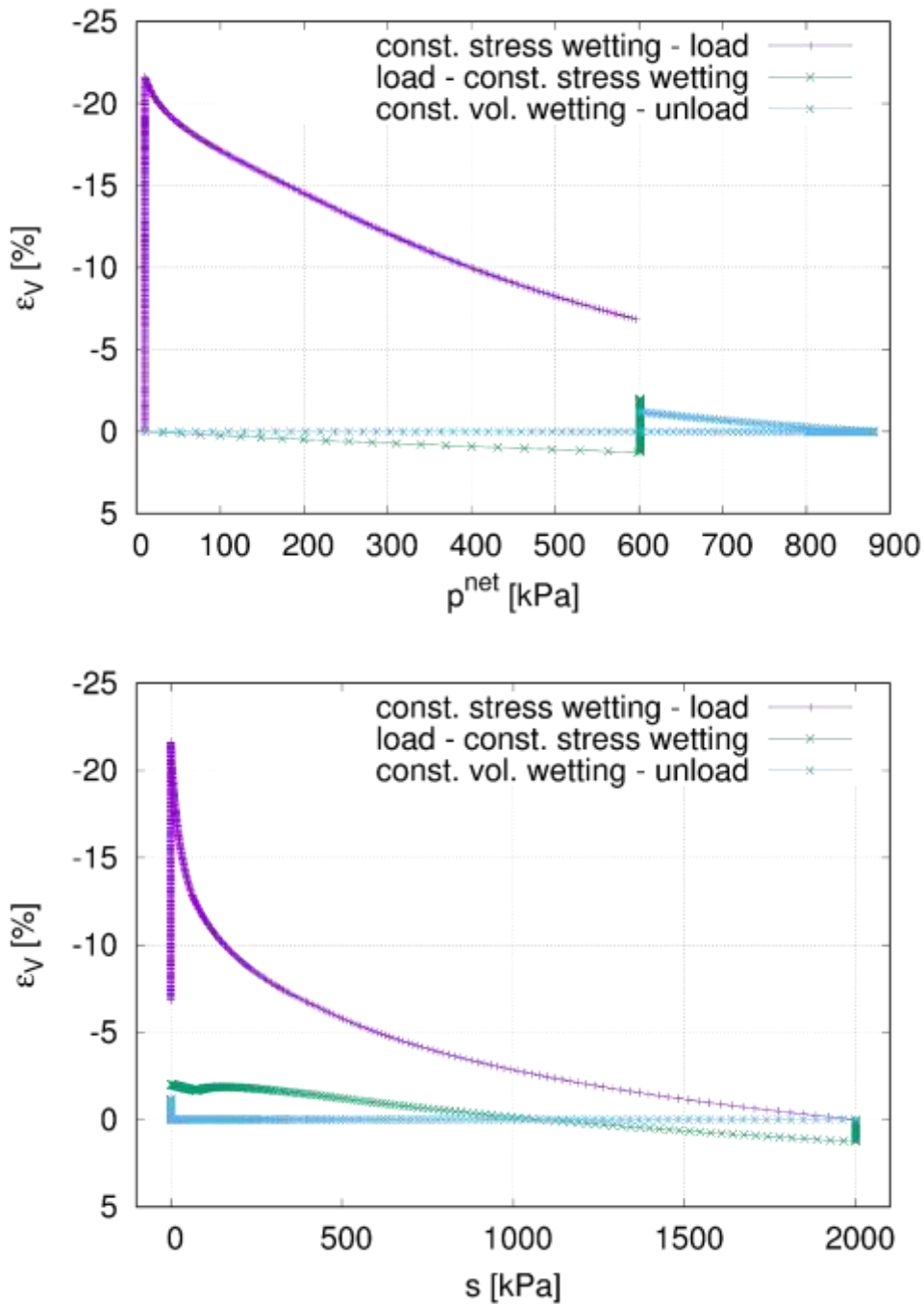


Figure 13: Results of the isotropic test representing stress path dependence from an unsaturated to a saturated state. Calculated using for Boom clay parameters from Mašín (2013) with the initial void ratio  $e=0.6$ .

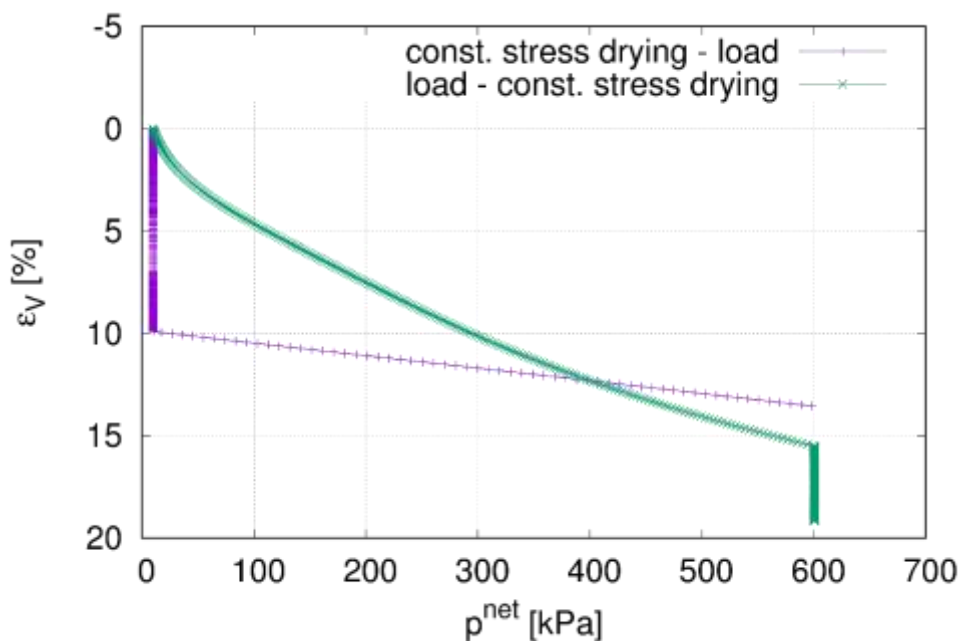
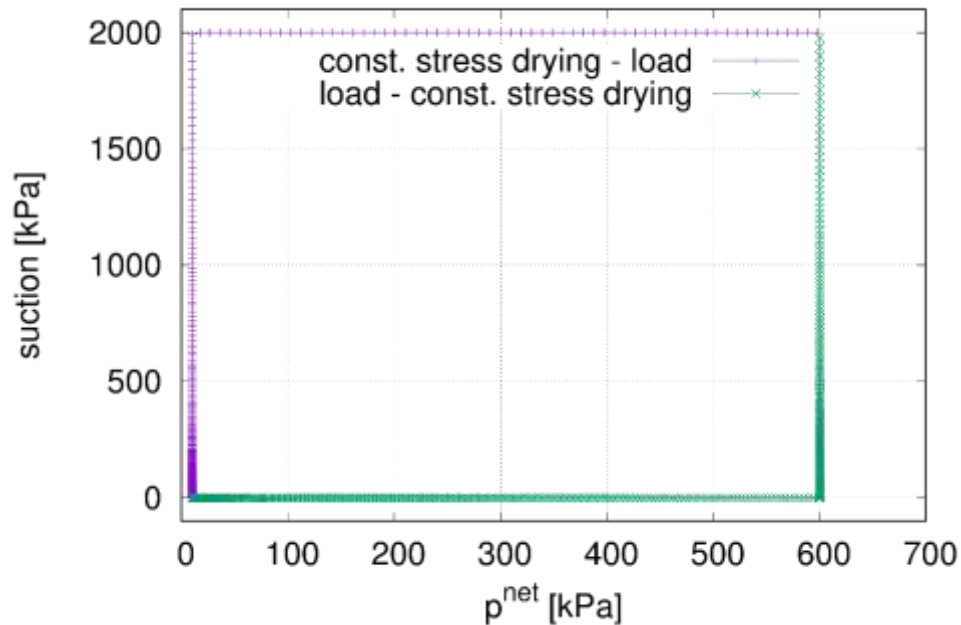
### 5.5 Stress path dependence from a saturated to an unsaturated state

Specification: Stress path dependency can be checked by simulating different stress paths starting at the same initial value stress and zero suction and finishing at a final common value of stress suction. Two paths are suggested (Figure 15):

- Increase of suction followed by an increase of stress at constant suction (red path).

- Increase of stress under zero suction followed by an increase of suction (brown path).

Model Performance: Simulation of the prescribed experiments are in Figure 14. Clearly, the model predicts suction - stress path dependency: the final volumetric strain depends on the path taken. Both the samples exhibit compaction at the end of the process, higher compaction showing the specimen loaded at saturated state.



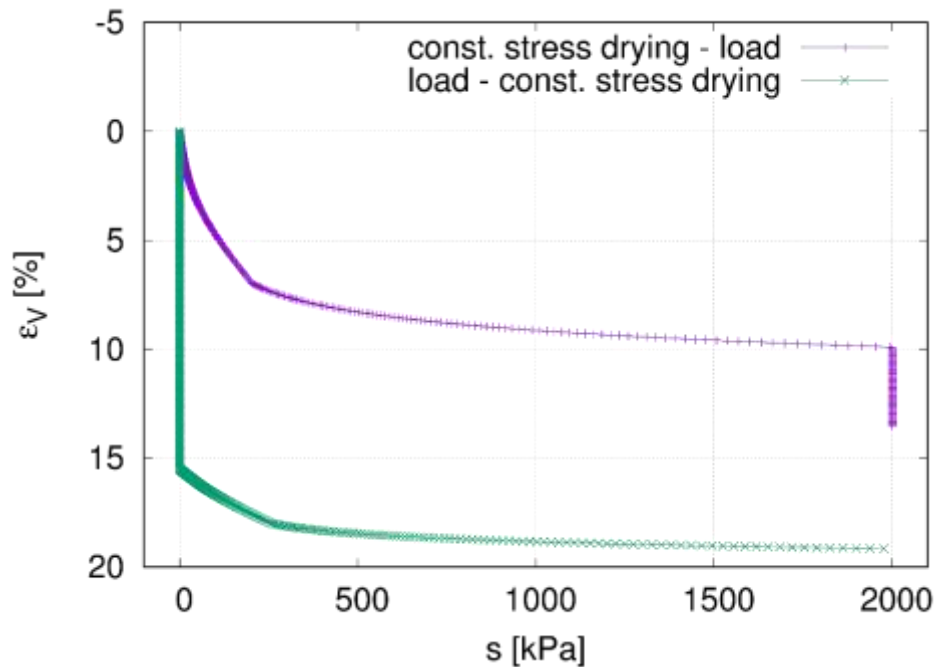


Figure 14: Results of the isotropic test representing stress path dependence from an saturated to an unsaturated state. Calculated using for Boom clay parameters from Mašín (2013) with the initial void ratio  $e=1.0$ .

## 5.6 Dependence of strains developed in a temperature cycle (increase/decrease) on OCR (or stress)

Specification: For the constitutive models that incorporate a thermal component, it is interesting to check the strains that develop during a cycle of increase/reduction of temperature and its dependence on OCR (overconsolidation ratio) or applied stress (Figure 16). Saturated conditions should be considered but it may also be of interest to observe this behaviour under different values of suction.

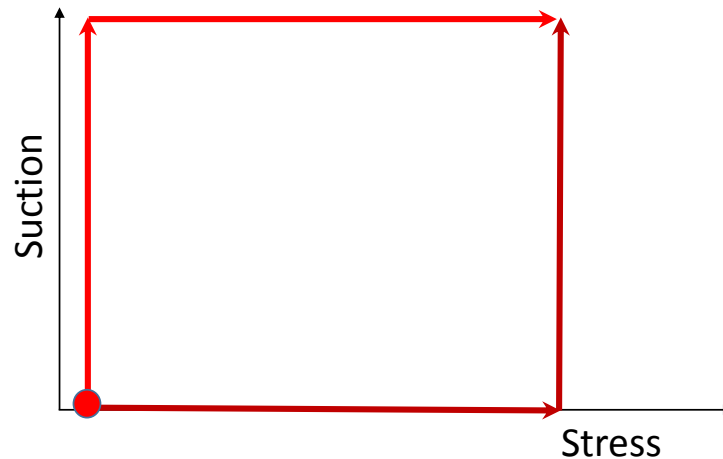


Figure 15: Suggested suction-stress paths to check stress path dependency from a saturated to an unsaturated state. Stress may be vertical total stress (in oedometer tests) or mean total stress (in isotropic loading tests)

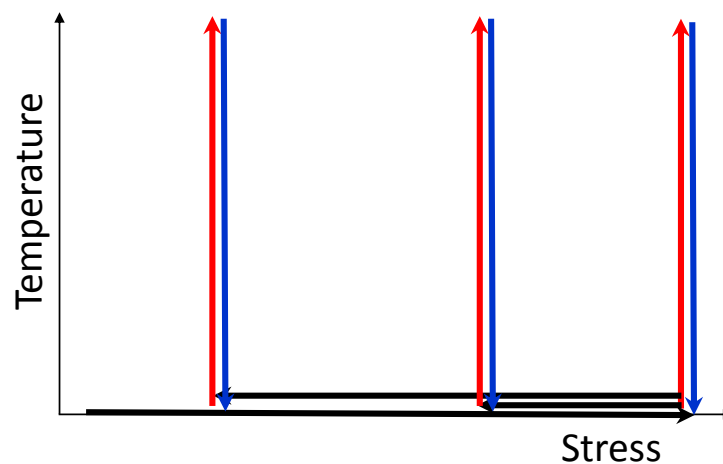


Figure 16: Temperature (increase/decrease) cycle at different stresses. Stress may be vertical total stress (in oedometer tests) or mean total stress (in isotropic loading tests)

Model Performance: The prescribed experiments have been simulated by Mašín (2017) and compared with experimental data by Tang et al. (2008) on MX80 bentonite. They are shown in Figure 17. The thermally-induced strains depend on both suction and stress levels. The samples at lowest suction exhibit initial thermally-induced compaction, whereas the other samples exhibit thermally-induced expansion. During cooling, all the samples contract.

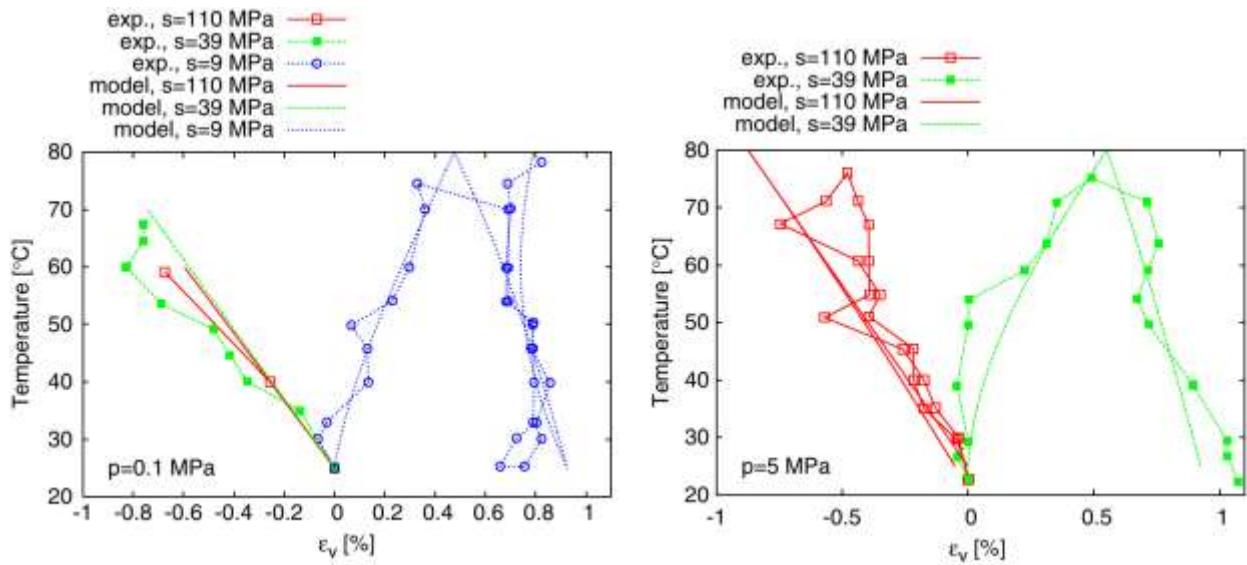


Figure 17: Volume change during isotropic tests due to heating-cooling cycles at various suctions and mean net stresses. Experimental data by Tang et al. (2008), figure from Mašín (2017).

### 5.7 Features Table

Summary of model properties is in Table 2.



Table 2: Features Table

Name of the constitutive law:		Hypoplasticity for Expansive Soils	
Behaviour feature	YES	NO	Remarks
<b>Mechanical behaviour</b>			
Dependence of swelling strain on applied stress (at the same dry density) (Figure1)	YES		
Dependence of swelling stress on dry density (at the same stress) (Figure 1)	YES		
Irreversibility of strains in wetting/drying cycles (Figure 2)	YES		
Dependence of swelling pressure on dry density (Figure 4)	YES		
Stress path dependence from an unsaturated to a saturated state (Figure 5)	YES		
Stress path dependence from a saturated to an unsaturated state (Figure 6)	YES		
Double structure/porosity considered?	YES		
Are temperature effects considered in the model?	YES		
Dependence of strains developed in a temperature cycle (increase/decrease) on OCR (or stress) (Figure 7)	YES		
<b>Hydraulic behaviour (retention curve)</b>			
Hysteresis	YES		
Dependence on void ratio	YES		
Double structure/porosity considered?	YES		



## 6 Final Remarks

In this report, we summarised mathematical structure of a hypoplastic model for expansive clays, its material parameters and demonstrated its performance by comparing model predictions with various benchmark tests. Whenever possible, comparison was quantitative to show not only good qualitative predictions, but also accuracy of representation of experimental data. Thanks to its non-linear hypoplastic formulation, combined with double structure modelling framework and hysteretic void-ratio dependent water retention curve, the model predicts all the features of bentonite behaviour which were identified as important for predicting its response in the report assignment (Table 2).

## 7 Acknowledgements

This project receives funding from the Euratom research and training programme 2014-2018 under grant agreement No 745942.

## 8 References

Alonso, E.E., Vaunat, J., Gens, A. (1999). Modelling the mechanical behaviour of expansive clays. *Engineering Geology* 54, 173–183.

Brooks, R., Corey, A. (1964). Hydraulic properties of porous media. Hydrology paper no. 3. Colorado State University.

Gens, A., Alonso, E. (1992). A framework for the behaviour of unsaturated expansive clays. *Canadian Geotechnical Journal* 29, 1013–1032.

Gudehus, G. (1996). A comprehensive constitutive equation for granular materials. *Soils and Foundations* 36 (1), 1–12.

Hausmannová, L. (2017). The influence of water pressure on the hydraulic conductivity and swelling pressure of Czech bentonites. Ph.D. thesis, Faculty of Civil Engineering, Czech Technical University.

Mašín, D. (2005). A hypoplastic constitutive model for clays. *International Journal for Numerical and Analytical Methods in Geomechanics* 29 (4), 311–336.

Mašín, D. (2010). Predicting the dependency of a degree of saturation on void ratio and suction using effective stress principle for unsaturated soils. *International Journal for Numerical and Analytical Methods in Geomechanics* 34, 73–90.

Mašín, D. (2012). Hypoplastic Cam-clay model. *Géotechnique* 62 (6), 549–553.



Mašín, D. (2013). Double structure hydromechanical coupling formalism and a model for unsaturated expansive clays. *Engineering Geology* 165, 73-88.

Mašín, D. (2014). Clay hypoplasticity model including stiffness anisotropy. *Géotechnique* 64 (3), 232–238.

Mašín, D. (2017). Coupled thermohydromechanical double structure model for expansive soils. *ASCE Journal of Engineering Mechanics* 143, No. 9.

Mašín, D., Khalili, N. (2008). A hypoplastic model for mechanical response of unsaturated soils. *International Journal for Numerical and Analytical Methods in Geomechanics* 32 (15), 1903–1926.

Mašín, D., and Khalili, N. (2016). Swelling phenomena and effective stress in compacted expansive clays. *Can. Geotech. J.*, 53(1), 134–147.

Tang, A.-M., Cui, Y.-J., and Barnel, N. (2008). Thermo-mechanical behaviour of a compacted swelling clay. *Géotechnique* 58(1), 45–54.

von Wolffersdorff, P. A. (1996). A hypoplastic relation for granular materials with a predefined limit state surface. *Mechanics of Cohesive-Frictional Materials* 1, 251–271.

## 9 Appendix

This Appendix presents complete mathematical formulation of the THM hypoplastic model, as has been published in Mašín (2017).

The mathematical formulation of the proposed model for expansive soils is summarized in the following. The behavior of two structural levels is linked through

$$\dot{\epsilon} = \dot{\epsilon}^M + f_m \dot{\epsilon}^m \quad (30)$$

with the following void ratio measures and their relationships:

$$\begin{aligned} \frac{\dot{e}}{1+e} &= \text{tr} \dot{\epsilon} \\ \frac{\dot{e}^M}{1+e^M} &= \text{tr} [\dot{\epsilon}^M + (f_m - 1) \dot{\epsilon}^m] \\ \frac{\dot{e}^m}{1+e^m} &= \text{tr} \dot{\epsilon}^m \end{aligned} \quad (31)$$

$$e = e^M + e^m + e^M e^m \quad (32)$$

$$S_r = S_r^M + \frac{e^m}{e} (S_r^m - S_r^M) \quad (33)$$

The mechanical behavior of the macrostructure is governed by

$$\dot{\sigma}^M = f_s (\mathcal{L} : \dot{\epsilon}^M + f_d \mathbf{N} \| \dot{\epsilon}^M \|) + f_u (\mathbf{H}_s + \mathbf{H}_T) \quad (34)$$

where  $\sigma^M$  = macrostructural effective stress defined by

$$\sigma^M = \sigma^{\text{net}} - \chi^M s \mathbf{1} \quad (35)$$

The macrostructural effective stress parameter  $\chi^M$  coincides with the macrostructural degree of saturation  $S_r^M$ :

$$S_r^M = \chi^M = \begin{cases} 1 & \text{for } s < s_e \\ \left(\frac{s_e}{s}\right)^\gamma & \text{for } s \geq s_e \end{cases} \quad (36)$$

where

$$s_e = s_{en} (a_e + a_{scan} - a_e a_{scan}) \quad (37)$$

with parameter  $a_e$  and state variable  $a_{scan}$  defined as

$$a_{scan} = \frac{s - s_W}{s_D - s_W} \quad (38)$$

where  $s_D$  = suction at the main drying curve; and  $s_W$  at the main wetting curve = current  $S_r^M$ .

It follows that

$$s_D = \frac{s_{en}}{s_e} s \quad (39)$$

with

$$s_{en} = s_{e0} \frac{e_0^M}{e^M} \left( \frac{a + bT}{a + bT_r} \right) \quad (40)$$

where  $a$ ,  $b$ , and  $T_r$  = parameters.

The rate equation for  $a_{scan}$  reads for  $s > a_e s_{en}$

$$\dot{a}_{scan} = \frac{1 - r_\lambda}{s_D(1 - a_e)} \dot{s} \quad (41)$$

Here  $r_\lambda$  is defined as

$$r_\lambda = \begin{cases} 1 & \text{for } s = s_D \text{ and } \dot{s} > 0 \\ 1 & \text{for } s = a_e s_D \text{ and } \dot{s} < 0 \\ \frac{\gamma_{scan}}{\gamma} & \text{otherwise} \end{cases} \quad (42)$$

where  $\gamma = 0.55$  and  $\gamma_{scan} = \gamma/10$  = slopes of the main wetting-drying and scanning curves respectively. If  $s \leq a_e s_{en}$ , then  $a_{scan} = 0$ . The macrostructural effective stress rate from Eq. (34) is given by

$$\dot{\sigma}^M = \dot{\sigma}^{net} + \mathbf{1}\chi^M \left[ (1 - r_\lambda)\dot{s} - \gamma_s \frac{\dot{e}^M}{e^M} + \frac{\gamma_s b \dot{T}}{a + bT} \right] \quad (43)$$

with  $\dot{e}^M$  calculated using Eq. (31). The hypoplastic tensor  $\mathcal{L}$ , which assumes transversely isotropic material (Mašín 2014), is calculated from

$$\mathcal{L} = \frac{1}{2} a_1 \dot{\mathbf{1}}\mathbf{1} + a_2 \mathbf{1} \otimes \mathbf{1} + a_3 (\mathbf{p} \otimes \mathbf{1} + \mathbf{1} \otimes \mathbf{p}) + a_4 \dot{\mathbf{p}}\mathbf{1} + a_5 \mathbf{p} \otimes \mathbf{p} \quad (44)$$

where  $\mathbf{p} = p_{ij} = n_i n_j$ , with  $n_i$  a unit vector normal to the plane of symmetry  $\mathbf{XY} = 1/2(X_{ik}Y_{jl} + X_{il}Y_{jk} + X_{jl}Y_{ik} + X_{jk}Y_{il})$

$$a_1 = \alpha_E \left( 1 - \nu_{pp} - 2 \frac{\alpha_E}{\alpha_v} \nu_{pp}^2 \right) \quad (45)$$

$$a_2 = \alpha_E \nu_{pp} \left( 1 + \frac{\alpha_E}{\alpha_v} \nu_{pp} \right) \quad (46)$$

$$a_3 = \alpha_E \nu_{pp} \left( \frac{1}{\alpha_v} + \frac{\nu_{pp}}{\alpha_v} - 1 - \frac{\alpha_E}{\alpha_v} \nu_{pp} \right) \quad (47)$$

$$a_4 = \alpha_E \left( 1 - \nu_{pp} - 2 \frac{\alpha_E}{\alpha_v} \nu_{pp}^2 \right) \frac{1 - \alpha_G}{\alpha_G} \quad (48)$$

$$a_5 = \alpha_E \left( 1 - \frac{\alpha_E}{\alpha_v} \nu_{pp}^2 \right) + 1 - \nu_{pp}^2 - 2 \frac{\alpha_E}{\alpha_v} \nu_{pp} (1 + \nu_{pp}) - \frac{2\alpha_E}{\alpha_G} \left( 1 - \nu_{pp} - 2 \frac{\alpha_E}{\alpha_v} \nu_{pp}^2 \right) \quad (49)$$

The hypoplastic barotropy factor  $f_s$  is

$$f_s = -\frac{3\text{tr}\sigma^M}{2\lambda_{act}^*} \left( \frac{1}{\lambda_{act}^*} + \frac{1}{\kappa^*} \right) \quad (50)$$

with  $\lambda_{act}^*$  calculated from (for derivation of  $\lambda_{act}^*$ , see Appendix II)

$$\lambda_{act}^* = \frac{\lambda^*(s, T) e^M (1 + e^m) - \kappa_m (1 + e^m) (p^M/p^m) \{ (1 + e^M) [n_s - l_s \ln(p^M/p_r)] + f_m e^M \}}{e^M (1 + e^m) - (1 + e) [n_s - l_s \ln(p^M/p_r)]} \quad (51)$$

and scalar  $A_m$  calculated as

$$A_m = \nu_{pp}^2 \left( \frac{4\alpha_E}{\alpha_v} - 2\alpha_E^2 + 2 \frac{\alpha_E^2}{\alpha_v^2} - 1 \right) + \nu_{pp} \left( \frac{4\alpha_E}{\alpha_v} + 2\alpha_E \right) + 2\alpha_E + 1 \quad (52)$$

The anisotropy coefficients can be calculated from

$$\alpha_E = \alpha_G^{(1/x_{GE})} \quad (53)$$

$$\alpha_v = \alpha_G^{(1/x_{Gv})} \quad (54)$$

$$x_{GE} = 0.8 \quad (55)$$

$$x_{Gv} = 1 \quad (56)$$

However, in the case of assumed elastic isotropy,  $\alpha_G$  from Eq. (45) is equal to 1, and thus also  $\alpha_E$  and  $\alpha_v$ . The hypoplastic nonlinear term is governed by

$$\mathbf{N} = -\frac{\mathcal{A}:\mathbf{d}}{f_s f_d} \quad (57)$$

with the fourth-order tensor  $\mathcal{A}$

$$\mathcal{A} = f_s \mathcal{L} + \frac{\sigma^M}{\lambda_{act}^*} \otimes \mathbf{1} \quad (58)$$

and the pyknotropy factor

$$f_d = \left( \frac{2p^M}{p_e} \right)^{\alpha_f} \quad (59)$$

Factor  $f_d^A$  controls the shape of the asymptotic state boundary surface:

$$f_d^A = 2^{\alpha_f} (1 - F_m)^{\alpha_f/\omega} \quad (60)$$

The Matuoka-Nakai factor  $F_m$  reads

$$F_m = \frac{9I_3 + I_1 I_2}{I_3 + I_1 I_2} \quad (61)$$

and the scalar  $\omega$  from Eq. (60) is

$$\omega = -\frac{\ln(\cos^2 \varphi_c)}{\ln 2} + a_f (F_m - \sin^2 \varphi_c) \quad (62)$$

with default value of  $a_f$

$$a_f = 0.3 \quad (63)$$

Stress invariants  $I_1$ ,  $I_2$ , and  $I_3$  are calculated from

$$I_1 = \text{tr} \sigma^M \quad (64)$$

$$I_2 = \frac{1}{2} [\sigma^M : \sigma^M - (I_1)^2] \quad (65)$$

$$I_3 = \det \sigma^M \quad (66)$$

Asymptotic strain rate direction  $d$  is given by

$$d = \frac{d^A}{\|d^A\|} \quad (67)$$

with

$$d^A = -\hat{\sigma}^{*M} + \mathbf{1} \left[ \frac{2}{3} - \frac{\cos 3\theta + 1}{4} F_m^{1/4} \right] \frac{F_m^{3/2} - \sin^2 \varphi_c}{1 - \sin^2 \varphi_c} \quad (68)$$

Lode angle function  $\cos 3\theta$  is given by

$$\cos 3\theta = -\sqrt{6} \frac{\text{tr}(\hat{\sigma}^{*M} \cdot \hat{\sigma}^{*M} \cdot \hat{\sigma}^{*M})}{[\hat{\sigma}^{*M} : \hat{\sigma}^{*M}]^{3/2}} \quad (69)$$

and

$$\xi = 1.7 + 3.9 \sin^2 \varphi_c \quad (70)$$

Normalized deviator stress  $\hat{\sigma}^{*M}$  reads

$$\hat{\sigma}^{*M} = \frac{\sigma^{*M}}{\text{tr} \sigma^{*M}} - \frac{\mathbf{1}}{3} \quad (71)$$

Nonlinear response inside the asymptotic state boundary surface is controlled by

$$\alpha_f = \frac{\ln \left[ \frac{\lambda^* - \kappa^*}{\lambda^* + \kappa^*} \left( \frac{3 + \alpha_f^2}{\alpha_f \sqrt{3}} \right) \right]}{\ln 2} \quad (72)$$

with

$$a_f = \frac{\sqrt{3}(3 - \sin \varphi_c)}{2\sqrt{2} \sin \varphi_c} \quad (73)$$

Hvorslev equivalent pressure is calculated from

$$p_e = p_r \exp \left[ \frac{N(s, T) - \ln(1 + e)}{\lambda^*(s, T)^*(s)} \right] \quad (74)$$

where  $p_r = 1$  = reference stress (kPa). Values of  $N(s, T)$  and  $\lambda^*(s, T)$  are represented by

$$\begin{aligned} N(s, T) &= N + n_s \left\langle \ln \frac{s}{s_e} \right\rangle + n_T \ln \left( \frac{T}{T_r} \right) \\ \lambda^*(s, T) &= \lambda^* + l_s \left\langle \ln \frac{s}{s_e} \right\rangle + l_T \ln \left( \frac{T}{T_r} \right) \end{aligned} \quad (75)$$

The variables  $N$ ,  $\lambda^*$ ,  $n_s$ ,  $l_s$ ,  $n_T$ , and  $l_T$  are model parameters. The tensorial terms  $\mathbf{H}_s$  and  $\mathbf{H}_T$  from Eq. (34) read

$$\mathbf{H}_s = -\frac{c_s r_\lambda \sigma^M}{s \lambda_{act}^*} \left( n_s - l_s \ln \frac{p_e}{p_r} \right) \langle -\dot{s} \rangle \quad (76)$$

$$\mathbf{H}_T = \frac{c_t \sigma^M}{T \lambda_{act}^*} \left( n_T - l_T \ln \frac{p_e}{p_r} \right) \langle T \rangle \quad (77)$$

for  $s > a_e s_{em}$  and  $\mathbf{H}_s = \mathbf{0}$  otherwise. The factor  $c_t$  reads

$$c_t = \frac{(\lambda_{act}^* + \kappa^*)(2\alpha_f - f_d) + 2\kappa^* f_d}{(\lambda_{act}^* + \kappa^*)(2\alpha_f - f_d^A) + 2\kappa^* f_d^A} \quad (78)$$

The factor controlling the collapsible behavior  $f_u$  is defined by

$$f_u = \begin{cases} \left( \frac{p^M}{p^{MA}} \right)^m & \text{for } p^M \leq p^{MA} \\ \left( \frac{p^M}{p^{MA}} \right)^{100} & \text{for } p^M > p^{MA} \end{cases} \quad (79)$$

where  $p^{MA}$  = value of the macrostructural effective stress corresponding to the current stress ratio at the asymptotic state boundary surface, which may be calculated as

$$p^{MA} = \frac{p_e}{2} (f_d^A)^{1/\alpha_f} \quad (80)$$

with  $m$  being a model parameter.

The behavior of the microstructure is governed by

$$\dot{\epsilon}_{nom}^m = \frac{\mathbf{1}}{3} \left( \alpha_s T - \frac{\kappa_m}{p^m} \dot{p}^m \right) \quad (81)$$

$$\dot{\epsilon}^m = (1 - f_{ul}) \dot{\epsilon}_{nom}^m \quad (82)$$

with parameter  $\kappa_m$ . The expression for the factor  $f_{ul}$  reads

$$f_{ul} = \begin{cases} \left( \frac{p^M}{p^{MA}} \right)^m & \text{for } p^M \leq p^{MA} \text{ and } \dot{\epsilon}_{nom}^m > 0 \\ 1 & \text{for } p^M > p^{MA} \text{ and } \dot{\epsilon}_{nom}^m > 0 \\ 0 & \text{for } \dot{\epsilon}_{nom}^m \leq 0 \end{cases} \quad (83)$$

The value  $\sigma^m$  is the microstructural effective stress given by

$$\sigma^m = \sigma^{act} - s = \sigma^{int} + u_w \quad (84)$$

The value  $e^m$  may be initialized through

$$e^m = \exp \left[ \kappa_m \ln \frac{s_r}{p^m} + \ln(1 + e_{r0}^m) + \alpha_s (T - T_r) \right] - 1 \quad (85)$$

with parameters  $e_{r0}^m$ ,  $s_r$ , and  $T_r$ .

Finally, the double-structure coupling function  $f_m$  reads

$$f_m = \begin{cases} 1 - (r_{em})^m & \text{for } \dot{p}^m \leq 0 \\ \left\langle \frac{c_{th} s}{s_e} \right\rangle & \text{for } \dot{p}^m > 0 \end{cases} \quad (86)$$

whereas  $f_m = 1$  if Eq. (86) leads to  $f_m > 1$ . The value  $r_{em}$  is the relative void ratio

$$r_{em} = \frac{e - e_d}{e_i - e_d} \quad (87)$$

with

$$e_i = \exp[N(s, T) - \lambda^*(s, T) \ln p^M] - 1 \quad (88)$$

and

$$e_d = e_m \quad (89)$$

# D3.1



## The Hysteresis Based Material model

### DELIVERABLE (D3.1)

### ANNEX C

Author(s): Mattias Åkesson, Ola Kristensson, Daniel Malmberg

Reporting period: e.g. 01/06/17 – 30/11/18

Date of issue of this report: **28/02/18**

Start date of project: **01/06/17**

Duration: 48 Months

This project receives funding from the Euratom research and training programme 2014-2018 under grant agreement No 745 942		
<b>Dissemination Level (choose)</b>		
<b>PU</b>	Public	X
<b>RE</b>	Restricted to a group specified by the partners of the Beacon project	
<b>CO</b>	Confidential, only for partners of the Beacon project	

### DISTRIBUTION LIST

Name	Number of copies	Comments
Athanasios Petridis (EC) Christophe Davies (EC)  Beacon partners		

## Abstract

This report describes the Hysteresis Based Material (HBM) model in its current state. This was originally developed for the homogenization task within the SKB Taskforce for Engineered Barrier Systems, and at the start of the Beacon project it had only been defined for water saturated conditions.

The model is based on an expression for the chemical potential of the clay water and its pressure dependence, which is further generalized to include both the hysteretic behaviour and the shear strength of bentonites.

During the preparation of this document the definitions have expanded so that they now also includes isotropic water unsaturated conditions, albeit only for paths with increasing degree of water saturation. Moreover, an expression for the thermal expansion of water-saturated bentonite was also developed during this work.

The performance of the model, as illustrated by the one-element tests presented here, is quite promising, especially since all presented calculations were made with a single set of parameter values.

# Content

<b>1</b>	<b>Introduction.....</b>	<b>5</b>
<b>2</b>	<b>Background .....</b>	<b>6</b>
<b>3</b>	<b>Basic hypotheses and scope.....</b>	<b>7</b>
3.1	Model for water saturated conditions .....	7
3.2	Model for water unsaturated conditions .....	8
<b>4</b>	<b>Mathematical description .....</b>	<b>9</b>
4.1	Material structure assumptions .....	9
4.2	Isotropic model for saturated conditions .....	10
4.3	Principal direction model for saturated conditions .....	12
4.4	Isotropic model for unsaturated conditions .....	12
<b>5</b>	<b>Input parameters and their sources.....</b>	<b>14</b>
5.1	Water saturated conditions .....	14
5.2	Water unsaturated conditions .....	16
<b>6</b>	<b>Performance.....</b>	<b>19</b>
6.1	Dependence of swelling strain on applied stress and on dry density.....	19
6.2	Irreversibility of strains in wetting/drying cycles.....	20
6.3	Behaviour during swelling stress test. Dependence of swelling pressure on dry density .....	21
6.4	Stress path dependence from a saturated to an unsaturated state.....	22
6.5	Dependence of strains developed in a temperature cycle on stress .....	23
6.6	Proposal for additional tests .....	24
<b>7</b>	<b>Conclusions .....</b>	<b>26</b>
	<b>References.....</b>	<b>27</b>
	<b>Appendix 1 .....</b>	<b>28</b>
	<b>Appendix 2 .....</b>	<b>30</b>
	<b>Appendix 3 .....</b>	<b>31</b>

# 1 Introduction

This report describes the Hysteresis Based Material model in its current state, and will be compiled together with descriptions of other models in Delivery 3.1 in the Beacon project.

The background and motives for the development of the model is briefly described in Chapter 2. The basic hypothesis and scope is outlined in Chapter 3. A general mathematical description is presented in Chapter 4 while the input parameters and their sources are presented in Chapter 5. The latter also entails definitions and parametrizations of functions used in the models. Chapter 6 presents the performance of the material model for a number of one-element tests provided by the work package. Finally, a few conclusions are made in Chapter 7.

## 2 Background

Engineered barrier systems are commonly composed of bentonite components with different initial dry density. These components can for instance be in form of compacted blocks, pellets-filled volumes, and powder-filled volumes; open, gas-filled, volumes are also often part of the engineered barrier systems.

Mechanisms governing the so called homogenization process (of the dry density) are active on the microscopic scale of the clay. The swelling of the bentonite is caused by the hydration of the interlayer cations and the osmotic transport of water into the interlayer solution. The water affinity is in turn caused by the negative layer charge of the montmorillonite which is balanced by cations located in the interlayer space. It is important to note that these processes can occur both under unsaturated or saturated conditions, i.e. with or without the presence of a gas phase in the material.

The homogenisation process is studied on the larger, component, scale. The initial state of the systems are commonly highly heterogenic and during the homogenisation process they undergo large changes in void ratios and water contents. It can be mentioned that some level of remaining heterogeneity is generally expected also after that the system has attained equilibrium.

Reliable hydro-mechanical modelling of the evolution of the systems requires a material model that can represent the macroscopic behaviour of the bentonite for a wide range of states in order to obtain a robust modelling tool with a high predictive capability.

A material model for compacted bentonite components was developed from a thermo-elastoplastic (TEP) constitutive law implemented in Code\_Bright (CIMNE, 2002). The TEP-model in turn was based on the Barcelona Basic Model (BBM) (Alonso et al. 1991). The modified TEP model and approach connected to its usage was first utilized for analyses of the homogenisation processes in initially water unsaturated KBS-3 buffer and backfill (Åkesson et al. 2010a), which was a part of SKB's safety assessment SR-Site. The modification and approach of usage consist of: modification of the TEP-law by incorporating a void ratio dependence of the swelling module; a strategy for parameter value identification and; a procedure for supporting the validity of the model results.

This has subsequently been used to analyse (and predict) the mechanical evolution of different field experiments: TBT (Åkesson et al. 2012); CRT (Åkesson et al. 2010b, Börgesson et al. 2016); Domplu (Börgesson et al. 2015; Grahm and Malm 2015); and Febex in situ test. It has also been used for HM analyses of the KBS-3H concept.

This material model has proven to be quite capable for prediction of the mechanical evolution of bentonite. Nevertheless, during usage some inconvenient limitations have been experienced; e.g. there are generally no defined void ratio dependences for the parameters; there is no mechanism for the yield surface to contract during isotropic swelling; and suction ( $>0$ ) cannot be represented for water saturated conditions. This has motivated the development of a new hydro-mechanical material model.

### 3 Basic hypotheses and scope

The Hysteresis Based Material (HBM) model has been developed with the aim to obtain a robust hydro-mechanical model for high density bentonite materials, with a high predictive capability. The overall guideline chosen for the development has been to mimic very simple test conditions to begin with and then successively considering more and more complex conditions. More specifically, this has meant that the starting point for the development was small strain water-saturated isotropic conditions, in particular for MX-80 bentonite with void ratios in the interval 0.7 to 3. From this state the model was then extended to also handle water-saturated non-isotropic conditions, which was the stage the model had reached at the beginning of the Beacon project. A subsequent extension of the model which was pursued during the preparation of this documents addressed water-unsaturated isotropic conditions. For the future, the model is envisaged to be generalised to water-unsaturated non-isotropic conditions.

#### 3.1 Model for water saturated conditions

The HBM model was defined for water saturated conditions by making the following three basic assumptions:

1) The model is based on an expression for the *chemical potential* of the clay water and its pressure dependence. From this follows (see derivation in the next chapter) that the sum of *suction* ( $s$ ) and *pressure* ( $p$ ) is equal to a quantity, denoted the *clay potential* ( $\Psi$ ), which in turn is a function of the void ratio ( $e$ ),  $s + p = \Psi(e)$ .

This means that the clay potential is equal to the suction value at unconfined conditions, and also that it equals the pressure at confined conditions with free access of water. The swelling pressure curve and the water retention curve can thereby be viewed as two sides of the same coin. It can also be noted that this relation is analogous to the effective stress concept according to which the deformations are governed by changes in effective stress, i.e. the difference between the (total) stress and the pore pressure.

2) In order to obtain a description which captures the *hysteretic behaviour* observed in oedometer tests and water retention measurements, and the *shear strength* observed in unconfined compression tests and triaxial tests, the following assumptions have been adopted.

- (i) The clay potential for a specific void ratio is assigned a value in an *allowed interval bounded by two functions*. One function during swelling conditions ( $\Psi_L = \Psi_M - \Psi_{\Delta/2}$ ) and the other for conditions during consolidation ( $\Psi_H = \Psi_M + \Psi_{\Delta/2}$ ).
- (ii) The actual state between these functions for a given direction is governed by the *history of the strains* in that direction.
- (iii) The difference between the states in different directions *should not exceed half the allowed interval* (i.e.  $\Psi_{\Delta/2}$ ).

3) The *density of water* ( $\rho_w$ ) is defined as a function of suction. This means that the compressibility of water ( $\partial\rho_w/\partial s$ ) is assumed to be applicable for positive suction values as well as for positive pore pressures (which basically are equivalent to negative suction values).

Models of the homogenisation process also include a hydraulic part in which the flow of water is governed by *Darcy's law*. An empirical relation between the hydraulic conductivity and the void ratio are used for this process. The influence of temperature can be incorporated in two ways in the defined hydro-mechanical framework: through the *thermal expansion of water* and can be implemented in definition of the density of water; and through the temperature dependence of the chemical potential of the clay water, which is related to the *difference in partial molar entropy between clay water and bulk water*, and can be implemented as an additional term in the clay potential function. The first of these alternatives were part of the performance assessment, see section 6.5.

### 3.2 Model for water unsaturated conditions

The generalization of the HBM model to water unsaturated conditions is based on the following assumptions:

- 1) The void space of the clay material (with void ratio  $e$ ) is divided in water-filled *micro voids* (with micro void ratio  $e_m$ ) and gas-filled *macro voids* (with macro void ratio  $e_M$ ).
- 2) The stress acting on the water-filled micro voids (i.e. saturated grains) is denoted the *contact stress*. The ratio between the total stress and the contact stress is equal to a quantity denoted as the *contact area fraction* ( $\alpha$ ). This is defined as a function of  $e_m$  and  $e$  and is equal to, or less than 1. This concept was proposed by Åkesson and Hökmark (2007).
- 3) The strains acting on the water-filled micro voids (i.e. saturated grains) is denoted the *micro-strains* and are related to the changes in  $e_m$ .
- 4) The *clay potential relation* defined for saturated conditions is *generalized to water unsaturated conditions* by replacing: total stresses with contact stresses, void ratios with micro-void ratios; and strains with micro-strains.
- 5) Due to the introduction of a new variable (i.e.  $e_m$ ), an *interaction function* which relates one quantity, e.g. the pressure, with two independent variables, e.g. the void ratio and the water content, has to be defined. This can be formulated as partial derivatives with respect to these variables:  $dp = \partial p / \partial e de + \partial p / \partial w dw$ . Such partial derivatives can in turn be formulated as functions.

Finally, it should be noted that this description was to a large degree developed during the preparation of this document, and the plan is therefore that it will be further refined later on. For instance, so far only isotropic micro-strains has been considered, as well as only paths with increasing degree of saturation.

## 4 Mathematical description

### 4.1 Material structure assumptions

For transparency the assumptions made regarding the structure of the material is explicitly described below. The representation of a water saturated material can be viewed as a special case of the water unsaturated material representation. In order to obtain the saturated representation the gas phase is removed from the formulation.

The material structure of the clay system is considered a mixture of different phases. A mixture volume element consists of: a solid phase volume element,  $dv_s$ , a liquid phase volume element,  $dv_l$ , and a gas phase volume element,  $dv_g$ . These different volume elements have the mass:  $dm_s$ ,  $dm_l$ , and  $dm_g$ , respectively. Corresponding mass densities,

$$\rho_s = \frac{dm_s}{dv_s}, \rho_l = \frac{dm_l}{dv_l} \text{ and } \rho_g = \frac{dm_g}{dv_g}, \quad (4-1)$$

and the water content,

$$w = \frac{dm_l}{dm_s}, \quad (4-2)$$

can thus be formed using the introduced entities.

The unsaturated material is considered a mixture on two different scales. The microscopic ( $m$ ) scale mixture is identical to the saturated material representation where a microscopic material volume element  $dv_m$  consists of a solid phase volume element  $dv_s$  and a liquid phase volume element  $dv_l$  according to,

$$dv_m = dv_s + dv_l. \quad (4-3)$$

The macroscopic ( $M$ ) scale mixture can be described by a macroscopic material volume element  $dv_M$  consisting of the microscopic material volume element and the gas phase volume element  $dv_g$  according to,

$$dv_M = dv_m + dv_g. \quad (4-4)$$

The notation has been chosen as to indicate that the microscopic mixture has the same role at the macroscopic scale as the solid phase volume element has at the microscopic scale. Thus, the microscopic mixture is considered a phase, immiscible with the gas phase, at the macroscopic scale. This has been utilized when forming the micro and macro void ratios according to,

$$e_m = \frac{dv_m - dv_s}{dv_s} \quad (4-5)$$

and

$$e_M = \frac{dv_M - dv_m}{dv_m}, \quad (4-6)$$

respectively. With the total void ratio defined as,

$$e = \frac{dv_M - dv_s}{dv_s}, \quad (4-7)$$

the following relation holds between the void ratios,

$$e = e_m + e_M + e_m e_M . \quad (4-8)$$

The void ratio in the current configuration,  $e$ , can be estimated by using the approximative expression,

$$e \approx \varepsilon_v (1 + e_0) + e_0 , \quad (4-9)$$

valid when the small-strain assumption is used.  $e_0$  denotes the void ratio in the reference configuration and  $\varepsilon_v \equiv \text{tr} \boldsymbol{\varepsilon}$  the volumetric strain, defined in terms of the small strain tensor  $\boldsymbol{\varepsilon}$ .

## 4.2 Isotropic model for saturated conditions

The chemical potential of the clay water ( $\mu$ ) was used as a starting point for the stress-strain relations of the model. This can be described as a function the water content ( $w$ ) and the pressure ( $p$ ) (e.g. Birgersson et al. 2010):

$$\mu = \mu_0 + RT \ln(RH(w)) + v_c p \quad (4-10)$$

where  $\mu_0$  is the chemical potential of a reference state,  $R$  is the universal gas constant,  $T$  is the absolute temperature,  $v_c$  is the molar volume of the clay water, and  $RH$  is the relative humidity of the clay at free swelling conditions. In the case of water saturated conditions  $RH$  can be described as a function of the void ratio instead of the water content. The relation above can then be rearranged as:

$$-\frac{\mu - \mu_0}{v_0} = -\frac{RT}{v_0} \ln(RH(e)) - \frac{v_c}{v_0} p \quad (4-11)$$

where  $v_0$  is the molar volume of bulk water. The term on the left hand side can be identified as *suction* ( $s$ ), while the first term on the right side from here on is denoted the *clay potential* ( $\Psi$ ). Assuming that  $v_0$  and  $v_c$  are equal, this can simply be expressed as:

$$s = \Psi(e) - p. \quad (4-12)$$

It should be noted that the suction corresponds to the RH in an external gas phase. Correspondingly, it corresponds to the negative value of an external water pressure. This means that the clay potential is defined in a similar way as an *effective stress*. It should also be noted that this description is based on the assumptions that the osmotic effect of any solution in the water can be disregarded and that the temperature is constant. It also assumes an *isotropic* stress state. Moreover, the description doesn't include any path dependence. This is taken into account by introducing a *void ratio history*, which from here on simply is denoted with  $e(t)$ , which means that equation (4-12) can be replaced with:

$$s = \Psi(e, e(t)) - p. \quad (4-13)$$

The clay potential function is here written on the following form:

$$\Psi(e, e(t)) = \Psi_M(e) + \Psi_{\Delta/2}(e)f(e(t)) \quad (4-14)$$

where  $\Psi_M$ ,  $\Psi_{\Delta/2}$  and  $f$  are denoted the *mid-line*, the *half allowed span*, and the *path variable*, respectively. It can be noted that  $\Psi_M$ , and  $\Psi_{\Delta/2}$  are defined as functions of the void ratio, whereas  $f$  is a variable, with values between -1 and +1, which depends on the void ratio

history. The clay potential is thus confined to a region with two bounding lines:  $\Psi_M + \Psi_{\Delta/2}$  (the consolidation line) and  $\Psi_M - \Psi_{\Delta/2}$  (the swelling line; see Figure 4-1).

The path variable ( $f$ ) is obtained by integration over time,

$$f = f_0 + \int_{t_0}^t \frac{\partial f}{\partial e} \dot{e} d\tau, \quad (4-15)$$

where the differential is given by,

$$\frac{\partial f}{\partial e} = -\frac{K'}{1 + e_0} (1 + \text{sgn}(\dot{e})f). \quad (4-16)$$

$K'$  is an introduced parameter, the sign of the time derivative of the void ratio determines whether the value of  $f$  changes asymptotically towards 1 or -1. The sign function is defined as:

$$\text{sgn}(x) = \begin{cases} -1 & \text{if } x < 0 \\ 0 & \text{if } x = 0 \\ 1 & \text{if } x > 0 \end{cases}. \quad (4-17)$$

Finally, it is in many cases necessary to define a relation between suction and the density of water thereby generalizing the compressibility of water ( $\beta$ ) to “negative pore pressures”:

$$\rho_w(s) = \rho_{w0} \exp(-\beta s). \quad (4-18)$$

Since the density of water is related to both water content and void ratio ( $\rho_w = \rho_s w / e$ ), this means that increments in suction is given by increments in water content and void ratio by the following simple relation:

$$ds = \frac{1}{\beta} \left( \frac{de}{e} - \frac{dw}{w} \right). \quad (4-19)$$

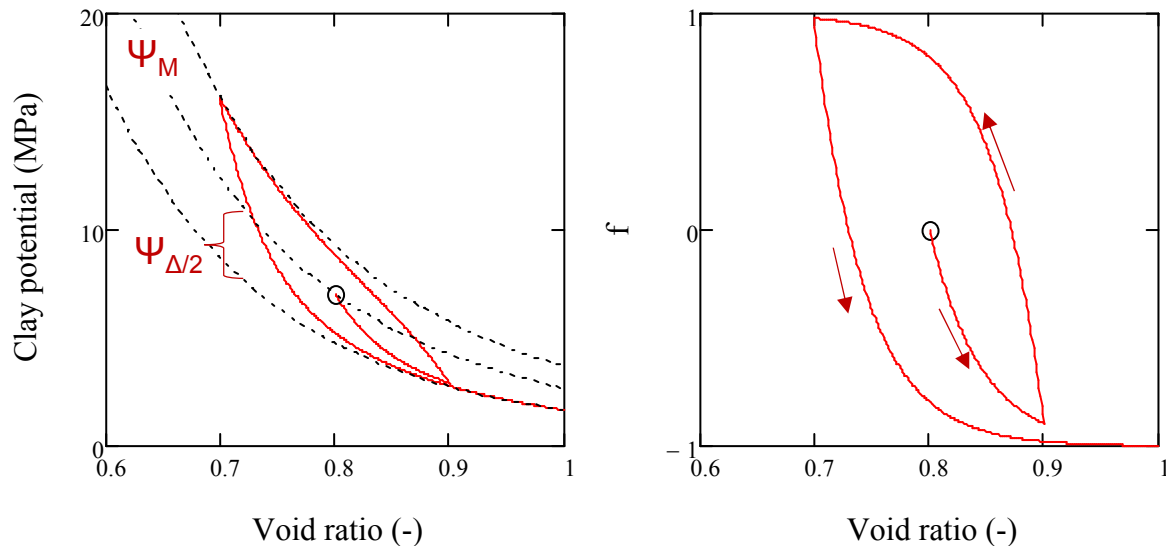


**Figure 4-1.** Clay potential and path variable ( $f$ ) versus void ratio. Right graph shows an example of the path variable for a case with swelling, followed by consolidation and followed by swelling. Left graph shows the same path mapped on the region for the clay potential.

### 4.3 Principal direction model for saturated conditions

This model is designed for the case when the principal directions correspond to the Cartesian basis  $\{\mathbf{e}_1, \mathbf{e}_2, \mathbf{e}_3\}$ .

$$\begin{aligned} -\boldsymbol{\sigma} &= \boldsymbol{\psi} - s\mathbf{1} \\ \boldsymbol{\psi} &= \tilde{\psi}_M(\varepsilon_v)\mathbf{1} + \tilde{\psi}_{\Delta/2}(\varepsilon_v)\mathbf{f} \\ \mathbf{f} &= \mathbf{f}_0 + \int_{t_0}^t \frac{\partial \mathbf{f}}{\partial \boldsymbol{\varepsilon}} \dot{\boldsymbol{\varepsilon}} d\tau \end{aligned} \quad (4-20)$$

The path dependent variable is a second order tensor,

$$\mathbf{f} = f_{11}\mathbf{e}_1 \otimes \mathbf{e}_1 + f_{22}\mathbf{e}_2 \otimes \mathbf{e}_2 + f_{33}\mathbf{e}_3 \otimes \mathbf{e}_3, \quad (4-21)$$

and its derivative with respect to strain is given by,

$$\begin{aligned} \frac{\partial \mathbf{f}}{\partial \boldsymbol{\varepsilon}} &= \frac{\partial f_{11}}{\partial \varepsilon_{11}} \mathbf{e}_1 \otimes \mathbf{e}_1 \otimes \mathbf{e}_1 \otimes \mathbf{e}_1 + \frac{\partial f_{22}}{\partial \varepsilon_{22}} \mathbf{e}_2 \otimes \mathbf{e}_2 \otimes \mathbf{e}_2 \otimes \mathbf{e}_2 + \\ &\quad \frac{\partial f_{33}}{\partial \varepsilon_{33}} \mathbf{e}_3 \otimes \mathbf{e}_3 \otimes \mathbf{e}_3 \otimes \mathbf{e}_3, \end{aligned} \quad (4-22)$$

The differential equation for the path variable in Eq (4-16) is generalized for the three principal directions:

$$\frac{\partial f_{\alpha\alpha}}{\partial \varepsilon_{\alpha\alpha}} = -K(\tilde{\kappa}(\mathbf{f}, \dot{\varepsilon}_{\alpha\alpha}) + \text{sgn}(\dot{\varepsilon}_{\alpha\alpha})f_{\alpha\alpha}), \quad (4-23)$$

where  $\alpha = \{1,2,3\}$  and no summation convention is to be used. It should be noted the parameter  $K$  is three times higher than  $K'$  in Eq (4-16), and the “1-term” is replaced with the  $\tilde{\kappa}$ -function:

$$\tilde{\kappa}(\mathbf{f}, \dot{\varepsilon}_{\alpha\alpha}) = 1 - \Phi(\tilde{\gamma}(\mathbf{f}, \dot{\varepsilon}_{\alpha\alpha}))\tilde{\gamma}(\mathbf{f}, \dot{\varepsilon}_{\alpha\alpha}), \quad (4-24)$$

where  $\Phi$  is the Heaviside step function, and the  $\tilde{\gamma}$ -function is defined as:

$$\tilde{\gamma}(\mathbf{f}, \dot{\varepsilon}_{\alpha\alpha}) = f_T + \text{sgn}(\dot{\varepsilon}_{\alpha\alpha})f_P, \quad (4-25)$$

Where  $f_T$  and  $f_P$  represents the “half-distance” and “mid-point” between the largest and smallest  $f$ -value, respectively:

$$f_T = \frac{\max(f_{ij}) - \min(f_{ij})}{2}, \quad f_P = \frac{\max(f_{ij}) + \min(f_{ij})}{2}, \quad (4-26)$$

The purpose of the  $\tilde{\kappa}$ - and the  $\tilde{\gamma}$ -function is to limit the *maximum difference* between the  $f$ -values in different directions to 1, thereby making sure that the shear strength of the material is taken into account, see section 5.1.

### 4.4 Isotropic model for unsaturated conditions

In order to generalize the material model to unsaturated conditions in a seamless way, the same constitutive equations defined for saturated conditions, i.e. Eq (4-13) to (4-16), should also be employed for unsaturated conditions. This can be achieved by modifying some of the governing variables in these equations. First, the void ratio ( $e$ ) at saturated conditions is replaced with the micro void ratio ( $e_m$ ), since these quantities are identical at saturated conditions, and both can be viewed as representing the interlayer distance between the clay sheets. Secondly, the strains are replaced with micro strains. For small strains the volumetric micro strain ( $\varepsilon_{mv}$ ) is related to the micro void ratio according to:

$$e_m \approx \varepsilon_{vm}(1 + e_{m0}) + e_{m0}, \quad (4-27)$$

where  $e_{m0}$  is the initial micro void ratio. Finally, the total pressure,  $p$ , is replaced with the contact pressure,  $p_m$ , (or contact stress for non-isotropic conditions) which is defined as the total pressure divided with a quantity denoted the contact area fraction ( $\alpha$ ), see Figure 4-2.

$$p_m = \frac{p}{\alpha(e_m, e)}. \quad (4-28)$$

$\alpha$  is defined as a function of  $e_m$  and  $e$ , and should have values below 1, except for saturated conditions for which it is precisely equal to 1.

With these variables in place, the constitutive equations can be redefined as:

$$\begin{aligned} s &= \Psi(e_m, \varepsilon_{mv}(t)) - p_m \\ \Psi(e_m, \varepsilon_{mv}(t)) &= \Psi_M(e_m) + \Psi_{\Delta/2}(e_m)f(\varepsilon_{mv}(t)) \\ f &= f_0 + \int_{t_0}^t \frac{\partial f}{\partial \varepsilon_{mv}} \dot{\varepsilon}_{mv} d\tau, \\ \frac{\partial f}{\partial \varepsilon_{mv}} &= -K'(1 + \text{sgn}(\dot{\varepsilon}_{mv})f) \end{aligned} \quad (4-29)$$

The introduction of a second measure of volume (or dual porosity) calls for the introduction of a relation between three variables (one dependent and two independent) denoted the interaction functions. This can be formulated in different ways, but as a first approach it can tentatively be defined as two partial derivatives of the pressure with respect to the void ratio and the water content:

$$dp = \frac{\partial p}{\partial e} de + \frac{\partial p}{\partial w} dw. \quad (4-30)$$

The quantification of the contact area fraction and the interaction functions are presented in the next chapter.

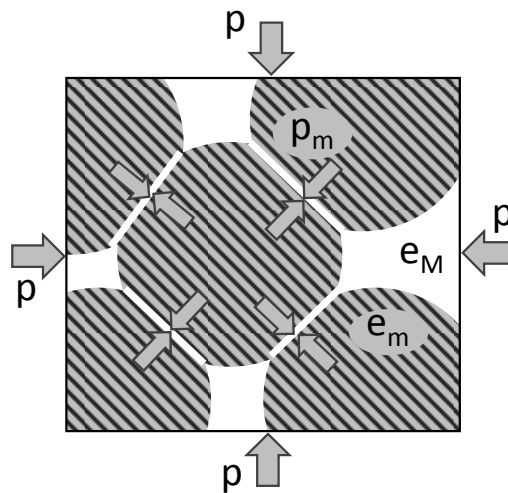


**Figure 4-2.** Schematic illustration of a dual porosity with water-filled micro voids and gas-filled macro voids, as well as for the distinction between the overall pressure and the contact pressure.

## 5 Input parameters and their sources

### 5.1 Water saturated conditions

The presented model is specified with three parameter sets: the clay potential (i.e.  $\Psi_M(e)$  and  $\Psi_{\Delta/2}(e)$ ), the  $K$  parameter, and the hydraulic conductivity  $K_H(e)$ . Two parameters are also required for the description of the density of water.

#### *Clay potential*

Several avenues may be available for the quantification of the clay potential, e.g. from data on retention properties for free swelling samples and oedometer tests with free access of water. In order to adhere to previously adopted material models, at least as far as possible, the presented analysis was based on two empirical relations: one between the swelling pressure ( $p_{sw}$ ) and the dry density ( $\rho_d$ ) (intentionally adopted at the lower end of measured data), and one between the von Mises stress at failure in a unconfined compression test ( $q_f = \sigma_1 - \sigma_3$ ) and the void ratio.

The swelling pressure function was adopted on the following form by Åkesson et al. (2010a), and with the following parameter values:  $c_0 = -4.74$   $c_1 = 4.12 \cdot 10^{-3}$ ;  $c_2 = -3.94 \cdot 10^{-7}$  ( $p_{sw}$  in MPa;  $\rho_d$  in  $\text{kg/m}^3$ ):

$$\log^{10}(p_{sw}(\rho_d)) = c_2 \rho_d^2 + c_1 \rho_d + c_0 \quad (5-1)$$

This can easily be converted to a function of the void ratio through the relation  $e = \rho_s / \rho_d - 1$ , where  $\rho_s$  is the solid density, for which the value  $2780 \text{ kg/m}^3$  has been used.

The relation for the von Mises stress at failure was adopted on the following form from experimental data presented by Dueck et al (2011), see Figure 5-1 (upper left):

$$q_f(e) = \frac{0.65}{(e - 0.14)^3} \text{ [MPa]} \quad (5-2)$$

The bounding lines was then simply quantified as:

$$\begin{cases} \Psi_L(e_m) = p_{sw}(e) \\ \Psi_H(e_m) = p_{sw}(e) + 2q_f(e) \end{cases} \quad (5-3)$$

A function with the same form as Eq (5-1) was adopted for the  $\Psi_H$  relation. The following parameter values were found:  $c_0 = -2.675$   $c_1 = 2.101 \cdot 10^{-3}$ ;  $c_2 = 1.669 \cdot 10^{-7}$  (MPa). The evaluated bounding lines are shown in Figure 5-1 (upper right) together with swelling pressure data. It should be noted that the used swelling pressure curve (5-1) to a large extent was based on free swelling retention data for an initial water content of 17%. This curve is therefore less relevant for void ratios below a level of approximately 0.7. The bounding lines are in turn used to adopt the mid-line:  $\Psi_M = (\Psi_L + \Psi_H)/2$ , and the half allowed span  $\Psi_{\Delta/2} = (\Psi_H - \Psi_L)/2$ .

#### *The K parameter*

The adoption of the  $K$  parameter was made through numerical integration of Eq (4-20) and (4-23). This was made for three triaxial tests presented by Dueck et al. (2010), see Figure 5-1 (lower graphs). The calculation was simplified by the conditions that: i) the radial stresses

( $\sigma_y$  and  $\sigma_z$ ) were equal, ii) that the radial strains ( $\varepsilon_y$  and  $\varepsilon_z$ ) were equal, and iii) that the water content was constant. The  $K$  value was then tuned in order to get approximately correct  $q$ -value for an axial strain of 2 %. This procedure resulted in a  $K$  value of 40.

*Hydraulic conductivity*

The hydraulic conductivity and its void ratio dependence were taken from the adoption by Åkesson et al. 2010a. Still, in order to mimic the results of the homogenization tests this parameterization was reduced with a factor of 2 which yields:

$$K_H(e) = 1.2 \cdot 10^{-13} e^{5.33} [m/s] \tag{5-4}$$

*Density of water*

The dependence of the water density on suction and on temperature was based on the compressibility ( $\beta = 4.5 \cdot 10^{-4} \text{ MPa}^{-1}$ ) and the thermal expansion ( $\alpha_T = -3.4 \cdot 10^{-4} \text{ C}^{-1}$ ) of water. Both values were taken from the Code\_Bright manual (CIMNE, 2002).

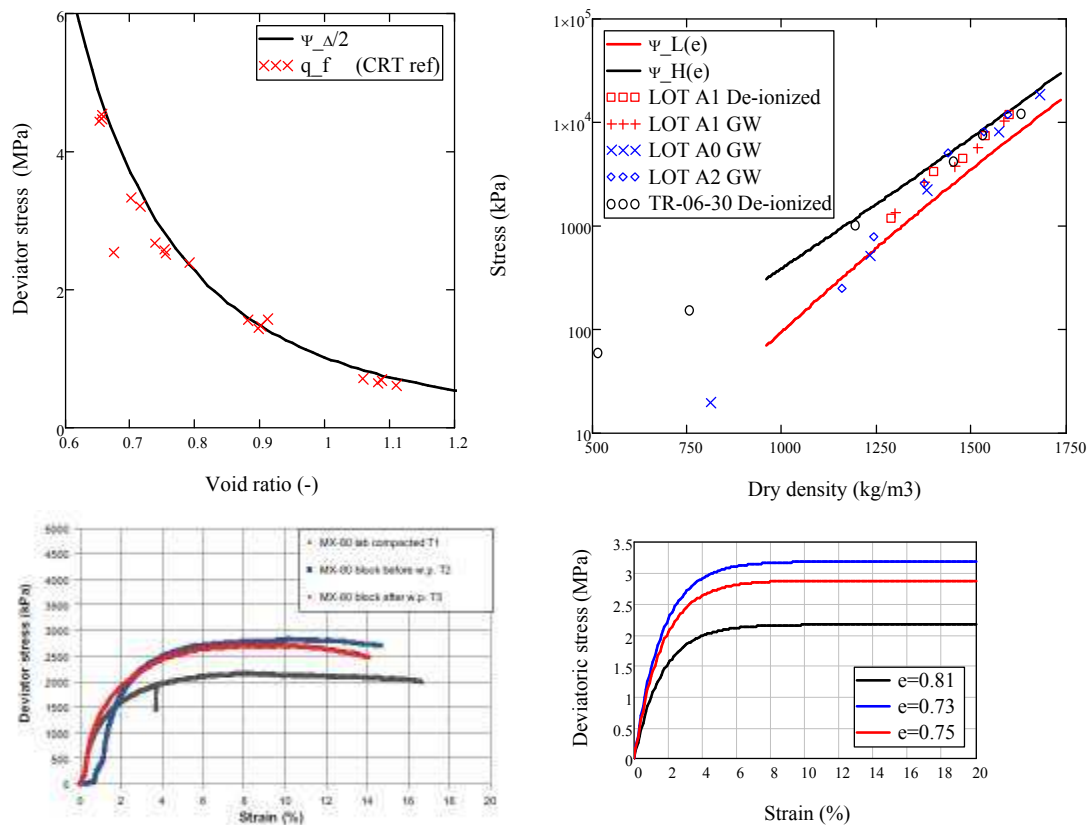


**Figure 5-1.** Adopted function from unconfined compression tests data (upper left); and comparison of clay potential bounding lines with swelling pressure data presented by Karnland et al. (2000), (2006) and (2009). Stress paths in  $q$ - $\varepsilon_{ax}$  plane for triaxial tests: experimental data (lower left) and model results (lower right).

## 5.2 Water unsaturated conditions

The functions introduced and defined for unsaturated conditions (contact area fraction and interaction function) have to be adopted and possibly calibrated from test results from different types of experiments. Such experiments can desirably be performed by keeping one of the macroscopic variables constant, for instance swelling pressure tests (constant volume), oedometer tests (constant water content) or swelling/shrinkage tests (constant load).

The contact area fraction  $\alpha$  comes into play under virtually any test condition (except unloaded cases) and therefore has to be adopted/calibrated iteratively. However, the area fraction should be related to the fraction between the volume of the grains ( $1 + e_m$ ) and the total volume ( $1 + e$ ). Moreover, this ratio is reduced as a power law with the exponent  $\gamma$ :

$$\alpha(e_m, e) = \left( \frac{1 + e_m}{1 + e} \right)^\gamma, \quad (5-5)$$

which means that the area fraction is significantly smaller than the volume fraction. For instance, a  $\gamma$ -value of 7 means that a volume fraction of 70% is reduced to an  $\alpha$ -value of 8 %. This type of expression together with a  $\gamma$ -value of 7 seems to generate fairly realistic behaviours according to the calculations presented in Chapter 6.

When it comes to the adoption of the interaction functions,

$$dp = \frac{\partial p}{\partial e} de + \frac{\partial p}{\partial w} dw, \quad (5-6)$$

it should be kept in mind that these should be formulated with some restrictions. For instance they should imply that suction reduces to zero when the degree of saturation approaches unity. Similarly, for dehydration paths, it can be foreseen (although this has not been investigated yet) that the pressure (or stresses) reduces to zero when the degree of saturation approaches zero.

The adoption of a  $\partial p/\partial e$ -function can be based on compression tests (e.g. oedometer) with constant water content. The situation is illustrated in Figure 5-2 (left) and the stress path direction can be formulated as:

$$\frac{\partial p}{\partial e} = - \frac{\ln \left[ \frac{p}{\Psi(e_m, f)} \right]}{\ln \left[ \frac{1 + e_m}{1 + e} \right]} \frac{p}{1 + e} \frac{\alpha(e_m, e) \Psi(e_m, f)}{p} \quad (5-7)$$

The dashed straight line in the figure ( $p = \alpha\Psi$ ) represents a condition with zero suction for the water content in question, and the stress path should move asymptotically towards a point along this line in which saturation is reached. The right hand side in the equation above is composed of three factors. The factor to the right gives a measure on how close the current pressure is to the “ $\alpha\Psi$ -line”. The other two factors gives the straight direction from the current state ( $e, p$ ) to the point of saturation ( $e_m, \Psi$ ) in a  $\ln(p) - \ln(1 + e)$  diagram. These factors combined yields the sought asymptotic behaviour. It can be noted that no parameters are introduced in this function, and (maybe unfortunately) that  $p$  has to exceed zero.

The  $\partial p/\partial w$ -function can be adopted from (5-7), and for a swelling test with constant load ( $dp = 0$ ).

The situation is illustrated in Figure 5-2 (right) for which a stress path direction can be formulated as:

$$\left. \frac{\partial e}{\partial w} \right|_{dp=0} = \frac{e(p, f) - e}{e(p, f) \frac{\rho_w(0)}{\rho_s} - e_m \frac{\rho_w(s)}{\rho_s}} \quad (5-8)$$

This is simply the straight direction from the current state  $(e, w)$  towards the point of saturation for the pressure in question  $(e(p, f)$  and  $w(p, f)$ ). It should be noted  $e(p, f)$  is an inverse function of the clay potential function Eq (4-14). By using the constraint  $dp = 0$  in Eq (4-30), a  $\partial p / \partial w$ -function can be derived as:

$$\frac{\partial p}{\partial w} = - \left. \frac{\partial p}{\partial e} \frac{\partial e}{\partial w} \right|_{dp=0} \quad (5-9)$$

Again, it can be noted that no parameters are introduced, and that  $p$  has to exceed zero.

The integration of any unsaturated path with increasing saturation degree is fairly straightforward except that a micro void ratio increment has to be calculated from increments in pressure, water content and void ratio. An expression for this can be derived by differentiating the basic expression for the clay potential:

$$ds + d\left(\frac{p}{\alpha}\right) = d\Psi. \quad (5-10)$$

The first term can be expressed in terms of increments of  $e_m$  and  $w$  (see Eq (4-19)):

$$ds = \frac{de_m}{\beta e_m} - \frac{dw}{\beta w}. \quad (5-11)$$

The second term is derived using the chain rule and by partial differentiation:

$$d\left(\frac{p}{\alpha}\right) = \frac{1}{\alpha} dp - \frac{p}{\alpha^2} \left( \frac{\partial \alpha}{\partial e_m} de_m + \frac{\partial \alpha}{\partial e} de \right) \quad (5-12)$$

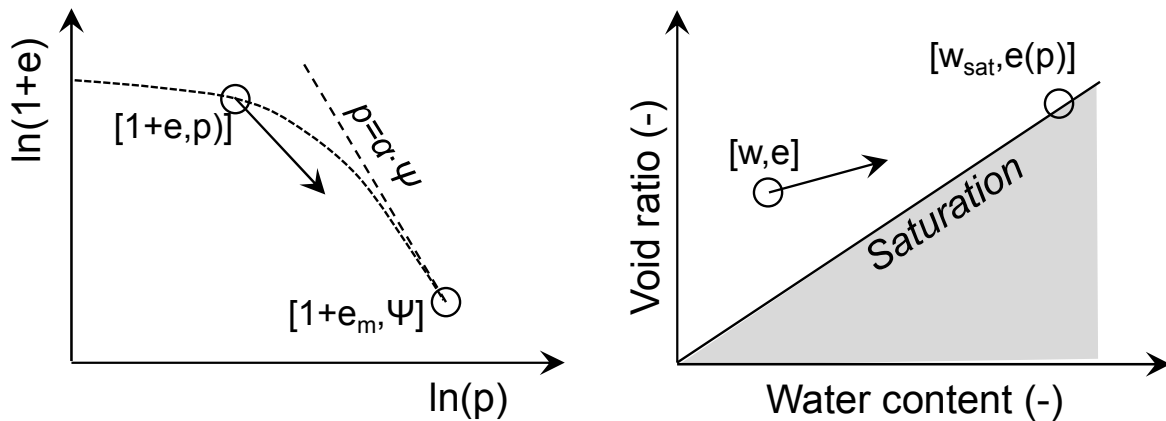


**Figure 5-2.** Schematic stress path directions used for adoption of interaction functions. Compression at constant water content (left) and swelling at constant load (right).

Finally, the third term is expressed in terms of an increment of  $e_m$ :

$$d\Psi = \frac{d\Psi}{de_m} de_m \quad (5-13)$$

although it should be observed that the derivative is composed of several terms:

$$\frac{d\Psi}{de_m} = \frac{d\Psi_M}{de_m} + f \frac{d\Psi_{\Delta/2}}{de_m} - \Psi_{\Delta/2} (1 + \text{sgn}(\dot{e}_m) f) \frac{K}{3(1 + e_{m0})} \quad (5-14)$$

Taken together, it can be seen that the micro void ratio increment can be derived from increments in  $p$ ,  $w$  and  $e$ :

$$\left[ \frac{p}{\alpha^2} \frac{\partial \alpha}{\partial e_m} + \frac{d\Psi}{de_m} - \frac{1}{\beta e_m} \right] de_m = \frac{1}{\alpha} dp - \frac{1}{\beta w} dw - \frac{p}{\alpha^2} \frac{\partial \alpha}{\partial e} de \quad (5-15)$$

This is illustrated in Figure 5-3 for cases with compression with constant water content. These tests were assumed to be performed starting from unsaturated conditions with an isotropic test geometry. Three void ratios were chosen (1, 1.3 and 1.6) and the initial  $f$ -value was set to zero. The initial pressure was set to 0.1 MPa. The initial water content for the three cases were 17, 23 and 39 %, respectively. The compression path was calculated by keeping  $w$  constant, by reducing  $e$ , and successively integrating  $p$ , with Eq (5-7);  $e_m$  with Eq (5-15);  $s$  with (5-11), and finally  $f$  with Eq (4-29). The calculated stress path in the  $(1 + e) - \ln(p)$  plane is shown in Figure 5-3. Corresponding cases with either constant volume or constant load are presented in the next Chapter.

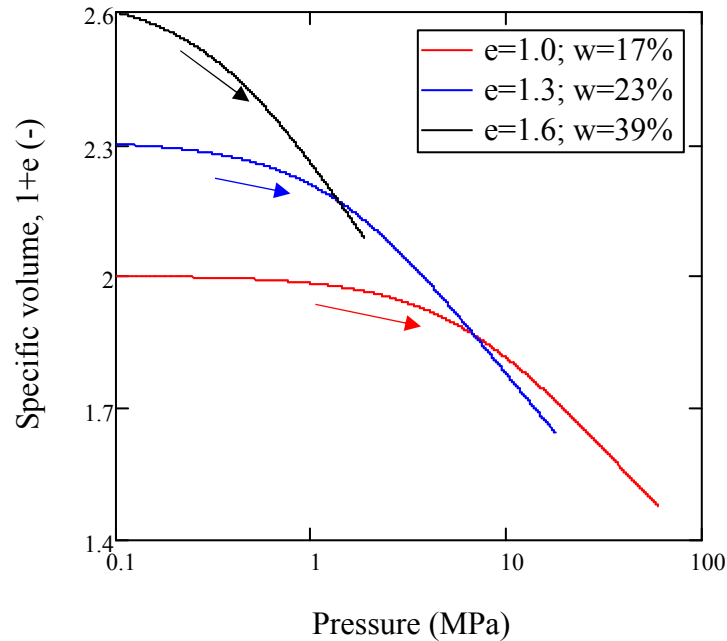


**Figure 5-3.** Calculated isotropic compression paths for cases with constant water content.

## 6 Performance

In order to illustrate the capabilities and limitations of the HBM model a number of single elements tests have been performed. These have been solved with simple programs written in a MathCad spreadsheet. The file is shown in full in Appendix. The selection of tests generally follows the instructions provided by the WP3 leader.

### 6.1 Dependence of swelling strain on applied stress and on dry density

These tests were assumed to be performed starting from unsaturated conditions with an isotropic test geometry. Six tests were performed, either with one void ratio (0.55) and three different pressures (0.2, 9 and 20 MPa), or with one pressure (1 MPa) and three different void ratios (0.55, 0.75 and 0.95). In all cases the initial water content was set to 13 % and the initial  $f$  value was set to zero. The void ratio evolution, shown in Figure 6-1, was calculated by keeping  $p$  constant, by increasing  $w$ , and successively integrating  $e$  with Eq(5-8);  $e_m$  with Eq (5-15);  $s$  with (5-11), and finally  $f$  with Eq (4-29).

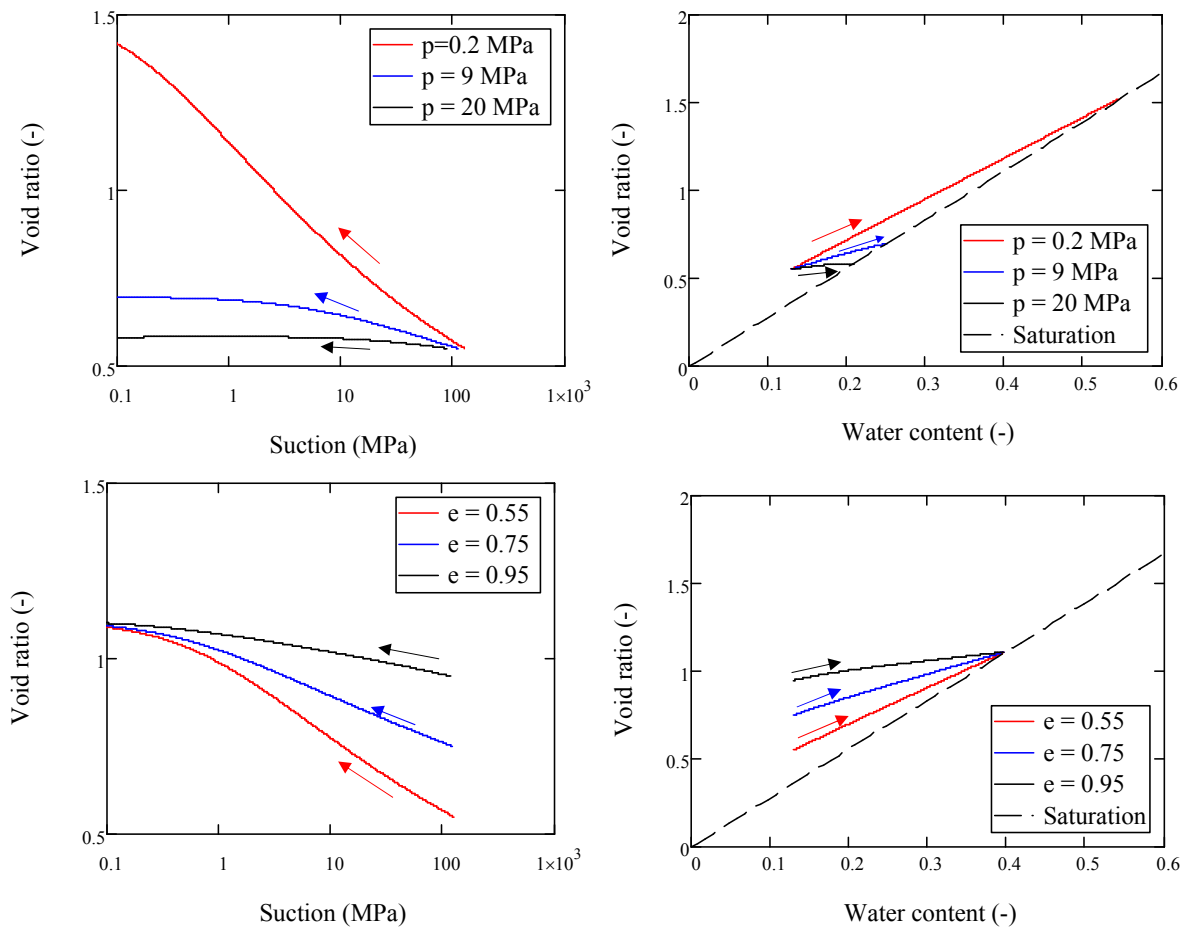


**Figure 6-1.** Swelling behaviour for cases with different pressures (upper) or with different initial void ratio (lower). Stress paths shown in  $e$ - $\ln(s)$  plane (left) and in  $e$ - $w$  plane (right).

## 6.2 Irreversibility of strains in wetting/drying cycles

These tests were assumed to be performed at saturated conditions with a 1D test geometry (i.e. oedometer). Three void ratios were chosen (0.6, 0.65 and 0.7). The initial value of the path variable ( $f$ ) was set to zero. This means that the initial clay potential values were 12.4, 16.9 and 23.4 MPa, respectively. The initial suction value was set to 10 MPa for all test cases which meant that the loads were 2.3, 6.9 and 13.4 MPa, respectively.

The calculation was performed by integrating Eq (4-20) and (4-23), by keeping the stress constant and changing the suction from the initial value down to zero, after which the suction value was increased to the initial value. Stress paths for these cycles are shown in Figure 6-2. It can clearly be seen that these cycles are irreversible.

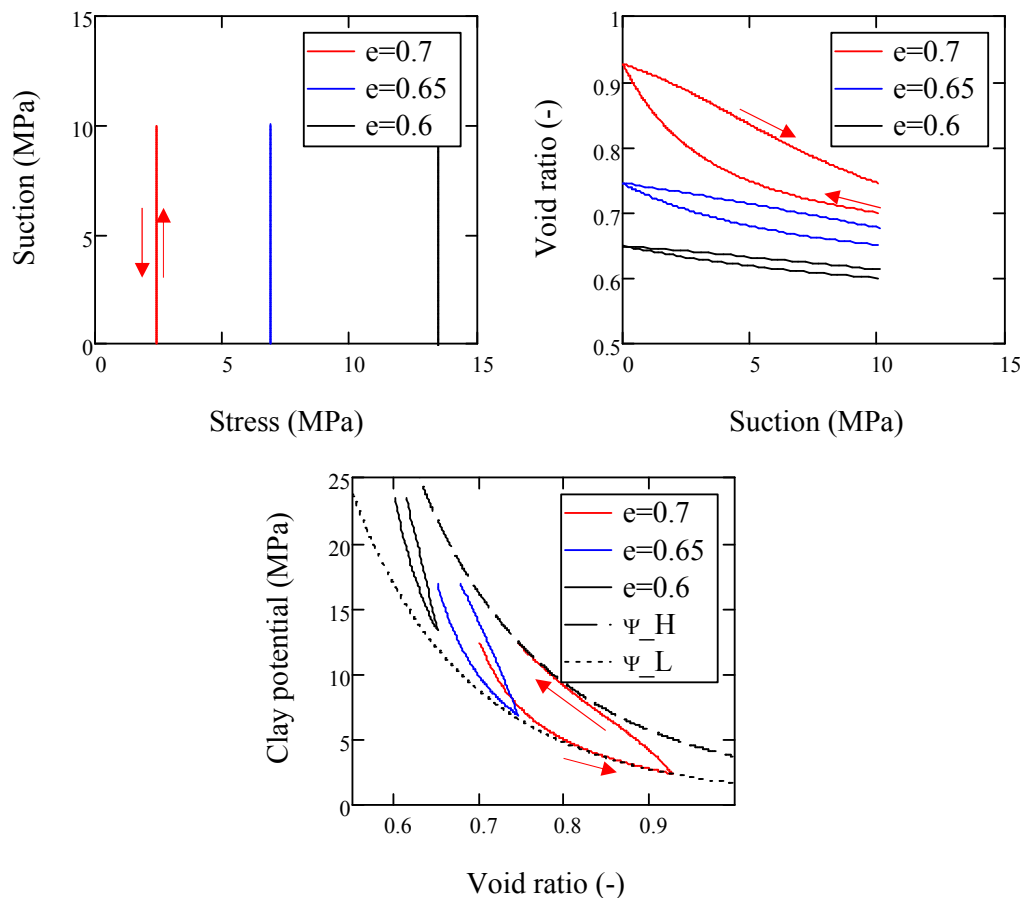


**Figure 6-2.** Calculated swelling/shrinkage path at constant load.

### 6.3 Behaviour during swelling stress test. Dependence of swelling pressure on dry density.

These tests were assumed to be performed starting from unsaturated conditions with an isotropic test geometry. Three void ratios were chosen (0.65, 0.75 and 0.85) and the initial  $f$  value was set to zero. The initial pressure was set to 0.1 MPa. An initial water content of 17 % was chosen, which implied that the initial clay potential as well as the suction value were approximately 54 MPa.

The pressure evolution was calculated by keeping  $e$  constant, by increasing  $w$ , and successively integrating  $p$  with Eq (5-9);  $e_m$  with Eq (5-15);  $s$  with (5-11), and finally  $f$  with Eq (4-29). The calculated stress path in the  $s - p$  plane is shown in Figure 6-3. The reduction of suction is also shown as a function of the degree of saturation (i.e.  $e_m/e$ ). This illustrates that the water retention curve is inherent from the material model. The dependence of the swelling pressure on the dry density is also illustrated. This shows the two bounding lines of the clay potential ( $\Psi_H$  and  $\Psi_L$ ) together with the final points of the calculated swelling pressure tests.

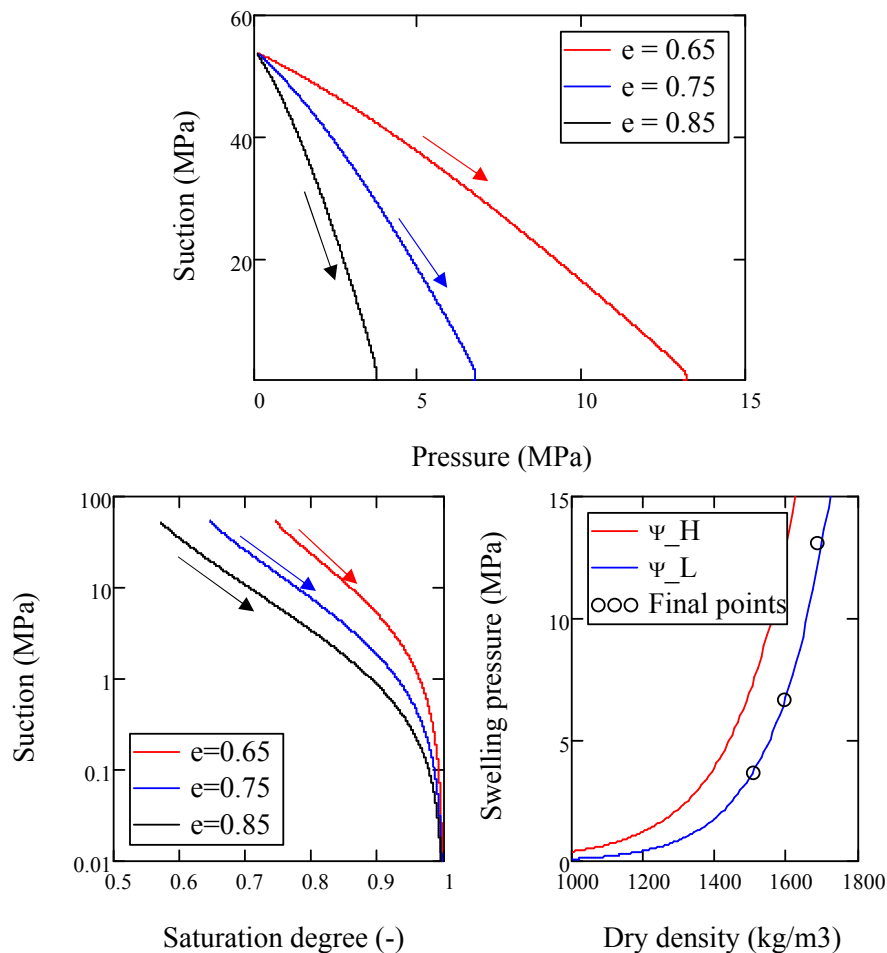


**Figure 6-3.** Calculated stress path in  $s-p$  plane for three different void ratios (upper). Evaluated water retention curves for the same test cases (lower left). Final pressure vs dry density compared with the two bounding lines of the clay potential (lower right).

## 6.4 Stress path dependence from a saturated to an unsaturated state

These single element tests addressed different stress path for dehydration of saturated bentonite. However, it can be argued that dehydration of water saturated bentonite does not recreate the “grainy” porous media similar to the original material. Instead, the dehydration affects the entire specimen, possibly with some occasional fracturing. This test case was therefore treated as if the specimen remained water-saturated throughout the changing state.

These tests were assumed to be performed at saturated conditions with a 1D test geometry (i.e. oedometer). An initial void ratio of 1.5 was chosen. The initial value of the path variable ( $f$ ) was set to zero which meant that the initial clay potential values was 0.48 MPa. The initial suction value was set to 0.2 MPa, which meant that the initial load was 0.28 MPa.

The calculation was performed by integration of Eq (4-20) and (4-23), by reducing the void ratio and by keeping either the stress or the suction value constant. Two types of stress paths were investigated: either by first keeping the stress constant and increasing suction up to 4 MPa after which the suction was kept constant while the stress was increased to 4 MPa; or by first keeping the suction constant and increasing the stress up to 4 MPa after which the stress was kept constant while the suction was increased to 4 MPa. The void ratio evolution for these two dehydration paths are shown in Figure 6-4. It can be noted that void ratio in the two cases ends up at the same value. This is a consequence of the monotonous void ratio decrease in the defined test case, and the fact that stress and suction are interchangeable for saturated conditions.

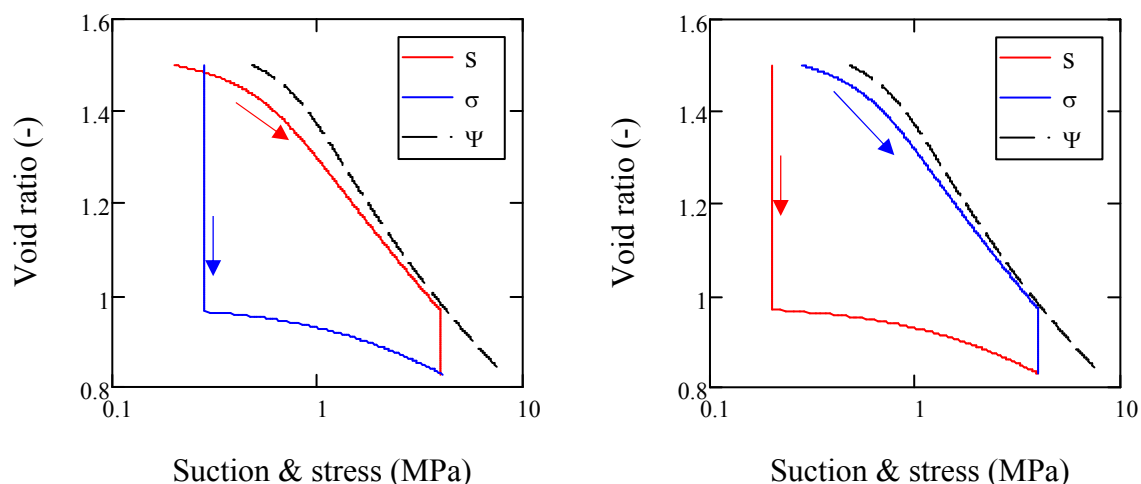


**Figure 6-4.** Calculated void ratio evolutions for two different dehydration paths.

## 6.5 Dependence of strains developed in a temperature cycle on stress

These tests were assumed to be performed at saturated conditions with a 1D test geometry. The tests were implemented in two steps: first as a consolidation/swelling cycle performed at zero suction (i.e. drained) conditions; secondly the specimen was heated at constant load and at constant water content. A consequence of the latter condition was the build-up of a negative suction value (i.e. a pore pressure) in the sample. The consolidation/swelling cycle was performed in a similar way as in the previous section. Starting from a void ratio of 1.8 the sample was consolidated to 10 MPa, and after that allowed to swell to either 7 or 0.1 MPa at which point the void ratio was 0.82 or 1.77, respectively (see Figure 6-5). After this the temperature was increased with constant load and constant water content, and these conditions implies a certain thermal expansion of the bentonite.

The constant water condition implies the following relation between increments in void ratio and water density:

$$de \rho_w + e d\rho_w = 0 \quad (6-1)$$

The constant load condition implies the following relation between increments of suction and of void ratio:

$$ds = \frac{d\Psi}{de} de \quad (6-2)$$

The function for the density of water is generalized to be defined as a function of suction and of temperature:

$$\rho_w(s, T) = \rho_{w0} \exp(-\beta s + \alpha_T T) \quad (6-3)$$

where  $\alpha_T$  is the thermal expansion of water. This expression can be differentiated which gives a relation between increments in water density, suction and temperature:

$$\frac{d\rho_w}{\rho_w} = -\beta ds + \alpha_T dT \quad (6-4)$$

All these relations are combined to yield the following expression for the apparent thermal expansion of the bentonite:

$$\frac{de}{dT} = -\frac{e\alpha_T}{1 - e\beta \frac{d\Psi}{de}} \quad (6-5)$$

This was utilised for calculating a void ratio evolution for increasing temperatures (Figure 6-5). The increase in void ratio was expressed as the strain  $de/(1 + e_0)$ , where  $e_0$  was the value at the end of the consolidation/swelling cycle. The pore pressure increase is also shown in Figure 6-5, and this amounted to approximately one tenth of the load.

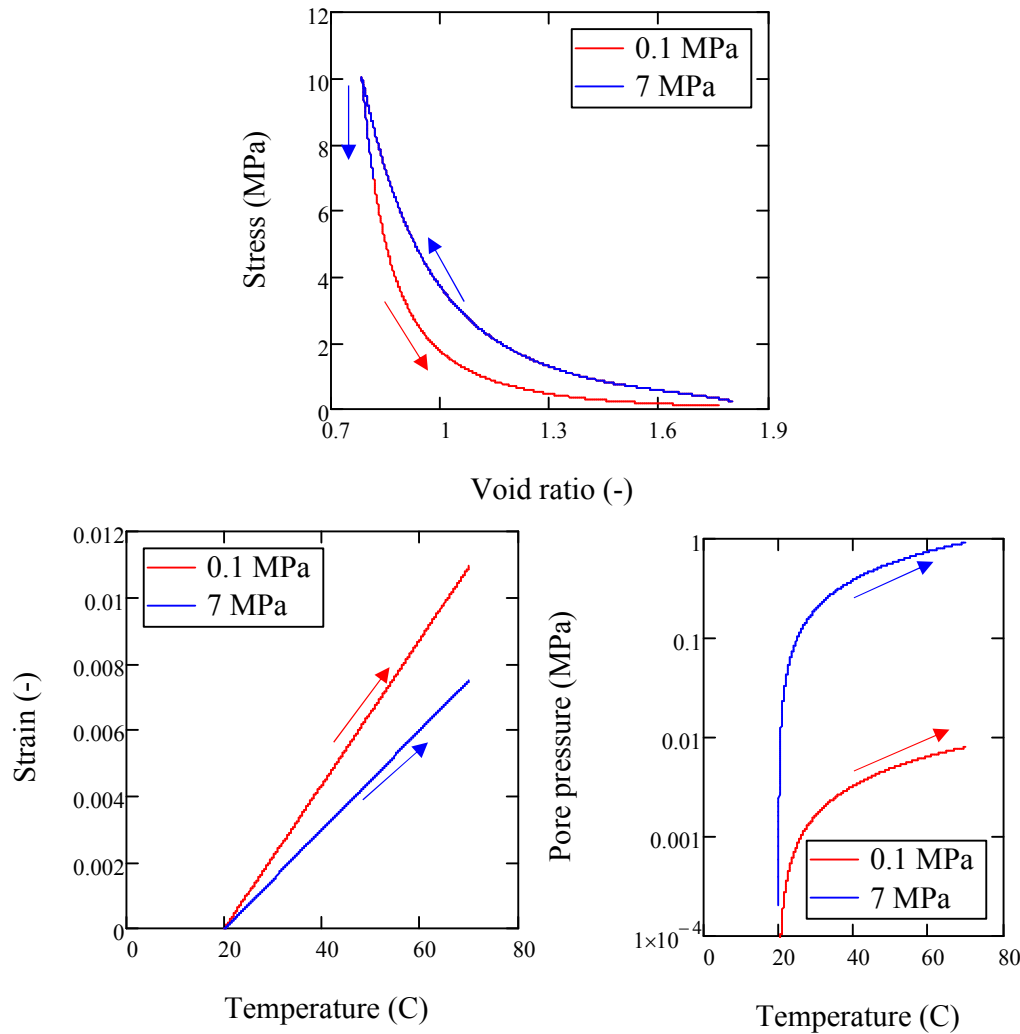


**Figure 6-5.** Stress paths for consolidation/swelling cycles (upper), thermal strain vs temperature (lower left) and pore pressure build-up vs. temperature (right).

## 6.6 Proposal for additional tests

Two additional test types can be proposed for further performance assessment within the work package.

One is unconfined compression tests and triaxial tests performed on water saturated bentonite specimen. These are quite simple and fundamental test conditions and the resulting von Mises stress at failure is a property of great importance for the KBS-3 concept.

Another very simple test condition is the oedometer test with water saturated conditions in which the void ratio, the vertical *and the lateral* stresses are analysed.

Name of the constitutive law:		Hysteresis Based Material model	
Behaviour feature	YES	NO	Remarks
<b>Mechanical behaviour</b>			
Dependence of swelling strain on applied stress (at the same dry density) (Figure1)	x		Only wetting direction has been defined
Dependence of swelling stress on dry density (at the same stress) (Figure 1)	x		Only wetting direction has been defined
Irreversibility of strains in wetting/drying cycles (Figure 2)	x		Assumed for saturated conditions
Dependence of swelling pressure on dry density (Figure 4)	x		Swelling pressure curve is equivalent to the clay potential as zero suction.
Stress path dependence from an unsaturated to a saturated state (Figure 5)	-	-	Has not been analysed
Stress path dependence from a saturated to an unsaturated state (Figure 6)		x	Saturated conditions assumed
Double structure/porosity considered?	x		For unsaturated conditions
Are temperature effects considered in the model?	x		First and foremost through the thermal expansion of water.
Dependence of strains developed in a temperature cycle (increase/decrease) on OCR (or stress) (Figure 7)	x		Thermal expansion influenced by the void ratio and load. Only temperature increase tested.
<b>Hydraulic behaviour (retention curve)</b>			
Hysteresis	x		Inherent from the HBM model
Dependence on void ratio	x		Inherent from the HBM model
Double structure/porosity considered?	x		Micro pores water-filled and macro pores gas-filled

## 7 Conclusions

The HBM model was originally developed for the homogenization task within the SKB Taskforce for Engineered Barrier Systems, and at the start of the Beacon project it had only been defined for water saturated conditions.

During the preparation of this document the definitions have expanded so that it now also includes isotropic water unsaturated conditions, albeit only for paths with increasing degree of water saturation. Moreover, an expression for the thermal expansion of water-saturated bentonite was also developed during this work. The performance of the model, as illustrated by the presented one-element tests, is quite promising, especially since all presented calculations could be made with a single set of parameter values.

If one deficiency of the model is to be highlighted it can arguably fall on the parametrization of the  $\Psi$ -function. It should be noted that the lower bounding curve ( $\Psi_L$ ) was adopted as a swelling-pressure curve and didn't take any water retention data for low water content (below 17 %) into account. This means that there is still a task ahead of a more complete parametrization of the clay potential. Moreover, for unsaturated conditions the model is still lacking definitions for non-isotropic states, as well as for dehydration paths. And for all conditions it would be desirable to formulate the model for general stress-strain states, and not only for principal directions. Finally, as a long term goal it would also be valuable to formulate all constitutive equations for large strains.

## References

- Alonso E, Gens A, Josa A, 1990.** Constitutive model for partially saturated soils, *Géotechnique* 40:405-430.
- Birgersson M, Karnland O, Nilsson U, 2010.** Freezing of bentonite. Experimental studies and theoretical considerations. SKB TR-10-40. Svensk Kärnbränslehantering AB.
- Börgesson L, Sandén T, Andersson L, Johannesson L-E, Goudarzi R, Åkesson M, 2014.** System design of Dome Plug. Preparatory modelling and tests of the sealing and draining components . SKB R-14-25. Svensk Kärnbränslehantering AB.
- Börgesson L, Åkesson M, Kristensson O, Dueck A, Hernelind J, 2016.** EBS-TF – THM modelling, BM 2 – Large scale field tests. SKB TR-13-07. Svensk Kärnbränslehantering AB.
- CIMNE, 2002.** Code\_Bright user's guide, Departamento de Ingeniería del Terreno, Universidad Politécnica de Cataluña.
- Dueck A, Börgesson L, Johannesson L-E, 2010.** Stress-strain relation of bentonite at undrained shear. Laboratory tests to investigate the influence of material composition and test technique. SKB TR-10-32, Svensk Kärnbränslehantering AB.
- Dueck A, Johannesson L-E, Kristensson O, Olsson S, 2011.** Report on hydro-mechanical and chemical-mineralogical analyses of the bentonite buffer in Canister Retrieval Test. SKB, TR-11-07. Svensk Kärnbränslehantering AB.
- Graham P, Malm R, Eriksson D, 2015.** System design and full-scale testing of the Dome Plug for KBS-3V deposition tunnels. Main report. SKB TR-14-23. Svensk Kärnbränslehantering AB
- Karnland O, Olsson S, Nilsson U, 2006.** Mineralogy and sealing properties of various bentonites and smectite-rich clay materials. SKB, TR-06-30. Svensk Kärnbränslehantering AB.
- Karnland O, Sandén T, Johannesson L-E, 2000.** Long term test of buffer material. SKB, TR-00-22. Svensk Kärnbränslehantering AB.
- Karnland O, Olsson S, Dueck A, Birgersson M, Nilsson U, Hernan-Håkansson T, Pedersen K, Nilsson S, Eriksen TE, Rosborg B, 2009.** Long term test of buffer material at the Äspö Hard Rock Laboratory, LOT project. Final report on the A2 test parcel. SKB, TR-09-29. Svensk Kärnbränslehantering AB.
- Åkesson M, Börgesson L, Kristensson O, 2010a.** SR-Site data report. THM modelling of buffer, backfill and other system components. SKB TR 10-44. Svensk Kärnbränslehantering AB.
- Åkesson M, Kristensson O, Börgesson L, Dueck A, Hernelind J, 2010b.** THM modelling of buffer, backfill and other system components. Critical processes and scenarios. SKB-10-11. Svensk Kärnbränslehantering AB.
- Åkesson M, Hökmark H, 2007.** Mechanical model for unsaturated MX-80. In: Schanz, T. (Ed.), *Theoretical and Numerical Unsaturated Soil Mechanics*, Springer Proceeding in Physics, vol. 113, pp. 3–10.

## Appendix 1

### Preliminaries

Index free notation is used to the major part, but sometimes index notation is used. A Cartesian coordinate frame, consisting of a reference point (the origin) and a positive orthonormal basis  $\{\mathbf{e}_1, \mathbf{e}_2, \mathbf{e}_3\}$ , is used. Using this a vector  $\mathbf{v}$  can be expressed,

$$\mathbf{v} = v_1 \mathbf{e}_1 + v_2 \mathbf{e}_2 + v_3 \mathbf{e}_3 = v_i \mathbf{e}_i$$

and a second order tensor  $\mathbf{T}$  can be expressed as,

$$\mathbf{T} = T_{11} \mathbf{e}_1 \otimes \mathbf{e}_1 + T_{12} \mathbf{e}_1 \otimes \mathbf{e}_2 + T_{13} \mathbf{e}_1 \otimes \mathbf{e}_3 + T_{21} \mathbf{e}_2 \otimes \mathbf{e}_1 + T_{22} \mathbf{e}_2 \otimes \mathbf{e}_2 + T_{23} \mathbf{e}_2 \otimes \mathbf{e}_3 + T_{31} \mathbf{e}_3 \otimes \mathbf{e}_1 + T_{32} \mathbf{e}_3 \otimes \mathbf{e}_2 + T_{33} \mathbf{e}_3 \otimes \mathbf{e}_3 = T_{ij} \mathbf{e}_i \otimes \mathbf{e}_j,$$

where  $\otimes$  denote the tensor product between vectors so that  $\mathbf{e}_i \otimes \mathbf{e}_j$  is a second order tensor. As can be seen in the right hand sides above, summation convention is used to compress the index notation. The second order unit tensor  $\mathbf{1}$  is defined by  $\mathbf{1}\mathbf{v} = \mathbf{v}$ , and the following is used when using index notation,

$$\mathbf{1} = \delta_{ij} \mathbf{e}_i \otimes \mathbf{e}_j, \delta_{ij} = \begin{cases} 1 & \text{if } i = j \\ 0 & \text{if } i \neq j \end{cases}.$$

Position vectors  $\mathbf{X}$  of material points in a body in the reference configuration together with a function  $\chi$  describing the motion of the points give position vectors  $\mathbf{x} = \chi(\mathbf{X}, t)$ , in the deformed configuration. For a fixed time the inverse mapping  $\mathbf{X} = \chi^{-1}(\mathbf{x}, t)$  exists. Displacements are defined by  $\mathbf{u} = \mathbf{x} - \mathbf{X}$ .

Taking the partial time derivative of the motion gives the velocity,

$$\dot{\chi}(\mathbf{X}, t) = \frac{\partial \chi(\mathbf{X}, t)}{\partial t},$$

which, by using the inverse map, also can be given by,

$$\mathbf{v}(\mathbf{x}, t) = \dot{\chi}(\chi^{-1}(\mathbf{x}, t), t).$$

In line with the above, fields may be defined over the body in both configurations, thus a field  $\varphi$  may be given as  $\varphi(\mathbf{X}, t)$  or  $\varphi(\mathbf{x}, t)$ , being the material description and spatial description, respectively.

The material time derivative  $\dot{\varphi}$  and spatial time derivative  $\varphi'$  of the  $\varphi$ -field are defined by:

$$\dot{\varphi}(\mathbf{X}, t) = \frac{\partial \varphi(\mathbf{X}, t)}{\partial t} \quad (\text{holding } \mathbf{X} \text{ fixed}),$$

and

$$\varphi'(\mathbf{x}, t) = \frac{\partial \varphi(\mathbf{x}, t)}{\partial t} \quad (\text{holding } \mathbf{x} \text{ fixed}),$$

respectively. When  $\varphi$  is a spatial field (given in terms of  $\mathbf{x}$ ) it's material time derivative is given by,

$$\dot{\varphi}(\mathbf{x}, t) = \varphi'(\mathbf{x}, t) + \frac{\partial \varphi(\mathbf{x}, t)}{\partial \mathbf{x}} \cdot \mathbf{v}(\mathbf{x}, t).$$

The deformation gradient,

$$\mathbf{F} = \frac{\partial \mathbf{x}}{\partial \mathbf{X}} = \frac{\partial (\mathbf{X} + \mathbf{u})}{\partial \mathbf{X}} = \mathbf{1} + \frac{\partial \mathbf{u}}{\partial \mathbf{X}},$$

is a kinematical entity linking an infinitesimal material fibre in the reference (undeformed) configuration,  $d\mathbf{X}$  to an infinitesimal material fibre in the deformed configuration,  $d\mathbf{x} = d\mathbf{X} + d\mathbf{u}$ . The determinant, 'det', of the deformation gradient, denoted  $J$ ,

$$J = \det \mathbf{F} = \frac{dv}{dv^0},$$

links a volume element  $dv^0$  in the reference configuration to a volume element,  $dv$ , in the deformed configuration.

In this paragraph a definition of the small strain tensor  $\boldsymbol{\varepsilon}$  and the underlying approximation made is given. The Lagrangean (large) strain tensor,

$$\mathbf{E} = \frac{1}{2} (\mathbf{F}^T \mathbf{F} - \mathbf{1}),$$

is used as a basis for describing the small strain approximation. Using the relation between the deformation gradient and the displacement gradient makes it possible to write,

$$\mathbf{E} = \frac{1}{2} \left( \left( \mathbf{1} + \frac{\partial \mathbf{u}}{\partial \mathbf{X}} \right)^T \left( \mathbf{1} + \frac{\partial \mathbf{u}}{\partial \mathbf{X}} \right) - \mathbf{1} \right) = \frac{1}{2} \left( \frac{\partial \mathbf{u}}{\partial \mathbf{X}} + \left( \frac{\partial \mathbf{u}}{\partial \mathbf{X}} \right)^T + \left( \frac{\partial \mathbf{u}}{\partial \mathbf{X}} \right)^T \frac{\partial \mathbf{u}}{\partial \mathbf{X}} \right).$$

If the displacement gradient is small, i.e.  $\partial \mathbf{u} / \partial \mathbf{X} = \mathbf{F} - \mathbf{1}$  is small, the last higher order term of the Lagrangean strain tensor becomes insignificant in relation to the first order terms. The Lagrangean strain may then be approximated by the small (infinitesimal) strain:

$$\mathbf{E} \approx \boldsymbol{\varepsilon} \equiv \frac{1}{2} \left( \frac{\partial \mathbf{u}}{\partial \mathbf{X}} + \left( \frac{\partial \mathbf{u}}{\partial \mathbf{X}} \right)^T \right).$$

As can be seen, conventional continuum mechanics sign conventions are adopted, when a material fibre undergoes elongation strain is positive. The same pass for stresses  $\boldsymbol{\sigma}$  being positive for tensile conditions.

The stress and strain tensors can be decomposed in a spherical part and a deviatoric part according to,

$$\boldsymbol{\sigma} = \frac{1}{3} \text{tr} \boldsymbol{\sigma} \mathbf{1} + \mathbf{s} = -p \mathbf{1} + \mathbf{s} \quad \text{and} \quad \boldsymbol{\varepsilon} = \frac{1}{3} \text{tr} \boldsymbol{\varepsilon} \mathbf{1} + \mathbf{e} = \frac{1}{3} \varepsilon_v \mathbf{1} + \mathbf{e},$$

where tr denotes the trace of the tensor, i.e.  $\text{tr} \boldsymbol{\sigma} = \boldsymbol{\sigma} \cdot \mathbf{1}$ .

Pressure,  $p$ , (positive in compression) and volumetric strain,  $\varepsilon_v$ , (positive for an increase in volume) are defined using the spherical part of the tensors according to,

$$p \equiv -\frac{1}{3} \text{tr} \boldsymbol{\sigma} \quad \text{and} \quad \varepsilon_v \equiv \text{tr} \boldsymbol{\varepsilon},$$

respectively.

## Appendix 2

Fundamental equations

The solid mass per mixture volume can be expressed,

$$\frac{dm_s}{dv} = \frac{dm_s}{dv_s} \frac{dv - dv_p}{dv} = \rho_s(1 - \phi).$$

Using this for the current and reference configuration together with an assumption of constant solid density give us,

$$(1 - \phi)dv = (1 - \phi^0)dv^0 \Rightarrow \phi = 1 - J_s^{-1}(1 - \phi^0),$$

Going back to the first expression and use the Reynold's transport relation<sup>1</sup> gives us the *solid mass balance equation*,

$$\dot{\rho}_s(1 - \phi) - \rho_s \dot{\phi} + \rho_s(1 - \phi) \operatorname{div} \mathbf{v}_s = 0,$$

and assuming a constant solid density gives,

$$\dot{\phi} = (1 - \phi) \operatorname{div} \mathbf{v}_s.$$

The liquid phase mass per mixture volume can be expressed as,

$$\frac{dm_l}{dv} = \rho_l \frac{dv - dv_s}{dv} = \rho_l \phi,$$

If again using Reynold's transport relation and introducing a source term,  $f_l$ , the *liquid mass balance equation* reads,

$$\dot{\rho}_l \phi + \rho_l \dot{\phi} + \rho_l \phi \operatorname{div} \mathbf{v}_l = f_l.$$

Combining this with the result from the solid mass balance gives,

$$[1 - J_s^{-1}(1 - \phi^0)][\dot{\rho}_l + \rho_l \operatorname{div}(\mathbf{v}_l - \mathbf{v}_s)] + \rho_l \operatorname{div} \mathbf{v}_s = f_l,$$

where  $\phi(\mathbf{v}_l - \mathbf{v}_s)$  is the flux commonly given by the Darcy flow model.

The quasi-static version of *balance of momentum* for the porous media reads,

$$\operatorname{div} \boldsymbol{\sigma} + \mathbf{b} = \mathbf{0},$$

where  $\boldsymbol{\sigma}$  denotes the Cauchy stress tensor and  $\mathbf{b}$  denotes a body force vector.

Thus, the balance equations to be solved are:

$$\begin{aligned} (1 - J_s^{-1}(1 - \phi^0))(\dot{\rho}_l + \rho_l \operatorname{div}(\mathbf{v}_l - \mathbf{v}_s)) + \rho_l \operatorname{div} \mathbf{v}_s &= f_l \\ \operatorname{div} \boldsymbol{\sigma} + \mathbf{b} &= \mathbf{0} \end{aligned}$$

In order to establish a full formulation and being able to solve the problem,  $\mathbf{u}_s$  and  $s$  are selected as the *independent variables*, for which the system of equations are solved, and  $\mathbf{v}_l - \mathbf{v}_s = \tilde{\mathbf{q}}(s)$ ,  $d\boldsymbol{\sigma} = d\tilde{\boldsymbol{\sigma}}(d\mathbf{u}_s, ds)$  and  $\rho_l = \tilde{\rho}_l(s)$  are the *dependent variables* given by the *constitutive equations* describing the material behaviour.

---

<sup>1</sup>  $\frac{\partial}{\partial t} \Big|_{\mathbf{x}} \left( \int_{\mathcal{P}} \varphi dv \right) = \int_{\mathcal{P}} (\dot{\varphi} + \varphi \operatorname{div} \mathbf{v}) dv$

## Appendix 3

Performance tests MathCad spreadsheets

<b>Clay potential</b>	$S1 := \left( -3.94 \times 10^{-7} \quad 4.117 \times 10^{-3} \quad -4.741 \right)^T$	$S2 := \left( 1.669 \times 10^{-7} \quad 2.101 \times 10^{-3} \quad -2.675 \right)^T$	$F1(x) := \left( x^2 \quad x \quad 1 \right)^T$
Lower and higher bounding lines	$\Psi_L(e1) := 10 \cdot \frac{F1 \left( \frac{p_s}{1+e1} \right) \cdot S1}{1+e1}$	$\Psi_H(e1) := 10 \cdot \frac{F1 \left( \frac{p_s}{1+e1} \right) \cdot S2}{1+e1}$	$\rho_s \equiv 2780$
Mid-line and half allowed span and their derivatives	$\Psi_M(e1) := 2^{-1} \cdot (\Psi_H(e1) + \Psi_L(e1))$	$\Psi_{\Delta 2}(e1) := 2^{-1} \cdot (\Psi_H(e1) - \Psi_L(e1))$	
Clay potential function	$d\Psi_M(e1) := \frac{d}{de1} \Psi_M(e1)$	$d\Psi_{\Delta 2}(e1) := \frac{d}{de1} \Psi_{\Delta 2}(e1)$	
Clay potential function	$\Psi_f(ex, fx) := \Psi_M(ex) + fx \cdot \Psi_{\Delta 2}(ex)$		
Path function derivative 1D case	$dfdxID(f, \Delta \varepsilon) := -(1 + f \cdot \text{sign}(\Delta \varepsilon)) \cdot K$		$K_{AV} := 40$
Clay potential derivatives 1D case	$d\Psi de1D(e1, e0, f1, \Delta e) := d\Psi_M(e1) + f1 \cdot d\Psi_{\Delta 2}(e1) + \Psi_{\Delta 2}(e1) \cdot \frac{dfdxID(f1, \Delta e)}{1 + e0}$		
Unsaturated isotropic cases	$dfdxem(f, em0, \Delta \varepsilon) := -(1 + f \cdot \text{sign}(\Delta \varepsilon)) \cdot K \cdot \frac{\Delta \varepsilon}{3 \cdot (1 + em0)}$		
Water density	$d\Psi de(em, em0, f1, \delta) := d\Psi_M(em) + f1 \cdot d\Psi_{\Delta 2}(em) + \left[ (1 + f1 \cdot \delta) \cdot \frac{K}{3 \cdot (1 + em0)} \right]$		
Water density	$\rho_{wT}(s) := \rho_0 \cdot \exp(-\beta \cdot s)$	$\rho_{wT}(s, T) := \rho_0 \cdot \exp(-\beta \cdot s + \alpha_T \cdot T)$	$\rho_0 := 998$
suction as a function of density	$s_f(\rho 1) := \frac{-1}{\beta} \cdot \ln \left( \frac{\rho 1}{\rho_0} \right)$		$\beta \equiv 4.5 \cdot 10^{-4}$
Contact area fraction and derivatives	$\alpha(e_{m, e1}) := \left( \frac{1 + e_m}{1 + e1} \right)^\gamma$	$d\alpha m(e_{m, e1}) := \frac{d}{de_{m, e1}} \alpha(e_{m, e1})$	$\alpha_T \equiv -3.4 \cdot 10^{-4}$
Interaction functions	$dpde(em, e1, f1, p1, s1) := \frac{\ln \left( \frac{\Psi_f(em, f1)}{p1} \right)}{\ln \left( \frac{1 + em}{1 + e1} \right)}$	$dpdw(em, e1, f1, p1, s1) := \frac{\Psi_f(em, f1) \cdot \alpha(em, e1)}{1 + e1}$	$\gamma \equiv 7$
		$e_f \leftarrow \text{root}(\Psi_f(e1, f1) - p1, e1, 0.1, 5)$	
		$\frac{\rho_s(e_f - e1) \cdot dpde(em, e1, f1, p1, s1)}{e_f \cdot \rho_{wT}(0) - em \cdot \rho_{wT}(s1)}$	

2018-02-27

WP3\_1\_delivery Febr 2018.xmcd

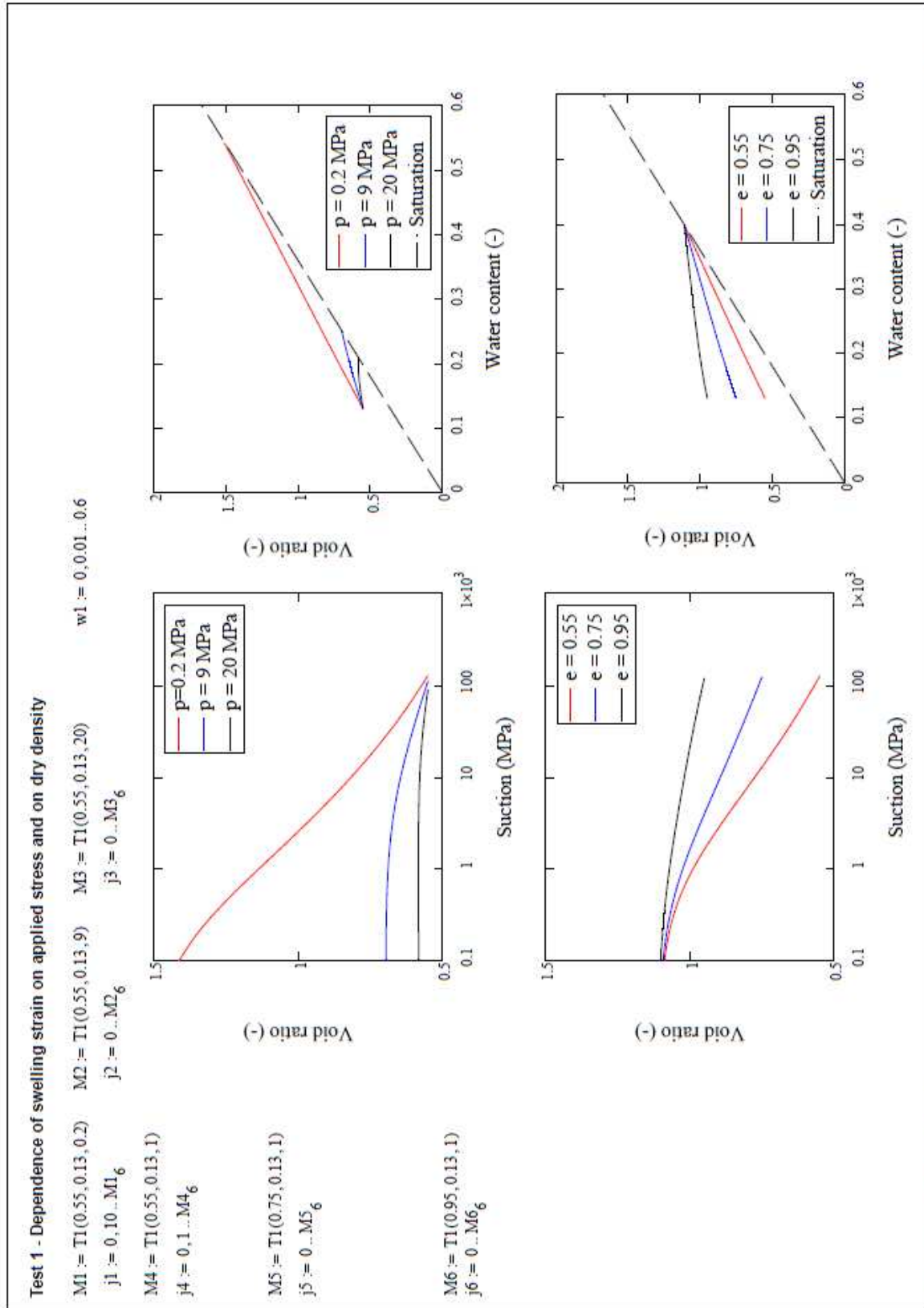
```

    dem(em, em0, e1, f1, p1, w1, dp, dw, de, Δem) :=
        dp·α(em, e1)-1 -  $\frac{dw}{\beta \cdot w1} - p1 \cdot \alpha(em, e1)^{-2} \cdot d\alpha1(em, e1) \cdot de$ 
        p1·α(em, e1)-2 · dom(em, e1) + dψ/de(em, em0, f1, sign(Δem)) -  $\frac{1}{\beta \cdot em}$ 

Test 1 - Dependence of swelling strain on applied stress and on dry density
T1(einit, winit, load) :=
    emin ← roof(ρs·winit - e1·ρw(ψM(e1) -  $\frac{load}{\alpha(e1, e_{init})}$ ), e1, 0, einit)
    (e01, em0, P0, s0, f0) ← (einit, emin, load, ψM(emin),  $\frac{load}{\alpha(e_{min}, e_{init})}$ , 0)
    w0 ← winit
    j ← 0
    while sj > 0.0001
        (dp, dw) ← (0, 0.00001)
        de ←  $-\left( \frac{dp \cdot dw}{dp \cdot de} \left( e_{m,j}, e_{1,j}, f_{j,j}, p_{j,j}, s_{j,j} \right) \right) \cdot dw$ 
        dem ← dem(em, emin, e1,j, fj,j, pj,j, wj, dp, dw, de, 1)
        ds ←  $\frac{de_m}{\beta \cdot e_{m_j}} - \frac{dw}{\beta \cdot w_j}$ 
        df ← dfdem(fj, emin, dem)
        (e1,j+1, em,j+1, pj+1) ← (e1,j + dem, em,j + dem, pj + dp)
        (wj+1, fj+1, sj+1) ← (wj + dw, fj + df, sj + ds)
        j ← j + 1
    (e1, em, p, s, f, w, j)T

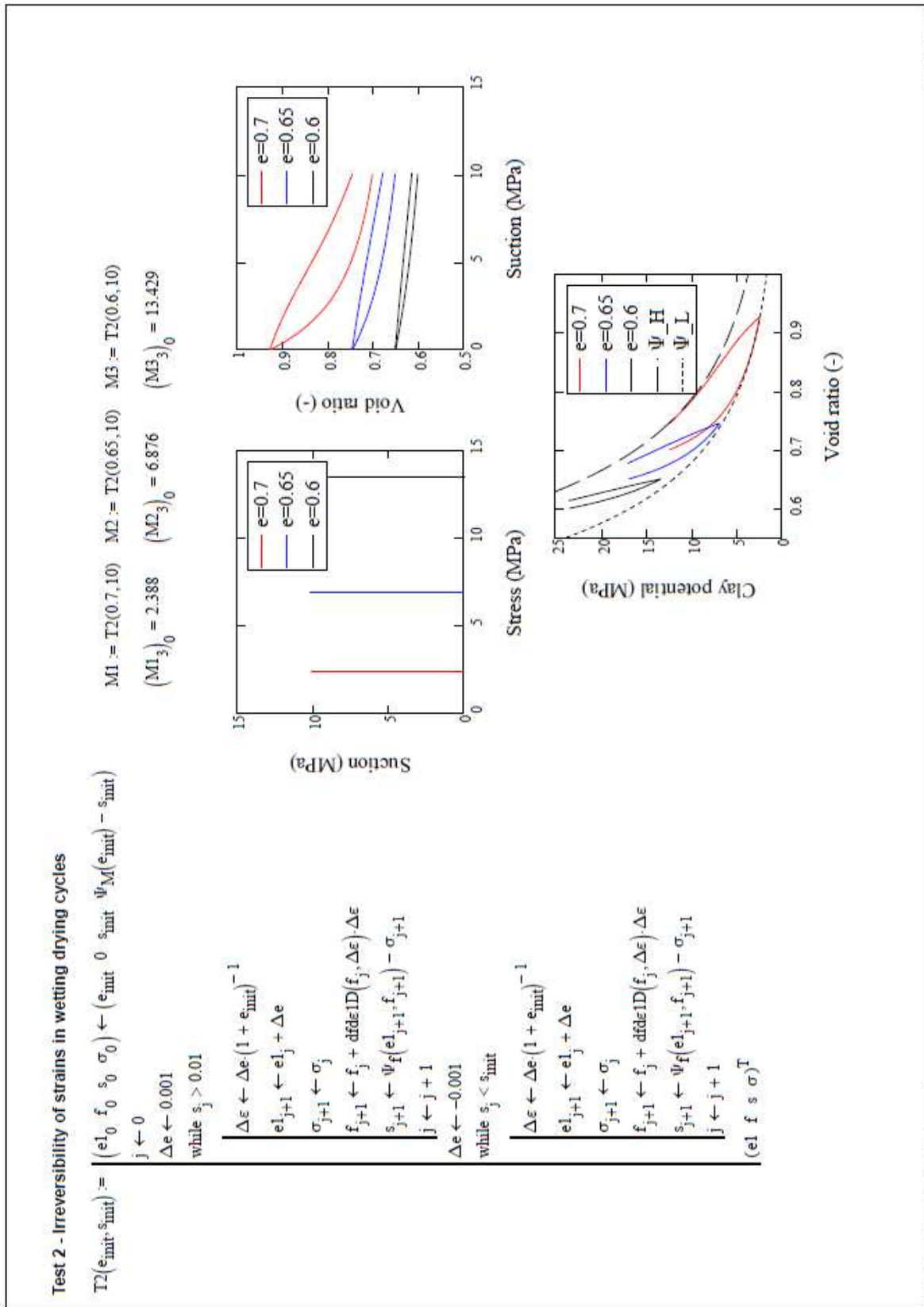
```

WP3\_1 delivery Febr 2018.xmcd 2018-02-27

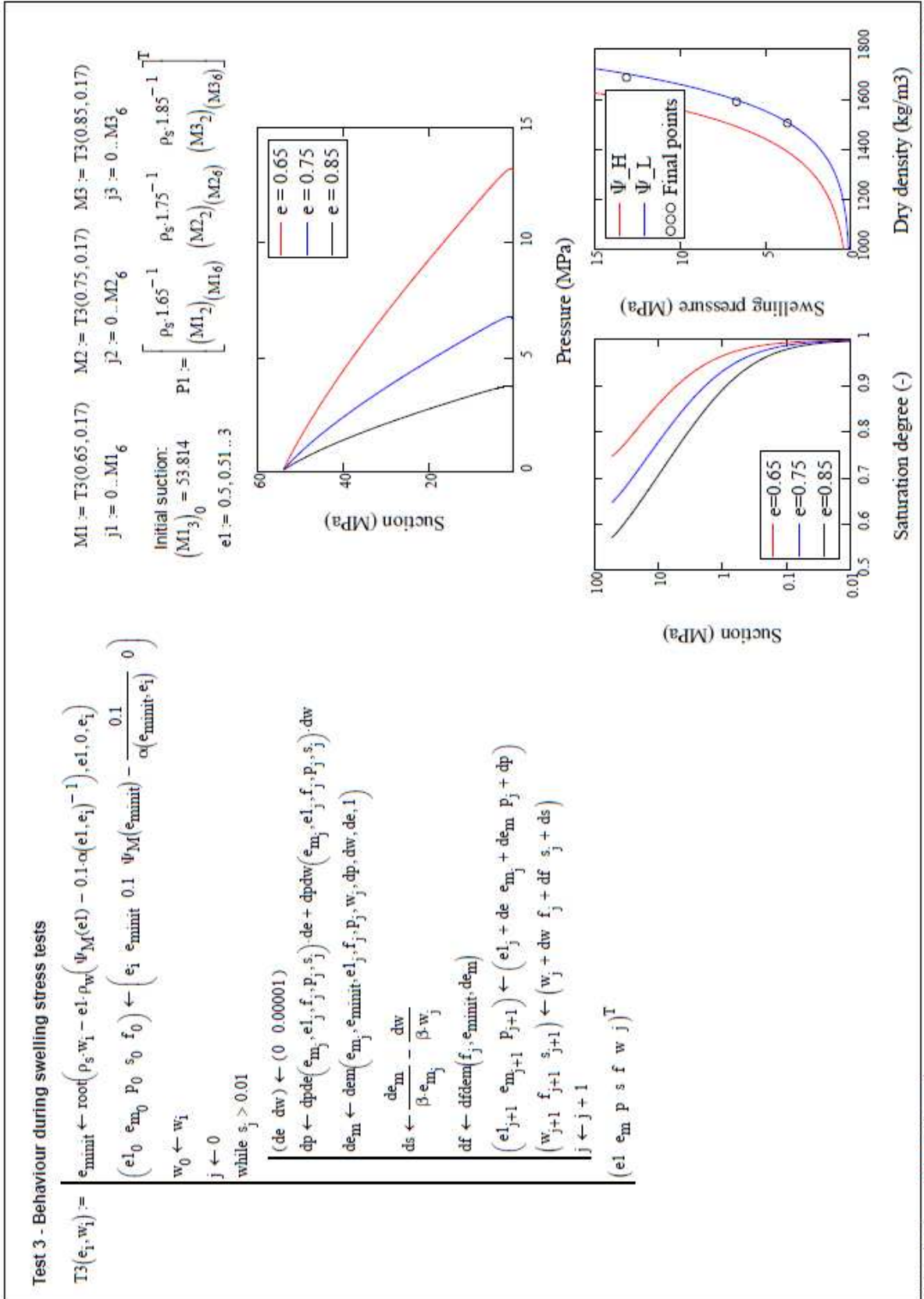


2018-02-27

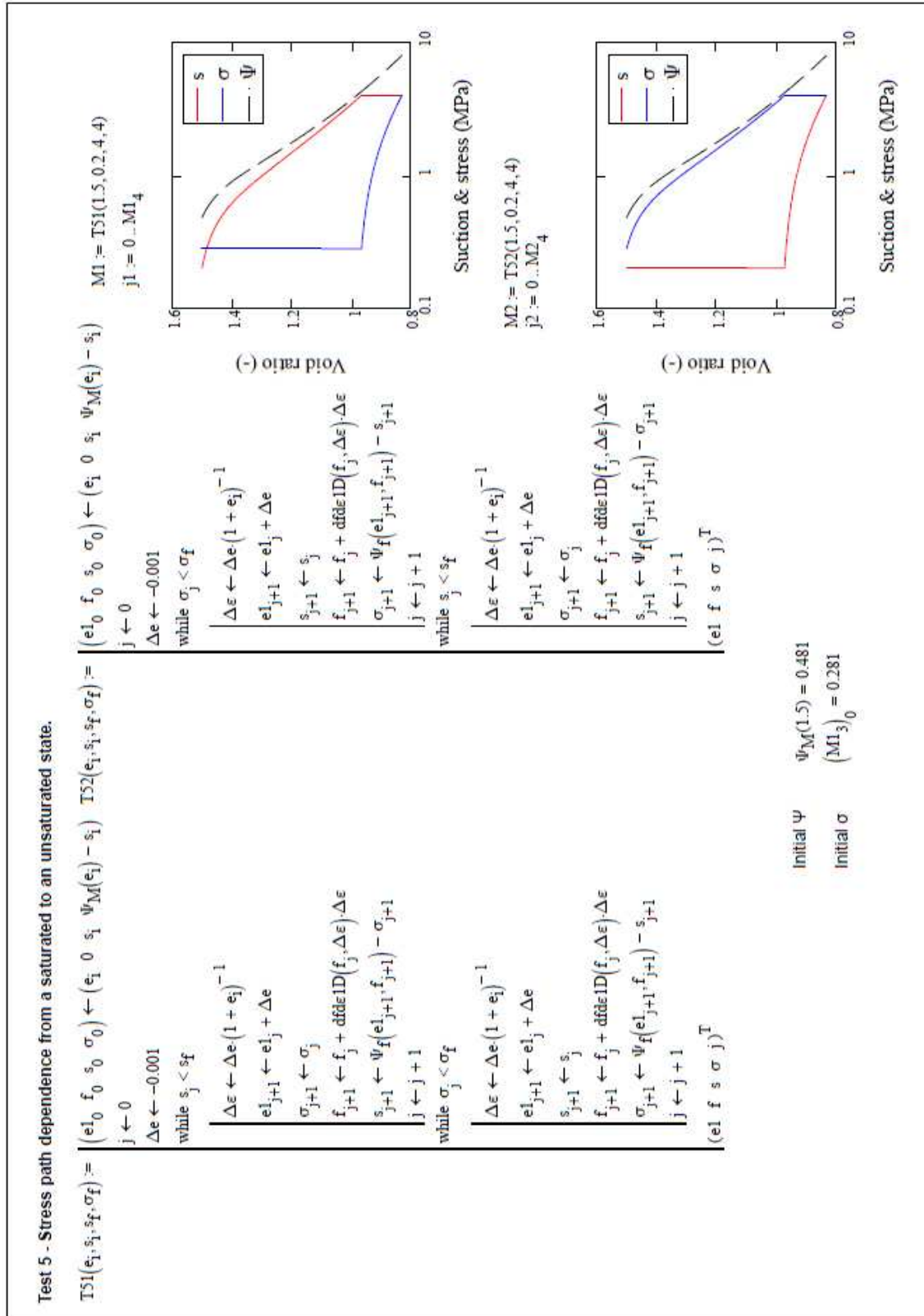
WP3\_1 delivery Febr 2018.xmcd



WP3\_1 delivery Febr 2018.xmcd

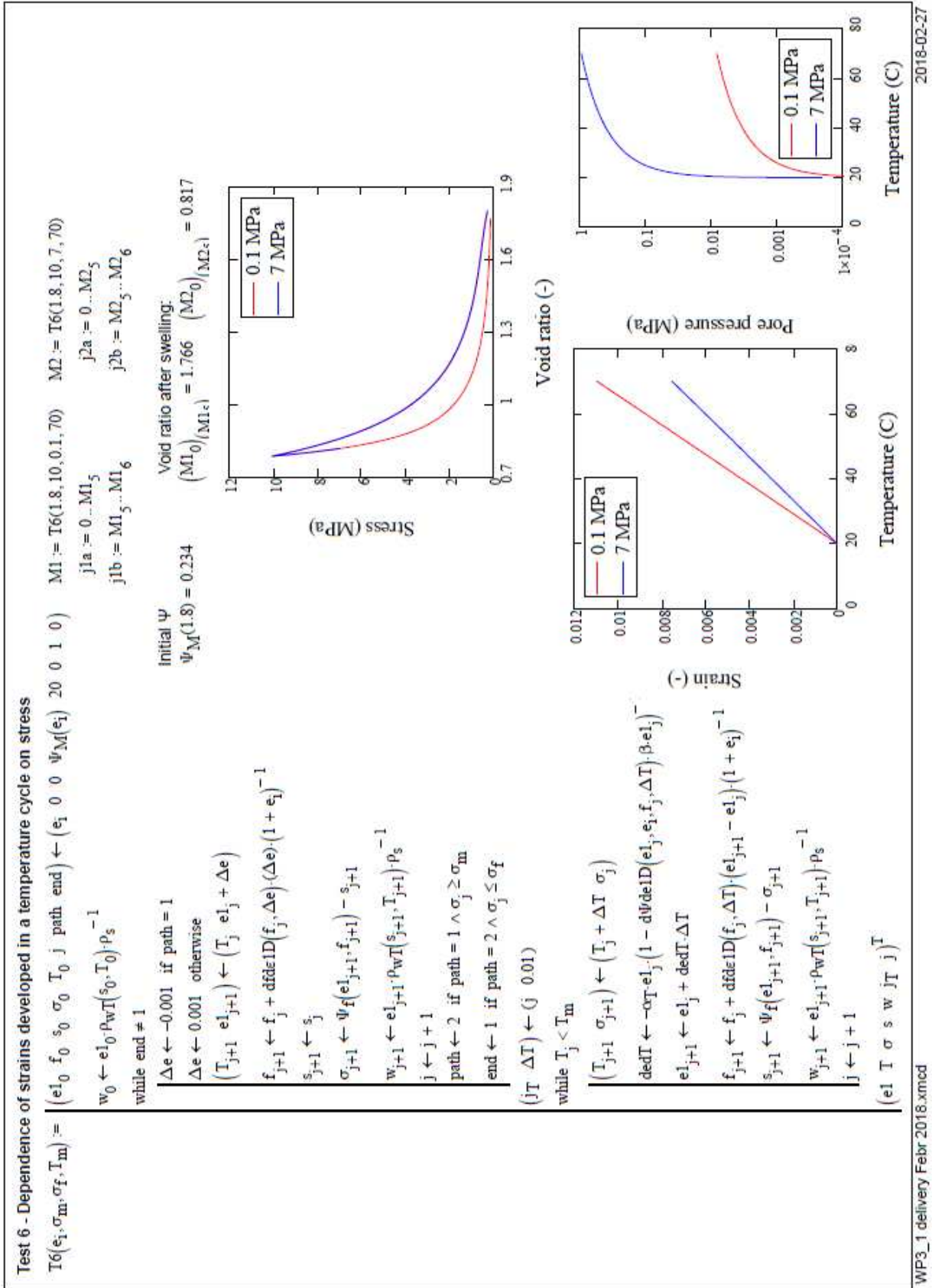


WP3\_1\_delivery Febr 2018.xmcd

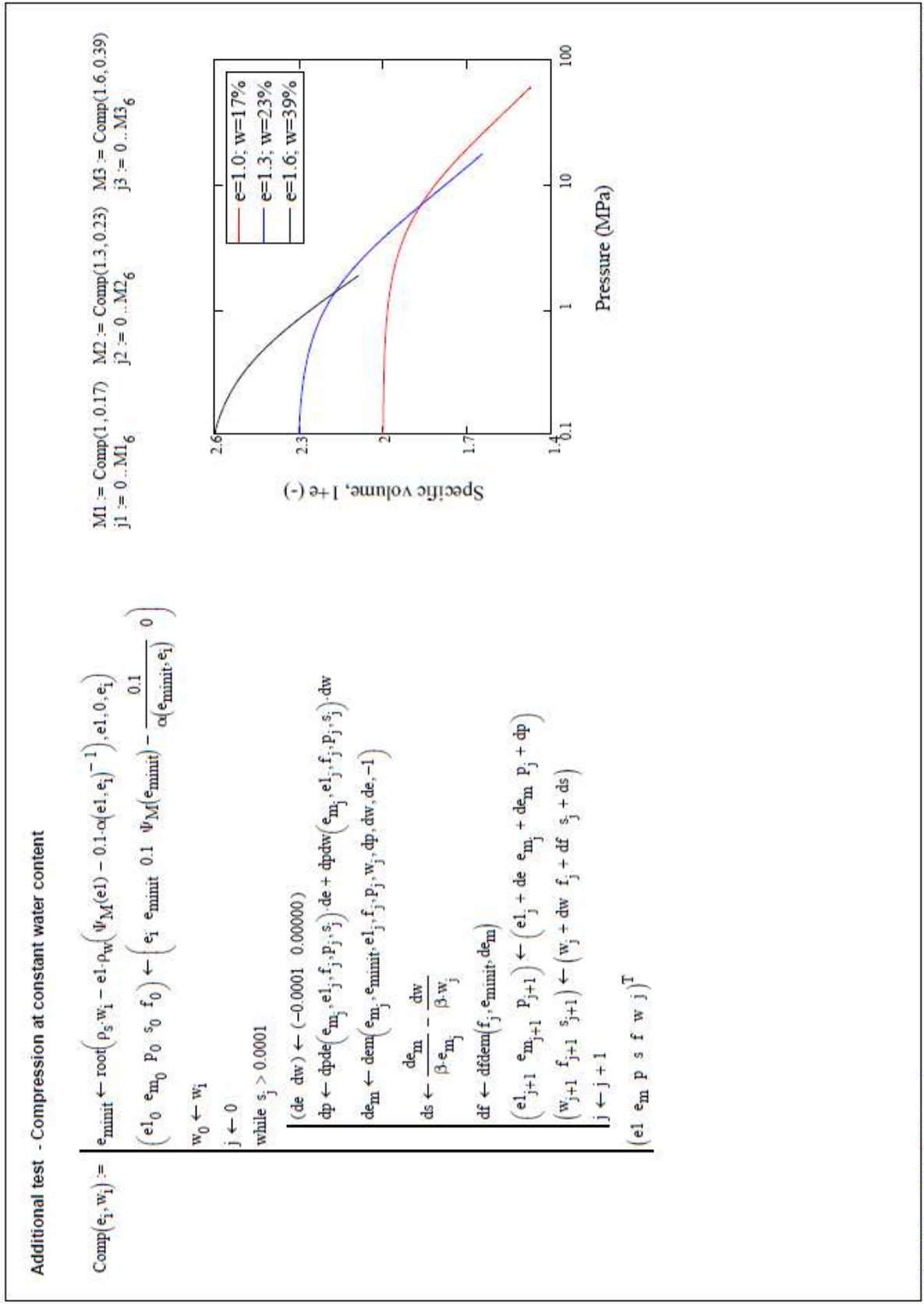


2018-02-27

WP3\_1 delivery Febr 2018.xmcd



WP3\_1 delivery Febr 2018.xmcd



WFP3\_1 delivery Febr 2018.xmcd 2018-02-27

# D3.1



## ACMEG-TS: Base formulation and application to bentonite

### DELIVERABLE (D3.1)

### ANNEX D

Author(s): **Jose A. Bosch, Alessio Ferrari and Lyesse Laloui (EPFL)**

Reporting period: 01/06/17 – 30/11/18

Date of issue of this report: **01/03/18**

Start date of project: **01/06/17**

Duration: 48 Months

This project receives funding from the Euratom research and training programme 2014-2018 under grant agreement No 745 942		
<b>Dissemination Level</b>		
<b>PU</b>	Public	
<b>RE</b>	Restricted to a group specified by the partners of the Beacon project	
<b>CO</b>	Confidential, only for partners of the Beacon project	

**REVIEW**

<b>Name</b>	<b>Internal/Project/External</b>	<b>Comments</b>

**DISTRIBUTION LIST**

<b>Name</b>	<b>Number of copies</b>	<b>Comments</b>
Athanasios Petridis (EC) Christophe Davies (EC)  Beacon partners		

## **Abstract**

In this report the formulation of ACMEG-TS, a constitutive model for unsaturated soils under non iso-thermal conditions, is presented. The suitability of the model to simulate the behaviour of bentonite is assessed under several stress paths involving changes in total stress, suction, saturated-unsaturated transitions and temperature cycles. The qualitative response obtained is satisfactory, including irreversibility and stress path dependency. In quantitative terms, the response can be improved. In particular, excessive collapse during suction decrease is obtained. The magnitude of swelling strain is underpredicted whereas values of swelling pressure are overpredicted.

# Contents

<b>Contents .....</b>	<b>4</b>
<b>1 Introduction .....</b>	<b>5</b>
<b>2 Background.....</b>	<b>5</b>
<b>3 Basic hypotheses and scope .....</b>	<b>5</b>
<b>4 Mathematical description. ....</b>	<b>6</b>
4.1 Mechanical model.....	6
4.2 Water retention model .....	9
<b>5 Model parameters.....</b>	<b>10</b>
<b>6 Model performance .....</b>	<b>12</b>
6.1 Dependence of swelling strain on applied stress and dry density .....	12
6.2 Irreversibility of strains in wetting/drying cycles .....	14
6.3 Behaviour during swelling pressure test.....	14
6.4 Stress path dependence from an unsaturated to a saturated state .....	16
6.5 Stress path dependence from a saturated to an unsaturated state .....	17
6.6 Dependence of strains developed in a temperature cycle on stress .....	18
6.7 Model features .....	20
<b>7 Conclusions .....</b>	<b>21</b>
<b>8 Acknowledgments .....</b>	<b>21</b>
<b>References .....</b>	<b>22</b>

## 1 Introduction

The ACMEG models (Advanced Constitutive Models for Environmental Geomechanics) have been developed during the last decades at EPFL in order to deal numerically with the behaviour of geomaterials under several environmental conditions. These are relevant for multiple geo-engineering applications, including the performance of radioactive waste repositories. In the context of the BEACON project, EPFL is further developing this family of models in order to better tailor ACMEG to the behaviour of bentonite materials under repository conditions.

In this report the formulation of the constitutive model ACMEG (version TS) is outlined, followed by several examples of its performance under various stress-suction-temperature paths aimed to simulate the behaviour of bentonite samples at the stress point level (laboratory scale). In light of the results obtained from the simulations, encouraging features and further improvements are discussed in the conclusions.

## 2 Background

ACMEG was developed initially to simulate the behaviour of low activity clays and silts under environmental actions such as changes in saturation/humidity, temperature, pore fluid salinity or biologically induced calcite precipitation.

A summary of the models and the different variables that each one consider is provided in table 1

*Table 1. Current ACMEG models*

Version	Modelled processes	Reference
ACMEG-S	Unsaturated states	Nuth (2009)
ACMEG-DC	Dessication cracks	Péron (2008)
ACMEG-2S	Aggregated soils in unsaturated conditions	Koliji (2008)
ACMEG-TS	Non-isothermal unsaturated conditions	François & Laloui (2008)
ACMEG-B	Biologically induced calcite precipitation	Fauriel & Laloui (2012)
ACMEG-C	Osmotic effects	Witteveen et al. (2013)

In this report the focus is on the non-isothermal model for unsaturated states, ACMEG-TS described in (François, 2008 and François & Laloui, 2008), which has been used for modelling bentonite materials. Among others, the real scale experiment FEBEX has been analysed using that model.

## 3 Basic hypotheses and scope

ACMEG-TS provides a stress-strain formulation suitable for the implementation in boundary value codes, such as finite element, dealing with non-isothermal conditions and transitions from saturated to unsaturated states.

It has been used to analyse the behaviour of geomaterials in the context of nuclear waste disposals (e.g. Dupray et al. (2013)) and energy geostructures (e.g. Di Donna (2015)).

The response of the material is dependent on the Bishop's effective stress using a volume average pore pressure, leading to a direct dependence of the mechanical response on the hydraulic state. In addition, the increase in apparent preconsolidation pressure with capillary suction and temperature is taken into account, defining a loading collapse curve.

The mechanical model is complemented with a water retention model that accounts for hysteresis and the mechanical and temperature effects on the hydraulic behaviour. This provides a two way coupling between mechanics and hydraulics.

## 4 Mathematical description.

### 4.1 Mechanical model

The model is formulated using an elasto-plastic framework based on the Hujieux's critical state model (Hujieux, 1979). In order to accommodate behaviour in unsaturated state, Bishop's effective stress and suction are used as constitutive variables. Bishop's coefficient is taken equal to the degree of saturation (Schrefler, 1984; Nuth and Laloui, 2008), leading to

$$\boldsymbol{\sigma}' = \boldsymbol{\sigma} - [S_r u_w + (1 - S_r) u_a] \mathbf{I} = \boldsymbol{\sigma}^n - S_r s \mathbf{I} \quad (1)$$

where  $\boldsymbol{\sigma}'$  is the effective stress tensor,  $\boldsymbol{\sigma}$  is the total stress tensor,  $S_r$  is the degree of saturation,  $u_w$  is water pressure;  $u_a$  is air pressure;  $s = u_a - u_w$  is suction and  $\boldsymbol{\sigma}^n = \boldsymbol{\sigma} - u_a \mathbf{I}$  is the net stress tensor.

Changes in effective stress are related to deformation of the material as

$$d\boldsymbol{\varepsilon} = \mathbf{C} : d\boldsymbol{\sigma}' \quad (2)$$

where  $\boldsymbol{\varepsilon}$  is the strain tensor and  $\mathbf{C}$  is the secant compliance tensor. To allow for irreversible deformation the strain tensor is divided as (isothermal conditions)

$$d\boldsymbol{\varepsilon} = d\boldsymbol{\varepsilon}^e + d\boldsymbol{\varepsilon}^p \quad (3)$$

being  $d\boldsymbol{\varepsilon}^e$  the elastic strain increment and  $d\boldsymbol{\varepsilon}^p$  the plastic strain increment. Elastic strains will be induced as long as the stress increment lies inside the yield surface. In such cases the response will be governed by the elastic compliance  $\mathbf{C}^e$

$$\mathbf{C}^e = C_{ijkl}^e = 2G\delta_{ik}\delta_{jl} + \left(K - \frac{2}{3}G\right)\delta_{ij}\delta_{kl} \quad (4)$$

where  $G$  is the shear modulus and  $K$  the bulk modulus. These moduli depend on the confining stress  $p'$  as

$$G = G_{ref} \left(\frac{p'}{p'_{ref}}\right)^{n^e} \quad K = K_{ref} \left(\frac{p'}{p'_{ref}}\right)^{n^e} \quad (5)$$

where  $G_{ref}$  and  $K_{ref}$  are the shear and bulk modulus respectively at a reference pressure  $p'_{ref}$  and  $n^e$  is a parameter controlling the nonlinear behaviour.

In non-isothermal conditions, additional elastic strains are induced by temperature changes according to

$$d\boldsymbol{\varepsilon}^e = \mathbf{C}^e : d\boldsymbol{\sigma}' - \left(\frac{1}{3}\beta_s \mathbf{I}\right) dT = \mathbf{C}^e : d\boldsymbol{\sigma}' - \boldsymbol{\beta}_T dT \quad (6)$$

where  $\boldsymbol{\beta}_T$  is the thermal expansion coefficient tensor and  $\beta_s$  is given by

$$\beta'_s = \beta'_{s0} \left(1 - \frac{T - T_0}{100}\right) \frac{p'_{cr0}}{p'} \quad (7)$$

where  $\beta'_{s0}$  is the thermal expansion coefficient at a reference temperature  $T_0$  and  $p'_{cr0}$  is the initial critical state pressure at the reference temperature.

If the effective stress state reaches the yield surface, plastic strains will develop. These might be induced by two mechanisms, namely isotropic  $d\boldsymbol{\varepsilon}_{iso}^p$  and deviatoric  $d\boldsymbol{\varepsilon}_{dev}^p$  plastic strains. Thus

$$d\boldsymbol{\varepsilon}^p = d\boldsymbol{\varepsilon}_{iso}^p + d\boldsymbol{\varepsilon}_{dev}^p \quad (8)$$

each mechanism corresponds to a different yield surface  $f$  whose expressions are respectively

$$f_{iso} = p' - p'_c r_{iso} = 0 \quad (9)$$

$$f_{dev} = q - Mp'[1 - b \ln\left(\frac{p'd}{p'_c}\right)]r_{dev} \quad (10)$$

Where  $p'_c$  is the preconsolidation pressure,  $q$  is the deviatoric stress,  $M$  is the slope of the critical state line in the  $(p' - q)$  plane;  $b$  is a material parameter defining the shape of the deviatoric yield surface;  $d = \frac{p'_c}{p'_{cr}}$  with  $p'_{cr0}$  the critical state pressure;  $r_{iso}$  and  $r_{dev}$  correspond to the degrees of plastification for each mechanism, allowing for plastic strains within the yield limits. It can be

readily observed that both mechanisms are coupled by means of the preconsolidation pressure  $p'_c$ .

Preconsolidation pressure depends on the volumetric plastic strain, temperature and suction as follows

$$p'_c = \begin{cases} p'_{c0} \exp(\beta \varepsilon_v^p) \left[ 1 - \gamma_T \log\left(\frac{T}{T_0}\right) \right] & \text{if } s < s_e \\ p'_{c0} \exp(\beta \varepsilon_v^p) \left[ 1 - \gamma_T \log\left(\frac{T}{T_0}\right) \right] \left[ 1 + \gamma_s \log(s/s_e) \right] & \text{if } s > s_e \end{cases} \quad (11)$$

where  $\beta$  is the plastic compressibility modulus (slope of the  $\varepsilon_v^p - \ln p'_c$  relation);  $s_e$  is the air entry suction value; and  $\gamma_T$  and  $\gamma_s$  account for the increase/decrease of elastic domain with suction and temperature. Figure 1 shows graphically how temperature and suction influence the size of the yield surface, decreasing when temperature increases and increasing when suction increases above the air entry suction.

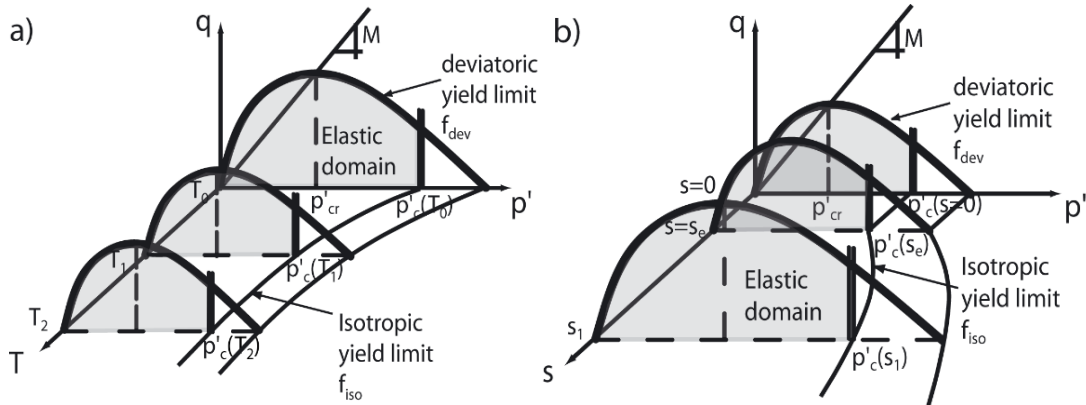


Figure 1. Graphical visualization of the yield surface evolution with temperature (right) and suction (left)

The flow rule of the isotropic mechanism is associated whereas that for the deviatoric mechanism can be non-associated. Thus the plastic potentials have the following form:

$$g_{iso} = p' - p'_c r_{iso} = 0 \quad (12)$$

$$g_{dev} = q - \frac{\alpha}{\alpha - 1} M p' \left[ 1 - \frac{1}{\alpha} \left( \frac{p' d}{p'_c} \right)^{\alpha - 1} \right] = 0 \quad (13)$$

where  $\alpha$  is a non-associativity parameter. The magnitude of plastic strains depends on the derivatives of these potentials as follows

$$d\varepsilon_{iso}^p = d\lambda_{iso}^p \frac{\partial g_{iso}}{\partial \sigma'} \quad (14.a)$$

$$d\varepsilon_{dev}^p = d\lambda_{dev}^p \frac{\partial g_{dev}}{\partial \sigma'} \quad (14.b)$$

where  $\lambda_{iso}^p$  and  $\lambda_{dev}^p$  are the plastic multipliers which are determined following Prager's consistency condition extended to multi-dissipative materials (Rizzi et al 1990):

$$\begin{aligned} d\mathbf{F} &= \frac{\partial \mathbf{F}}{\partial \boldsymbol{\sigma}'} : d\boldsymbol{\sigma}' + \frac{\partial \mathbf{F}}{\partial \boldsymbol{\pi}} \cdot \frac{\partial \mathbf{F}}{\partial \boldsymbol{\pi}} \cdot d\boldsymbol{\lambda}^p \leq 0, \\ d\boldsymbol{\lambda}^p &\geq 0, \quad d\mathbf{F} \cdot d\boldsymbol{\lambda}^p = 0 \end{aligned} \quad (15)$$

where  $\mathbf{F} = (f_{iso} \ f_{dev})$  is the yield surface vector,  $\boldsymbol{\pi} = (p'_c \ r_{iso} \ r_{dev})$  is the internal variable vector and  $\boldsymbol{\lambda}^p = (\lambda_{iso}^p \ \lambda_{dev}^p)$  is the plastic multiplier vector.

## 4.2 Water retention model

In order to account for unsaturated conditions a relationship between degree of saturation and suction is introduced (François, 2008). An elastoplastic approach is used to model water retention. This includes hysteretic behaviour controlled by two yield surfaces corresponding to drying and wetting paths. The conceptual model is represented in Figure 2. Desaturation (or saturation) is induced when suction reaches either the wetting limit or the drying limit, satisfying respectively

$$f_{dry} = s - s_d, \quad f_{wet} = s_d s_{hys} - s \quad (16)$$

Where  $f_{dry}$  and  $f_{wet}$  stand for the yield activated during a wetting or drying process respectively,  $s_d$  is the drying yield limit which during a desaturation/saturation process (i.e.  $f_{dry} = 0$  or  $f_{wet} = 0$ ) remains equal to the actual value of  $s$ ; and  $s_{hys}$  a material parameter controlling the size of the water retention hysteresis.

If the initial state is saturated,  $s_{d0}$  is equal to the air entry suction  $s_{e0}$  and increases when suction exceeds this value according to the following hardening law

$$s_d = s_e \exp(-\beta_h \Delta S_r) \quad (17)$$

where  $\beta_h$  is the slope of the retention curve in the  $(S_r - \ln s)$  plane (see figure 2). The same process is activated for a wetting path in the opposite way (expression (16)). Thus, expression (17) describes the hardening process that leads to changes in  $S_r$ . A limiting condition is imposed so that when  $S_r$  reaches the residual degree of saturation  $s_d$  is kept constant.

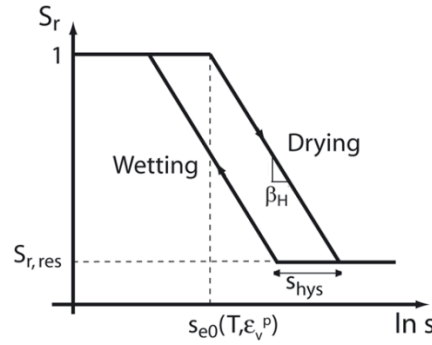


Figure 2. conceptual model of the adopted water retention model. Parameters defined in the text

To account for the dependency of water retention on dry density and temperature,  $s_e$  is taken as a function that depends on the material state as

$$s_e = s_{e0} \left[ 1 - \theta_T \log\left(\frac{T}{T_0}\right) - \theta_E \log(1 - \varepsilon_v) \right] \quad (18)$$

where  $s_{e0}$  is the initial air entry suction, and  $\theta_T$  and  $\theta_E$  describe the evolution of air entry suction with temperature and volumetric strain respectively.

Based on the same framework, more advanced models have been developed in Nuth & Laloui (2009) and Salager et al. (2013). Changes respond mainly to a more progressive slope approaching the air entry suction and the assumption that a common asymptotic behaviour for low saturation states exists regardless of dry density (or void ratio). These models are more suitable to represent the behaviour of bentonite and therefore will be incorporated into ACMEG-TS.

## 5 Model parameters

The simulations presented in the following have been performed using parameters determined from experimental results on MX-80 bentonite in granular form (Seiphoori (2014), Seiphoori et al. (2014)) and powder (Tang (2005), Yigzaw et al. (2016)).

Elastic moduli  $K_{ref}$  and  $G_{ref}$ , have been calibrated using swelling under constant load tests and swelling pressure tests. As it will be shown one of the limitations of the model is the inconsistency resulting from these moduli to simulate satisfactorily both types of tests, resulting in either low swelling strains or high swelling pressure. The plastic modulus is taken from isotropic tests under saturated conditions.

For the assessment of the model, dry density values of 1.50, 1.65 and 1.80 Mg/m<sup>3</sup> are considered. Since the response of the model does not depend explicitly on void ratio (i.e. dry density) a relationship between preconsolidation and initial dry density, based on the experimental results of Seiphoori (2014), is established as

$$p'_{c0} = a \exp(b\gamma_d) \text{ (MPa)} \quad (19)$$

where dry density  $\gamma_d$  is expressed in  $\text{Mg/m}^3$  and  $a = 0.000252$  and  $b = 5.25$  are fitting parameters. The resulting curve for usual ranges of dry density is shown in Figure 3. Thus, preconsolidation pressure, together with air entry suction, are the main parameters accounting for the effects of initial dry density on model responses.

The set of parameters corresponding to thermal behaviour is selected based on the experimental results of Tang (2005). Performance of the model simulating such tests can be found in François & Laloui (2008).

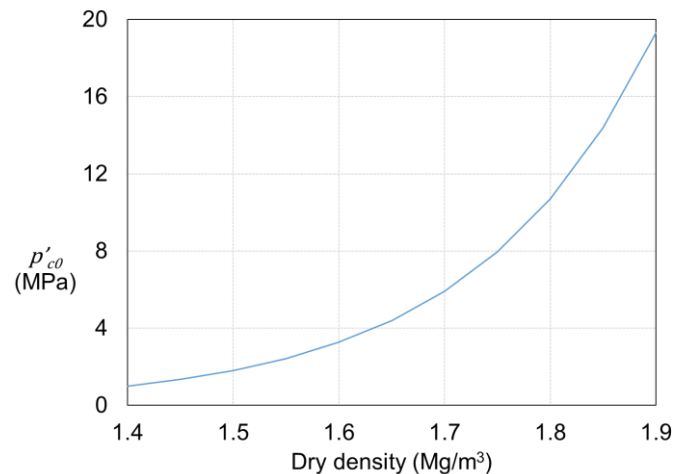


*Figure 3. Adopted preconsolidation pressure in the simulations to account for dry density variations*

A comprehensive set of data on water retention behaviour under confined conditions was presented in Seiphoori et al. (2014) (Figure 4a). Those results are used to calibrate the parameters corresponding to the water retention model, which is shown in Figure 4. Note that  $s_{hys}$  is chosen such that water retention does not exhibit significant hysteresis. This would lead to a lack of representativeness at high suction levels and resulting in significant errors when computing the effective stress, besides, it is thought to be of minor importance for the examined cases herein. Nevertheless, this is a point that shall be overcome in the near future adopting more realistic models for water retention (e.g. Salager et al. (2013)).

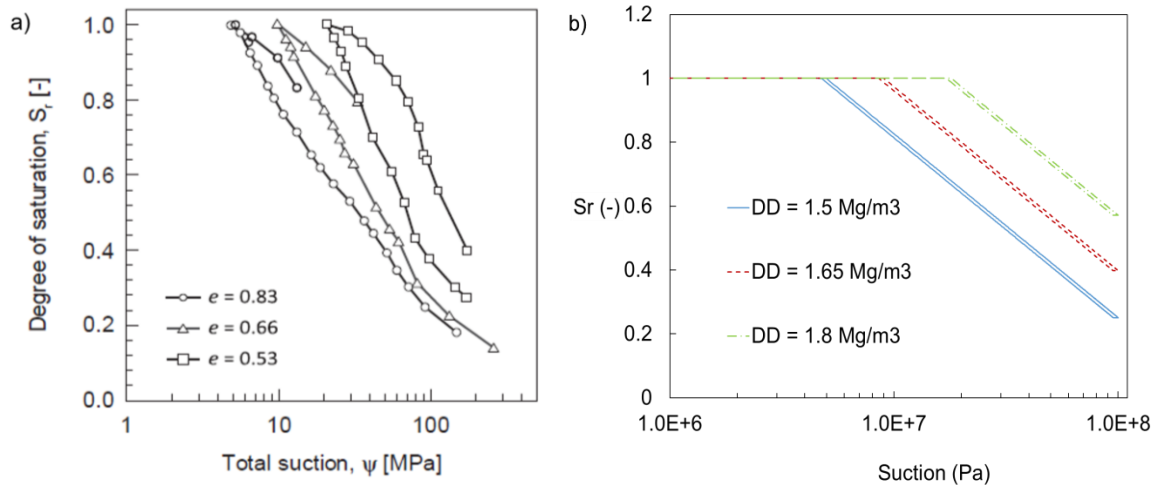


Figure 4. a): Experimental results on confined water retention curves for three values of dry density (1.5, 1.67 and 1.8 Mg/m<sup>3</sup>) (Seiphoori et al. 2014). b): Water retention model used in the simulations, where DD stands for dry density.

In Table 2 model parameters used for the simulations are summarized.

Table 2. Model parameters used for the simulations, representative of MX80 bentonite.

Elastic parameters		
$K_{ref}, G_{ref}, n^e, \beta'_s$	[MPa], [MPa], [-], [°C <sup>-1</sup> ]	20, 15, 1, $4.2 \times 10^{-5}$
Isotropic plastic parameters		
$\beta_m, \gamma_s, \gamma_T, r_{iso}^e, p'_c, \Omega$	[-], [-], [-], [-], [-], [MPa], [-]	15, 3.85, 0.2, 1, *, 0
Deviatoric plastic parameters		
$b, d, M, g, \alpha, a, r_{dev}^e$	[-], [-], [-], [-], [-], [-], [-]	0.5, 2.0, 1.0, 0, 1, 0.001, 1
Water retention parameters		
$s_{e0}, \beta_h, \theta_T, \theta_e, s_{hys}$	[MPa], [-], [-], [-], [-]	*, 4, 0, 0, 0.95

\*depending on dry density, see the text for its actual values.

## 6 Model performance

The model is evaluated by following the stress paths suggested in the deliverable instructions, including swelling under constant load, swelling pressure tests, transition from saturated to unsaturated states and vice versa and temperature cycles. The sign convention for stress is compression as positive, and swelling strains are taken positive.

### 6.1 Dependence of swelling strain on applied stress and dry density

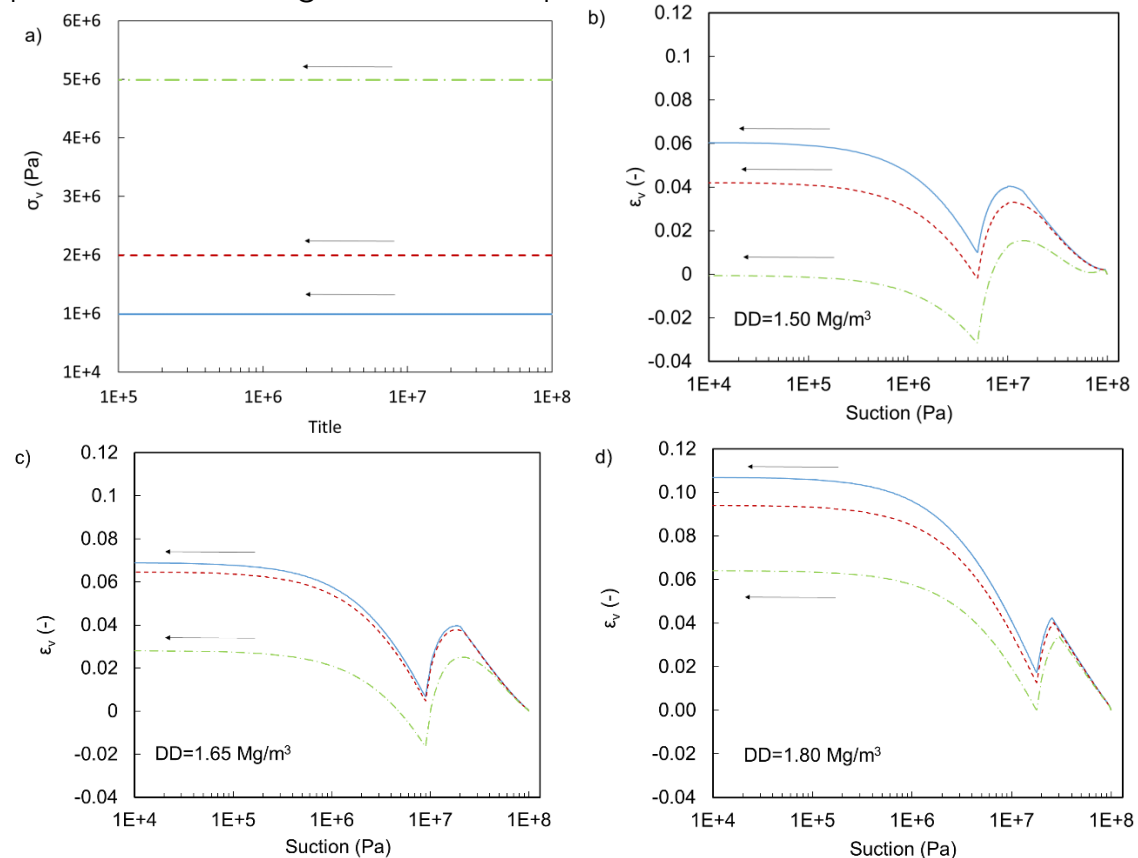
Figure 5 shows the stress paths that have been imposed in order to evaluate the suitability of the model for such experiments. In the same figure model responses in terms of swelling strains are shown. In all simulations, initial suction is 100 MPa and is reduced up to 0 under constant vertical loads of 1, 2 and 5 MPa. Initial stress is isotropic and radial deformation is constrained as in oedometric conditions. Each path has been simulated assuming different

initial dry densities, corresponding to 1.50, 1.65 and 1.80 Mg/m<sup>3</sup>.

It is observed that for a given vertical load the final swelling strain increases as dry density increases. The drop in swelling strain (collapse) observed at a given suction corresponds to the point at which the stress path reaches the yield surface. When the suction value decreases to the air entry value swelling takes place again, this is due to the assumption that when the material is saturated suction does not affect the preconsolidation pressure (equation 11). Similar qualitative behaviour is observed in the experiments (e.g. Yigzaw et al. (2016)), although in such experiments the actual collapse is lower and it practically disappears when the imposed load is relatively low. In contrast, the model predicts similar amounts of strain collapse for all cases.

It is also of interest to study the model response in terms of effective stress. As it is observed in Figure 5(e), the initial (elastic) response is similar for the three tests differing only on the initial point due to the different applied loads.

Figure 5(f) shows the stress paths together with the initial loading collapse curve, from which the origin of discrepancies between the three tests can be derived. Indeed the stress paths cross the loading collapse curve at different points, thus resulting in different responses.



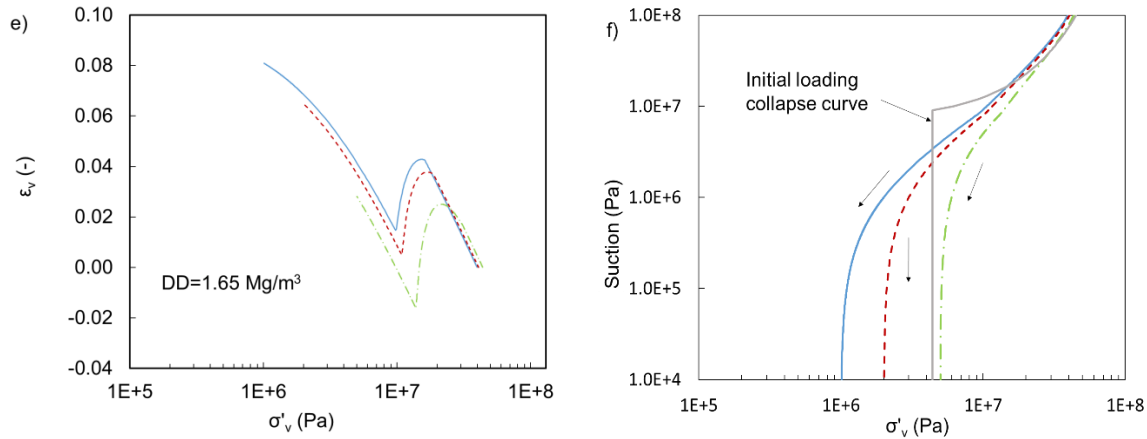


Figure 5. (a): Stress path followed to simulate swelling tests under constant load. (b), (c) and (d): Model output corresponding to dry densities (DD) of 1.50, 1.65 and 1.80 Mg/m<sup>3</sup> respectively. (e): Model response in terms of effective stress. (f): Effective stress-suction paths together with the initial loading collapse curve for a DD=1.65 Mg/m<sup>3</sup>

## 6.2 Irreversibility of strains in wetting/drying cycles

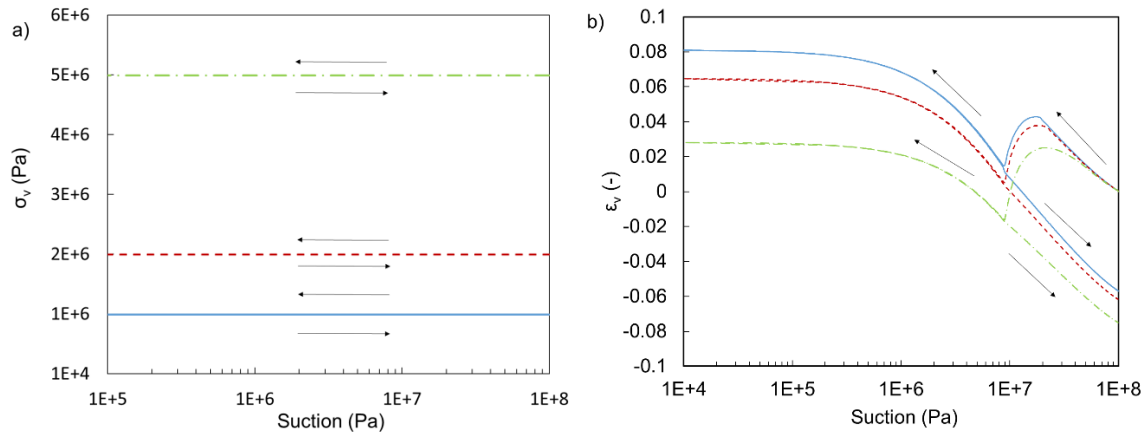
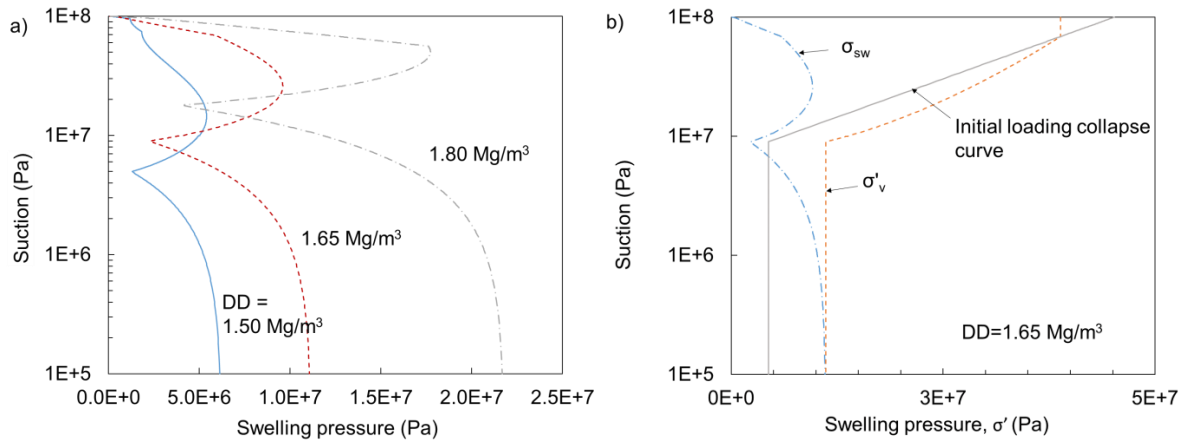


Figure 6. (a): Stress paths used to simulate a cycle in swelling/shrinkage under load test. (b) Model results corresponding to a dry density of 1.65 Mg/m<sup>3</sup>.

Figure 6 shows the stress cycle followed in order to assess model response in terms of irreversible behaviour. The initial path corresponds to the previous cases and a subsequent reduction to the initial stress state is performed. The assumed dry density for this case is 1.65 Mg/m<sup>3</sup>.

The initial response is of course the same as in the previous example. After subsequent suction increase a first part is observed in which the response follows closely that of the initial path. It is after reaching the air entry value that the strains obtained differ from those obtained initially, reaching a final state with a significant shrinkage with respect to the initial volume.

## 6.3 Behaviour during swelling pressure test



**Figure 7. Swelling pressure-suction paths followed during wtting (suction reduction) under constant volume conditions for three different dry densities (DD). b) Effective stress path together with the initial loading collapse curve for a dry density of 1.65 Mg/m<sup>3</sup>.**

Swelling pressure tests were simulated starting from a suction value of 100 MPa and an isotropic confining stress of 50 kPa. The stress path simulated corresponds to a suction decrease up to 100 kPa under constant volume, which results in the development of swelling pressure (total stress) shown in Figure 7. Three dry densities, 1.50, 165 and 1.80 Mg/m<sup>3</sup>, were considered for the simulations.

The simulated swelling pressure - suction paths follow the same trend observed experimentally in Lloret et al, (2003) for Febex bentonite, where three zones (swelling-collapse-swelling) can be differentiated along suction. The interpretation of this behaviour according to the model is as follows. From the initial value of 100 MPa an elastic swelling is first developed, until the effective stress path reaches the loading collapse curve. From there on both elastic and plastic strains develop compensating each other. During this stage total stress decreases in order to equilibrate with the decrease in effective stress that follows closely the loading collapse curve. This drop in stress continues until the air entry suction value is reached, after which preconsolidation pressure remains constant and total stress increases proportional to the decrease in pore water pressure. The process can be observed in Figure 7(b) where total stress (swelling pressure) is plotted in the same plane with the initial preconsolidation pressure and the effective stress path.

The final swelling pressure increases nonlinearly with dry density, as observed experimentally, although with values that exceed the typical measurements. The obtained values of final swelling pressure against dry density are plotted in Figure 8.

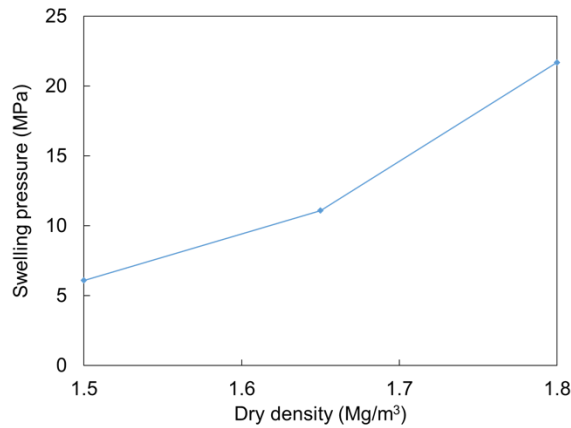


Figure 8. Swelling pressure obtained from three dry densities

Shortcomings of the model relate mainly to excessive swelling pressures and to the high collapse observed during the elasto-plastic regime. It is expected that a refined expression for the loading collapse curve, predicting more reasonable values of preconsolidation pressure for high suction ranges, especially when simulating high dry density samples, would result in less abrupt responses of the model.

#### 6.4 Stress path dependence from an unsaturated to a saturated state

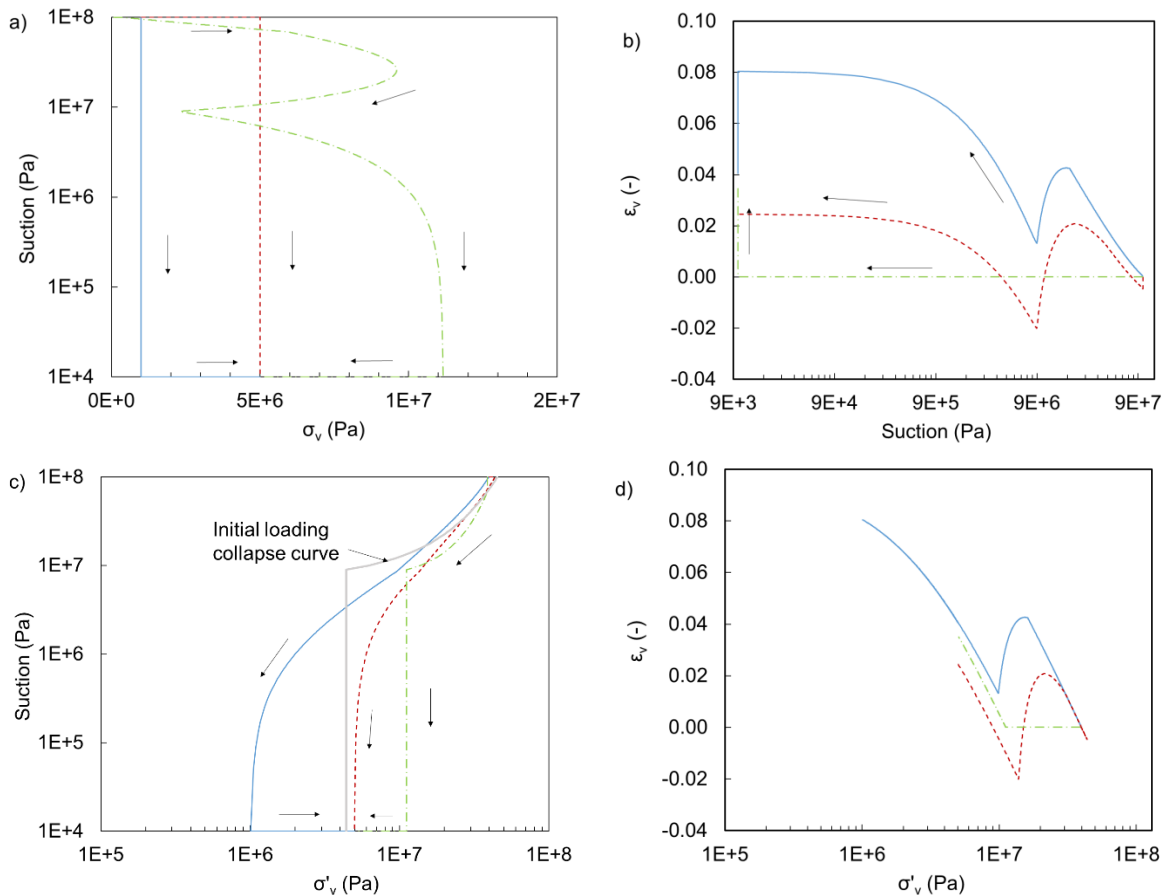


Figure 9. a): Stress-suction paths followed to assess path dependency, including swelling pressure test. b): Model

Beacon

D3.1 – ACMEG-TS: Formulation and application to bentonite

Dissemination level: PU

Date of issue: **01/03/18**

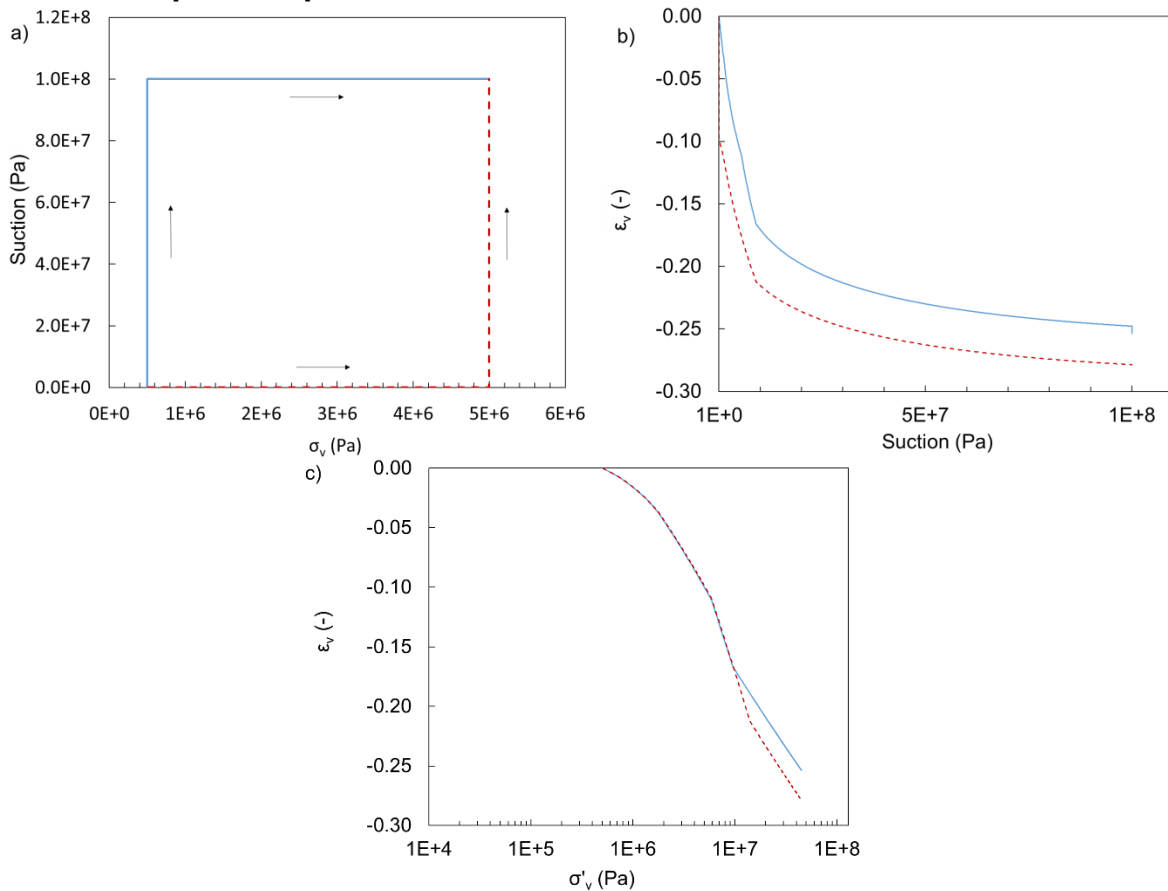
*response. c): Effective stress- suction paths together with the initial loading collapse curve. d): Model response in terms of effective stress.*

To assess stress path dependency, three different paths are simulated as shown in Figure 9(a). The initial state corresponds to a suction of 100 MPa and a vertical stress of 1 MPa, whereas the final state is at a suction of 10 kPa and a vertical stress of 5 MPa, being the same for the three cases. An initial dry density of 1.65 Mg/m<sup>3</sup> is considered for the three cases.

It is seen that the final strain state is different for all three cases, showing once more the suitability of the framework to represent such tests in a consistent manner. Although different processes contribute to the differences observed at the end of the simulations, final strains differ mainly due to different compressibility under saturation and unsaturated (at high suction) states. Under constrained volume plastic strains are developed that differ from those obtained from the other two stress paths.

More information on the process can be obtained by following the effective stress paths as in Figure 9(c-d). It is seen how the different stress paths activate the yield surface at different points which results in the differences between responses.

### 6.5 Stress path dependence from a saturated to an unsaturated state

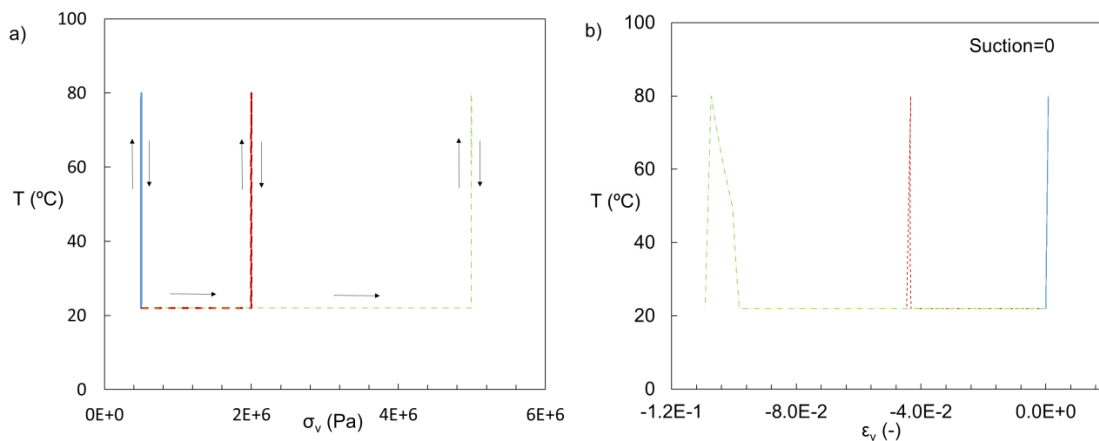


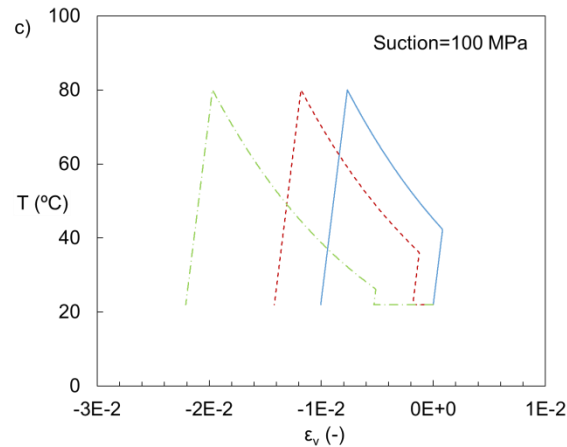
**Figure 10. a): Stress paths followed to assess path dependency from saturated state. b): Model response in terms of suction. c): Model response in terms of effective stress.**

Figure 10 shows the stress paths followed to evaluate model responses along a transition between saturated state (null value of suction) with a vertical load of 0.5 MPa up to an unsaturated state with a suction value of 100 MPa and a vertical load of 5 MPa. An initial dry density of 1.65 Mg/m<sup>3</sup> was considered in both cases.

Once again, depending on the path followed, different responses are obtained. As explained previously, the higher compressibility under saturated state results in higher strains for the test that involves compression before suction is increased. Along the suction reduction path a significant change of slope in the (suction-strain) plane is observed after reaching the air entry value, corresponding to the shrinkage limit. During the stage of suction decrease both responses follow the same trend although with a slightly higher slope for the test under initial low stress. Strains obtained in this case well exceed those that were obtained for the unsaturated-saturated transition. In this case the volumetric strain decreases reaching values of more than 20%. When the response is plotted in terms of effective stress it is observed that the initial response is identical. This is because under saturated state an increase in suction has the same effect that an increase in total stress. Only when the air entry value is reached (9 MPa) the response diverges due to the lower effect of an increase in suction compared to an increase in total stress.

### 6.6 Dependence of strains developed in a temperature cycle on stress





*Figure 11. a): Temperature-stress paths simulated. b): Model response under a constant nul suction. c): Model response under a suction value of 100 MPa.*

The simulated stress paths together with the obtained response are shown in figure 11. The same stress-temperature paths have been applied under a null value of suction and under a value of 100 MPa of suction. The response clearly depends on the stress state and history (OCR). Temperature effects are more noticeable in the case of a null suction state. In both cases plastic strains develop although with quantitative differences.

## 6.7 Model features

Name of the constitutive law:		ACMEG-TS	
Behaviour feature	YES	NO	Remarks
<b>Mechanical behaviour</b>			
Dependence of swelling strain on applied stress (at the same dry density)	X		As expected: the higher the stress, the lower the swelling
Dependence of swelling <b>strain</b> on dry density (at the same stress)	X		The higher the dry density (preconsolidation stress), the higher the swelling stress
Irreversibility of strains in wetting/drying cycles	X	X	Irreversible behaviour but final cumulated shrinkage.
Dependence of swelling pressure on dry density	X		Well captured
Stress path dependence from an unsaturated to a saturated state	X		
Stress path dependence from a saturated to an unsaturated state	X		
Double structure/porosity considered?		X	
Are temperature effects considered in the model?	X		Both elastic (thermal expansion/compression) and plastic (thermal collapse) effects are considered
Dependence of strains developed in a temperature cycle (increase/decrease) on OCR (or stress)	X		Low OCRs induce thermal collapse upon heating
<b>Hydraulic behaviour (retention curve)</b>			
Hysteresis	X		
Dependence on void ratio	X		

Double structure/porosity considered?		X	
---------------------------------------	--	---	--

## 7 Conclusions

The qualitative features of the behaviour of bentonite materials at laboratory scale (stress point level) are well accounted by the ACMEG-TS model. Several coupling mechanisms between mechanical, hydraulic and thermal effects, allow for the stress path dependency and irreversible behaviour in a consistent way.

Nevertheless, in some cases, differences in quantitative terms are obtained that motivate the further development of the model to deal with the specific behaviour of bentonite. Generally speaking, swelling strains are under predicted whereas swelling pressure is over predicted. In particular, future work aims at reviewing the following points:

- Loading collapse curve. Dominates both free swelling and constrained swelling, in particular when high values of air entry suction are considered, (corresponding to high dry densities), discrepancies between experiments and simulations are obtained.
- Water retention curve. Experimental results show that the slope differs for different dry densities. On top of that the behaviour at high suction ranges seems to be independent of the dry density. More suitable models have been previously developed that are planned to be coupled with ACMEG-TS. Also, a dual porosity framework could be a better approach for these materials.
- Irreversible features are incorporated without the need of a double porosity interaction. However, it is expected that model extensions aiming to deal with pellet based materials will need to take explicitly the double porosity in the mechanical model, thus accounting for differences in collapse behaviour and swelling pressure depending on the overall fabric characteristics. This would also allow for a precise model of water flow in the case of boundary value problems.
- It is yet unclear whether the current expression for the effective stress is suitable using total suction as the suction variable. Experimental results are usually obtained in terms of total suction, although matric suction and osmotic suction are responsible for different effects on the behaviour of geomaterials and, in particular, bentonite. A refined expression for the effective stress is therefore to be developed.

## 8 Acknowledgments

This project receives funding from the Euratom research and training programme 2014-2018 under grant agreement No 745942.

## References

- Bishop AW. (1959), The principle of effective stress. *Teknisk Ukeblad*; 39:859–863.
- Di Donna, A., and Laloui, L. (2015), Numerical analysis of the geotechnical behaviour of energy piles. *Int. J. Numer. Anal. Meth. Geomech.*, 39: 861–888. doi: 10.1002/nag.2341.
- Dupray F., B. François, L. Laloui, (2013), Analysis of the FEBEX multi-barrier system including thermoplasticity of unsaturated bentonite, *International Journal for Numerical and Analytical Methods in Geomechanics*, 2013, 37, 4, 399
- Fauriel S. and L. Laloui (2012), A bio-chemo-hydro-mechanical model for microbially induced calcite precipitation in soils. *Comput Geotech*, 46, pp. 104-120.
- François B. (2008), Thermo-plasticity of fine grained soils at various saturation states: Application to nuclear waste storage. PhD Thesis, Ecole Polytechnique Fédérale de Lausanne, Lausanne, Switzerland.
- Francois B. and Laloui L. (2008), ACMEG-TS: A constitutive model for unsaturated soils under non-isothermal conditions. *International Journal for Numerical and Analytical Methods in Geomechanics*. 32:1955-1988.
- Hujeux J.C. (1979), Calcul numérique de problèmes de consolidation élastoplastique. PhD Thesis, Ecole Centrale, Paris, France.
- Koliji A. (2008), Mechanical behaviour of unsaturated aggregated soils. PhD Thesis, Ecole Polytechnique Fédérale de Lausanne, Lausanne, Switzerland.
- Lloret A., M. V. Villar, M. Sánchez, A. Gens, X. Pintado, and E. E. Alonso (2003). Mechanical behaviour of heavily compacted bentonite under high suction changes. *Géotechnique* 53:1, 27-40
- Nuth M. (2009), Constitutive modelling of unsaturated soils with hydro-geomechanical couplings. PhD Thesis, Ecole Polytechnique Fédérale de Lausanne, Lausanne, Switzerland.
- Nuth M and Laloui L. (2008), Effective stress concept in unsaturated soils: Clarification and validation of a unified framework. *International Journal for Numerical and Analytical Methods in Geomechanics*. 32(7):771-801.
- Nuth, M., & Laloui, L. (2009), Advances in modelling hysteretic water retention curve in deformable soils. *Computers and Geotechnics*. 35, No. 6, 835-844.
- Péron H. (2008), Desiccation cracking of soils. PhD Thesis, Ecole Polytechnique Fédérale de Lausanne.
- Rizzi E., Maier G., and Willam K. (1996), On failure indicators in multidissipative materials. *International Journal of Solids and Structures*. 33(20-22):3187-3214.
- Salager S, Nuth M, Ferrari A, Laloui L. (2013), Investigation into water retention

behaviour of deformable soils. *Canadian Geotechnical Journal* 50(2): 200-208.

Schrefler B.A. (1984), The finite element method in soil consolidation (with applications to surface subsidence). PhD Thesis. University College of Swansea, C/Ph/76/84.

Seiphoori A. (2014), Thermo-hydro-mechanical characterisation and modelling of MX-80 granular bentonite. PhD Thesis, Ecole Polytechnique Fédérale de Lausanne, Lausanne, Switzerland.

Seiphoori A., Ferrari A. & Laloui L. (2014), Water retention behaviour and microstructural evolution of MX-80 bentonite during wetting and drying cycles. *Géotechnique* 64(9): 721–734.

Tang A.M., Cui Y.J and Barnel N. (2008), Thermo-mechanical behaviour of a compacted swelling clay. *Géotechnique*, 58(1). 45-54.

Witteveen P., Ferrari A., and Laloui L. (2013), An experimental and constitutive investigation on the chemo-mechanical behaviour of a clay. *Géotechnique* 63:3, 244-255 .

Yigzaw, Z. G., Cuisinier, O., Massat, L., and Masroui, F. (2016), Role of different suction components on swelling behavior of compacted bentonites. *Applied Clay Science*, 120, 81–90.

# D3.1



## IC DSM / Imperial College Double Structure Model

### **DELIVERABLE (D3.1)**

### **ANNEX E**

Author(s): **Lidija Zdravkovic, Giulia Ghiadistri**

Reporting period: 01/06/17 – 30/11/18

Date of issue of this report: **28/02/18**

Start date of project: **01/06/17**

Duration: 48 Months

This project receives funding from the Euratom research and training programme 2014-2018 under grant agreement No 745 942		
<b>Dissemination Level</b>		
<b>PU</b>	Public	X
<b>RE</b>	Restricted to a group specified by the partners of the Beacon project	
<b>CO</b>	Confidential, only for partners of the Beacon project	

**REVIEW**

<b>Name</b>	<b>Internal/Project/External</b>	<b>Comments</b>
David Potts	Internal	OK

**DISTRIBUTION LIST**

<b>Name</b>	<b>Number of copies</b>	<b>Comments</b>
Athanasios Petridis (EC) Christophe Davies (EC)  Beacon partners		

## **Abstract**

This report presents a contribution to the Deliverable 3.1 from Imperial College London (ICL), describing the current state of the constitutive modelling capabilities of this project partner, available for modelling the mechanical evolution of bentonite as part of the Beacon project.

## Content

<b>2</b>	<b>Introduction</b> .....	<b>5</b>
<b>3</b>	<b>Background to IC DSM model development</b> .....	<b>5</b>
<b>4</b>	<b>Scope and hypotheses</b> .....	<b>5</b>
4.1	Double-porosity structure .....	5
4.2	Stress variables.....	6
<b>5</b>	<b>IC DSM model formulation</b> .....	<b>7</b>
5.1	Yield and plastic potential surfaces .....	7
5.2	Elastic behaviour.....	10
5.3	Hardening rules.....	11
5.4	Extended formulation for the IC DSM.....	11
<b>6</b>	<b>Summary of input parameters</b> .....	<b>14</b>
<b>7</b>	<b>Model performance</b> .....	<b>15</b>
<b>8</b>	<b>Conclusions</b> .....	<b>20</b>
	<b>References</b> .....	<b>21</b>
	<b>Appendix 1 Features table</b> .....	<b>22</b>

## 2 Introduction

This report forms a contribution to Deliverable 3.1 from Imperial College London (ICL). It describes the current modelling capabilities of this project partner in addressing the constitutive behaviour of a bentonite buffer, acting as part of the protection system for high level nuclear waste storage. The constitutive model to be presented is the Imperial College Double Structure Model (IC DSM), Ghiadistri et al. (2018), which is implemented in the bespoke finite element code ICFEP (Potts & Zdravkovic, 1999, 2001). The report summarises the background to model development and its main hypotheses, its brief mathematical formulation and input parameters, as well as the main aspects of its performance.

## 3 Background to IC DSM model development

The double-structure model for unsaturated highly expansive clays, IC DSM of Ghiadistri et al. (2018), is developed in the framework of elasto-plasticity and critical state-based soil mechanics. The model is an extension of a single structure model, IC SSM, developed for unsaturated moderately expansive clays, and described in Georgiadis et al. (2003), (2005); Tsiampousi et al. (2013). The latter model (IC SSM) is a modified and generalised version of the Barcelona Basic Model (BBM, Alonso et al., 1990), while the former model (IC DSM) adopts the conceptual basis of the Barcelona Expansive Model (BExM, Gens & Alonso, 1992; Sanchez et al., 2005). Both IC SSM and IC DSM are implemented in the Imperial College Finite Element Program (ICFEP), Potts & Zdravkovic (1999), which is applied here to demonstrate the performance of the double-structure model.

## 4 Scope and hypotheses

### 4.1 Double-porosity structure

The formulation of the IC DSM adopts the concept of double porosity in the structure of a compacted clay. One level of porosity is the void space between the clay aggregates, defined as macro- or inter-aggregate porosity (as sketched in Figure 4-1). The second level of porosity is the void space within an aggregate, defined as micro- or intra-aggregate porosity (Figure 4-1). Macro-porosity is associated with the evolution of negative pore water pressures (suctions) in the clay, while micro-porosity governs the physico-chemical processes associated with the clay mineralogy. It is believed that the interaction between the two levels of structure upon saturation of compacted clays contributes to their swelling potential, which is the principal mechanism of developing a protection layer around nuclear waste canisters.

The existence of this structure is evidenced by the electro-scanning micrographs (ESEMs) of compacted clay and/or mercury intrusion porosimetry

(MIP) tests performed on samples of compacted clay (e.g. Romero et al., 1999; Sanchez et al., 2005; Monroy et al., 2010; Seiphoori et al., 2014). Example graphs in Figure 4-2(a) show a clear dual concentration of pore sizes in compacted FEBEX bentonite, with the dominant intra-aggregate (micro) pore size of  $\sim 10$  nm, and the inter-aggregate (macro) pore size greater than  $\geq 10$   $\mu\text{m}$ . The figure also shows the dependency of the macro-porosity on the dry density,  $\rho_d$ , of the compacted clay, with a larger value of  $\rho_d$  ( $= 1.8 \text{ Mg/m}^3$ ) generating larger and a greater quantity of macro-pores, compared to the sample of lower  $\rho_d$  ( $= 1.5 \text{ Mg/m}^3$ ). Figure 4-2(b) shows a very similar double porosity initial structure for compacted MX-80 bentonite (“as compacted” curve). Additionally, it also shows that, upon full hydration, the macro-pores seem to disappear, leaving a higher concentration of micro-pores (“fully saturated” curve). This interaction creates a low-permeability buffer, which should prevent the escape of radionuclides into the surrounding ground.

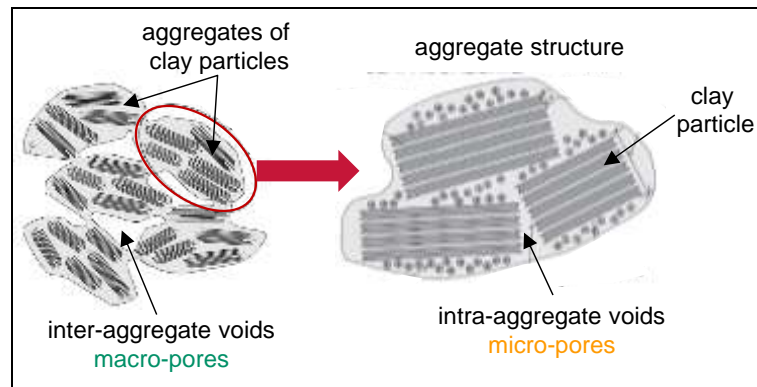
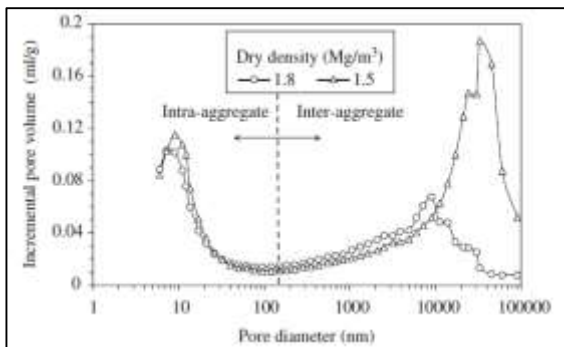
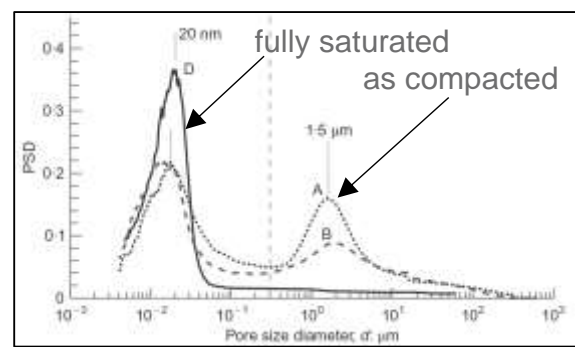


**Figure 4-1: Conceptual illustration of a double-porosity structure in compacted clays**



**(a) Sanchez et al. (2005): compacted FEBEX bentonite**



**(b) Seiphoori et al. (2014): compacted MX-80 bentonite**

**Figure 4-2: MIP evidence of a double-porosity structure in compacted clays**

## 4.2 Stress variables

The mathematical formulation of the IC DSM adopts two independent stress variables to describe the mechanical behaviour of unsaturated soils: the matric suction,  $s = u_{air} - u_w$ , defined as the difference between the air pressure,  $u_{air}$ , and water pressure,  $u_w$ , in the macro pores; and net stress,

$\bar{\sigma} = \sigma_{tot} - u_{air}$ , defined as the difference between the total stress,  $\sigma_{tot}$ , and the pore air pressure. Additionally, to enable a seamless transition from a saturated to an unsaturated state, and vice versa, the model introduces the equivalent suction,  $s_{eq} = s - s_{air}$ , where  $s_{air}$  is the air-entry value of suction. This necessarily leads to the introduction of equivalent stress,  $\sigma = \bar{\sigma} + s_{air}$ .

## 5 IC DSM model formulation

The IC DSM model is generalised in the  $J - p - \theta - s_{eq}$  space, as an extension of the IC SSM model, where  $p$  is the mean equivalent stress (Equation 5-1),  $J$  is the generalised deviatoric stress (Equation 5-2), and  $\theta$  is the Lode's angle (Equation 5-3).

$$p = \frac{\sigma_x + \sigma_y + \sigma_z}{3} \quad (5-1)$$

$$J = \left( \frac{1}{6} \left[ (\sigma_x - \sigma_y)^2 + (\sigma_y - \sigma_z)^2 + (\sigma_x - \sigma_z)^2 \right] + \tau_{xy}^2 + \tau_{xz}^2 + \tau_{yz}^2 \right)^{1/2} \quad (5-2)$$

$$\theta = -\frac{1}{3} \cdot \sin^{-1} \left[ \frac{3\sqrt{3}}{2} \cdot \frac{\det \mathbf{s}}{J^3} \right] \quad (5-3)$$

where

$$\det \mathbf{s} = \begin{vmatrix} \sigma_x - p & \tau_{xy} & \tau_{xz} \\ \tau_{xy} & \sigma_y - p & \tau_{yz} \\ \tau_{xz} & \tau_{yz} & \sigma_z - p \end{vmatrix} \quad (5-4)$$

Similarly, the strain invariants  $\varepsilon_{vol}$  (volumetric strain) and  $E_d$  (generalised deviatoric strain) are calculated as:

$$\varepsilon_{vol} = \varepsilon_x + \varepsilon_y + \varepsilon_z \quad (5-5)$$

$$E_d = \left( \frac{1}{6} \left[ (\varepsilon_x - \varepsilon_y)^2 + (\varepsilon_y - \varepsilon_z)^2 + (\varepsilon_x - \varepsilon_z)^2 \right] + \gamma_{xy}^2 + \gamma_{xz}^2 + \gamma_{yz}^2 \right)^{1/2} \quad (5-6)$$

Figure 5-1 shows a three-dimensional view of the model's yield surface in the  $p - s_{eq} - J$  space, distinguishing the load-collapse (LC) curve and the increase of cohesion with equivalent suction,  $f(s_{eq})$ , on the primary yield surface, as well as the secondary yield surface (SI). Sections 5.1 to 5.3 describe the formulation that is common to both the IC SSM and IC DSM.

### 5.1 Yield and plastic potential surfaces

#### 5.1.1 Formulation in the $p - J$ plane

The model adopts versatile primary yield ( $F_{LC}$ ) and plastic potential ( $G_{LC}$ ) surfaces, with projections in the  $p - J$  plane as shown in Figure 5-2(a). The

surface is defined originally in Georgiadis et al. (2005) for the single structure model and reproduced in Equation 5-7. This function can reproduce some of the well-known shapes of yield surfaces, including Sinfonietta Classica (Nova, 1988), Cam clay (Roscoe & Schofield, 1963), or modified Cam clay (Roscoe & Burland, 1968), the latter surface being adopted in the BBM model (Alonso et al., 1990). The yield and the plastic potential surfaces can be different and the model is therefore capable of reproducing both associated and non-associated plasticity. The advantage of this formulation is its ability to produce a more accurate simulation of the strength of overconsolidated clays on the 'dry side' of the critical state, which is otherwise significantly over-estimated by the modified Cam clay's elliptical shape. More recently, the nonlinear Hvorslev surface was added to the model's formulation on the dry side, with a non-associated plastic potential surface (Tsiampousi et al., 2013).

$$\frac{F_{LC}}{G_{LC}} = \frac{p + k \cdot s_{eq}}{p_0 + k \cdot s_{eq}} \frac{\left(1 + \frac{\eta}{K_2(\alpha, \mu)}\right)^{K_2(\alpha, \mu) / \beta_f(\alpha, \mu)}}{\left(1 + \frac{\eta}{K_1(\alpha, \mu)}\right)^{K_1(\alpha, \mu) / \beta_f(\alpha, \mu)}} \quad (5-7)$$

where  $p_0$  is the hardening parameter of the yield surface;  $\eta$  is the generalised normalised stress ratio;  $\alpha_F$  and  $\mu_F$  are the model parameters controlling the shape of the yield surface; and  $\alpha_G$  and  $\mu_G$  are the model parameters controlling the shape of the plastic potential surface.

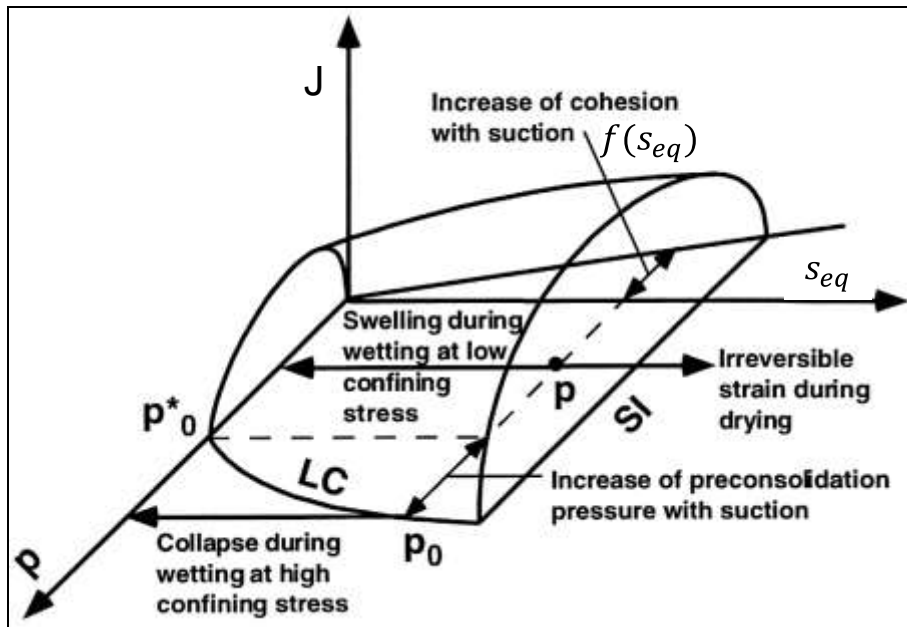


Figure 5-1: General shape of the yield surface in the  $J - p - s_{eq}$  plane (adapted from Alonso et al., 1999)

Additionally, the critical state strength is defined by the maximum stress ratio  $\eta = M_j = J / (p + f(s_{eq}))$ , as shown in Figure 5-2(b), which is a model parameter.

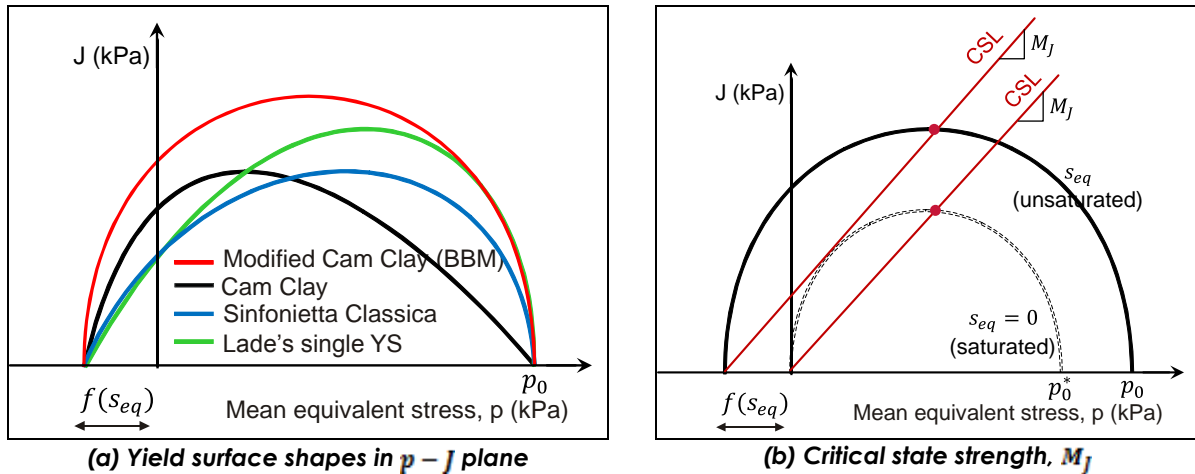


Figure 5-2: IC DSM yield and plastic potential surfaces in the  $p - J$  plane

### 5.1.2 Formulation in the isotropic plane

Figure 5-3(a) shows the projection of the yield surface in the  $p - s_{eq}$  plane, where  $p_0^*$  is the size of the yield surface in a saturated state. The expansion of the yield surface,  $f(s_{eq}) = k \cdot s_{eq}$ , into the tensile region of the mean equivalent stress, due to the increase of equivalent suction,  $s_{eq}$ , can be defined either by a constant gradient,  $k$  (the same as the BBM), or as a function of the degree of saturation, i.e.  $k = S_r$ . The latter option is more realistic as it limits the increase of the surface at very large suctions. Apart from  $k$ , the size of the secondary yield surface,  $s_{eq,0}$ , is also a model parameter.

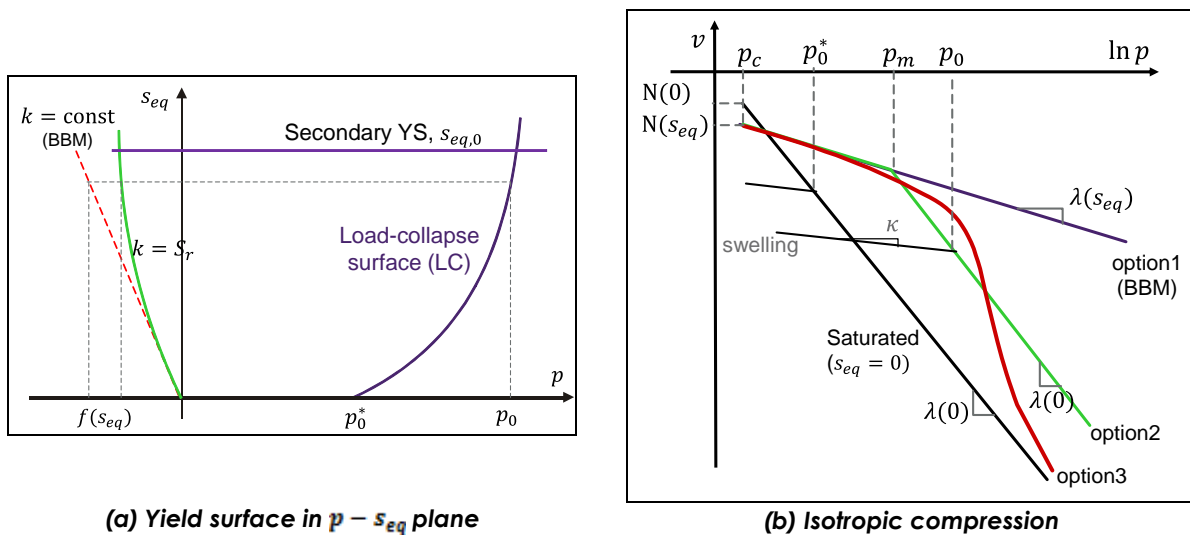


Figure 5-3: Parameters of the yield surface in the isotropic plane

There are three options to describe the isotropic compression of an unsaturated clay in the  $\ln p - v$  plane (Figure 5-3(b), where  $v$  is the specific volume. Option 1 is that of a normal compression line with a constant slope,

$\lambda(s_{eq})$ , the magnitude of which depends on the value of equivalent suction,  $s_{eq}$ . This option is the same as in the BBM model and predicts an increasing magnitude of the potential collapse with increasing stress level, from a stress state on an unsaturated compression line to that on a fully saturated compression line with a slope  $\lambda(0)$ . Experimental evidence from (Josa et al., 1992) has shown this to be unrealistic and a nonlinear Option 3 was introduced for the compression line to reflect those experiments. Finally, as a simplification of this option, Option 2 compression line follows initially the  $\lambda(s_{eq})$  line, the same as Option 3, continuing subsequently with the  $\lambda(0)$  slope upon reaching the stress level  $p_m$ . The magnitude of  $p_m$  is determined from the equations of the two curves.

Figure 5-3(b) also indicates the parameters of the load-collapse (LC) curve on the primary yield surface, which is defined as:

$$p_0 = p_c \cdot \left(\frac{p_0^*}{p_c}\right)^{[\lambda(0)-\kappa]/[\lambda(s_{eq})-\kappa]} \quad (5-8)$$

where

$$\lambda(s_{eq}) = \lambda(0) \cdot [(1-r) \cdot e^{-\beta \cdot s_{eq}} + r] \quad (5-9)$$

and  $p_c$  is a characteristic pressure,  $\kappa$  is the swelling coefficient,  $r$  is the soil stiffness parameter and  $\beta$  is the stiffness increase parameter. Together with  $\lambda(0)$ , the latter parameters are model input parameters that describe the behaviour in isotropic compression for Option 1. Details for Options 2 and 3 can be found in Georgiadis et al. (2005).

### 5.1.3 Formulation in the deviatoric plane

The final aspect of the primary yield surface is its formulation in the deviatoric (or  $\pi$ ) plane, which adopts the Matsuoka-Nakai shape (Matsuoka & Nakai, 1974), as shown in Figure 5-4. This differs from the BBM yield surface, which adopts a circular shape in the deviatoric plane, in line with the classical critical state approach. However, the circular shape implies a variable angle of shearing resistance,  $\phi'$ , for geomaterials, from triaxial compression ( $\theta = -30^\circ$ ) to triaxial extension ( $\theta = +30^\circ$ ). This variation is unrealistically high and unsupported by experimental data, and is therefore unconservative for the design of geotechnical problems. The Matsuoka-Nakai surface also implies variable  $\phi'$ , but this variation resembles that experimentally measured. Potts & Zdravkovic (2001) further discuss this pitfall of the circular yield surface in deviatoric plane.

## 5.2 Elastic behaviour

The formulation of the yield and plastic potential surfaces described in Section 5.1 is common for both the single structure model (IC SSM, Georgiadis

et al., 2003) and the double structure model (IC DSM, Ghiadistri et al., 2018). The IC SSM, like the BBM, assumes elastic behaviour inside the yield surface depicted in Figure 5-1. The elastic volumetric strain,  $\Delta \varepsilon_{vol}^e$ , has contributions from both the stress change,  $\Delta p$ , and the suction change,  $\Delta s_{eq}$ , as given by Equation 5-10:

$$\Delta \varepsilon_{vol}^e = \frac{\kappa}{v \cdot p} \cdot \Delta p + \frac{\kappa_s}{v \cdot (s_{eq} + p_{atm})} \cdot \Delta s_{eq} \quad (5-10)$$

where  $\kappa_s$  is the elastic swelling coefficient for changes in suction and is a model parameter, while  $p_{atm}$  is the atmospheric pressure, equal to 101.3 kPa.

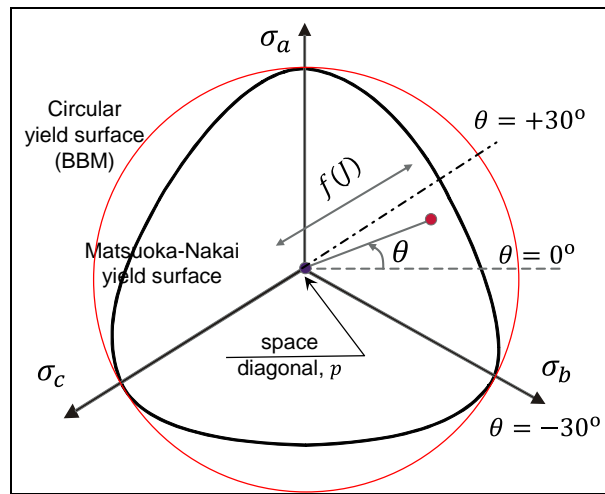


Figure 5-4: Yield surface in the deviatoric plane

### 5.3 Hardening rules

The magnitude of the plastic volumetric strains,  $\varepsilon_{vol}^p$ , when either of the two yield surfaces is activated is related to the change of the hardening / softening parameters  $p_0^*$  and  $s_{eq,0}$ , through the following equations:

- primary yield surface:

$$\frac{dp_0^*}{p_0^*} = \frac{v}{\lambda(0) - \kappa} \cdot d\varepsilon_{vol}^p \quad (5-11)$$

- secondary yield surface:

$$\frac{ds_{eq,0}}{s_{eq,0} + p_{atm}} = \frac{v}{\lambda(s_{eq}) - \kappa_s} \cdot d\varepsilon_{vol}^p \quad (5-12)$$

### 5.4 Extended formulation for the IC DSM

The model formulation presented above is valid for a single porosity structure, which is governed by the evolution of suction in the inter-aggregate (macro) pores. As described in Section 4.1, a double porosity model introduces the

second level of structure in terms of intra-aggregate (micro) pores. The formulation assumes that the micro-structure is saturated, elastic and volumetric, hence the associated changes are expressed in terms of effective stresses,  $\{\sigma'\} = \{\sigma\} + \{s_{eq}\}$ . The following assumptions are introduced into the IC SSM formulation to additionally take account of the micro-structure in the new IC DSM formulation.

#### 5.4.1 Additional plastic strains

The first assumption is that the elastic volumetric deformations of the micro-structure,  $\Delta\varepsilon_{vol,m}^e$ , induce additional volumetric plastic deformations of the macro-structure,  $\Delta\varepsilon_{vol,M,\beta}^p$ , via the so-called  $\beta$  interaction mechanism, Equation 5-13. The model formulation introduces a line of neutral loading in the  $p - s_{eq}$  plane. The zero stress change,  $\Delta p' = 0$ , implies the stress state is on the neutral line, which does not generate micro-strains. If  $\Delta p' > 0$ , the suction increase promotes micro-structural compression, whereas  $\Delta p' < 0$  triggers a reduction in suction and hence micro-structural swelling (Figure 5-5). Consequently, the material behaviour below the primary yield surface is no longer elastic and the total volumetric plastic strain is the sum of the plastic strains from the primary yield surface (macro-mechanism) and those from the  $\beta$  mechanism, Equation 5-14.

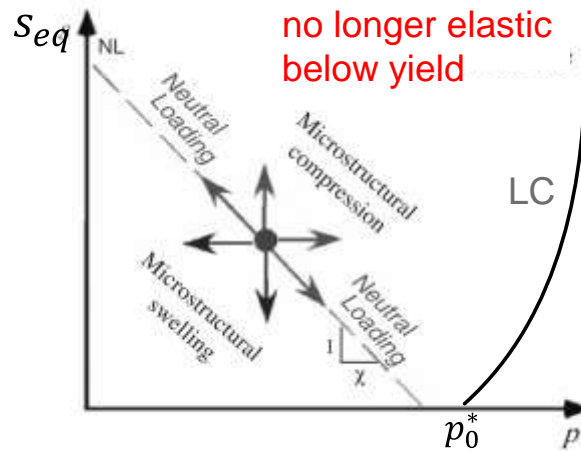


Figure 5-5: Introduction of micro-structural effects in the  $p - s_{eq}$  plane

$$\Delta\varepsilon_{vol,M,\beta}^p = f_{\beta} \cdot \Delta\varepsilon_{vol,m}^e \quad (5-13)$$

$$\Delta\varepsilon_{vol}^p = \Delta\varepsilon_{vol,M,LC}^p + \Delta\varepsilon_{vol,M,\beta}^p \quad (5-14)$$

The micro-structural elastic volumetric strain is calculated as:

$$\Delta\varepsilon_{vol,m}^e = \frac{\Delta p'}{K_m} \quad (5-15)$$

with the micro-structural bulk modulus being:

$$K_m = \frac{1 + e_m}{\kappa_m} \cdot p' \quad (5-16)$$

where  $e_m$  is the void ratio of the micro-pores and  $\kappa_m$  is the elastic compressibility of the micro-structure and is an additional model parameter (compared to the IC SSM model).

#### 5.4.2 $\beta$ interaction mechanism

The function  $f_\beta$  in Equation 5-14 describes a nonlinear interaction between the two levels of structure, as shown in Figure 5-6. This interaction depends on the current stress state with respect to the yield surface, which is represented by the stress ratio  $p_r/p_0$ , as shown in Figure 5-7.

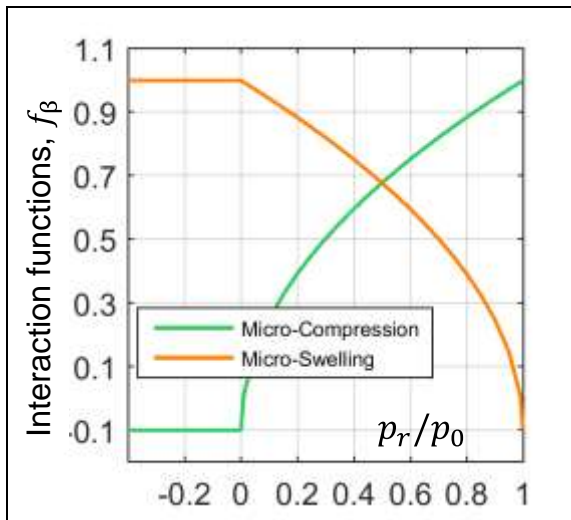


Figure 5-6:  $f_\beta$  interaction functions

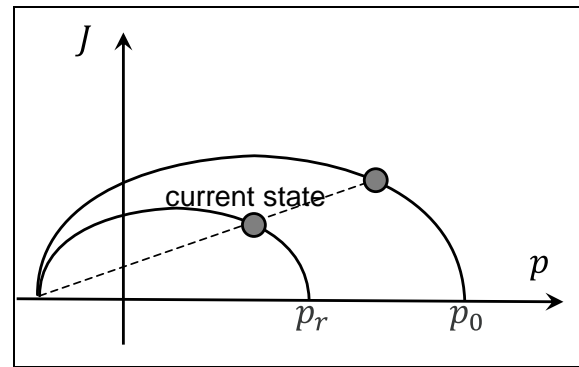


Figure 5-7: Stress state estimate for  $f_\beta$  functions

The empirical expressions for  $f_\beta$  take the following form:

- micro-compression

$$f_\beta = \begin{cases} c_{c1} + c_{c2} \cdot \left(\frac{p_r}{p_0}\right)^{c_{cs}} & \text{if } \frac{p_r}{p_0} \geq 0 \\ c_{c1} & \text{if } \frac{p_r}{p_0} < 0 \end{cases} \quad (5-17)$$

- micro-swelling

$$f_\beta = \begin{cases} c_{s1} + c_{s2} \cdot \left(\frac{p_r}{p_0}\right)^{c_{ss}} & \text{if } \frac{p_r}{p_0} \geq 0 \\ c_{s1} & \text{if } \frac{p_r}{p_0} < 0 \end{cases} \quad (5-18)$$

with  $c_{c1}, c_{c2}, c_{c3}$  being the shape coefficients for micro-compression and, similarly,  $c_{s1}, c_{s2}, c_{s3}$  being the shape coefficients for micro-swelling. These coefficients are also additional input parameters for the double-structure model, IC DSM.

### 5.4.3 Void factor

The final input to the double-structure model is the void factor,  $VF = e_m/e$ , defined as a ratio of the micro void ratio,  $e_m$ , to the total void ratio,  $e = e_m + e_M$  (with  $e_M$  being the macro void ratio). Its role is to monitor the evolution of the micro void ratio and is therefore introduced as a new hardening parameter for the IC DSM, defined as:

$$\Delta VF = \frac{\Delta e}{e} \cdot \frac{\Delta p'}{K_m \cdot \Delta \varepsilon_{vol}} \quad (5-19)$$

## 6 Summary of input parameters

A summary of the input parameters is given in Table 6-1, distinguishing between those required for the IC SSM model, and the additional parameters required for the IC DSM model.

**Table 6-1: Summary of model parameter**

	Parameter	Source
Input parameters for IC SSM	Parameters controlling the shape of the yield surface, $\alpha_p, \mu_F$	Triaxial compression; relationship between dilatancy and $l/p$ ratio
	Parameters controlling the shape of the plastic potential surface, $\alpha_G, \mu_G$	Triaxial compression
	Generalized stress ratio at critical state, $M_f$	Triaxial compression, related to the angle of shear resistance $\phi'_{CS}$
	Characteristic pressure, $p_c$ (kPa)	Limiting confining stress at which $p_0 = p_0^* = p_c$
	Fully saturated compressibility coefficient, $\lambda(0)$	Fully saturated isotropic loading
	Elastic compressibility coefficient, $\kappa$	Fully saturated isotropic unloading
	Maximum soil stiffness parameter, $r$	Isotropic compression tests at constant value of suction
	Soil stiffness increase parameter, $\beta$ 1/kPa)	Isotropic compression tests at constant value of suction
	Elastic compressibility coefficient for changes in suction, $\kappa_s$ (kPa)	Drying test and constant confining stress
	Poisson ratio, $\nu$	Triaxial compression test
	Plastic compressibility coefficient for changes in suction, $\lambda_s$	Drying test and constant confining stress
	Air-entry value of suction, $s_{air}$ (kPa)	From the retention curve
	Yield value of equivalent suction, $s_0$ (kPa)	Usually a high value if it is not to be mobilised
Additional input parameters for IC DSM	Microstructural compressibility parameter, $\kappa_m$	No direct test
	Void factor, $VF$	No direct test – potentially from MIP interpretation
	Coefficients for the micro swelling function, $c_{s1}, c_{s2}, c_{s3}$	No direct test – potentially from MIP interpretation
	Coefficients for the micro compression function, $c_{c1}, c_{c2}, c_{c3}$	No direct test – potentially from MIP interpretation

## 7 Model performance

To demonstrate the general performance of the IC DSM model, a cylindrical sample, 50 mm in diameter and 12 mm high, is simulated under oedometric conditions (restraining vertical displacement along the bottom boundary and horizontal displacement along the vertical boundary of the sample). For the cases simulating the swelling pressure tests the top boundary of the sample is also restrained from displacing vertically.

### 7.1 Dependence of swelling strain on applied stress and on dry density

Two wetting paths, from 10 MPa to 0 suction, and at two different stress levels, as shown in Figure 5-8, are simulated for samples with different initial dry density,  $\rho_d$ . The resulting swelling strains,  $\epsilon_y$ , upon wetting are plotted against the total vertical stress,  $\sigma_y$ , in Figure 5-9(a) for the sample with  $\rho_d = 1.6 \text{ Mg/m}^3$  and in Figure 5-9(b) for the sample with  $\rho_d = 1.1 \text{ Mg/m}^3$ .

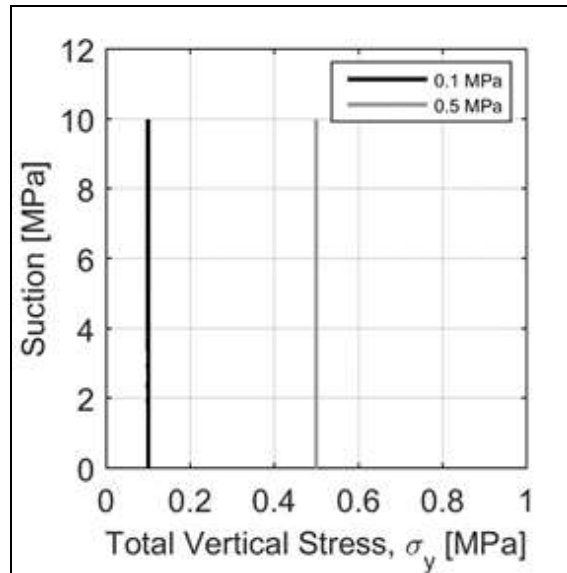


Figure 5-8: Stress paths of swelling tests at constant stress

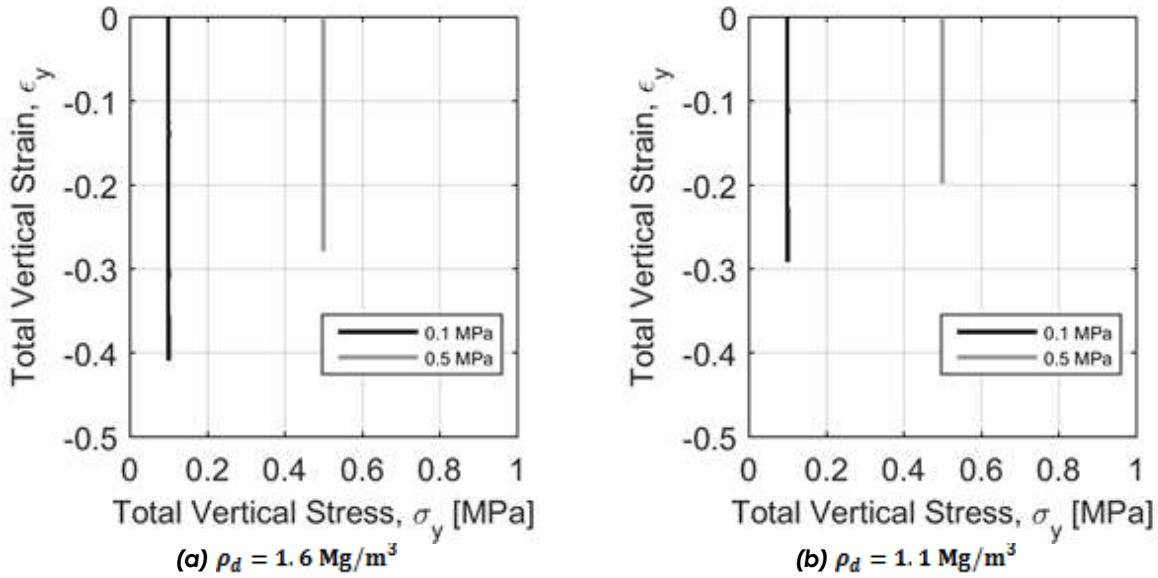


Figure 5-9: Swelling strain upon wetting at constant stress

The model predicts smaller swelling strains when a larger stress is applied, for both the loose and the dense sample. Furthermore, the predicted total swelling strains are smaller for the looser sample. This is in agreement with findings in the literature that denser samples have higher swelling potential.

### 7.2 Irreversibility of strains in wetting/drying cycles

The paths similar to those in Figure 5-8 are simulated next, but this time involving first a reduction in suction from 10 MPa to 0, followed by suction increase from 0 to 10 MPa, under two different levels of vertical stress. A single dry density of  $\rho_d = 1.6 \text{ Mg/m}^3$  is considered.

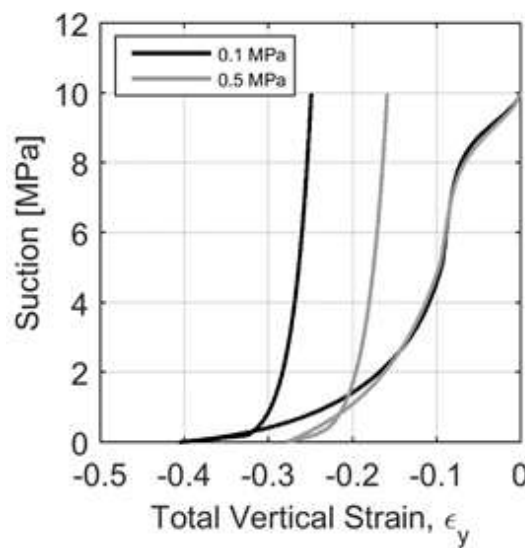


Figure 5-10: Evolution of vertical strain with suction

Figure 5-10 shows the resulting evolution of the vertical total strains with suction, demonstrating irreversible deformations. The strains are larger at smaller applied stress, which is consistent with the results in the previous section.

### 7.3 Behaviour during swelling stress test. Dependence of swelling pressure on dry density

Two swelling stress tests are simulated for two values of dry density, under the condition of constant volume, both starting from a total vertical stress,  $\sigma_y = 0.5 \text{ MPa}$ , and reducing the suction from 10 MPa to 0. It is assumed that the contribution of the micro-structure is more significant in the denser sample ( $\rho_d = 1.6 \text{ Mg/m}^3$ ), which is deemed reasonable considering the implications of the compaction effort and the formation of the double porosity structure discussed in Section 4.

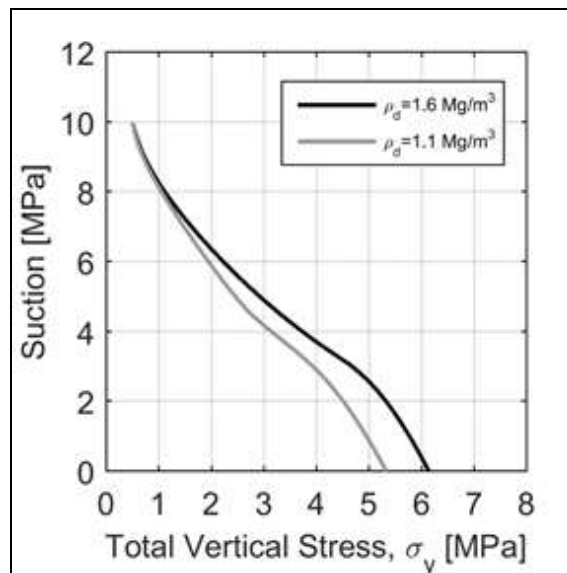


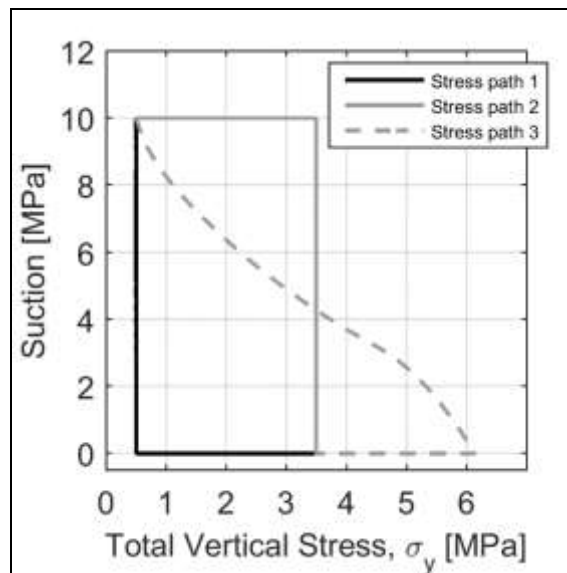
Figure 5-11: Evolution of the swelling pressure in a confined volume wetting test for different dry density

Figure 5-11 shows the evolution of the swelling pressure, in terms of the total vertical stress,  $\sigma_y$ , for initially looser ( $\rho_d = 1.1 \text{ Mg/m}^3$ ) and denser ( $\rho_d = 1.6 \text{ Mg/m}^3$ ) samples. Higher values of  $\sigma_y$  are predicted for the denser sample, which is consistent with the usual experimental findings. However, the predicted magnitude of  $\sigma_y$  for the looser sample is relatively higher than expected (i.e. the difference between the two swelling pressures does not seem very large). This requires further investigation with the IC DSM model.

### 7.4 Stress path dependence from an unsaturated to a saturate state

Three different stress paths, depicted in Figure 5-12, are simulated for this exercise, starting from the same initial unsaturated conditions of suction (10 MPa) and vertical stress (0.5 MPa), and finishing at the same saturated state,

with 0 MPa suction and vertical stress at 3.5 MPa. The relative density for all three paths is  $\rho_d = 1.6 \text{ Mg/m}^3$ . The stress path 1 involves initial wetting to 0 suction at  $\sigma_y = 0.5 \text{ MPa}$ , followed by loading at zero suction to  $\sigma_y = 3.5 \text{ MPa}$ . The stress path 2 is loading first to  $\sigma_y = 3.5 \text{ MPa}$  at constant suction of 10 MPa, followed by wetting to 0 suction at constant  $\sigma_y$ . The final stress path, no. 3, involves confined swelling to zero suction, followed by the reduction at 0 suction of total vertical stress,  $\sigma_y$ , to 3.5 MPa.



**Figure 5-12: Stress paths for simulated changes from unsaturated to saturated stress state**

The predicted evolutions of the total vertical strain for each of the applied stress paths are presented in Figure 5-13 against the total vertical stress, and are entirely plausible. Initial full hydration in stress path 1 results in a swelling (tensile) strain, which reduces subsequently under the applied compressive vertical stress. Stress path 2 yields initial compressive strain under the applied compressive stress, followed by the swelling (tensile) strain under a constant vertical stress. Finally, the initial confined hydration results in zero vertical strain, followed by a tensile strain due the reduction in the vertical stress.

The magnitude of the strain at the end of each of the three paths is different, thus further highlighting the stress path dependency captured by the model.

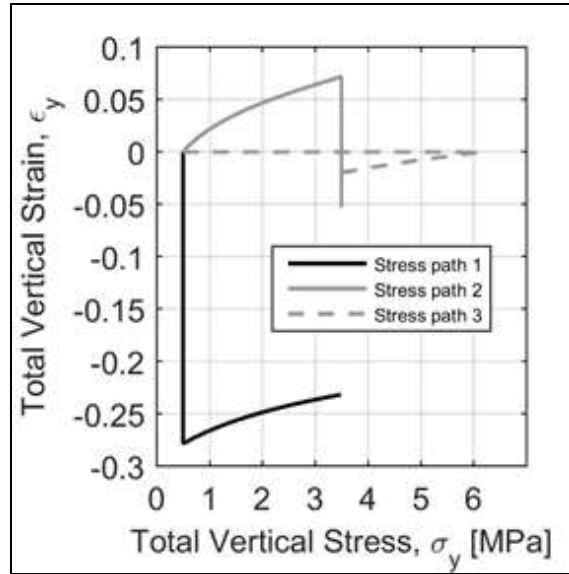


Figure 5-13: Predicted evolution of total strain for changes from unsaturated to saturated stress state

### 7.5 Stress path dependency from a saturated to an unsaturated state

Two different stress paths, depicted in Figure 5-14, are simulated for this exercise, starting from the same initial saturated conditions of 0 suction and 0.5 MPa vertical stress, and finishing at the same unsaturated state, with 10 MPa suction and vertical stress at 3.5 MPa. The relative density for both paths is  $\rho_d = 1.6 \text{ Mg/m}^3$ . The stress path 1 involves initial increase in suction to 10 MPa at  $\sigma_y = 0.5 \text{ MPa}$ , followed by loading at 10 MPa suction to  $\sigma_y = 3.5 \text{ MPa}$ . The stress path 2 applies the loading first to  $\sigma_y = 3.5 \text{ MPa}$  at 0 suction, followed by increase in suction to 10 MPa at constant  $\sigma_y$ .

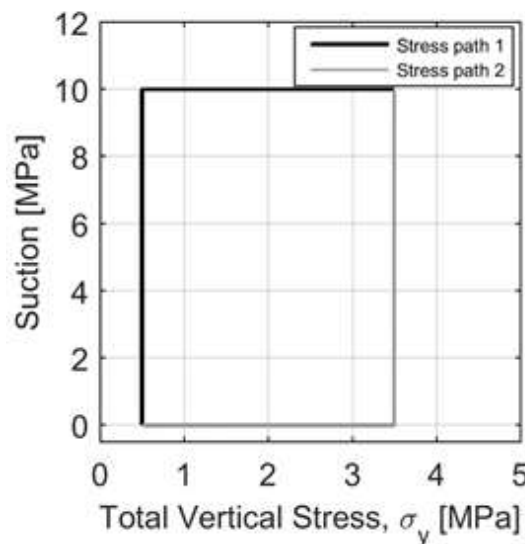
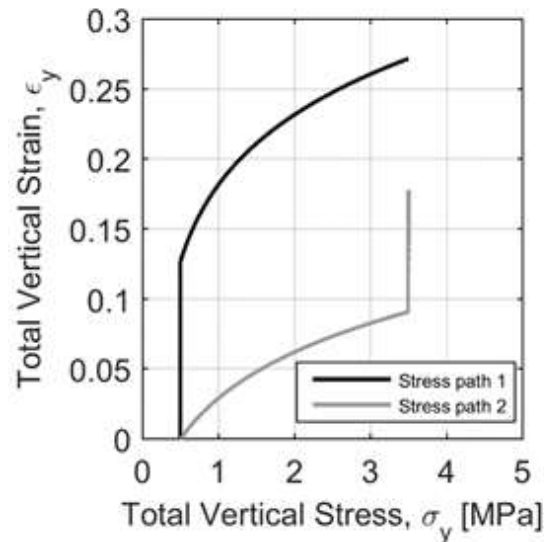


Figure 5-14: Stress paths for simulated changes from saturated to unsaturated stress state

The predicted evolution of total strains from the two stress paths is shown in Figure 5-15. Stress path 1 results initially in shrinking (compressive) strain, which further increases with the applied compressive stress. Stress path 2 initially produces a compressive strain under the applied compressive stress, followed by further compression due to increase in suction (shrinkage). Again, stress path dependency is captured by the model.



*Figure 5-15: Predicted evolution of total strain for changes from saturated to unsaturated stress state*

## 8 Conclusions

This deliverable presents a brief overview of a constitutive model currently available at Imperial College London for the simulation of the mechanical evolution of compacted bentonite, for its application as a buffer material in deep nuclear waste disposal. The model, IC DSM, is developed in the framework of elasto-plasticity and critical state soil mechanics, introducing the concept of the double-porosity structure that is particularly relevant for compacted clays.

Using the computational platform of the bespoke finite element code ICFEP, a number of stress paths are simulated, demonstrating the model's capability to capture stress path dependency of material behaviour.

Model parameters, together with their meaning and the source for derivation, are summarised and explained. References are provided for further details of the model's formulation and implementation.

## References

- Alonso EE, Gens A, Josa A, 1990.** A constitutive model for partially saturated soils. *Geotechnique* **40** (3): 405-430
- Gens A, Alonso EE, 1992.** A framework for the behaviour of unsaturated expansive clays. *Canadian Geotechnical Jnl.* **29** (6): 1013-1032
- Georgiadis K, Potts DM, Zdravkovic L, 2003.** The influence of partial soil saturation on pile behaviour. *Geotechnique* **53** (1): 11-25.
- Georgiadis K, Potts DM, Zdravkovic L, 2005.** Three-dimensional constitutive model for partially and fully saturated soils. *ASCE Jnl. of Geomechanics* **5** (3): 244-255
- Ghiadistri GM, Zdravkovic L, Potts DM, Tsiampousi A, 2018.** A double-porosity model for unsaturated expansive clays. Submitted to *Geotechnique*.
- Josa A, Balmaceda A, Gens A, Alonso EE, 1992.** An elastoplastic model for partially saturated soils exhibiting a maximum of collapse. Proc. 3<sup>rd</sup> Int. Conf. on Computational Plasticity, Barcelona, Spain.
- Matsuoka H, Nakai T, 1974.** Stress-deformation and strength characteristics of soil under three different principal stresses. *Proc. JSCE* **232**: 59-70.
- Monroy R, Zdravkovic L, Ridley A, 2010.** Evolution of microstructure in compacted London Clay during wetting and loading. *Geotechnique* **60** (2): 105-119.
- Nova R, 1988.** Sinfonietta classica: an exercise on classical soil modelling. *Proc. Int. Symp. Constitutive Eq. for Granular Non-cohesive Soils*. Cleveland: 501-520
- Potts DM, Zdravkovic L, 1999.** Finite element analysis in geotechnical engineering: theory. Thomas Telford, London.
- Potts DM, Zdravkovic L, 1999.** Finite element analysis in geotechnical engineering: application. Thomas Telford, London.
- Romero E, Gens A, Lloret A, 1999.** Water permeability, water retention and microstructure of unsaturated compacted Boom clay. *Eng. Geology* **54**: 117-127.
- Roscoe KH, Burland JB, 1968.** On the generalised stress-strain behaviour of 'wet' clay. In *Engineering Plasticity*, Cambridge Univ. Press; 535-609.
- Roscoe KH, Schofield AN, 1963.** Mechanical behaviour of an idealised 'wet' clay. *Proc. 2<sup>nd</sup> Euro. Conf. Soil Mech. and Foundation Eng.*, Wiesbaden, vol. 1: 47-54.
- Sanchez M, Gens A, do Nascimento Guimaraes L, Olivella S, 2005.** A double structure generalized plasticity model for expansive materials. *Int. Jnl. Numer. and Analyt. Meth. Geomechanics* **29**: 751-787.
- Seiphoori A, Ferrari A, Laloui L, 2014.** Water retention behaviour and microstructural evolution of MX-80 bentonite during wetting and drying cycles. *Geotechnique* **64** (9): 721-734.
- Tsiampousi A, Zdravkovic L, Potts DM, 2013.** A new Hvorslev surface for critical state type unsaturated and saturated constitutive models. *Computers and Geotechnics* **48**: 156-166.

## Appendix 1

Features table

Name of the constitutive law:		IC DSM	
Behaviour feature	YES	NO	Remarks
<b>Mechanical behaviour</b>			
Dependence of swelling strain on applied stress (at the same dry density)	x		
Dependence of swelling stress on dry density (at the same stress)	x		We have assumed that this is a typo and refers to "swelling strains" instead of "swelling stress".
Irreversibility of strains in wetting/drying cycles	x		
Dependence of swelling pressure on dry density	x	x	The swelling pressure predicted for the loose sample seems high. We need to investigate this further.
Stress path dependence from an unsaturated to a saturated state	x		
Stress path dependence from a saturated to an unsaturated state	x		
Double structure/porosity considered?	x		
Are temperature effects considered in the model?		x	Not in the present formulation.
Dependence of strains developed in a temperature cycle (increase/decrease) on OCR (or stress)		x	No temperature effects are considered.
<b>Hydraulic behaviour (retention curve)</b>			
Hysteresis	x		
Dependence on void ratio	x		
Double structure/porosity considered?		x	

# D3.1



## Quintessa's Internal Limit Model

### DELIVERABLE (D3.1)

### ANNEX F

Authors: Rebecca Newson, Kate Thatcher

Reporting period: 01/06/17 – 30/11/18

Date of issue of this report: **28/02/18**

Start date of project: **01/06/17**

Duration: 48 Months

This project receives funding from the Euratom research and training programme 2014-2018 under grant agreement No 745 942		
<b>Dissemination Level</b>		
<b>PU</b>	Public	
<b>RE</b>	Restricted to a group specified by the partners of the Beacon project	
<b>CO</b>	Confidential, only for partners of the Beacon project	

**REVIEW**

<b>Name</b>	<b>Internal/Project/External</b>	<b>Comments</b>

**DISTRIBUTION LIST**

<b>Name</b>	<b>Number of copies</b>	<b>Comments</b>
Athanasios Petridis (EC) Christophe Davies (EC)  Beacon partners		

# Content

<b>1</b>	<b>Introduction .....</b>	<b>4</b>
<b>2</b>	<b>Background .....</b>	<b>4</b>
<b>3</b>	<b>Basic hypothesis and scope .....</b>	<b>6</b>
<b>4</b>	<b>Mathematical description .....</b>	<b>7</b>
4.1	Theoretical framework .....	7
4.2	Equations .....	7
<b>5</b>	<b>Input parameters and their sources .....</b>	<b>10</b>
<b>6</b>	<b>Performance .....</b>	<b>10</b>
6.1	Oedometer Test Cases .....	11
6.1.1	Dependence of swelling strain on applied stress and on dry density .....	11
6.1.2	Irreversibility of strains in wetting/drying cycles .....	12
6.1.3	Behaviour during swelling stress test. Dependence of swelling pressure on dry density. ....	12
6.1.4	Stress path dependence from an unsaturated to a saturated state .....	13
6.1.5	Stress path dependence from a saturated to an unsaturated state .....	14
6.1.6	Dependence of strains developed in a temperature cycle on stress .....	15
6.2	SEALEX mock up experiment .....	17
6.2.1	Description of the Experiment .....	17
6.2.2	Model Description .....	18
6.2.3	Modelling Results .....	19
6.3	FEBEX in situ experiment .....	20
6.3.1	Description of the Experiment .....	20
6.3.2	Model Description .....	21
6.3.3	Modelling Results .....	22
<b>7</b>	<b>Conclusions .....</b>	<b>23</b>
	<b>References .....</b>	<b>25</b>

## 1 Introduction

The Internal Limit Model (ILM, Thatcher et al., 2016) was developed by Quintessa as part of the DECOVALEX-2015 project to model data from experiments on a 70/30 by mass mixture of MX-80 bentonite and sand used in the SEALEX experiments (Barnichon et al 2011). It was inspired by correlations in experimental data that relate stress, suction and failure to dry density and water content, making it possible to couple hydraulic and mechanical processes more explicitly than in the Barcelona Basic Model (BBM). The model can be parameterised using widely available data and aims to prioritise reproduction of general trends over exact details of observations. After successful application to the SEALEX experiments, the ILM was then used to model FEBEX bentonite as part of the FEBEX-DP project (Thatcher, 2017).

## 2 Background

Amongst the measurements that are regularly made of the properties of bentonite are three common data sets:

- The swelling pressure of the bentonite versus dry density;
- Suction versus water content;
- Void ratio versus vertical stress for loading and unloading (oedometer tests).

These three data sets were available for a 70/30 by mass MX-80 bentonite / sand mixture during the DECOVALEX-2015 project. Comparison of these three data sets showed that a curve of the form:

$$p = p_0 * \exp\left(\frac{-e}{\lambda}\right) \quad (1)$$

( $p$  - stress [MPa],  $e$  – void ratio [-]) can be fit to all three data sets, using the same values of parameters  $p_0$  and  $\lambda$  for each data set. For swelling pressure versus dry density data (Figure 2-1),  $p$  is swelling pressure and  $e$  is void ratio which is converted to dry density ( $\rho_{dry}$  [Mg/m<sup>3</sup>]) using the equation:

$$e = \frac{1 - \rho_{dry}/\rho_{grain}}{\rho_{dry}/\rho_{grain}} \quad (2)$$

where  $\rho_{grain}$  [Mg/m<sup>3</sup>] is the density of the solid grains.

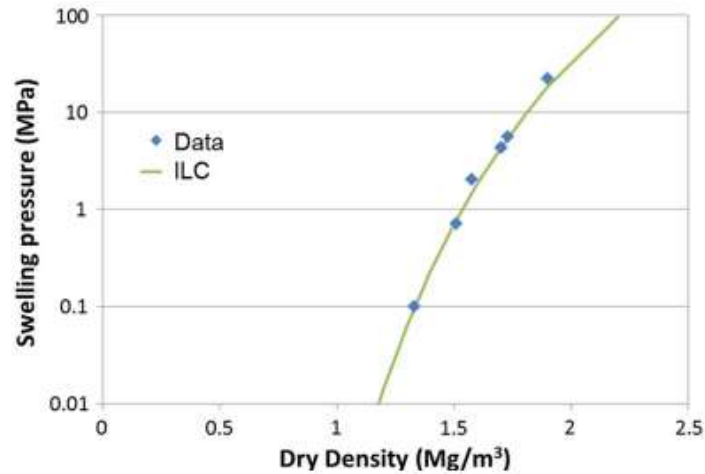


**Figure 2-1: Swelling pressure data for the final dry density of bentonite in a 70/30 bentonite/sand mixture (Wang et al. 2012) plotted against the Internal Limit Curve (Equation 1, parameterised to fit the swelling data).**

For suction versus water content data, the same equation can be applied, but now  $p$  is suction and water content is calculated from void ratio assuming that all pore space is filled with water (Figure 2-2).

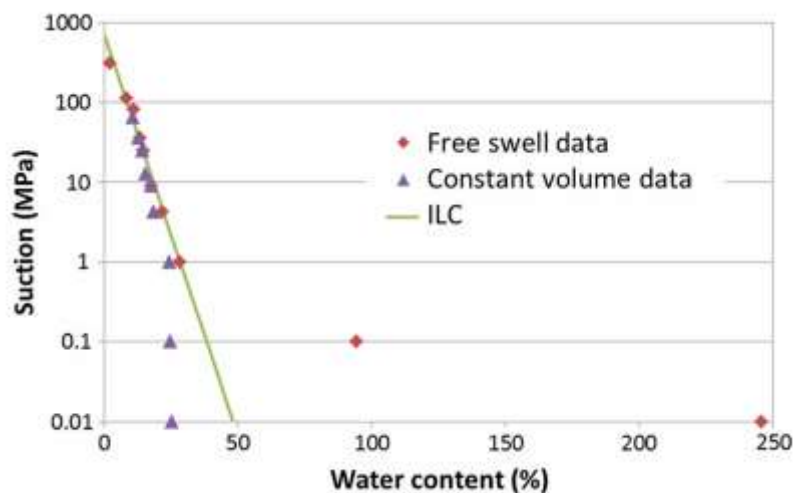


**Figure 2-2: Water retention data for free swelling and constant volume samples (Wang et al. 2013a) alongside the ILC curve modified to give saturated water content for a given dry density, but using the same parameters as Figure 2-1.**

Finally, the same equation can be plotted with data from oedometer tests, with  $p$  equal to vertical stress (Figure 2-3).

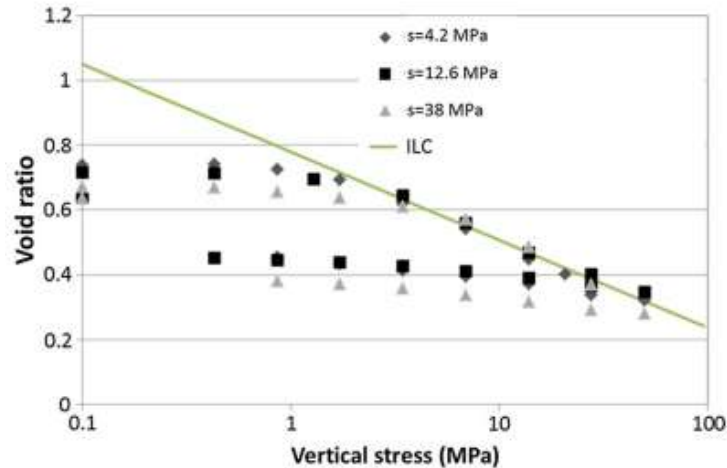


**Figure 2-3: Data from the oedometer tests at a constant initial dry density (Wang et al. 2013a) plotted with the ILC, using the same parameterisation for the ILC as in Figure 2-1 and Figure 2-2.**

In Figure 2-1, Figure 2-2 and Figure 2-3, the ILC line has the same parameter values for  $p_0$  and  $\lambda$ . For the swelling data (Figure 2-1), the curve fits the data well. For the water retention data (Figure 2-2), the curve fits free swell data at lower water contents well. The two data points at water contents > 50% show much higher suctions that the ILC curve would suggest and we hypothesise that this is due to a different mechanism causing suction at higher water contents. The ILC curve also fits the virgin consolidation part of the oedometer test well (Figure 2-3). These observations suggest that for a given dry density of bentonite there is a limiting stress that the sample can support, be that stress due to swelling, compaction or suction.

These observations, alongside a suggestion given by Dueck (2004) that suction ( $\Psi$ ) in bentonite is related to free swelling suction ( $\Psi^{\text{free}}$ ) and stress ( $\sigma$ ) by

$$\Psi = \Psi^{\text{free}} - \sigma, \quad (3)$$

form the background to the model.

### 3 Basic hypothesis and scope

The ILM is a fully coupled thermo-hydro-mechanical model, with plastic deformation based on the Modified Cam Clay (MCC) model. It uses the observations described in Section 2 to parameterise both the water retention curve and the virgin consolidation curve in the model. The model also uses the relationship between stress and suction suggested by Dueck (2004). Both of these relationships result in strong coupling between the hydraulic and mechanical behaviour.

The model is based on the concept of water content, rather than water saturation, as it has been shown by some that it is possible for water

saturations to become greater than 1 in strongly swelling clays (Jacinto et al., 2014), due to changes in water density as it is incorporated within the bentonite structure.

The modelling philosophy is to create a model with as few parameters as possible whilst maintaining the ability to fit the key features of experimental data. Where parameters are introduced, they should, as far as possible, be easily determined from available data.

## 4 Mathematical description

### 4.1 Theoretical framework

The ILM is based on Richards' equation for the hydraulics, momentum balance for the mechanics and the MCC model to represent plastic deformation. Thermal processes were later coupled to the model, which are based on the diffusion equation.

### 4.2 Equations

The mechanical problem is expressed in terms of conservation of momentum, which is otherwise referred to as the Navier equation (Howell et al. 2009):

$$\rho \frac{\partial^2 \bar{u}}{\partial t^2} = \nabla \bar{\sigma} - \rho \bar{g} \quad (4)$$

where  $\rho$  [kg/m<sup>3</sup>] is the solid density,  $\bar{u}$  [m] is the displacement vector,  $t$  [s] is time,  $\bar{\sigma}$  [MPa] is the stress tensor and  $\bar{g}$  [m/s<sup>2</sup>] is the vector of the acceleration due to gravity. The equation effectively ensures a local force balance for pseudo-steady state. The stress vector [ $\bar{\sigma}$ ] assumes a pseudo-steady state and is given by:

$$\bar{\sigma} = \bar{S}(\bar{\varepsilon} - \bar{\gamma}) - P \quad (5)$$

where  $\bar{S}$  [MPa] is the elastic stiffness matrix,  $\bar{\varepsilon}$  [-] is the strain vector,  $\bar{\gamma}$  [-] represents arbitrary additional strains, e.g. swelling strain and plastic strain, and  $P$  [MPa] is fluid pressure.

For swelling bentonite at a constant temperature, it is assumed that there are two additional sources of strain: swelling strains due to changes in water content of the bentonite and plastic strains due to plastic failure of the bentonite. Swelling strains are discussed later as they are coupled to the hydraulics.

Plastic strains are calculated according to the MCC model (Roscoe and Burland 1968). The plastic yield surface is given by:

$$\left[\frac{q}{M}\right]^2 + p'(p' - p_c) = 0 \quad (6)$$

whilst the virgin consolidation line in the MCC model, which describes how the yield surface changes with stress, has the equation:

$$v = \Gamma - \lambda \ln p' \quad (7)$$

where  $v$  [-] is the specific volume ( $v = 1 + e$ , where  $e$  [-] is the void ratio),  $p'$  [MPa] is the effective confining stress,  $q$  [MPa] is deviatoric stress,  $p_c$  [MPa] is the pre-consolidation pressure (which is a point on the virgin consolidation line) and  $M$ ,  $\Gamma$  and  $\lambda$  [-] are all constant parameters. The plastic strain is calculated as the derivative of the plastic yield surface.

The hydraulic problem is expressed in terms of conservation of mass:

$$\frac{\partial}{\partial t}(\theta \rho_f \varphi) = -\nabla \cdot (\rho_f u) + Q \quad (8)$$

where  $\theta$  [-] is porosity,  $\rho_f$  [kg/m<sup>3</sup>] is fluid density,  $\varphi$  [-] is saturation,  $u$  [m/s] is the fluid velocity and  $Q$  [kg/m<sup>3</sup>/s] is a source or sink.

A number of different formulations can be used to represent the fluid migration in the ILM, including full multiphase flow. In the models described below, Richards' equation has been chosen. Richards' equation can be used where gas flow is very fast compared to water flow, so that gas flow does not need to be solved for in the equations. It was found that model results using Richards' equation were as good as full multiphase flow, but since gas flow was not represented, fewer free parameters were required:

$$u = -\frac{k}{\mu} \nabla(P + \rho g z) \quad (9)$$

where  $u$  [m/s] is the fluid velocity tensor,  $k$  [m<sup>2</sup>] is the effective permeability tensor,  $\mu$  [Pa s] is the fluid viscosity and  $z$  (m) is height.

Water pressure ( $P_w$  [MPa]) is calculated by subtracting the net suction ( $\Psi$  [MPa]) from the gas pressure ( $P_g$  [MPa]):

$$P_w = P_g - \Psi. \quad (10)$$

Suction is determined from the Internal Limit Curve (ILC).

To calculate the net suction when the sample is not swelling freely, an approach modified from that suggested by Dueck (2004) (Equation 10) has been adopted. The net suction is the free swell suction minus stress, but

localised according to stress direction, following the argument that bentonite interlayers will be constrained in terms of their water content most significantly by the plate normal stress. This is calculated in three principal directions in the model as:

$$\Psi_{nn} = \Psi_{nn}^{free} - \sigma_{nn} \quad \text{for } n = i, j, k \quad (11)$$

where  $\sigma_{nn}$  is the stress component  $nn$ , with the total suction given by:

$$\Psi = \frac{1}{3}(\Psi_{ii} + \Psi_{jj} + \Psi_{kk}). \quad (12)$$

The water content in the three directions is constrained such that the net suction in each of the three directions is equal. The conceptual model behind considering water content and suction in three directions is that the bentonite grains are oriented in random directions such that a third of the grains are aligned to each principal direction.

Note that this suction model is a significant departure from the conventional Richards' model where suction is defined purely as a function of fluid saturation. The approach shown above allows stress to be coupled into the suction relationship directly, at the expense of always enforcing a strict constraint on volume conservation of the water. Not enforcing such a volume constraint (although local and global mass balance is retained at all times), as one might do for a conventional porous material, is justified on the basis of recent work (Jacinto et al. 2012) which suggests that when water is present as a crystalline phase in the bentonite inter-layers, the density of that water may depart significantly from the equivalent liquid water density due to the presence of charged ions in the bentonite, allowing water molecules to sit closely together. Hence water saturation could exceed unity in the models.

In the ILM, swelling strain is calculated based on the change in water content in the bentonite. Swelling strain is calculated in the three principal directions as follows:

$$\epsilon_{nn}^{swell} = \frac{\frac{a}{3}(w_{nn} - w_0)m_s}{\rho_w V_{comp}} \quad (13)$$

where  $w_0$  is the initial water content [kg/kg],  $w_{nn}$  is the water content in the direction  $nn$ ,  $m_s$  is the mass of solids [kg],  $\rho_w$  is the density of water [kg/m<sup>3</sup>],  $V_{comp}$  is the compartmental volume [m<sup>3</sup>] and  $a$  is a swelling efficiency term which reflects that not all additional water will cause a volume increase, some will just fill void space in the sample. The calculation is considered in three principal directions following the conceptual model that bentonite grains are aligned principally in one of the three directions. The amount of stress in the three principal directions is different, so the free suction, and

therefore water content, will be different in the three directions; however, the net suction will be the same.

## 5 Input parameters and their sources

To parameterise the Internal Limit Curve (ILC), one of the following three sets of data are required:

1. Water retention curve (suction vs water content)
2. Infiltration test (swelling pressure vs dry density)
3. Oedometer test (void ratio vs vertical stress)

These ILM parameters are material properties for a given composition of bentonite. These parameters should not need to be calibrated to individual experiments.

The remaining hydraulic parameters are standard parameters (e.g. intrinsic permeability, relative permeability) that can be estimated from previous studies or calibration to simple experiments e.g. infiltration tests.

The remaining mechanical parameters are standard parameters relating to elasticity and the MCC. These parameters can be taken from previous work or calibrated to simple experiments e.g. oedometer tests.

## 6 Performance

The Internal Limit Model was originally developed during modelling of the SEALEX experiments, to explain some of the correlations that were seen in the data (Thatcher et al., 2016). It was then applied to the FEBEX experiments, to test its validity on an alternative FEBEX bentonite (Thatcher, 2017). A summary of this modelling work and the performance of the ILM in each case is given in Sections 6.2 and 6.3 respectively.

To demonstrate some specific features of the ILM, several simple oedometer tests were developed and qualitative results are presented in Section 6.1. The features to be demonstrated are:

1. Dependence of swelling strain on applied stress and on dry density
2. Irreversibility of strains in wetting/drying cycles
3. Behaviour during swelling stress test and dependence of swelling pressure on dry density
4. Stress path dependence from an unsaturated to a saturated state
5. Stress path dependence from a saturated to an unsaturated state
6. Dependence of strains developed in a temperature cycle on stress

All the models described in this section were implemented in the multi-physics finite volume/mixed element code QPAC (Maul 2013; Bond et al. 2013; Benbow et al. 2014).

## 6.1 Oedometer Test Cases

For the following tests of the model features, a simple oedometer model has been built in QPAC, with only mechanical effects considered initially. The model geometry consists of a cylinder of bentonite with radius 0.5 m and height 5 m. The model is discretised to have two vertical compartments, with no radial or angular discretisation, as the numerical model used cannot calculate strains for a single-compartment model. Water flows are not explicitly modelled; water content is instead calculated from the suction of the whole sample, which is specified as an input. For tests 1-5, the model is isothermal at a temperature of 20°C.

The material properties used are for a mixture of MX-80 bentonite and quartz sand, taken from the SEALEX experiment (see Section 6.2).

### 6.1.1 Dependence of swelling strain on applied stress and on dry density

To test whether the swelling strain generated in the model is dependent on applied stress and on dry density, the oedometer test was run as a swelling test. The bentonite is radially confined but can swell vertically upwards. Friction between the bentonite and the container is neglected for this simple test. A constant vertical stress is applied on the top boundary. To represent the saturation of the bentonite, the suction is linearly decreased from 15 MPa to 0 MPa over 1 year.

The model was run using specified vertical stresses of 0.1, 1, 5 and 10 MPa. It was also repeated using initial dry bentonite densities of 1550, 1600, 1650 and 1700 kg/m<sup>3</sup>. The resulting final (axial) strain was output for each case.

A dependency of final strain on dry density and vertical stress can be seen (Figure 6-1).

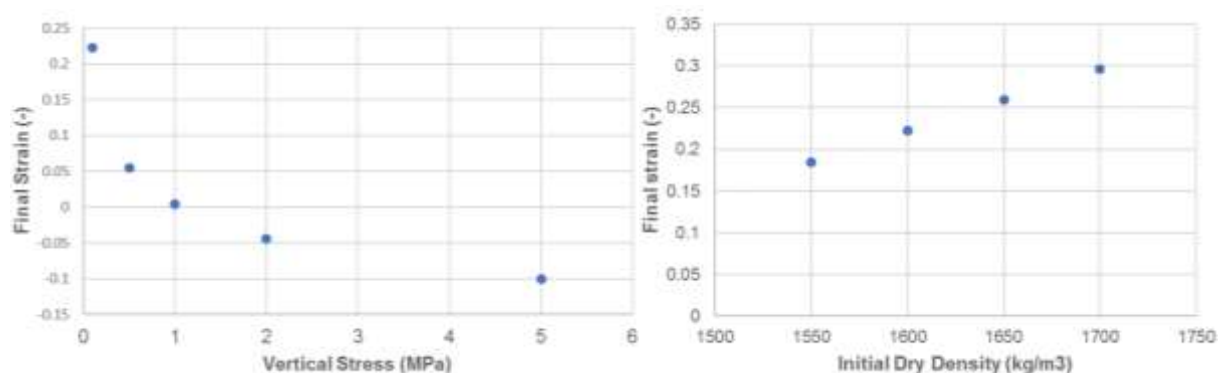


**Figure 6-1. QPAC model output illustrating strain dependency on a) applied vertical stress and b) initial dry density.**

**6.1.2 Irreversibility of strains in wetting/drying cycles**

To test the irreversibility of strains, the model was initially run in the same way as before, under a constant vertical stress of 0.1 MPa whilst the suction is decreased from 15 MPa to 0 MPa. However, after 1 year, the suction was linearly increased back to 15 MPa. The strain path was output during both the saturation and de-saturation phases (Figure 6-2). The original dimension of the sample was not recovered; there had been irreversible strains produced, due to plastic deformation of the bentonite.

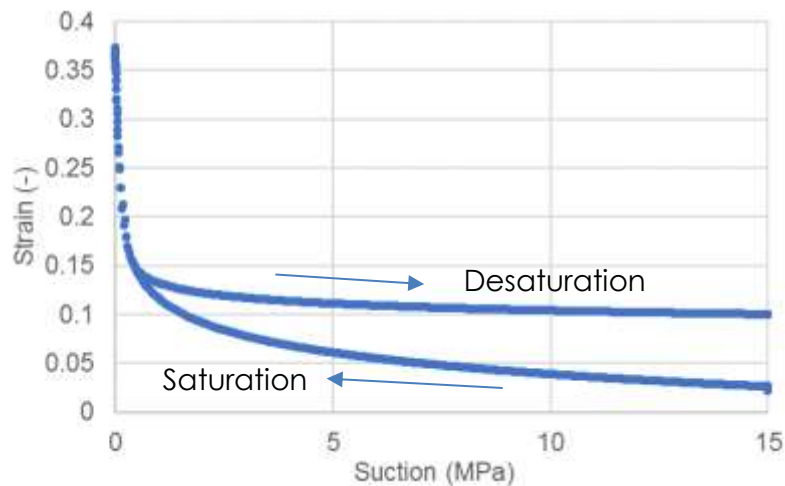


**Figure 6-2. QPAC model output illustrating irreversibility of strain during saturation/de-saturation.**

**6.1.3 Behaviour during swelling stress test. Dependence of swelling pressure on dry density.**

The model was adapted to be a swelling stress test at constant volume. This was done by changing the boundary condition at the top of the bentonite from a specified vertical stress to a zero vertical displacement constraint. As the suction is reduced from 50 MPa to 0 MPa, the stress in the sample increases and this resultant build-up of swelling pressure is output (Figure 6-3).

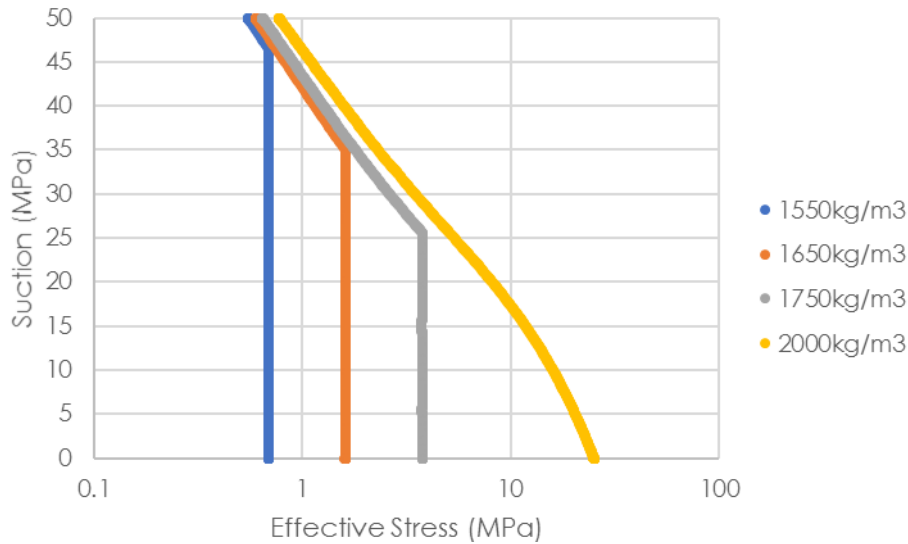


**Figure 6-3. QPAC model output illustrating suction-stress paths at different bentonite dry densities.**

As the suction is reduced, the bentonite hits the plastic failure limit and begins to deform plastically with no further increase in stress. This limit is dependent on dry density.

The test was repeated for bentonite dry densities of 1550, 1600, 1650, 1700 and 1750 kg/m<sup>3</sup>. An exponential dependence of swelling pressure on dry density can clearly be seen (Figure 6-4). This corresponds to the Internal Limit Curve used to parameterise the model.

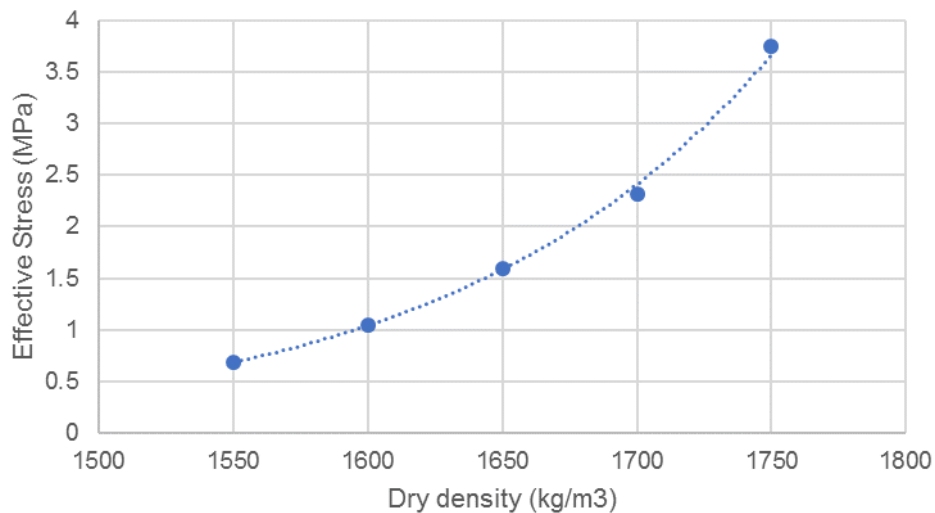


**Figure 6-4. QPAC model output showing swelling pressure dependence on dry density, with an exponential trend line fitted through the points.**

#### 6.1.4 Stress path dependence from an unsaturated to a saturated state

The stress path dependence of the properties of saturated bentonite was tested by comparing bentonite properties resulting from three different saturation stress paths with the same initial and final stress/suction:

- a) Linear reduction of suction from 50 MPa to 0 MPa at a fixed vertical stress of 0.5 MPa, followed by a linear increase of stress to 5 MPa.
- b) Linear increase of vertical stress from 0.5 MPa to 5 MPa under a constant suction of 50 MPa, followed by a reduction of suction to 0 MPa.
- c) Swelling pressure test under confined conditions during which suction is reduced from 50 MPa to 0 MPa (and stress freely increases), followed by an increase in stress to 5 MPa.

The resulting stress paths are shown in Figure 6-5. Stress Path C shows that the bentonite hits the plastic failure limit at 30 MPa.

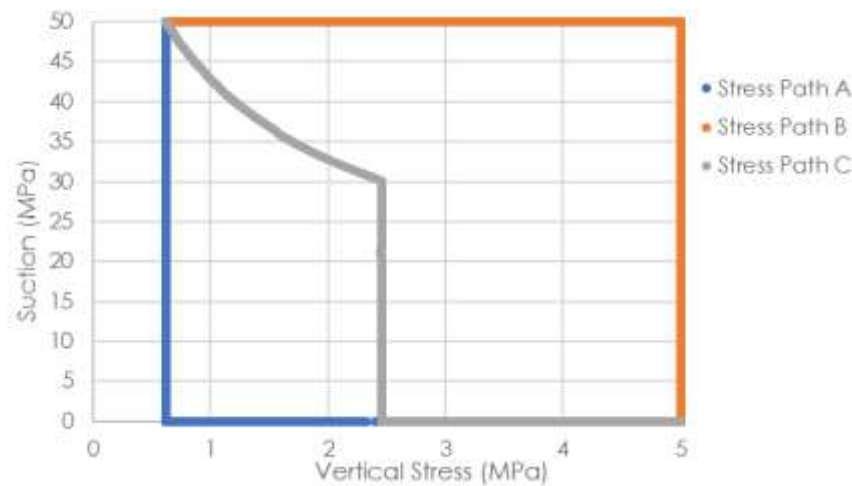


**Figure 6-5. QPAC model output showing vertical stress against suction for three different models.**

The final strain and water content were compared for each stress path and were found to be very different (Table 6-1). Hence, there is a stress path dependency of the bentonite properties.

**Table 6-1**

Parameter	Stress path a	Stress path b	Stress path c
Final water content (-)	0.295	0.198	0.211
Final vertical strain (-)	-0.0804	0.046	0.0382

### 6.1.5 Stress path dependence from a saturated to an unsaturated state

This test is similar to the previous test, except the bentonite moves from a saturated to an unsaturated state (suction decreases). Two different stress paths were compared (see Figure 6-6):

- a) Increase of stress from 0.1 MPa to 5 MPa at zero suction, followed by an increase in suction to 15 MPa.
- b) Increase of suction from 0 MPa to 15 MPa, followed by an increase of stress from 0.1 MPa to 5 MPa at constant suction.

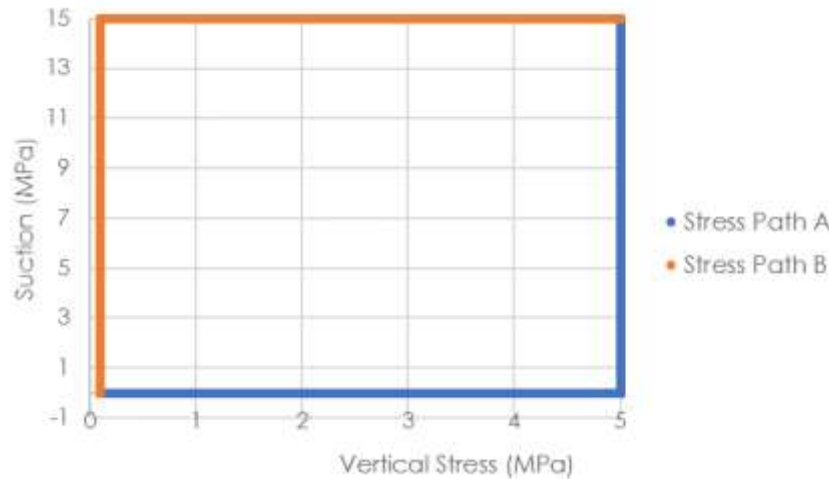


**Figure 6-6. QPAC model output showing vertical stress against suction for two different models.**

The final strain and water content were compared for each stress path and were found to be different. Hence, there is stress path dependency of the bentonite properties.

**Table 6-2**

Parameter	Stress path a	Stress path b
Final water content (-)	0.304	0.15
Final strain (-)	-0.107	-0.0382

### 6.1.6 Dependence of strains developed in a temperature cycle on stress

In this test, thermally-induced strains were investigated. Thermal expansion was added to the mechanical model (with coefficients of thermal expansion taken from Tang, 2008). Temperature changes were specified directly, so a fully-coupled TM model was not required.

For the first case, the sample was saturated (with 0 suction) and at a constant vertical stress of 0.1 MPa. The temperature was increased from 20 C to 100 C after one year and then decreased back to 20 C. The net strain resulting from this temperature cycle was output. There is some permanent plastic deformation of the bentonite – it expands due to heating but upon cooling, its volume reduces to less than its original size (see Figure 6-7).

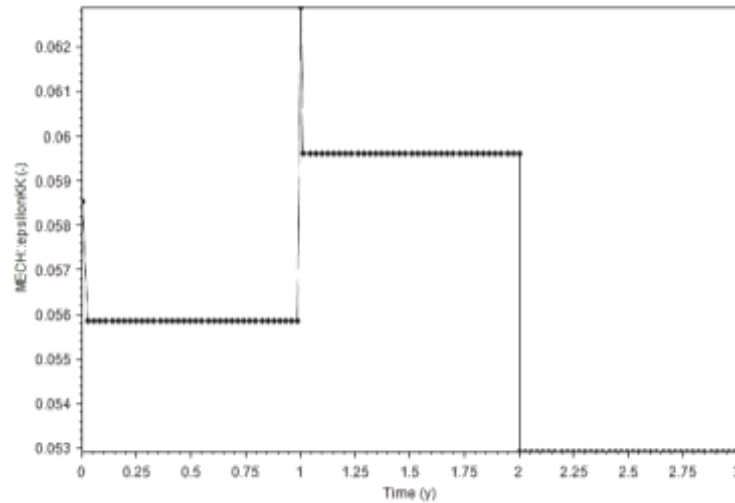


**Figure 6-7. QPAC model output showing strain resulting from a temperature cycle against time. The temperature is 20°C from 0-1 y and 2-3 y, and 100°C from 1-2 y. Plastic spikes in the strain are visible at 0 years and 1 year.**

The model was run with different fixed applied stresses between 0.1 and 5 MPa.

This stress dependency of the thermally-induced strain was then investigated for an unsaturated sample, with a suction of 10 MPa.

In both the saturated and un-saturated samples, a clear dependency of thermally-induced strain on applied stress can be seen.

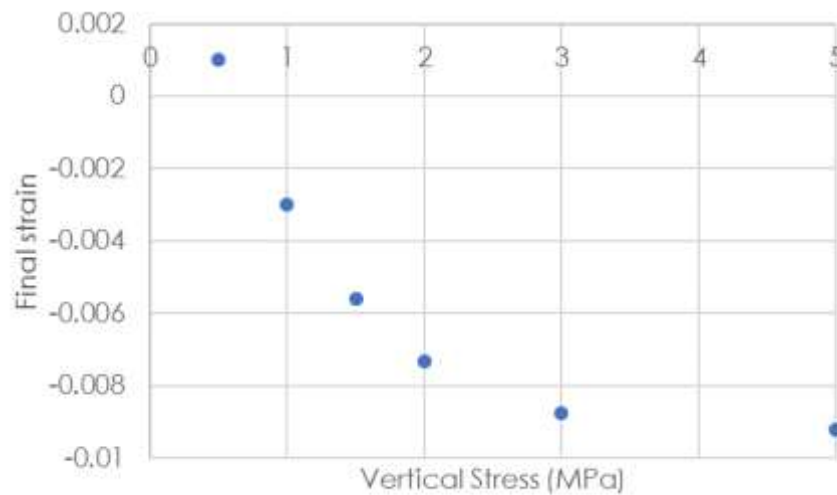


**Figure 6-8. QPAC model output showing strain resulting from a temperature cycle against applied vertical stress, for a saturated sample.**

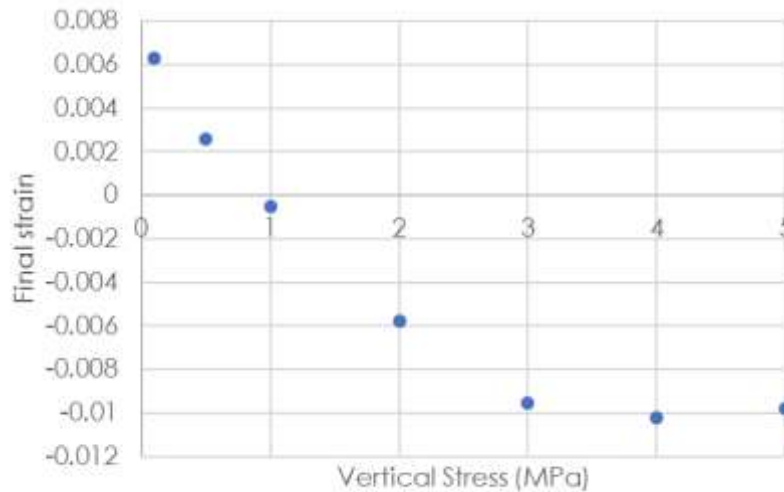


**Figure 6-9. QPAC model output showing strain resulting from a temperature cycle against applied vertical stress, for an unsaturated sample with suction of 10 MPa.**

## 6.2 SEALEX mock up experiment

### 6.2.1 Description of the Experiment

The SEALEX experiments (Barnichon et al. 2011) were run by the Institut de Radioprotection et de Sûreté Nucléaire (IRSN) in France at the Tournemire URL. These experiments were designed to improve understanding of the long-term performance and resaturation of bentonite-based seals. A 1/10<sup>th</sup> scale mock-up of the in situ experiments was carried out in the laboratory to reproduce the behaviour of the 70/30 MX-80 and quartz sand mixture, without the added complication of understanding the interaction with the argillite (Wang et al. 2013b).

The material parameters used for the MX-80/sand mixture are given in Table 6-3.

**Table 6-3 Parameters used in the test oedometer cases and SEALEX models.**

ILM parameters		
$\alpha$	$1.3 \times 10^{-6}$ (MPa)	Fitted to Wang et al. (2012)
$\beta$	8.5 (m <sup>3</sup> /Mg)	Fitted to Wang et al. (2012)
Hydraulic parameters		
$k_0$	$0.75 \times 10^{-20}$ (m <sup>2</sup> )	Calibrated to infiltration test
Mechanical parameters		
Poisson's ratio	0.27 (-)	Assumed
$k_0$	50 (MPa)	Calibrated to SEALEX lab data
$\kappa_1$	30 (-)	Calibrated to SEALEX lab data
$M$	1.25 (-)	Calibrated to SEALEX lab data
$\alpha$	0.5 (-)	Calibrated to SEALEX lab data

The relative permeability of the material is taken to be  $k_{rel} = \varphi^4$  where  $\varphi$  is its

saturation. Intrinsic permeability is dependent on a function of dry density  $D(\rho_{dry})$  calibrated against the infiltration test:

$$k = k_0 10^{D(\rho_{dry})} \quad (14)$$

The seal in this experiment is 120 mm long with a diameter of 55.5 mm and the hydration cell has a radius of 60 mm so that there is a gap (“technological void”) between the seal and the cell. The mock-up experiment is set up in a vertical cell, and the gap is uniform around the sample (see Figure 6-10).

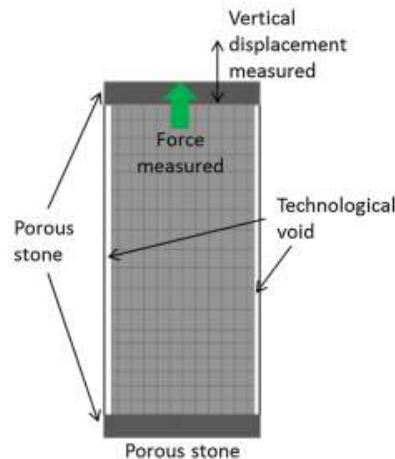


**Figure 6-10. Schematic of the mock-up test showing the model grid and the technological void (Thatcher, 2016).**

The mock-up experiment proceeded in three phases:

1. Phase 1, Initial hydration: vertical deformation was prevented and the sample was hydrated by injection of water into a porous plate at the base of the sample. During this phase, the build-up of vertical pressure was monitored. This phase continued for 1 year.
2. Phase 2, Vertical swelling: the confining pressure was released and the sample was allowed to swell in the vertical direction. Initially hydration only occurred from the base of the sample, but once 2.8% vertical strain was reached, the sample was also hydrated from the top until 20% strain was reached.
3. Phase 3, Confinement: vertical deformation was again prevented and the build-up of vertical swelling pressure recorded. Hydration continued at both the top and bottom of the cell during this phase.

The data available from the mock-up experiment include the mass of water injected into the experiment, the change in vertical stress with time, and the vertical displacement during Phase 2.

### 6.2.2 Model Description

An axially symmetric cylindrical model was used to represent the geometry of

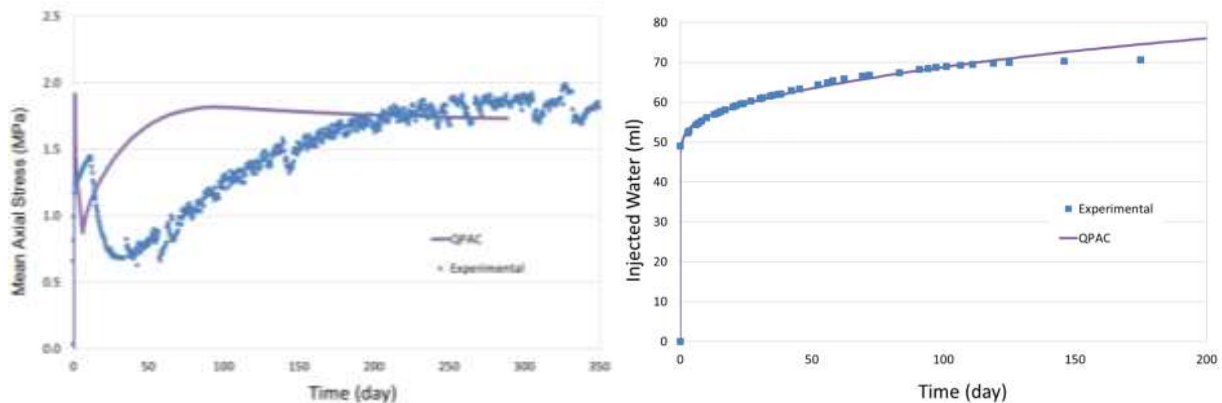
the mock-up experiment.

The “technological void” that was present at the start of the experiment has been represented in the model by the boundary conditions imposed on the radial surface of the model. The technological void is assumed to fill with water at the start of the experiment and then the bentonite swells into the void, closing the gap. The mechanical boundary is a strain dependent stress boundary, which becomes very stiff when the radial displacement of the sample is 2.25 mm, i.e. large enough to fill the technological void. A constant water pressure boundary at 0.1 MPa allows water to enter the sample here, but the boundary is turned to no-flow once the volume of water that has flowed in through this boundary reaches the volume of the technological void.

The bottom boundary has zero displacement and a constant water pressure of 0.1 MPa. The top boundary has a time and strain dependent stress to mimic periods of confinement and free swell. In Phase 1, the boundary is made very stiff so that a small displacement creates a large stress, effectively preventing any displacement. In Phases 2 and 3, the sample is allowed to swell to 20% strain, but thereafter, a small increase in displacement caused a large stress on the boundary thereby preventing further swelling. The hydraulic boundary condition at the top boundary is also strain dependent, with no flow at strains less than 2.8% and then a constant water pressure of 0.1 MPa at higher strains.

### 6.2.3 Modelling Results

The model captures the main features of the data well including the initial rapid increase in stress followed by plastic collapse seen in the data, although the timings are approximately a factor of 2 too fast in the model (Figure 6-11a). The peak swelling pressure is also captured in the model, but by 100 days, the swelling pressure in the model is falling very slightly, while in the experiment the swelling pressure continues to rise slightly. The drop in swelling pressure in the model is due to the bentonite homogenising; this may be starting to happen in the data, at around 300 days, but a longer time series would be needed to confirm this behaviour.



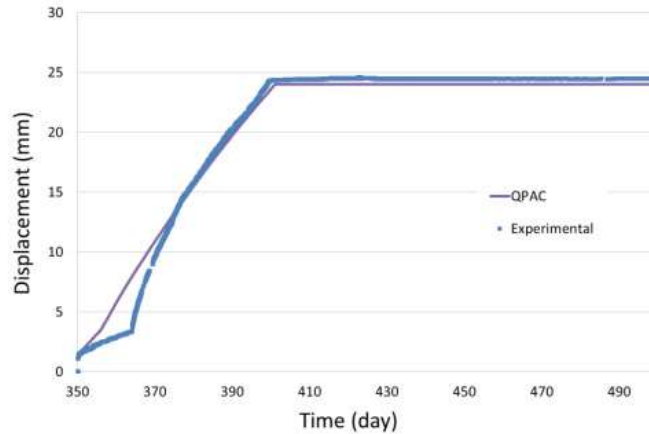


**Figure 6-11. Comparison between data and model for the 1/10th SEALEX mock-up test: a) axial stress (swelling pressure) in Phase 1; b) mass of water injected during Phase 1; c) axial displacement measured in Phase 2 and 3.**

The model fits the injection data well, but after 100 days, the rate of injection slows down in the data but not in the model (Figure 6-11b). This could indicate that the model doesn't capture water flow well at higher water content.

A common theme throughout the modelling was that it was difficult to get the correct swelling pressure in both Phase 1 and Phase 3. There was a tendency to over-predict swelling in Phase 1 and under-predict in Phase 3, and improved calibration in one phase resulted in a less good calibration in the other phase.

## 6.3 FEBEX in situ experiment

### 6.3.1 Description of the Experiment

The FEBEX experiment at the Grimsel Test Site in Switzerland was an in situ full-scale Engineered Barrier System (EBS) test performed under natural re-saturation conditions. The FEBEX experiment was based on the Spanish reference concept for spent fuel disposal. In the experiment, two simulant waste containers containing heating elements were emplaced in a tunnel in granitic host rock and were surrounded by FEBEX bentonite. The first heater was removed from the experiment after 5 years of heating, and the second heater was removed in 2015 after 18 years of heating (see Figure 6-12). In the FEBEX-DP project, dismantling of the FEBEX experiment was completed.

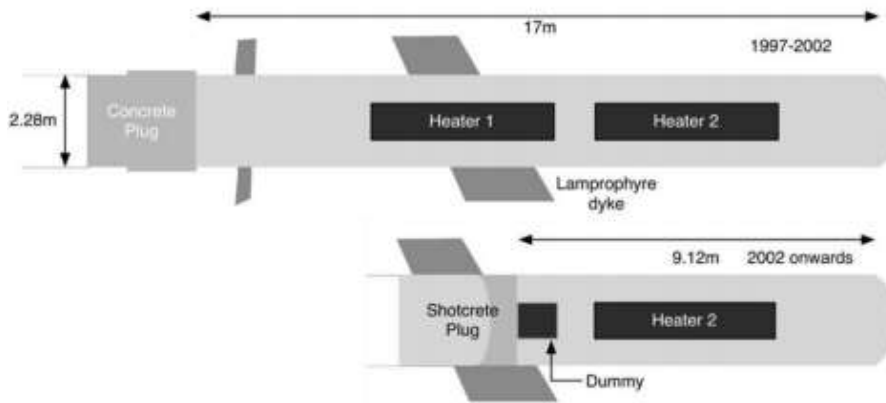


Figure 6-12. Schematic diagram of the FEBEX in situ experiment, before and after the removal of Heater 1 (Lanyon and Gaus, 2013).

### 6.3.2 Model Description

To test whether the Internal Limit Model was transferable and could be successfully applied to an alternative bentonite, the ILC was re-calibrated for FEBEX bentonite across data from the in situ test and all supporting laboratory experiments (Figure 6-13). Only the permeability had to be calibrated separately for each experiment.

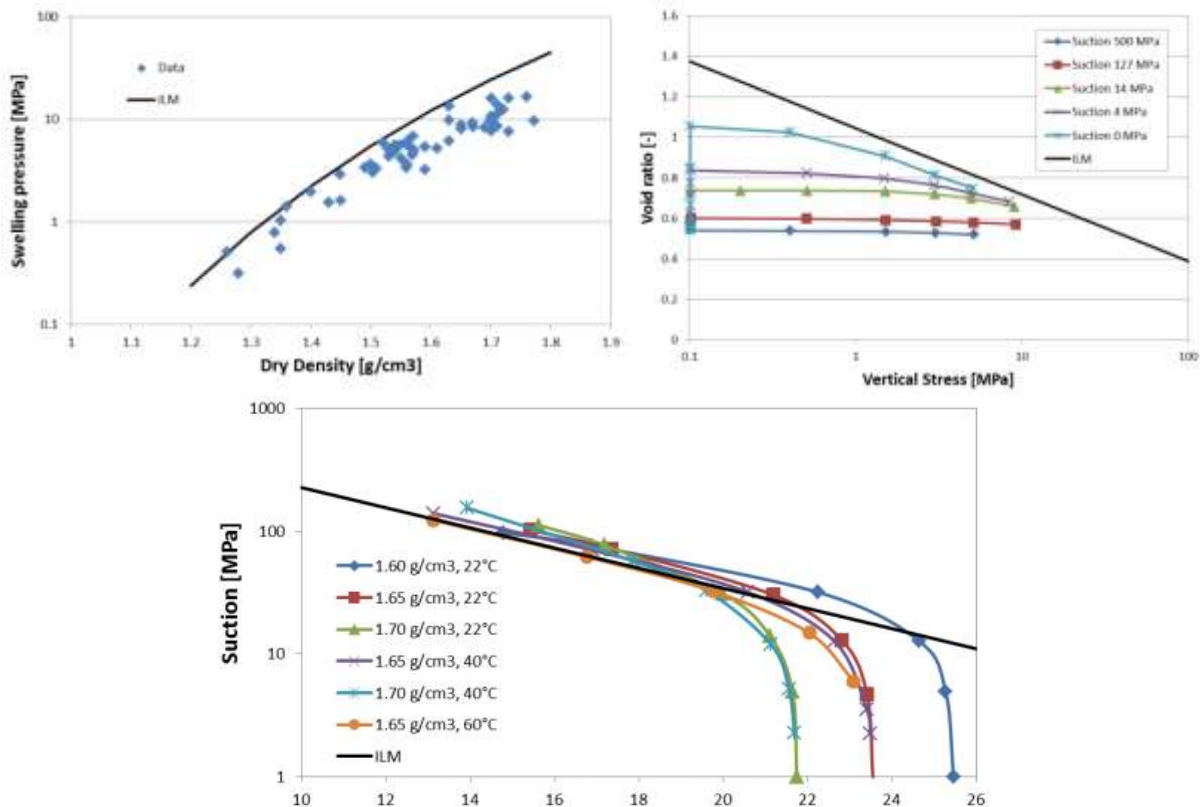


Figure 6-13. Graphs used to parameterise the ILC for FEBEX bentonite (Lloret et al., 2005): a) swelling data; b) oedometer test data; c) confined water retention data at different dry densities and temperatures.

For the FEBEX bentonite, suction is higher than would be predicted based on the swelling and oedometer data using the relationships derived for MX-80

bentonite. This could be due to the differing chemistry of the MX-80 bentonite and the FEBEX bentonite which could affect how water is distributed between interlayers and macropores. Alternatively, the suction in the SEALEX experiments could have been affected by mixing bentonite with sand. Nevertheless, there are clearly relationships between suction, swelling and compressive stress in the FEBEX bentonite and the ILM curve has the same general form as the data so the approach was used to look at experiments using FEBEX bentonite.

Thermal effects were also considered in the FEBEX modelling, so a fully-coupled THM model based on the ILM was used, with thermal processes based on the diffusion equation. Water retention curves at different temperatures were used to determine a thermal dependency of the ILM parameters.

The model was first tested on laboratory experiments performed throughout the FEBEX programme, including suction controlled oedometer tests and infiltration tests with a thermal gradient. The model was then applied to the FEBEX in situ experiment. The material parameters used are given in Table 6-4.

**Table 6-4 Parameters used in the FEBEX model.**

ILM parameters		
$\rho_0$	$-7.895 \text{ (MPa/}^\circ\text{C)T} + 1674 \text{ (MPa)}$	Fitted to FEBEX lab data
$\lambda$	-7	Fitted to FEBEX lab data
Thermal parameters		
$c_p^b$ (bentonite heat capacity)	1100 (J/kg/K)	Bond and Watson (2008)
$c_p^w$ (heat capacity of water)	4182 (J/kg/K)	Bond and Watson (2008)
Hydraulic parameters		
$k_0$	$2.5 \times 10^{-21} \text{ (m}^2\text{)}$	Calibrated to in situ experiment
Mechanical parameters		
Poisson's ratio	0.27 (-)	Assumed
$k_0$	100 (MPa)	Calibrated to in situ experiment
$\kappa_1$	30 (-)	Thatcher et al. (2016)
$M$	1.25 (-)	Thatcher et al. (2016)
$\alpha$	0.5 (-)	Thatcher et al. (2016)

### 6.3.3 Modelling Results

Overall, the ILM behaved well (Figure 6-14). Some consistent disagreements between the model and experimental data were noted. Several cases showed the model over-predicting swelling pressure and under-predicting volume of swelling. Two possible reasons for these observations are; that the ILM curves require an alternative calibration and the swelling model needs further refinement.

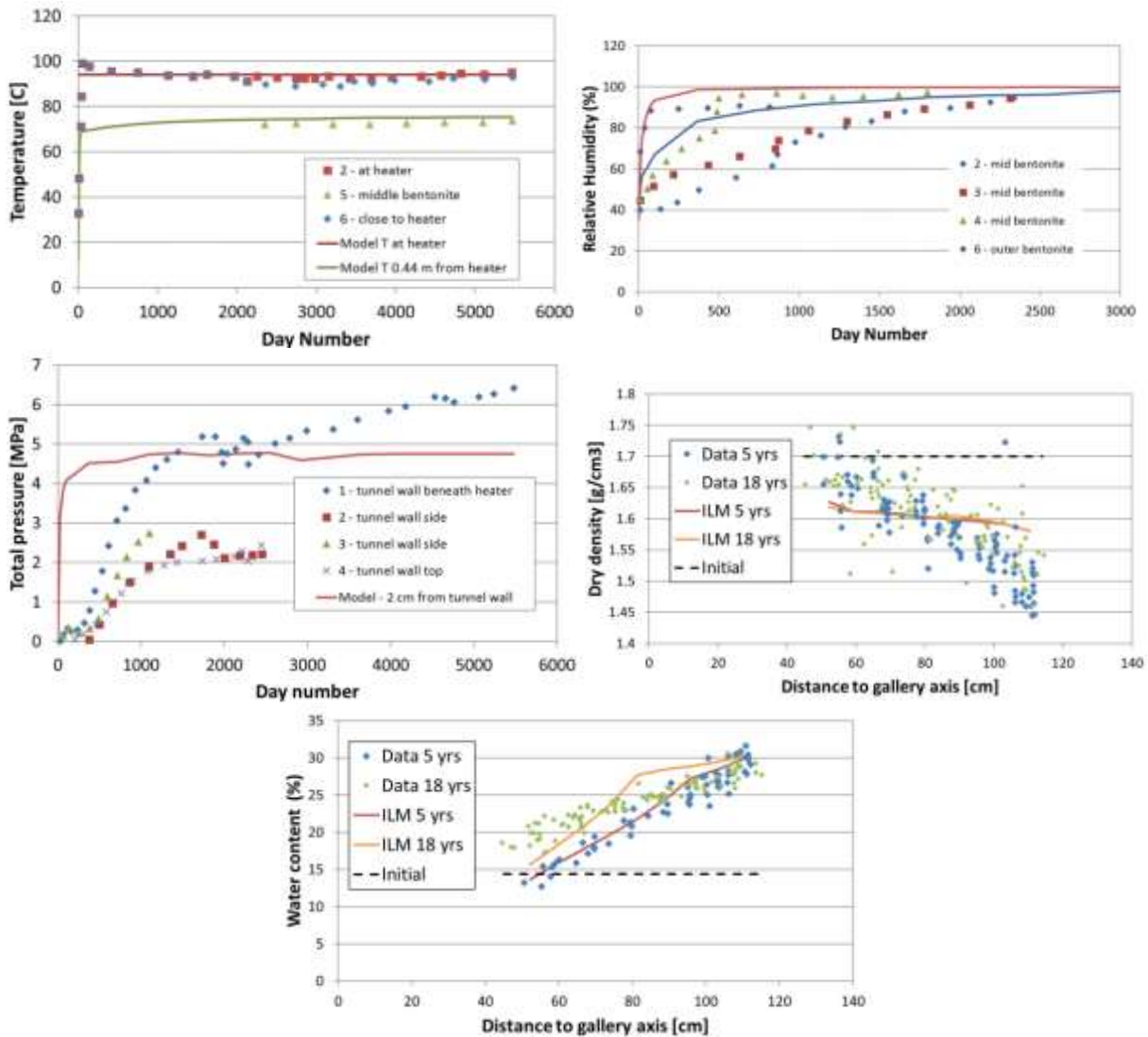


**Figure 6-14. Comparison between data and model for the FEBEX in situ test (Lanyon and Gaus, 2013): a) temperature; b) relative humidity; c) pressure in the rock wall; d) dry density; e) water content at the central section of Heater 1.**

With minimal calibration, the ILM that was set up for an MX80 bentonite and sand mixture could be applied to FEBEX bentonite in a suite of laboratory and field scale experiments and produce results that broadly reproduced the data. With some additional work, the ILM was able to produce a better fit to the experimental data. The major update to the ILM involved removing equivalent body forces when the geometry of the system involves radial expansion. This is an interesting concept because it implies that bentonite shows very little classical elastic behaviour which could lead to alternative conceptual models for representing bentonite.

## 7 Conclusions

The Internal Limit Model is a proposed hydro-mechanical model of bentonite, based on the observation that there appears to be a limiting stress that a

sample of bentonite can be under, whether that stress is caused by swelling, compaction or suction. This observation enables linking of the hydraulic and mechanical models through a single equation called the Internal Limit Curve.

The ILM has been successfully used to represent a range of experiments conducted under the SEALEX and FEBEX experimental programmes. The approach to modelling the experiments was to find a single parameter set that could be used to model each bentonite and this was achieved in most cases with good results. With minimal calibration, the ILM has been used to successfully model coupled THM behaviour of bentonite (for example in the in situ FEBEX experiment), although chemical behaviour is not considered in the model.

Whilst the model generally performs well, there is scope for improvement. The hydraulic properties of the bentonite when the water content is high would merit further work, to improve the time-dependent behaviour of the model, and some further work on swelling could improve the SEALEX mock-up test results in Phases 1 and 3. The SEALEX experiments did not contain data on the spatial distribution of properties or radial/triaxial swelling so further work could be undertaken to verify the behaviour of the ILM in these cases.

In addition, the ILM is a single-porosity model which is effective for compacted blocks of bentonite but its applicability to other forms of bentonite such as pellets needs to be investigated.

The ILM was developed specifically for the MX-80/sand mixture used in the SEALEX experiments but was found to be applicable to FEBEX bentonite. The model should be applicable more generally to a range of bentonite types and mixtures; further work is required to confirm that this is the case.

## References

- Barnichon J-D, Dick P, Bauer C, 2011.** The SEALEX in situ experiments: performance tests of repository seals. In: Zhou Y, Qian Q (eds) Harmonising rock engineering and the environment. Taylor & Francis, London, pp 1391-1394. ISBN 978-0-415-80444-8
- Benbow S J, Rivett M O, Chittenden N, Herbert A W, Watson S, Williams S J, Norris S, 2014.** Potential migration of buoyant LNAPL from Intermediate Level Waste (ILW) emplaced in a geological disposal facility (GDF) for UK radioactive waste. J Contam Hydrol 167:1-22
- Bond A, Thatcher K, Chittenden N, McDermott C, Fraser-Harris A, 2015.** RWM Coupled Processes Project: Third Annual Report for RWM Participation in DECOVALEX-2015 Tasks A and C1. RWM report RWMD/03/020.
- Bond A, Millard A, Nakama S, Zhang C, Garitte B, 2013.** Approaches for representing hydromechanical coupling between large engineered voids and argillaceous porous media at ventilation experiment, Mont Terri. J Rock Mech Geotech Eng 5(2):85-96
- Bond A, Watson C, 2008.** The use of QPAC-EBS for Project THERESA Benchmarking Studies. Quintessa report number QRS-3009A-1, v3.0.
- Dueck A, 2004.** Hydro-mechanical properties of a water unsaturated sodium bentonite. Ph.D thesis, Lund University.
- Howell P, Kozyreff G, Ockenden J, 2009.** Applied Solid Mechanics. Cambridge University Press, Cambridge.
- Jacinto A C, Villar M, Ledesma A, 2012.** Influence of water density on the water retention curve of expansive clays. Géotechnique 62(8):657-667
- Lanyon G W, Gaus I, 2013.** Main outcomes and review of the FEBEX In Situ test (GTS) and Mock-up after 15 years of operation. Nagra report NAB 13-96.
- Lloret A, Romero E, Villar M V, 2005.** FEBEX II Project Final report on thermo-hydro-mechanical laboratory tests. ENRESA report ISSN: 1134-380X.
- Maul P, 2013.** QPAC: Quintessa's general-purpose modelling software. Quintessa report QRS-QPAC-11. [www.quintessa.org](http://www.quintessa.org)
- Roscoe K H, Burland J B, 1968.** On the generalised stress-strain behaviour of 'wet clay'. In: Heyman J, Leckie F A (eds) Engineering plasticity. Cambridge University Press, Cambridge, pp 535-609.
- Tang A, Cui Y-J, Barnel N, 2008.** Thermo-mechanical behaviour of a compacted swelling clay. ENPC/CERMES.
- Thatcher K E, Bond A E, Robinson P, McDermott C, Fraser Harris A P, Norris S, 2016.** A new hydro-mechanical model for bentonite resaturation applied to the SEALEX experiments. Environ Earth Sci 75:1-17. doi:10.1007/s12665-016-5741-z
- Thatcher K, 2017.** FEBEX-DP: THM modelling. Quintessa report to RWM QRS-1713A-R2.
- Wang Q, Tang A M, Cui Y-J, Delage P, Gatmiri B, 2012.** Experimental study of the swelling behaviour of bentonite/claystone mixture. Eng Geol 124:59-66. doi:10.1016/j.enggeo.2011.10.003

**Wang Q, Tang A M, Cui Y-J, Delage P, Barnichon J-D, Ye W-M, 2013a.** The effects of technological voids on the hydro-mechanical behaviour of compacted bentonite-sand mixture. *Soils Found* 53:232-245. doi:10.1016/j.enggeo.2013.05.2009

**Wang Q, Tang A M, Cui Y-J, Barnichon J-D, Ye W-M, 2013b.** A comparative study on the hydro-mechanical behaviour of compacted bentonite/sand plug based on laboratory and field infiltration tests. *Eng Geol* 162:79-87. doi:10.1016/j.enggeo.2013.05.009

Table 1. Features Table

Name of the constitutive law: Internal Limit Model (ILM)			
Behaviour feature	YES	NO	Remarks
<b>Mechanical behaviour</b>			
Dependence of swelling strain on applied stress (at the same dry density) (Figure1)	✓		
Dependence of swelling stress on dry density (at the same stress) (Figure 1)	✓		
Irreversibility of strains in wetting/drying cycles (Figure 2)	✓		
Dependence of swelling pressure on dry density (Figure 4)	✓		
Stress path dependence from an unsaturated to a saturated state (Figure 5)	✓		
Stress path dependence from a saturated to an unsaturated state (Figure 6)	✓		
Double structure/porosity considered?		X	
Are temperature effects considered in the model?	✓		
Dependence of strains developed in a temperature cycle (increase/decrease) on OCR (or stress) (Figure 7)	✓		
<b>Hydraulic behaviour (retention curve)</b>			
Hysteresis		X	
Dependence on void ratio	✓		
Double structure/porosity considered?		X	

# D3.1



## THcM model status at VTT

### DELIVERABLE (D3.1)

## ANNEX G

Authors:  
Heidar Gharbieh  
Veli-Matti Pulkkanen  
VTT Technical Research Centre of Finland Ltd

Reporting period: 01/06/17 – 30/11/18

Date of issue of this report: **28/02/18**

Start date of project: **01/06/17**

Duration: 48 Months

This project receives funding from the Euratom research and training programme 2014-2018 under grant agreement No 745 942		
<b>Dissemination Level</b>		
<b>PU</b>	Public	x
<b>RE</b>	Restricted to a group specified by the partners of the Beacon project	
<b>CO</b>	Confidential, only for partners of the Beacon project	

**REVIEW**

<b>Name</b>	<b>Internal/Project/External</b>	<b>Comments</b>

**DISTRIBUTION LIST**

<b>Name</b>	<b>Number of copies</b>	<b>Comments</b>
Athanasios Petridis (EC) Christophe Davies (EC)  Beacon partners		

## **Abstract**

This report is a part of deliverable D3.1 of Beacon project. The aim of the deliverable is to describe the models that are available at the beginning of the project. The emphasis is on the conceptual bases, mathematical description as well as model capabilities and shortcomings. This particular report is VTT's part of the deliverable, i.e., it briefly describes a model framework that is available for VTT at this moment of time. The model framework can be utilized, at most general, to create models that can be categorised as a double porosity thermo-hydro-chemo-mechanical (THcM, small c for limited chemical model) models. The framework makes it also possible to limit the modelled phenomena to any subset of the letters (e.g. HM) for needs of specific simulations.

## Content

<b>2</b>	<b>Introduction</b> .....	<b>5</b>
<b>3</b>	<b>Background</b> .....	<b>5</b>
3.1	Processes needed to be covered in a model for swelling clays in disposal environment at the wetting phase .....	5
3.2	Double porosity soil scientific approach.....	6
3.3	Mathematical setting: material frame .....	6
3.4	Numerical solver and implementation.....	6
<b>4</b>	<b>Basic hypotheses and scope</b> .....	<b>6</b>
4.1	Water .....	7
4.2	Air .....	7
4.3	Heat.....	7
4.4	Mechanical .....	7
4.5	Chemical.....	8
4.6	THcM variations .....	8
<b>5</b>	<b>Mathematical description</b> .....	<b>9</b>
5.1	Balance laws .....	9
5.2	Constitutive equations.....	9
5.2.1	Liquid and gas flow model .....	9
5.2.2	Salinity model .....	11
5.2.3	Thermal model .....	12
5.2.4	Mechanical model.....	12
<b>6</b>	<b>Input parameters Heidar</b> .....	<b>13</b>
<b>7</b>	<b>Performance</b> .....	<b>13</b>
<b>8</b>	<b>Conclusions</b> .....	<b>13</b>
<b>9</b>	<b>References</b> .....	<b>14</b>
<b>10</b>	<b>Appendix 1</b> .....	<b>17</b>

## 2 Introduction

The final disposal of spent nuclear fuel in Finland is planned according to KBS-3 concept (Figure 2-1), in which swelling clay components play an important role. The bentonite buffer surrounding the disposal canisters in the deposition holes is supposed to swell to create a tight seal such that 1) the flow of water and the transport chemical species near the canister become slow (corroding agents to and radionuclides from the canister), 2) the microbial activity is low and 3) the buffer protects the canister from bedrock shear displacements. The deposition tunnel backfill (consisting also of swelling clay) has similar purpose (with the exception of not protecting the canister directly), but it should also contribute to stabilising the bedrock surrounding the tunnels.

The buffers is planned to be installed as compacted bentonite blocks and the surrounding installation gaps are filled with bentonite pellets. The main body of the tunnel backfill is also planned to be constructed from compacted clay blocks, which are surrounded by pellets. Consequently, the installation configuration has an uneven density distribution that will evolve during the wetting phase for these engineered barriers. This mechanical evolution can be studied experimentally and by modelling (in sense of computer simulations). Lately, VTT has cooperated with Universidad de Castilla - La Mancha (UCLM) in a Posiva Oy sponsored development project that aims at 1) creating a model framework for bentonite that can be used for these modelling activities (and also others), 2) implementing it to a numerical solver and 3) testing and qualifying the framework with a number of modelling exercises. This report summarizes the main features of this model framework.

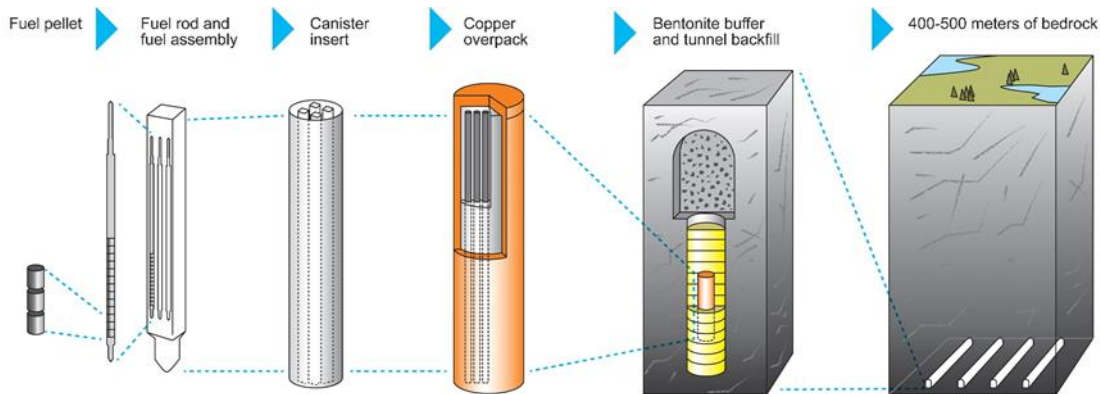


Figure 2-1. KBS-3V disposal concept according to Posiva Oy.

## 3 Background

### 3.1 Processes needed to be covered in a model for swelling clays in

## **disposal environment at the wetting phase**

The clay components are planned to be emplaced in the disposal site with relative low water content. When the surrounding fractured rock supplies local groundwater to the emplaced components, they begin to swell. To model this behaviour, the water movement in the clay and the deformation of the clay have to be described mathematically, that is, there is a need for hydro-mechanical (HM) model. When disposed, the spent fuel still produces heat meaning that thermal phenomena are also relevant for clay modelling (T model). From experiments, it is evident that the chemical composition (e.g. the interlayer cation type) of the clay greatly affects the HM behaviour of it. The clay for the buffer and the tunnel backfill is dug from natural deposits and moved to a new chemical environment that is controlled by the disposal site groundwater, which means that clay chemical composition also begins to evolve after emplacement. Therefore, also the chemical evolution should be modelled (C model). In practice, combining all the models to a single THCM model is however somewhat complicated. Thus, in the approach for the model framework here, only three chemical species representing mono- and divalent cations ( $\text{Na}^+$  and  $\text{Ca}^{2+}$ ) and anions ( $\text{Cl}^-$ ) (and their counterparts in the interlayers) are considered (small c model, totalling to THcM model).

### **3.2 Double porosity soil scientific approach**

The starting point for the model development has been adapting a double pore structure for the clays, since such conceptualization is needed for describing the swelling behaviour of clays adequately.

### **3.3 Mathematical setting: material frame**

In practical applications of swelling clay models, the deformations are large (strain is more than a few percent). Therefore, large deformation (or finite strain) mathematical construction should be used, at least in principle. The model development here has been carried out in material (or Lagrangian) frame, but the work on complete large deformation formulation is left for future.

### **3.4 Numerical solver and implementation**

COMSOL Multiphysics was chosen as the numerical solver for the model due its flexibility in implementing the different model features.

## **4 Basic hypotheses and scope**

The swelling clays are conceptualized to have a double pore structure (Figure 4-1), where the macroscopic porosity is the pore space between clay aggregates and the microscopic porosity consists of the interlayers and the pore space within clay aggregates. The micro porosity is assumed to be fully saturated with water all the time and it forms the solid part of the clay

---

Beacon

D3.1 – THcM model status at VTT

Dissemination level: PU

Date of issue: **28/02/18**

together with the clay mineral phase.

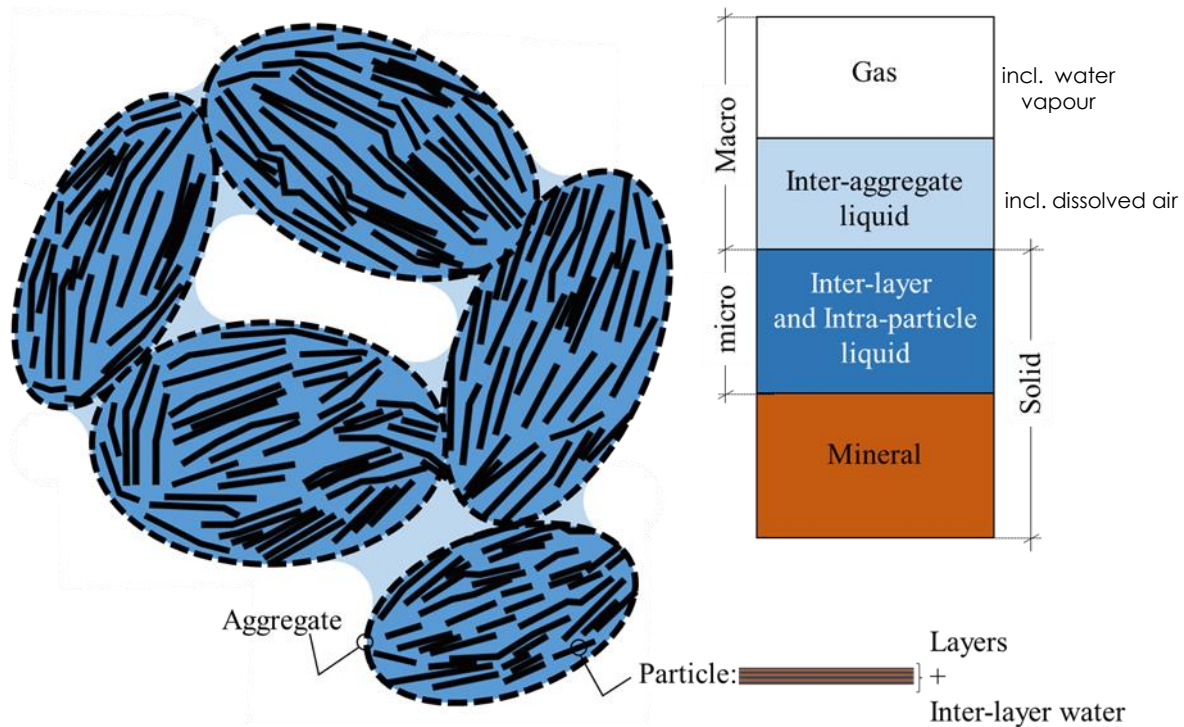


**Figure 4-1.** Conceptualisation of clay structure adopted from Navarro and Alonso (2000) and Alonso et al. (1991). The gas phase includes air and water vapour and the macrostructural liquid phase consists of liquid water and dissolved air.

#### 4.1 Water

In the conceptualized double structure, water can occupy the micro porosity, the macro porosity as liquid water or as water vapour. The model framework allows to specify the movement of all of these along the clay, but currently only the macrostructural liquid water and the vapour mass fluxes are defined.

#### 4.2 Air

In unsaturated conditions, the macro porosity is partly occupied by a gas phase that, besides water vapour, consists of (dry) air, which can also be dissolved in the macrostructural liquid water.

#### 4.3 Heat

Thermal effects on e.g. the water movement in the clay can be significant near heat sources. Therefore, the model framework allows specifying thermal evolution and heat fluxes in clay by two options: 1) taking account thermal properties of each component (solid skeleton, micro- and macrostructural water, water vapour and air) or 2) taking account only the average thermal properties.

#### 4.4 Mechanical

For the deformations of bentonite bodies, the elastoplastic Barcelona Basic Model (BBM) and Barcelona Expanding Model (BExM) frameworks are adopted. However, only the standard Cam-clay type and load-collapse yield surfaces are taken into account in the developed THcM model framework (no suction increase or decrease yield surfaces). For free swelling simulations, the model also allows to use an elastic formulation developed especially for those conditions.

#### **4.5 Chemical**

The chemical part of the model frameworks considers movement and cation exchange reactions of three chemical species:  $\text{Na}^+$  (representing monovalent cations),  $\text{Ca}^{2+}$  (divalent cations) and  $\text{Cl}^-$  (anions) as well as cation exchange sites, where these species can be attached (i.e. the species are in the interlayers). Thus, there are six chemical variables in the model (2 x ( $\text{Na}^+$ ,  $\text{Ca}^{2+}$ ,  $\text{Cl}^-$ )). The purpose of the chemical model is 1) to allow simulations of chemical evolution of bentonite in the disposal conditions and 2) to describe the effect of chemical changes on the HM behaviour of bentonite. Especially the back-coupling term that describes the effect of pressure component of stress on the amount of microstructural water (through the chemical model) and, thus, the swelling state of the clay is important: high pressure (component of stress) means less water in micropores.

#### **4.6 THcM variations**

One aim of the model development and implementation was to allow flexible simulations also with subsets of the above phenomena with the model framework. Consequently, it is possible to exclude any of the phenomena and result to, for example, HM model (including gas transport) or a model that considers only liquid water and mechanical behaviour.

## 5 Mathematical description

### 5.1 Balance laws

The mass and energy balance equations are written using the Lagrangian approach. Therefore, the solid skeleton serves as a reference and all fluxes of mass or energy are described relatively to it.

Conservation of mass is achieved by solving the mass balance equations for:

- macrostructural water in liquid and gaseous state
- air in gaseous state and dissolved in the liquid macrostructural water
- microstructural water
- the chemical species calcium and chloride in the macro- and microstructural water, respectively (two mass balance equations are enough, because of the equilibrium reactions and charge balance).

Conservation of energy is achieved by solving enthalpy balance equation and mechanical equilibrium is achieved by solving the momentum balance equation.

The resulting set of dependent variables comprises:

- Liquid pressure
- Gas pressure
- Microstructural void ratio
- Calcium concentration in the macrostructural water
- Chloride concentration in the microstructural water
- Temperature
- Displacement (and internal variables for plasticity)

### 5.2 Constitutive equations

#### 5.2.1 Liquid and gas flow model

##### ***Macrostructural level***

The fluid in the macrostructural voids can be composed of 1) a liquid phase containing liquid water and dissolved air, and 2) a gas phase being a binary mixture of dry air and water vapour that are treated as ideal gases. The movement of the liquid phase in the macrostructure is formulated as an advective flow due to hydrodynamic gradients and gravity. Henry's law is used for dissolution of air in the liquid macrostructural water. The flow of the components of the gas phase is driven by advection and diffusion. The advective flow of dry air, that is assumed to be linked to the advective flow of the entire gas phase, can be described similar to the flow of the liquid phase in the macrostructure but neglecting gravitational effects (Scanlon et al., 2002; Yoshimi and Osterberg, 1963). As for the flow of dry air, the advection of

water vapour is linked to the flow of the entire gas phase and is induced by hydrodynamic gradients.

The advection of the macrostructural liquid phase (liquid water and dissolved air) and the gas phase (dry air and water vapour) is modelled using a generalised Darcy's law. The degree of macrostructural saturation is calculated using the van Genuchten model (van Genuchten, 1980) for the retention curve and therefore depends on the capillary suction expressed as the difference between gas and liquid pressures. For the liquid phase in the macrostructure, the relative permeability is expressed using a generalized power law according to Brooks and Corey (1964) and Gens et al. (2011). An exponential law proposed by Gens et al. (2011) describes the intrinsic macrostructural liquid phase permeability, which is taken as isotropic. The dynamic viscosity of the macrostructural liquid water is adopted from Ewen and Thomas (1989).

The density of water vapour is obtained by using the psychrometric law (Edlefsen and Anderson, 1943; Pollock, 1986) and the formulation of Ewen and Thomas (1989) to calculate the density of the reference water vapour. The dynamic viscosity of the gas phase is taken as the sum of the dynamic viscosity of dry air (Lemmon and Jacobsen, 2003) and the dynamic viscosity of water vapour (IAPWS, 2008).

For the relative and the isotropic intrinsic permeability of the gas phase the expressions proposed by Yoshimi and Osterberg (1963) are adopted.

Disregarding hydrodynamic dispersion, the diffusion of water vapour can be simulated by molecular diffusion only. As proposed by Navarro and Alonso (2000), the sum of the diffusions of the two gaseous components dry air and water vapour must be zero. Consequently, the diffusion of air is of the same magnitude as the diffusion of water vapour but in opposite direction. With respect to diffusion, the diffusion coefficient of water vapour is determined as in Pollock (1986) and Philip and De Vries (1957) and as proposed by Olivella and Gens (2000), the soil tortuosity is assumed to be equal to one.

#### ***Microstructural level***

At current, flow of water in the microstructure is not considered. Since the microstructure is assumed to be saturated, no water vapour nor dissolved air is present. Flow of liquid microstructural water driven by hydrodynamic gradients is excluded (van Genuchten and Wierenga, 1976). However, with the developed modelling framework it is easily possible to include flow of liquid microstructural water induced by gradients in chemo-electro-osmotic potential at a later stage.

### ***Water mass exchange between macrostructure and microstructure***

As the driving force for the water mass exchange between macrostructure and microstructure, the difference in chemical potential of the water of the two structural levels accounting for different salinity conditions has been identified according to Navarro and Alonso (2001) and Alonso and Navarro (2005). For the definition of the water mass transfer rate, two different options, namely firstly a non-linear approach described in Navarro et al. (2013) and Navarro et al. (2016), and secondly a state surface approach (Navarro et al., 2015), are included in the formulation. The latter defines the relationship between the microstructural void ratio and the structural suction in the microstructure, which can be understood as the affinity of water for the soil particles and is based on the analysis of the change of the microstructural water content.

#### **5.2.2 Salinity model**

The concentrations of calcium, sodium and chloride in the micro- and macrostructural water are considered in a simplified geochemical model. The ion distribution between the both structural levels is conditioned by assuming electro-chemical equilibrium and by taking into account the cation exchange capacity of the clay particles. The electro-chemical formulation is based on a Donnan equilibrium approach (Revil et al., 2011; Tournassat and Appelo, 2011), in which the electrostatic potential in the macrostructure is assumed to equal to zero and serves as a reference value. The proposed model takes advantage of a partitioning coefficient relating the ion concentrations in the micro- and in the macrostructure is by introducing electro-neutrality (Navarro et al., 2017). Therefore, the chemical species mass balance equations can be solved using only one species concentration in the macro and one species concentration in the micro as dependent variables, that are the microstructural chloride and macrostructural calcium concentrations in the proposed model. The micro- and macrostructural sodium concentrations are obtained implicitly by applying electro-neutral conditions. The activity coefficients of water and the chemical species present in the two structural levels are taken as one at the current stage of model development but deviating definitions may be introduced in future, see for example De la Morena et al., 2017.

The transport of chemical species is governed by advection in the macrostructure, which is directly related to the advective flow of the macrostructural liquid phase, and by diffusion in the two structural levels. Mechanical dispersion is neglected and therefore the diffusion process is described using Fick's law for molecular diffusion. The molecular diffusion coefficients are taken from Cussler (1997) and the effective diffusion coefficients for the micro- and for the macrostructure are calculated as in Bourg et al. (2006).

At a later stage, the formulation of diffusion of chemical species can be extended by including chemo-osmotic or electro-kinetic terms as proposed by Revil et al. (2011), Malusis et al. (2012) and Dominijanni et al. (2013).

### **5.2.3 Thermal model**

According to Navarro and Alonso (2000) and Sánchez et al. (2016), local thermal equilibrium between the soil constituents is assumed. While radiation is generally neglected in relation to conduction (Fredlund et al., 2012), conduction and convection are the heat transfer mechanisms considered in the proposed model. The enthalpy is used as the defining variable for the energy balance equation.

The conductive energy flow is expressed as in Fourier's law, whereas two different options are considered for the thermal conductivity, which is assumed to be isotropic at present. The first option is to compute the thermal conductivity as the volume-weighted average of the thermal conductivities of dry soil, macrostructural liquid water, water vapour and air. The second option is to average the thermal conductivities of dry and saturated soil as proposed by Pollock (1986), Olivella et al. (1994) and Sánchez et al. (2016). The advection of enthalpy related to the macrostructural liquid water, water vapour and dry and dissolved air is directly connected to the respective advective and diffusive fluxes described in section 5.2.1.

The specific heats at constant pressure for all soil constituents, as needed for the energy balance, are obtained by linear laws, for which the initial values are taken from Pollock (1986) and Sánchez et al. 2016.

The latent heat is taken into account in the formulation of the specific heat of water vapour.

### **5.2.4 Mechanical model**

The elastoplastic mechanical model for the double porosity soil structure is based on an additive decomposition of strains by considering elastic and plastic strain components and by distinguishing between macrostructural strains and microstructural strains and further by allowing for mechanical coupling between the micro- and the macrostructure, i.e. macrostructural strains induced by microstructural strains (swelling and shrinkage). The two constitutive mechanical models Barcelona Basic Model (BBM, Alonso et al., 1990) and Barcelona Expansive Model (BExM, Alonso et al., 1999) are adopted as modelling frameworks for the macro- and the microstructure and the coupling between them in confined conditions. Accordingly, the net mean stress (excess of mean pressure over air pressure) together with the matric suction, defined as the difference of gas and liquid pressure, serve as a pair of stress magnitudes defining the stress-strain relationship. Note that, no suction increase/decrease yield surfaces nor a formulation for plastic

thermally induced strains have been implemented to the model at present. The formulation of the BBM and BExM has been modified to allow for anisotropy in the stress-strain relationship. In addition, the model has been extended by the formulation proposed by Navarro et al. (2017), using the same state surface as in section 5.2.1 for the water mass exchange between the micro- and the macrostructure and therefore allowing for chemo-mechanical coupling and for free-swelling processes.

## **6 Input parameters**

At the current state, the model has been used for model qualifications ("verification and validation") exercises (approximately 20 of them), which vary from simple comparisons to analytical solutions to coupled THcM simulations. The input parameters are defined by the specific exercises, where different types of soils and conditions are considered. Consequently, general and detailed parameter determination for any specific bentonite type have not been carried out yet.

## **7 Performance**

The performance of the model with respect to different stress, suction and thermal cycles is summarized in Appendix 1 (Table 10-1).

## **8 Conclusions**

VTT and UCLM have cooperated in a Posiva Oy sponsored project to develop and implement a THcM model framework for swelling clays. The framework allows flexible creation of full THcM models or simpler models where only a subset of the phenomena are considered. The model framework has been implemented into COMSOL Multiphysics for numerical solution and running simulations. The model has been qualified with around 20 exercises, which vary from simple comparisons with analytical solutions for single phenomenon to coupled THcM simulations of real-life applications and experiments. The model framework will be used in Beacon project for running lab to large scale simulations of the clay component evolution. The next steps in improving the model is to parametrise it to specific bentonite types, modify it to be applicable for pellet fillings, possibly adding features such as hysteresis and possibly generalizing it properly to large deformations.

## 9 References

- Aaltonen J, Gustafsson C, Nilsson P, 2003.** Oskarshamn site investigation. RAMAC and BIPS logging and deviation measurements in boreholes KSH01A, KSH01B and the upper part of KSH02. SKB P-03-73, Organisation XX.
- Alonso EE, Gens A, Josa A, 1990.** A constitutive model for partially saturated soils. 10.1680/geot.1990.40.3.405.
- Alonso EE, Gens A, Lloret A, 1991.** Double structure model for the prediction of long-term movements in expansive materials. Proceedings of the 7th International Conference on Computational Methods and Advances in Geomechanics, Cairns 1991, pp 541-548.
- Alonso EE, Navarro V, 2005.** Microstructural model for delayed deformation of clay: loading history effects. 10.1139/T04-097.
- Alonso, E.E., Vaunat, J., Gens, A, 1999.** Modelling the mechanical behaviour of expansive clays. 10.1016/S0013-7952(99)00079-4.
- Bourg IC, Sposito G, Bourg ACM, 2006.** Tracer diffusion in compacted, water-saturated bentonite. 10.1346/CCMN.2006.0540307.
- Brooks RM, Corey AT, 1964.** Hydraulic properties of porous media. Colorado State University, Fort Collins, Colorado
- Cussler EL, 1997.** Diffusion: mass transfer in fluid systems. 2nd ed. Cambridge University Press, ISBN 9780521450782, 600 pp.
- De la Morena G, Asensio L, Yustres Á, Navarro V, 2017.** Characterisation of free swelling processes accounting for solute concentration effects. Scientific Research Abstracts, Vol. 7, p. 186. Digilabs Pub., Bari, Italy, pp. 833.
- Dominijanni A, Manassero M, Puma S, 2013.** Coupled chemical-hydraulic-mechanical behaviour of bentonites. 10.1680/geot.SIP13.P.010.
- Edlefsen NE, Anderson ABC, 1943.** Thermodynamics of soil moisture. 10.3733/hilg.v15n02p031.
- Ewen J, Thomas HR, 1989.** Heating unsaturated medium sand. 10.1680/geot.1989.39.3.455.
- Fredlund DG, Rahardjo H, Fedlund MD, 2012.** Unsaturated Soil Mechanics in Engineering Practice. John Wiley and Sons, ISBN 1118133595, 9781118133590, 926 pp.
- Gens, A, Valleján B, Sánchez M, Imbert C, Villar MV, van Geet M, 2011.** Hydromechanical behaviour of a heterogeneous compacted soil: experimental observations and modelling. 10.1680/geot.SIP11.P.015.
- IAPWS, 2008.** Release on the IAPWS Formulation 2008 for the Viscosity of Ordinary Water Substance, IAPWS R12-08, The International Association for the Properties of Water and Steam (IAPWS).  
<http://www.iapws.org/relguide/visc.pdf>.
- Lemmon EW, Jacobsen RT, 2003.** Viscosity and Thermal Conductivity Equations for Nitrogen, Oxygen, Argon, and Air. Int J Thermophysics 25(1).  
trc.nist.gov/refprop/FAQ/NAO.PDF.
- Leskinen N, Ronneteg U, 2011.** Tillverkning av kapselkomponenter. SKBdoc 1175208 ver 5.0, Svensk Kärnbränslehantering AB. (In Swedish.)

---

Beacon

D3.1 – THcM model status at VTT

Dissemination level: PU

Date of issue: **28/02/18**

- Malusis MA, Shackelford CD, Maneval JE, 2012.** Critical review of coupled flux formulations for clay membranes based on nonequilibrium thermodynamics. 10.1016/j.jconhyd.2012.06.003. doi.org/10.1016/S0266-352X(00)00002-1
- Navarro V, Alonso EE, 2000.** Modeling swelling soils for disposal barriers. *Computers and Geotechnics*, Volume 27, Issue 1, July 2000, pp 19-43.
- Navarro V, Alonso EE, 2001.** Secondary compression of clays as a local dehydration process. 10.1680/geot.2001.51.10.859.
- Navarro V, Asensio L, De la Morena G, Pintado X, Yustres Á, 2015.** Differentiated intra- and inter-aggregate water content models of MX-80 bentonite. 10.1016/j.clay.2015.10.015.
- Navarro V, Asensio L, Yustres Á, De la Morena G, Pintado X, 2016.** Swelling and mechanical erosion of MX-80 bentonite: Pinhole test simulation. 10.1016/j.enggeo.2016.01.005.
- Navarro V, Asensio L, Yustres Á, Pintado X, Alonso J, 2013.** Volumetric deformability and water mass exchange of bentonite aggregates. 10.1016/j.enggeo.2013.09.011.
- Navarro V, Yustres Á, Asensio L, De la Morena G, González-Arteaga J, Laurila T, Pintado X, 2017.** Modelling of compacted bentonite swelling accounting for salinity effects. 10.1016/j.enggeo.2017.04.016.
- Navarro V, Yustres Á, Asensio L, De la Morena G, González-Arteaga J, Laurila T, Pintado X, 2017.** Modelling of compacted bentonite swelling accounting for salinity effects. 10.1016/j.enggeo.2017.04.016.
- Olivella S, Carrera J, Gens , Alonso EE, 1994.** Nonisothermal multiphase flow of brine and gas through saline media. 10.1007/BF00613282
- Olivella S, Gens A, 2000.** Vapour Transport in Low Permeability Unsaturated Soils with Capillary Effects. *Transport in Porous Media*, Volume 40, Issue 2, pp 219–241. doi.org/10.1023/A:1006749505937.
- Philip JR, De Vries DA, 1957.** Moisture movement in porous materials under temperature gradients. 10.1029/TR038i002p00222.
- Pollock DW, 1986.** Simulation of Fluid Flow and Energy Transport Processes Associated With High-Level Radioactive Waste Disposal in Unsaturated Alluvium. 10.1029/WR022i005p00765.
- Revil A, Woodruff WF, Lu N, 2011.** Constitutive equations for coupled flows in clay materials. 10.1029/2010WR01000210.1680/geot.1993.43.3.457.
- Sánchez M, Gens A, Villar MV, Olivella S, 2016.** Fully Coupled Thermo-Hydro-Mechanical Double-Porosity Formulation for Unsaturated Soils. 10.1061. (ASCE)GM.1943-5622.0000728.
- Scanlon et al., 2002.** Choosing appropriate techniques for quantifying groundwater recharge. *Hydrogeology Journal*, Volume 10, Issue 1, pp 18–39. <https://doi.org/10.1007/s10040-001-0176-2>.
- Sena C, Grandia F, Arcos D, Molinero J, Duro L, 2008.** Complementary modelling of radionuclide retention in the near-surface system at Forsmark. Development of a reactive transport model using Forsmark 1.2 data. SKB R-08-107, Svensk Kärnbränslehantering AB.
- SKB, 2003.** Planning report for the safety assessment SR-Can. SKB TR-03-08,

Svensk Kärnbränslehantering AB.

**Tournassat C, Appelo CAJ, 2011.** Modelling approaches for anion-exclusion in compacted Na-bentonite. 10.1016/j.gca.2011.04.001.

**van Genuchten MT, 1980.** A closed-form equation for predicting the hydraulic conductivity of unsaturated soils. 10.2136/sssaj1980.03615995004400050002x.

**van Genuchten MT, Wierenga, PJ, 1976.** Mass transfer studies in sorbing porous media I. Analytical solutions. 10.2136/sssaj1976.03615995004000040011x.

**Yoshimi Y, Osterberg JO, 1963.** Compression of partially saturated cohesive soils. Journal of Soil Mechanics and Foundations Division of the American Society of Civil Engineers, 89, 1–24.

## 10 Appendix 1

Table 10-1. Features table

Name of the constitutive law:			
Behaviour feature	YES	NO	Remarks
<b>Mechanical behaviour</b>			
Dependence of swelling strain on applied stress (at the same dry density) (Figure1)	x		Through the dependency of microwater chemical potential on pressure component of the stress and the water exchange term
Dependence of swelling stress on dry density (at the same stress) (Figure 1)	x		Through the dependency of microwater chemical potential on pressure component of the stress and the water exchange term
Irreversibility of strains in wetting/drying cycles (Figure 2)		x	no suction increase/decrease yield surfaces, but possibly plastic strains with the implemented yield surfaces
Dependence of swelling pressure on dry density (Figure 4)	x		Through the dependency of microwater chemical potential on pressure component of the stress and the water exchange term
Stress path dependence from an unsaturated to a saturated state (Figure 5)			Possibly, depends on the simulation setup (no specific mechanisms determined for this behaviour, though)
Stress path dependence from a saturated to an unsaturated state (Figure 6)			Possibly, depends on the simulation setup (no specific mechanisms determined for this behaviour, though)
Double structure/porosity considered?	x		
Are temperature effects considered in the model?	x		Thermal expansion
Dependence of strains developed in a temperature cycle (increase/decrease) on OCR (or stress) (Figure 7)		x	
<b>Hydraulic behaviour (retention curve)</b>			
Hysteresis		x	
Dependence on void ratio	x		
Double structure/porosity considered?	x		



**COUPLED HYDROMECHANICAL MODELLING OF UNSATURATED  
EXPANSIVE CLAYS.  
PROJECT BEACON**

**CONSTITUTIVE MODEL FORMULATION**

**DELIVERABLE (D3.1)**

**ANNEX H**

**D.F. Ruiz, A. Gens, J. Vaunat**

**International Center for Numerical Methods in Engineering (CIMNE)**

**Universitat Politècnica de Catalunya (UPC)**

**DELIVERABLE 3.1.**

**Barcelona, February 28th, 2018**

## Table of contents

1	Introduction .....	3
2	Expansive clays—Bentonite .....	4
2.1	Physical features .....	5
2.1.1	Main hydro-mechanical (HM) features .....	6
3	A double-structure hydro-mechanical (HM) formulation .....	9
3.1	Theoretical framework .....	9
3.2	Problem formulation .....	10
3.3	Governing equations .....	12
3.4	Mass transfer mechanism between structural levels .....	15
3.5	Constitutive equations .....	15
3.5.1	Hydraulic constitutive equations .....	15
3.5.2	Mechanical constitutive equations .....	16
3.6	Input parameters .....	21
3.7	Partial performance .....	23
3.7.1	Dependence of swelling strain on applied stress at the same dry density .....	24
3.7.2	Dependence of swelling pressure on dry density .....	25
3.7.3	Irreversibility of strains in wetting/drying cycles .....	26
4	Concluding remarks and future developments .....	29
5	References .....	30

## 1 Introduction

This report contains the Hydro-Mechanical (HM) constitutive formulation for expansive clays, based in the double structure concept. Two main sections are distinguished: a) the physical features and, b) the hydro-mechanical formulation.

After this introductory description, the Chapter 2 presents the main physical aspects of the expansive clays. Under the consideration of the bentonite as a multiphase porous media, the following features are briefly explained:

- Mineral structure and swelling mechanisms.
- Dependency of Swelling pressure and hydraulic conductivity on dry density.
- The identification of two predominant pore levels through microstructural insights.

From the experimental data (field and laboratory), three important aspects of the bentonite can be remarkable: the heterogeneity, the strain irreversibility and the stress path dependency. The performance of a numerical model, model formulation and numerical implementation, should include the above features in order to deal with boundary value problems.

The Hydro-Mechanical (HM) formulation is shown in the Chapter 3. After define the phenomenological approach as theoretical framework, the governing equations are formulated. They consider a multiphase system composed by two structural levels. In order to close the whole formulation the constitutive equations have to be considered. Some of the key points of the formulation are described as follow:

- A critical reflection on the concepts of volume fraction and macro- and micro-porosities in order to overcome some imprecise definitions from previous formulation.
- The possibility to consider the micro-structural level as unsaturated media.
- Different hydraulic potential may be found at each structural levels; therefore, the mass transfer mechanism between them is taken into account. This time dependent mechanism is the relaxation of one of the main hypothesis of the original double structure model formulation (Alonso, Vaunat and Gens, 1999) in which the hydraulic equilibrium between both structural levels is considered.
- From the mechanical point of view, the scheme proposed by Sánchez, (2004) is followed. A classical plasticity model based on net stress and suction for the macro-structure, a non-linear elasticity based on the bishop effective stress for the micro-structure and finally a generalized plasticity to treat the coupling between both levels of structures.

Finally, the Chapter 4 gives the concluding remarks and the future developments in order to have an operative numerical tool.

## 2 Expansive clays—Bentonite

In a historical perspective, in the middle 20th century the engineering and research community has denominated the expansive clays as “problematic soils” due to the important damage on the civil infrastructure. Since the end of the 20th century, the geotechnical engineering face new challenges additional to civil infrastructure. Energy geo-technology comes as one of the main drivers for research and practical activities. This fact changed completely the perspective relate to materials, engineering solutions and modelling approaches.

Some features of the expansive clays that causes damage in the infrastructure were founded useful to use it as “engineering material”. Due to their low hydraulic, plasticity, swelling and absorptive capacity for contaminants, active clays have been used to inhibit the migration of contaminant to the environment. Therefore, in isolating contaminants from the biosphere, clays act as natural barriers.

The nuclear waste disposal impose a huge increasing in dangerous contaminants and timescales analyses. The aim of geological disposal of radioactive waste is to remove it from human environment and to ensure that any radionuclide release rates remain below prescribed limits (Chapman and Mc Kinley, 1987). The deep geological repositories are the best option for the nuclear waste isolation.

Gens, (2003) pointed out the main uses of expansive clays in this kind of repositories:

During the operation phase, its role is the multi-barrier disposal concept, majority for high-level nuclear waste (HLW). If one observes the potential path of a long-lived radionuclides from inside the canister to the biosphere, it is clear that it will need to cross several barriers, the canister itself, the expansive clay backfill (engineered barrier) and the host rock (geological barrier).

Prior to repository closure, it will be necessary to seal and backfill access tunnels and shafts so that they do not become preferential radionuclide migration pathways. The design of seal structures has as main purposes: i) low permeability plugs ii) long term mechanical support for the underground openings, iii) additional locations for radionuclide sorption, and iv) some protection against human intrusion. Again, the bentonites seals are at present the preferred option because of their high sealing capacity. The issues concerning seal behaviour are similar to those arising in the design of multi-barriers, with the important difference that no high temperatures are expected. Ruiz *et al.*, (2017a) and Ruiz *et al.*, (2017b) have shown that the performance of this structures is totally related to the entire life of the deep repository and their hydro-mechanical evolution takes thousands of years.

Undoubtedly, the main consequence of the large timescales involved in the nuclear waste disposal is the necessity for consider the physical laws of the materials over the classical empiricism of the soil mechanics. The constitutive models and numerical simulations have to

obey to the physical features, material structure and its coupled evolution during the time scale considered (several hundred or thousand years).

## 2.1 Physical features

Clay behaviour depends on the interaction between solid skeleton and pore fluid. A great part of this interaction is chemical, or electrochemical. This arises from unsatisfied charge of clay platelet, which is the fundamental clay structural element. The presence of electrical charge at the surface and edges of a platelet affects the arrangement and behaviour of water in platelet vicinity. These well-known facts are widely believed to endow clays with their peculiar hydro-mechanical properties, especially in the active or expansive clays.

Actually, the engineering behaviour of moderately expansive (or non-expansive) and highly expansive clays is really influenced by their mineralogical composition. Sridhara, (2001) conducted a systematic experimental comparison between kaolinitic and montmorillonitic clays. Aspects such as liquid limit, shrinkage limit, swell potential, volume change behaviour, drained and undrained shear strength relying mainly on the mineralogical composition. Of course, all these aspects were measured at the same experimental conditions. The most important conclusion of this experimental study was that the driven mechanisms in the kaolinitic and montmorillonitic clays are quite different. Both are influenced by the mineral arrangement. However, the montmorillonitic clay is dominated by the diffuse double layer repulsion and the kaolinitic clay is governed by net attractive force (Santamarina *et al.*, 2001).

Probably, the first mention of soil structure can be attributed to Schmertmann, (1964). From his pioneer idea, many works were conducted in order to analyse the factors that controls the soil behaviour, in addition to the classical stress-strain actions. Finally, Mitchell, (1976) stated the soil structure as the combination of *fabric* (particle arrangement) and *interparticle bonding*.

The soil structure is the combined result of such factor as the mineralogy, water chemistry during deposition, pressure, temperature and organic content, deposition and consolidation rates and strain paths. Extensive research has been oriented to the structural effects on natural clays and claystones (Burland, 1990; Leroueil and Vaughan, 1990; Gens, 2009; Chandler, 2010) and compacted moderately and highly expansive clay (Romero, 1999; Alonso, Pinyol and Gens, 2013; Musso, Romero and Della Vecchia, 2013).

The essential part of the expansive clay structure is the organization of its pore space and water. From the former qualitative observations by Scanning Electron Microscopy (SEM) (Collins and McGown, 1974) until the late innovative techniques like Environmental Scanning Electron Microscopy (ESEM) and Mercury Intrusion Porosimetry (MIP) (Romero, Della Vecchia and Jommi, 2011; Musso, Romero and Della Vecchia, 2013); the fabric of active clays can be loosely identified as a mixture of macroparticles (clay aggregates) formed by clay platelets. This double porosity system is filled, total or partially, with water adsorbed to the aggregates or in bulk state. Concerning to interparticle “bonding”, Alonso, Gens and

Josa, (1990) proved that water menisci, in the unsaturated state, acts as cohesive factor (see Figure 2-1).

From the above fact, the (Thermo)-Hydro-Mechanical behaviour of the bentonite will be determined by the evolution of its double-structure. In the nuclear waste disposal activities, one of the main feature of the bentonite is the heterogeneity. This comes from the design and emplacement of the fills and barriers. The conception of the waste disposal has evolved during the last four decades and several material proposals have been formulated: bentonite powder, compacted blocks, pellets and mixtures such as powder/pellets or sand/bentonite. Besides, geometrical irregularity of the tunnels, presence of technological gaps and voids and segregation of granular material imposes additional source of heterogeneity.

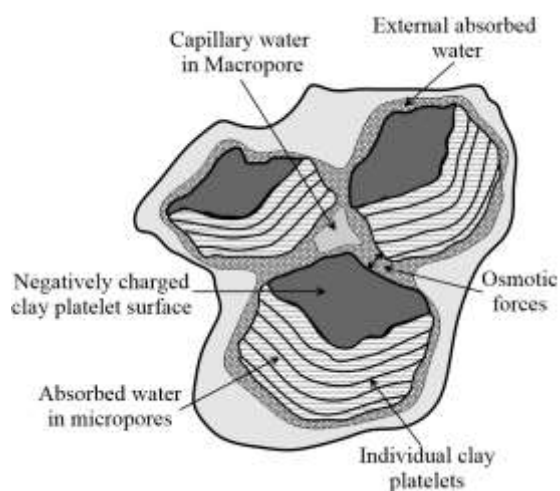


Figure 2-1. Sketch of expansive clay as double-structure porous medium (modified from Hueckel, Loret and Gajo, 2001).

### 2.1.1 Main hydro-mechanical (HM) features

#### Swelling mechanism

Murad and Cushman, (2000) give a clear explanation of swelling mechanism of the expansive clays. For the most common among expansive mineral, that is smectite, the negative charge is neutralized by exchangeable cations. When a bentonite is exposed to water, the water penetrates the superimposed layers and forces them apart causing swelling. The attraction (hydrophilicity) of montmorillonite to water is one of the causes of swelling. The force causing clay to swell upon hydration is commonly called *the hydration force*. Hydration causes the water properties to vary with the proximity to solid surface. The interlamellar water is termed adsorbed water (or vicinal water) to distinguish it from its bulk or free-phase counterpart (i.e. water free of any adsorptive force)(Figure 2-1). The properties of vicinal water depend in a complex way on the structure of surfaces and distance between surfaces (Jacinto, Villar and Ledesma, 2012). In addition, the large specific surface areas of the 2:1 layer silicates and their charged character magnify the effects of hydration forces.

Dependency of Swelling pressure and hydraulic conductivity on dry density

The dry density ( $\gamma_d$ ) is the most powerful indicator of the soil compaction procedure. Combined with the water content ( $w$ ), they determine the initial state at which the bentonite fill is placed. Experimental programs with porosimetry analysis have revealed that these engineering parameters ( $\gamma_d$ ,  $w$ ) are totally linked with the bentonite fabric (Romero, 1999; Lloret *et al.*, 2003; Musso, Romero and Della Vecchia, 2013). Therefore, hydro-mechanical aspects such as swelling pressure and hydraulic conductivity are function of dry density (Figure 2-2).

From the tracking the dry density evolution is possible to determine the evolution of the heterogeneous bentonite barriers and seal under the hydro-mechanical actions (homogenization phenomenon).

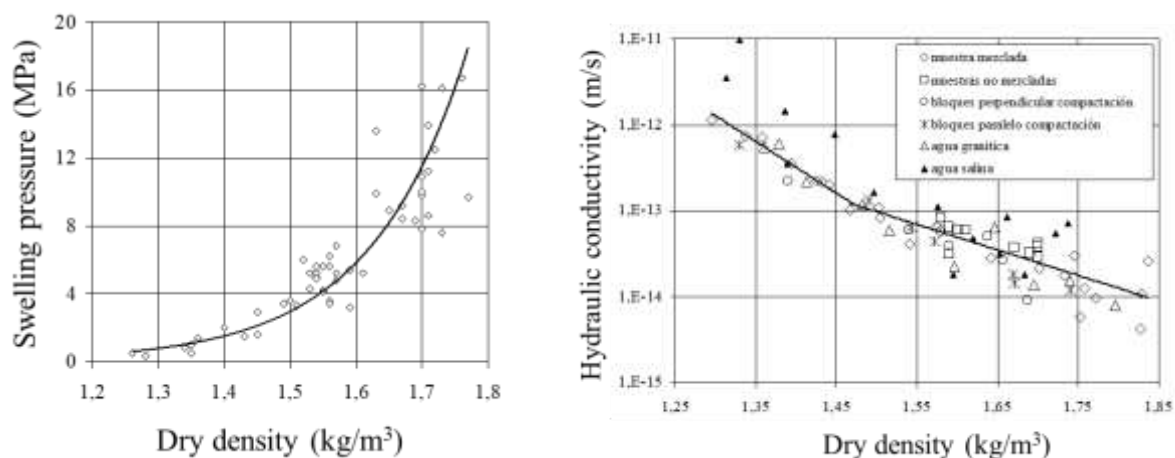


Figure 2-2. Dependence of swelling pressure and hydraulic conductivity on compaction dry density— Bentonite (Na-Ca-Mg) (Lloret *et al.*, 2003).

The engineering parameters  $\gamma_d$  and  $w$  can be related to key parameters of elasto-plastic models in order to handle the numerical modelling of the hydro-mechanical coupling. This aspect is explored in the Sections 3.7.1 and 3.7.2.

Strain irreversibility and stress path dependency

The strain response of bentonite under hydro-mechanical actions is marked by the irreversibility and the stress path dependency. Irreversible expansion is obtained as a consequence of wetting-drying cycles. In terms of structure these kind of results are generally explained as a change in the fabric of the soil induced by the water content change (suction changes).

The stress path dependency of swelling strains and swelling pressures exhibit by the expansive soils have been long recognized. The Figure 2-3 shown the stress path dependency

through the experimental testing performed by Brackley, (1975). Three techniques were used to predict the heave under given load of 50 kPa:

- a) Free swell and subsequent loading
- b) Loading to 50 kPa and swell under pressure
- c) Saturation at constant volume and subsequent unloading to 50 kPa.

The three methods generate different swelling value. The first method yields the maximum swelling, the third methods gives the smallest deformation and the second methods results in an intermediate swelling value.

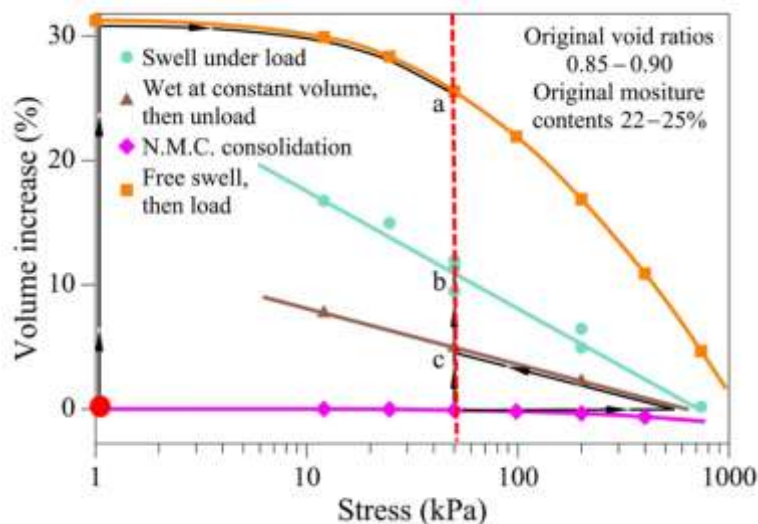


Figure 2-3. Stress path dependency (Lloret *et al.*, 2003).

### 3 A double-structure hydro-mechanical (HM) formulation

The complex behaviour of geomaterials requires a suitable physical description (laboratory and field experiments) and the use of appropriate theoretical frameworks that lead the good reproduction of their coupling behaviour. Key aspects from continuum and soil mechanics, poromechanics and elasto-plasticity are used to handle the hydro-mechanical (HM) modelling of the expansive clays.

The proposed framework assumes the presence of two structural levels, indeed porous media, linked through a mechanical interactions and mass transfer between them.

#### 3.1 Theoretical framework

As pointed Schrefler, (2002), the porous material are classified as those with an internal structure. They comprise the solid phase and pores geometry. According to the physical features of the expansive clays presented above, the expansive clay was defined as double-structure material composed by the arrangement of clay aggregates and micro- and macropores (Figure 3-1).

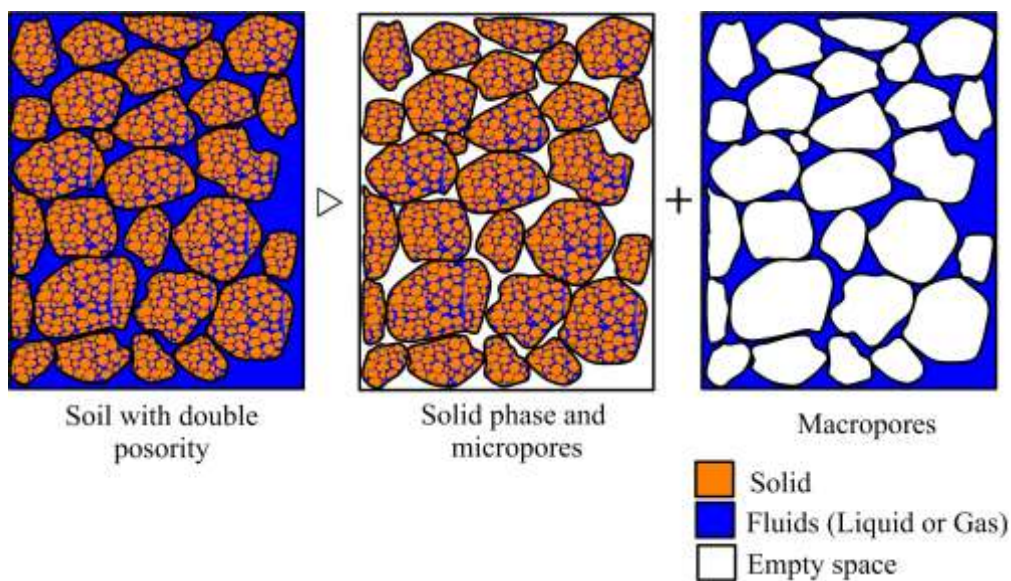


Figure 3-1. Schematic representation of the double-structure porous medium as the addition of two media: aggregates composed by solid and micropores filled by fluids and macropores also occupied by fluids. (After Coussy, 2004; Borja and Koliji, 2009; Borja and Choo, 2016).

This work uses the macroscopic approach developed by Olivella *et al.*, (1994) and Olivella, (1995) which originally was formulated for saline media. The extension for broad spectrum of geomaterials was a consequence of the continuous evolving and the generation of a numerical simulator (Olivella *et al.*, 1996). Specifically for the expansive clays, Sánchez, (2004) expressed the governing and constitutive equations for a double-structure porous media. In the following items, several changes and reviews about these aspects are presented.

### 3.2 Problem formulation

The porous media under study consist of three phases [solid (s), liquid (L) and gas (g)] and three main components [solid (s), water (w) and air (a)]. An important difference respect to the original formulation (Olivella *et al.*, 1994) is that each structural level contains air and water in gas and liquid state (Figure 3-2). Additionally, the possibility to have unsaturated states in the micro-structural level represents a new feature respect to the formulation of Sánchez, (2004). This means a general state of the expansive clay, because strong drying paths or some compaction procedures (e.g. bentonite pellets) can induce this state in the micropores.

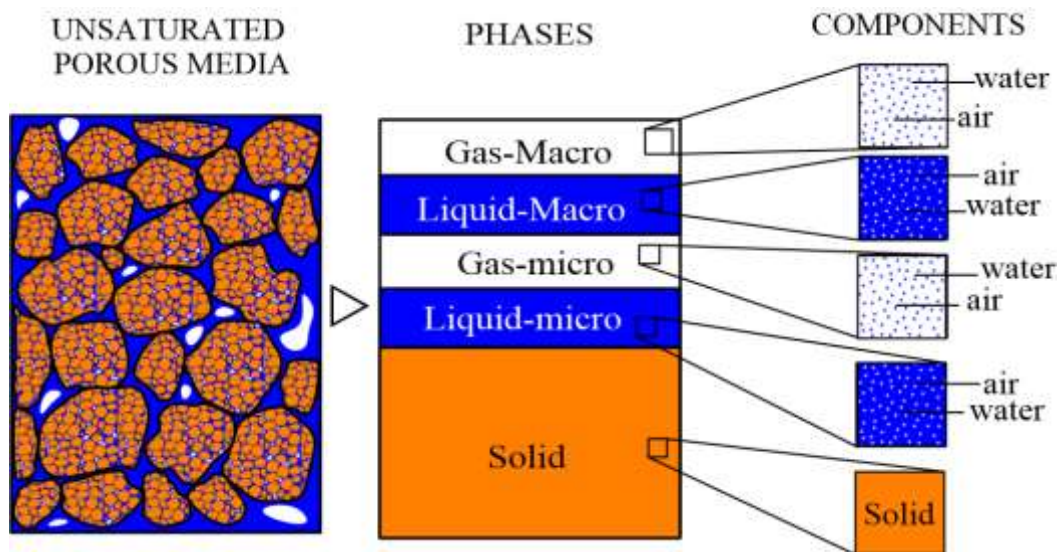


Figure 3-2. Continuum approximation of unsaturated double-structure porous media. Phases and components at each structural levels.

One of the main requires in the coupled HM formulation is the reference of the quantities respect to the whole volume control. From this point, the *volume fraction concept* plays a key role. Volume fractions are given by the ratio of the volume of the constituents to the total volume of the control space. The macroscopic approach is intrinsically integrated by the concept of the volume fraction concept (Lewis and Schrefler, 1998 ; de Boer, 2005; Borja and Koliji, 2009; Salimzadeh and Khalili, 2016).

The Figure 3-3 shows the phase volumes distribution in a double-structure porous media. It is useful to determine the porosities and volume fractions.

Based on the structural levels of an expansive clays, it is possible to define the *micro pore volume fraction* (Eq. 3-1) and *macro pore volume fraction* (Eq. 3-2). The above expressions relate the volume of pores at the macro- and micro-structure with the total volume of the control space. An ideal situation to express the balance equations of any medium. Besides to the pore volume fractions, there is also a *solid volume fraction*, which is defined in the equation (Eq. 3-3). This involves the solid particles contained in the clay aggregates (micro-structure).

$$\bar{\phi}_{\text{micro}} = \frac{(V_{\text{Pores}})_{\text{micro}}}{V} \quad (\text{Eq. 3-1})$$

$$\bar{\phi}_{\text{Macro}} = \frac{(V_{\text{Pores}})_{\text{Macro}}}{V} \quad (\text{Eq. 3-2})$$

$$\bar{\phi}_{\text{Solid}} = \frac{(V_{\text{Solid}})_{\text{micro}}}{V} \quad (\text{Eq. 3-3})$$

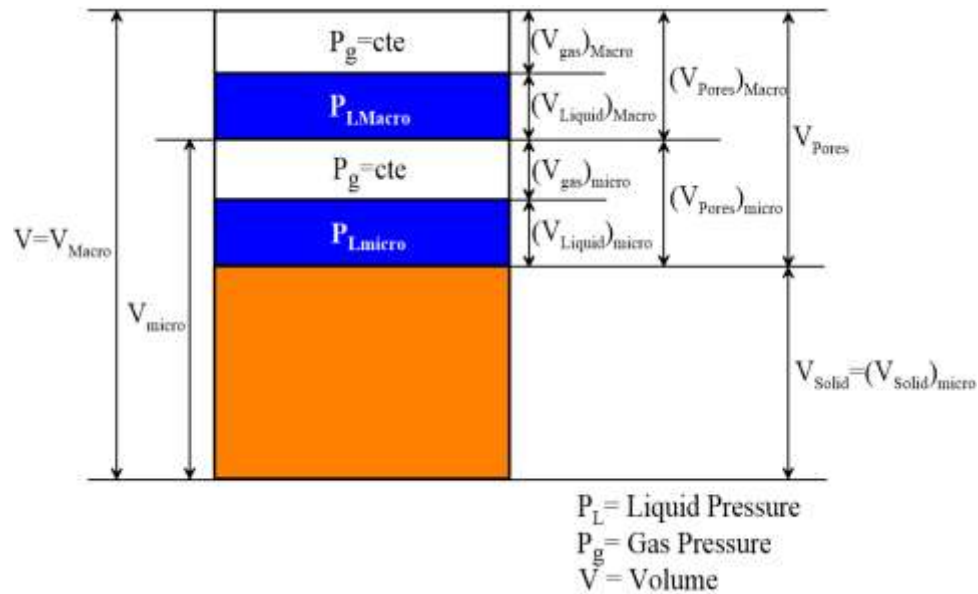


Figure 3-3. Phase diagram of an unsaturated double-structure soil—Volumes.

The physical constraint over the volume fraction condition is that the sum of the volume fractions have to be equal to one (Eq. 3-4).

$$\sum \bar{\phi} = \bar{\phi}_{\text{micro}} + \bar{\phi}_{\text{Macro}} + \bar{\phi}_{\text{Solid}} = 1 \quad (\text{Eq. 3-4})$$

Another interesting aspect is that the *total porosity* of the double-structure soil is given by the summation of both pore volume fractions (Eq. 3-5).

$$\phi = \bar{\phi}_{\text{micro}} + \bar{\phi}_{\text{Macro}} \quad (\text{Eq. 3-5})$$

A detailed revision of the pore volume fractions ( $\bar{\phi}_{\text{micro}}$  and  $\bar{\phi}_{\text{Macro}}$ ) indicates that they are not the strictly definition of the porosities in the structural levels, as they are defined in classical soil mechanics. The *micro porosity*  $\phi_{\text{micro}}$  comes from the relation of the volume of micro-pores and the volume of the micro-structural level. In this kind of porous media, the definition of *macro porosity* ( $\phi_{\text{macro}}$ ) is not clear, because the volume of the macro-structural level coincides with the total volume. The macro-structure can be conceived as a “virtual”

medium that would be found for the case in which the whole volume of the micro-structure is occupied only by solid phase.

An interesting point is that the porosities of the micro- and macro-structure don't satisfy the physical constrain expressed in the equation (Eq. 3-4), therefore, they are not a smart choice for the statement of the governing equations.

Previous models defines the pore volume fractions as the porosities of the structural levels. This does not mean a wrong modelling, however, the analysis of the evolving structure can be confusing. Probably, these imprecise definitions come from the fact that in single-structure materials the pore volume fraction is equal to the porosity. Clearly, this is not true in the double-structure porous media.

### 3.3 Governing equations

In this part, we derive the mass balance of different components at micro and macro structural levels and the balance of momentum for the medium as a whole is reduced to the stress equilibrium. Balance of momentum for fluid phases are reduced to the constitutive equations (i.e. Fick's and Darcy's laws).

The formulation described here is based on the general approach of Olivella *et al.*, (1994) and Olivella, (1995) applied to the specific case of isothermal problems involving double-structure unsaturated soils.

A detailed description of the variable notation (Table 3-1) is necessary to the right comprehension of the mathematical statement of the governing equations and the hydro-mechanical (HM) formulation. The solution requires specifying an equal number of unknown variables and equations. Thus, the state variables are as follows: solid velocity,  $\dot{\mathbf{u}}$  (in three spatial direction) and the liquid and gas pressure in both structural levels,  $P_{L\_Macro}$ ,  $P_{L\_micro}$ ,  $P_{g\_Macro}$  and  $P_{g\_micro}$ .

Table 3-1. Equation and variable summary (modified from Olivella, 1995)

General	
$(\cdot)_{\alpha}$	Subscript used to identify the structural level (1=micro, 2= macro) and/or phases (s=solid, L=liquid, g=gas)
$(\cdot)^i$	Superscript used to identify the components (s=solid, w=water, a=air)
$\bar{\phi}$	Volume fraction
$\phi$	Porosity
$\rho, \tilde{\rho}$	Local and global density
$\omega, \omega_{\alpha}^i$	Mass fraction and mass fraction of the component i in phase $\alpha$
$\theta_{\alpha}^i$	Mass fraction of the component i in phase

	$\alpha$ per unit of volume of phase $\alpha$
S	Saturation degree
$\mathbf{j}, \mathbf{j}_\alpha^i$	Mass flux respect to the solid skeleton and mass flux respect to the solid skeleton of the component i in phase $\alpha$ per unit of volume of phase $\alpha$
<b>Balance equations unknowns</b>	
Solid mass balance	$\bar{\phi}$ – Volume fraction
Water mass balance for macro-structure	$P_{L2}$ – Liquid pressure at macro-structural level.
Water mass balance for micro-structure	$P_{L1}$ – Liquid pressure at micro-structural level.
Air mass balance for macro-structure	$P_{g2}$ – Gas pressure at macro-structural level.
Air mass balance for micro-structure	$P_{g1}$ – Gas pressure at micro-structural level.
Momentum balance	$\dot{\mathbf{u}}$ – Solid Velocity

The following equations present a considerable extension, therefore it is convenient a compact variable names. From now, we refer the micro-structural level with the subscript 1, the macro-structural level with the subscript 2 and the double-structural porous media without subscript.

Solid mass balance equation:

$$\frac{D\bar{\phi}_2}{Dt} = \frac{(1 - \bar{\phi}_1 - \bar{\phi}_2)}{\rho_s} \frac{D\rho_s}{Dt} + (1 - \bar{\phi}_1 - \bar{\phi}_2) \frac{d\varepsilon_v^{1 \rightarrow 2}}{dt} - \frac{D\bar{\phi}_1}{Dt} \quad (\text{Eq. 3-6})$$

where:

- $\varepsilon_v^{1 \rightarrow 2}$  is the volumetric deformation of the macro-structural level due to change in volume of the micro-structural level.

This is a clear theoretical explanation of the mechanical interaction of the structural levels in a double-structure porous media. This idea was the key component from the early framework (Gens and Alonso, 1992) until the latest formulations (Alonso, Vaunat and Gens, 1999; Sánchez *et al.*, 2005; Gens *et al.*, 2011; Guimaraes *et al.*, 2013). The mathematical expressions of this interaction will be explained in the constitutive description.

Water mass balance equation for macrostructure:

$$\frac{D(\theta_{L2}^w S_{L2} + \theta_{g2}^w S_{g2})}{Dt} \bar{\phi}_2 + (\theta_{L2}^w S_{L2} + \theta_{g2}^w S_{g2}) \left( \frac{d\bar{\varepsilon}_{v2}}{dt} \right) \nabla \cdot (\mathbf{j}_{L2}^w + \mathbf{j}_{g2}^w) = - \Gamma^w \quad (\text{Eq. 3-7})$$

where:

- $\bar{\epsilon}_{v2}$  is the volumetric deformation of the macro-structural level respect to the total volume of the porous medium. This term imposes a clear hydro-mechanical coupling.
- $\Gamma^w$  is the term related to the water mass exchange between the two structural levels.

Water mass balance equation for microstructure:

$$\begin{aligned} \bar{\phi}_1 \frac{D(\theta_{L1}^w S_{L1} + \theta_{g1}^w S_{g1})}{Dt} + (\theta_{L1}^w S_{L1} + \theta_{g1}^w S_{g1}) \left( \frac{d\bar{\epsilon}_{v1}}{dt} \right) \nabla \cdot (\mathbf{j}_{L1}^w + \mathbf{j}_{g1}^w) \\ = \Gamma^w - (\theta_{L1}^w S_{L1} + \theta_{g1}^w S_{g1})(1 - \phi) \frac{d\rho_s}{\rho_s} \end{aligned} \quad (\text{Eq. 3-8})$$

where:

- $\bar{\epsilon}_{v1}$  is the volumetric deformation of the micro-structural level respect to the total volume of the porous medium.

Water mass balance equation for macrostructure:

$$\begin{aligned} \bar{\phi}_1 \frac{D(\theta_{L1}^w S_{L1} + \theta_{g1}^w S_{g1})}{Dt} - (\theta_{L1}^w S_{L1} + \theta_{g1}^w S_{g1}) \left( \frac{d\bar{\epsilon}_{v1}}{dt} \right) \\ = \Gamma^w - (\theta_{L1}^w S_{L1} + \theta_{g1}^w S_{g1})(1 - \phi) \frac{d\rho_s}{\rho_s} \end{aligned} \quad (\text{Eq. 3-9})$$

The hydraulic constitutive laws of the volumetric advective fluxes  $\mathbf{j}_{L2}^w, \mathbf{j}_{g2}^w$  are explained in the Section 3.5.1.

Air mass balance equation for macrostructure:

$$\bar{\phi}_2 \frac{D(\theta_{L2}^a S_{L2} + \theta_{g2}^a S_{g2})}{Dt} + (\theta_{L2}^a S_{L2} + \theta_{g2}^a S_{g2}) \left( \frac{d\bar{\epsilon}_{v2}}{dt} \right) + \nabla \cdot (\mathbf{j}_{L2}^a + \mathbf{j}_{g2}^a) = -\Gamma^a \quad (\text{Eq. 3-10})$$

Air mass balance equation for microstructure:

$$\begin{aligned} \bar{\phi}_1 \frac{D(\theta_{L1}^a S_{L1} + \theta_{g1}^a S_{g1})}{Dt} - (\theta_{L1}^a S_{L1} + \theta_{g1}^a S_{g1}) \left( \frac{d\bar{\epsilon}_{v1}}{dt} \right) \\ = \Gamma^a - (\theta_{L1}^a S_{L1} + \theta_{g1}^a S_{g1})(1 - \phi) \frac{d\rho_s}{\rho_s} \end{aligned} \quad (\text{Eq. 3-11})$$

Momentum balance equation:

The equation of equilibrium stresses of the double-structure porous media is given by Cauchy's expression.

$$\nabla \cdot \boldsymbol{\sigma} + \mathbf{b} = 0 \quad (\text{Eq. 3-12})$$

where the body forces are given by the gravity and the global density of the medium:

$$\mathbf{b} = \tilde{\rho} \mathbf{g} \quad (\text{Eq. 3-13})$$

$$\tilde{\rho} = \rho_s(1 - \phi) + (\rho_{L1} S_{L1} + \rho_{g1} S_{g1}) \bar{\phi}_1 + (\rho_{L2} S_{L2} + \rho_{g2} S_{g2}) \bar{\phi}_2 \quad (\text{Eq. 3-14})$$

The equations (Eq. 3-6), (Eq. 3-7), (Eq. 3-9), (Eq. 3-10), (Eq. 3-11) and (Eq. 3-12) are the set of fundamental balance equations that must be satisfied simultaneously at every instant of time and at every point of the domain of interest.

### 3.4 Mass transfer mechanism between structural levels

The hydraulic equilibrium between two structural levels is not assumed; that is, at each point of the domain the water potentials ( $\psi$ ) in the macro- and micro-structure may be different, leading to an exchange of mass water and air between them. Sánchez, (2004) and Gens *et al.*, (2011) propose a linear relationship where mass exchangeable,  $\Gamma^i$  ( $i = w, a$ ). The gas pressure is assumed to be the same in both structural levels. Thus, the mass transfer mechanism is only due to the water exchange.

$$\Gamma^w = \gamma(\psi_1 - \psi_2) \quad (\text{Eq. 3-15})$$

where:

- $\psi$  is the total water potential for micro(1)- and macro-structure (2);
- $\gamma$  is a parameter that control the rate of water transfer (often called the leakage parameter).

It is assumed that only matric and gravitational potential contribute to the total potential of the macrostructure but an additional osmotic component may also contribute to the microstructural potential (Gens, 2010). Here, potential is defined in pressure units. As the water exchange is local in space, the gravitational potential will be the same for the two media. Water exchange will therefore be driven by suction differences alone.

$$\Gamma^w = \gamma(s_1 - s_2) \quad (\text{Eq. 3-16})$$

where suction is defined as

$$s = \max(P_g - P_L, 0) \quad (\text{Eq. 3-17})$$

### 3.5 Constitutive equations

The set of balance equations has to be completed with the hydraulic and mechanical constitutive equations. Each structural level behaves according the following way.

#### 3.5.1 Hydraulic constitutive equations

The volumetric advective fluxes used in the balance equations are defined by the mass fraction of the component times the mass flow with respect to the solid phase.

$$\mathbf{j}_\alpha^i = \theta_\alpha^i \mathbf{q}_\alpha \quad (\text{Eq. 3-18})$$

where:

- $i$  indicates the component (w=water and a=air);
- $\alpha$  refers to the phase (L=liquid and g=gas).

The generalized Darcy's law governs liquid and gas flow. This is only formulated for macro-structural level, due to the neglected advective fluxes in the micro-structure.

$$\mathbf{q}_{\alpha 2} = -\frac{\mathbf{k}_2 k_{r\alpha 2}}{\mu_\alpha} (\nabla P_{\alpha 2} - \rho_{\alpha 2} \mathbf{g}) \quad (\text{Eq. 3-19})$$

where:

- $\mathbf{k}_2$  is the intrinsic permeability tensor of the macro-structure;
- $k_{r\alpha 2}$  is the relative permeability of gas and liquid;
- $\mu_\alpha$  is the fluid viscosity which is function of temperature;
- $P_{\alpha 2}$  is the gas or liquid pressure at macro-structure;
- $\rho_{\alpha 2}$  is the fluid density;
- $\mathbf{g}$  is the gravity force.

A power law defines the intrinsic permeability, which expresses the effect of degree of saturation (or suction) on global permeability (Eq. 3-20). Intrinsic permeability depends on many factors such as pore size distribution, pore shape, tortuosity and porosity. Here a dependence of intrinsic permeability on porosity is adopted (Eq. 3-21).

$$(k_r)_\alpha = [(S_e)_\alpha]^c \quad (\text{Eq. 3-20})$$

$$\mathbf{k}_2 = \mathbf{k}_{o2} \exp[b(\bar{\Phi}_2 - (\bar{\Phi}_o)_2)] \quad (\text{Eq. 3-21})$$

where:

- $c$  is the power for relative permeability law;
- $S_e$  is the relative saturation degree;
- $\mathbf{k}_{o2}$  is the initial intrinsic permeability tensor.

Finally, the retention curve relates suction (or matric potential) with degree of saturation at both structural levels. Van Genuchten law has been used here. However, there are a number of different expressions designed to fit experimentally determined retention curves.

$$S_e = \left[ 1 + \left( \frac{S}{P_o} \right)^{1/(1-\lambda_o)} \right]^{-\lambda_o} \left( 1 - \frac{S}{P_d} \right)^{\lambda_d} \quad (\text{Eq. 3-22})$$

where  $P_o$ ,  $P_d$ ,  $\lambda_o$  and  $\lambda_d$  are model parameters depicted in the Table 3-4.

This model has the capability to represent the different features of micro- and macro-structure. The Figure 3-8 shows the marked difference between the retention curves of both structural levels. High air entry pressure values and low desaturation rates describe the water properties at the clay aggregates.

### 3.5.2 Mechanical constitutive equations

The framework proposed by Gens and Alonso, (1992) has been an strong foundation for the developing of constitutive models and their implementation in finite element codes. A

subsequent series of works (Alonso, Vaunat and Gens, 1999; Guimaraes, 2002; Sánchez, 2004; Gens *et al.*, 2011) has defined a successful research activity.

Following the work of Sánchez, (2004); phenomenological response of the expansive soils is accomplished by the consideration of several plastic mechanisms that can act jointly or not at different stages of the analysis. The governing small strain-stress equations have been derived in the framework introduced by Rizzi, Maier and Willam, (1996), which provides a consistent and formal mathematical (Eq. 3-23). The microstructure is the seat of the basic physical-chemical phenomena occurring at clay particle level, which is the main responsible of the expansive soils behaviour (Gens & Alonso,1992). This level plays a crucial role in the interpretation of the behaviour exhibited by expansive materials. On the other hand, deformations due to loading and collapse will have a major effect at the macrostructural level. This behaviour can be described by concepts and models of unsaturated non-expansive soils, such as the elasto-plastic Barcelona Basic Model (BBM) developed by Alonso, Gens and Josa, (1990).

A fundamental assumption of the framework is that micro-structural behaviour is not affected by the macrostructure state but it only responds to changes in the driving variables (i.e. stresses and suction) at local microstructural level. In contrast, plastic macro-structural strains may result from deformations of the microstructure.

$$\dot{\varepsilon} = \dot{\varepsilon}^e + \dot{\varepsilon}^p = \dot{\varepsilon}^e + \sum_{n=1}^{na} \dot{\varepsilon}^p \quad (\text{Eq. 3-23})$$

na: number of actives plastic mechanism— $\beta$  and LC

### Constitutive variables

There is a general agreement that at least two constitutive variables are generally required to represent adequately the full range of unsaturated soil behaviour, that is, including strength and deformation. In a valuable analysis, Gens, (2010) call them as the first and second constitutive variables (FCV and SCV). Usually, the FCV tries to account for the overall stress state of the soil, whereas the SCV tends to address mainly the effect of suction changes. The Table 3-2 shows the constitutive variables selected for this constitutive model.

Table 3-2. Constitutive variables used for the double-structure model

	<b>First constitutive variables FCV</b>	<b>Second constitutive variables SCV</b>
<b>micro-structural level</b>	Bishop's effective stress $\sigma'_1 = \sigma_1 - P_{g1} \mathbf{I} + S_1 s_1 \mathbf{I}$	micro-suction $s_1 = \max(P_{g1} - P_{L1}, 0)$
<b>Macro- structural level</b>	Net stress $\sigma''_2 = \sigma_2 - P_{g2} \mathbf{I}$	Macro-suction $s_2 = \max(P_{g2} - P_{L1}, 0)$

### Micro-structural behaviour

The strain fully reversible obeys to the non-linear elasticity. According with the theoretical formulation, the mechanical behaviour of porous media is related to the evolution of the pore volume fraction, that is, in this case  $\bar{\phi}_1$ .  $d\bar{\epsilon}_1$  measures the variation of the micropores with respect to the total volume of the soil. Therefore, the constitutive relation states:

$$d\bar{\epsilon}_1 = \bar{\mathbf{D}}_1^{-1} d\sigma'_1 \quad (\text{Eq. 3-24})$$

$$\bar{\mathbf{D}}_1 = \begin{bmatrix} \bar{K}_1 + \frac{4}{3}\bar{G}_1 & \bar{K}_1 - \frac{2}{3}\bar{G}_1 & \bar{K}_1 - \frac{2}{3}\bar{G}_1 & 0 & 0 & 0 \\ \bar{K}_1 - \frac{2}{3}\bar{G}_1 & \bar{K}_1 + \frac{4}{3}\bar{G}_1 & \bar{K}_1 - \frac{2}{3}\bar{G}_1 & 0 & 0 & 0 \\ \bar{K}_1 - \frac{2}{3}\bar{G}_1 & \bar{K}_1 - \frac{2}{3}\bar{G}_1 & \bar{K}_1 + \frac{4}{3}\bar{G}_1 & 0 & 0 & 0 \\ 0 & 0 & 0 & \bar{G}_1 & 0 & 0 \\ 0 & 0 & 0 & 0 & \bar{G}_1 & 0 \\ 0 & 0 & 0 & 0 & 0 & \bar{G}_1 \end{bmatrix} \quad (\text{Eq. 3-25})$$

$$\bar{K}_1 = \frac{1+e}{1+e_1} K_1 \quad (\text{Eq. 3-26})$$

$$K_1 = \frac{p'_1}{(1+\phi_1)\kappa_1} \quad (\text{Eq. 3-27})$$

where

- $e$  is the void ratio of the expansive clay;
- $e_1$  is the void ratio at macro-structural level;
- $\bar{K}_1$  and  $\bar{G}_1$  are the bulk and shear modulus;
- $p'_1$  is the mean Bishop's effective stress at micro-structure.

From the mean effective stress state  $p'_1$  and suction  $s_1$ , it is possible to determine if the micro-structure (clay aggregates) swell or contract.

### Macro-structural behaviour

The inclusion of this structural level in the analysis allows the consideration of phenomena that affect the skeleton of the material (such as macro-structural collapses), which have a strong influence on the macroscopic response of expansive materials. This model is able to reproduce many of the basic patterns of behaviour observed in non-expansive soils (Alonso, Gens and Josa, 1990). In that sense, it is a proper law to model the macro-structural behaviour.

The BBM is an elasto-plastic strain-hardening model, which extends the concept of critical state for saturated soils to the unsaturated conditions. The constitute behaviour at this level is given by:

$$\sigma''_2 = \mathbf{D}_2 (d\epsilon_2 - d\epsilon_{s_2}^r - d\epsilon_{LC}^p) \quad (\text{Eq. 3-28})$$

where

- $\boldsymbol{\varepsilon}_{s_2}^r$  is the reversible strain tensor due to suction changes;
- $\boldsymbol{\varepsilon}_{LC}^p$  is the plastic strains at macro-structural level;
- $\boldsymbol{\varepsilon}_2$  is the strain at macro-structure;
- $\mathbf{D}_2$  is the constitutive tensor. Equivalent to  $\bar{\mathbf{D}}_1$  at this level.

The assumption of null fabric changes at the elastic range seems physically reasonable (Figure 3-4). This means that the slips between the clay aggregates are the main factor of irreversibility at macro-structural level. This imposes geometrical restriction that relates the elastic modulus of micro- and macro-structure.

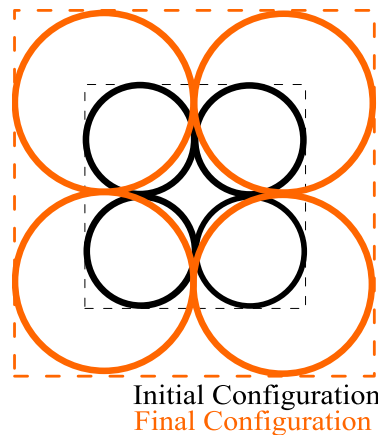


Figure 3-4. Constant fabric of the double-structure porous media at purely reversible behaviour.

$$\bar{K}_2 = \max \left[ \frac{1 + \bar{e}_2}{\bar{\kappa}_2} p_2'', (\bar{K}_2)_{\min} \right] \quad (\text{Eq. 3-29})$$

$$\bar{G}_2 = \frac{3(1 - 2\nu)}{2(1 + \nu)} \bar{K}_2 \quad (\text{Eq. 3-30})$$

$$K_s = \max \left[ \frac{(1 + \bar{e}_2)(s_2 + p_{\text{atm}})}{\kappa_s}, (K_s)_{\min} \right] \quad (\text{Eq. 3-31})$$

$$K = K_1 = \bar{\phi}_2 \bar{K}_2 \quad (\text{Eq. 3-32})$$

$$G = G_1 = \bar{\phi}_2 \bar{G}_2 \quad (\text{Eq. 3-33})$$

In the BBM the yield surface depends not only on the stress level and on the history variables (as in a critical state model) but also on the matric suction, as it can be observed in Figure 3-5. A basic point of the model is that the size of the yield surface increases with suction. The trace of the yield function on the isotropic p-s plane is called the LC (Loading-Collapse) yield curve, because it represents the locus of activation of irreversible deformations due to loading increments or collapse (when the suction reduces). The constitutive formulae for define the yield surface and plastic potential are:

$$F_{LC} = C_F g_F^2(\theta) J^2 - (p + p_s)(p_o - p) \quad (\text{Eq. 3-34})$$

$$C_F = \frac{3}{M_F^2 g_F^2\left(-\frac{\pi}{6}\right)} \quad (\text{Eq. 3-35})$$

$$M_F = \frac{6 \sin \varphi}{3 - \sin \varphi} \quad (\text{Eq. 3-36})$$

$$p_o = p_c \left( \frac{p_o^*}{p_c} \right)^{\frac{\lambda_{\text{sat}} - \bar{\kappa}_2}{\lambda(s_2) - \bar{\kappa}_2}} \quad (\text{Eq. 3-37})$$

$$G = G_1 = \bar{\phi}_2 \bar{G}_2 \quad (\text{Eq. 3-38})$$

$$p_s = (p_s)_o + k_s s_2 \quad (\text{Eq. 3-39})$$

$$\lambda(s_2) = \lambda_{\text{sat}} [r + (1 - r)e^{-\beta s_2}] \quad (\text{Eq. 3-40})$$

$$G_{LC} = \alpha_{\text{BBM}} \frac{3}{M_F^2} \frac{g_G^2(\theta)}{g_G^2\left(-\frac{\pi}{6}\right)} J^2 - (p + p_s)(p_o - p) \quad (\text{Eq. 3-41})$$

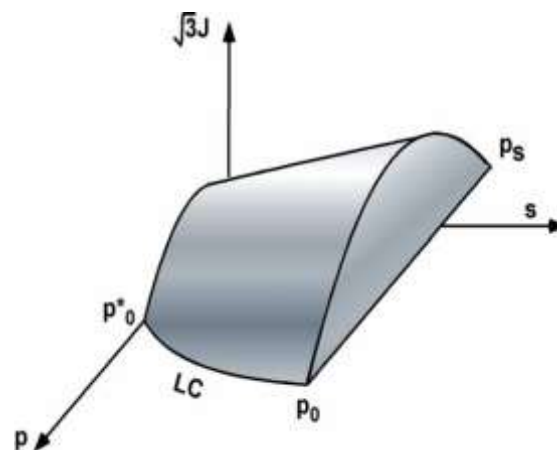


Figure 3-5. Three-dimensional representation of the *BBM* yield surface

Finally, the position of the LC curve is given by the value of the hardening variable  $p_o^*$ , which is the pre-consolidation yield stress of the saturated state (Eq. 3-42).

$$\frac{dp_o^*}{d\varepsilon_v^p} = \frac{(1 + \bar{e}_2)p_o^*}{\lambda_{\text{sat}} - \bar{\kappa}_2} = \frac{p_o^*}{(1 - \bar{\phi}_2)(\lambda_{\text{sat}} - \bar{\kappa}_2)} \quad (\text{Eq. 3-42})$$

#### Mechanical interaction of the structural levels ( $\beta$ )

According to Gens and Alonso (1992), the plastic macro-structural strain induced by micro-structural effects can be evaluated by the expression:

$$d\varepsilon_\beta = f_\beta d\bar{\varepsilon}_1 \quad (\text{Eq. 3-43})$$

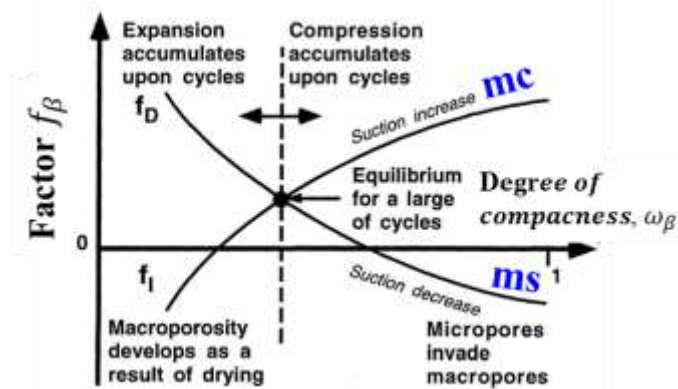


Figure 3-6. Interaction functions

Two interaction functions are defined: **mc** for microstructural contraction paths and **ms** for microstructural swelling paths. In the case of generalized load, the interaction function depends on the degree of compactness. Figure 3-6 presents a generic representation of the interaction function. Several expressions have been formulated for these functions. Here, the proposal of Gens *et al.*, (2011) is adopted. The source of this structural interaction comes from the geometrical reorganization of the clay aggregates under hydro-mechanical actions.

Finally, the hardening of the whole double-structure medium is given by the evolution of the isotropic yield stress due to the plastic strains of the structural interaction and macro-structure itself.

$$dp_o^* = \frac{(1 + \bar{e}_2)p_o^*}{\lambda_{sat} - \kappa_2} d\epsilon_v^p = \frac{(1 + \bar{e}_2)p_o^*}{\lambda_{sat} - \kappa_2} (d\epsilon_{LC}^p + d\epsilon_\beta) \quad (\text{Eq. 3-44})$$

### 3.6 Input parameters

The overall hydro-mechanical formulation of the expansive clays as multiphase double-structure material requires a large number of parameter (Table 3-3). It is necessary to stress the fact that most of them have physical meaning and they are easily measurable. Gens *et al.*, (2011) proven that from a systematic experimental program all of them can be determined.

Table 3-3. Input parameters of the double structure model (UPC team)

<b>Effective stress for micro-structural level</b>	$\chi$	Bishop's effective stress parameter for micro-structure
<b>Non-linear elasticity</b>	$\bar{\kappa}_2$	Slope of the unloading/reloading related to the Macro-structure
	$\kappa_s$	Slope of the drying/wetting related to expansive clay
	$(\bar{K}_2)_{min}$	Minimum value of volumetric elastic modulus related to the Macro-structure.
	$(K_s)_{min}$	Minimum value of volumetric elastic modulus related to the suction at Macro-structure.
	$\nu$	Poisson's ratio

<b>Mechanical interaction Macro-micro Interaction functions</b>	$f_{ms0}$	Parameters for the case of micro-structure swelling
	$f_{ms1}$	
	$n_{ms}$	
	$f_{mc0}$	Parameters for the case of micro-structure contraction
	$f_{mc1}$	
	$n_{mc}$	
<b>Macro-structural level Plastic mechanism (BBM)</b>	$\varphi$	Friction angle
	$p_c$	Parameter in LC curve (MPa)
	$\lambda_{sat}$	Slope of the virgin loading at saturated state
	$r$	Parameter in LC curve
	$\beta$	Parameter in LC curve
	$k_s$	Coefficient setting the increase of tensile strength with suction
	$\alpha$	Coefficient of non-associativity
<b>Hydraulic interaction Macro-micro</b>	$\gamma$	Leakage parameter (kg/s.m <sup>3</sup> )
<b>Liquid density at micro-structural level</b>	$\rho_{L10}$	Reference density (default= 1002.6 kg/m <sup>3</sup> )
	$\beta_{\rho L10}$	Compressibility (default= 4.5x10 <sup>-40</sup> MPa <sup>-1</sup> )
	$\alpha_{\rho L10}$	Volumetric thermal expansion coefficient for water (default= -3.4x10 <sup>-40</sup> C <sup>-1</sup> )
	$\gamma_{\rho L10}$	Solute variation (default=0.6923)
	$P_{L10}$	Reference pressure (default=0.1 MPa)
<b>Liquid density at Macro-structural level</b>	$\rho_{L20}$	Reference density (default= 1002.6 kg/m <sup>3</sup> )
	$\beta_{\rho L20}$	Compressibility (default= 4.5x10 <sup>-40</sup> MPa <sup>-1</sup> )
	$\alpha_{\rho L20}$	Volumetric thermal expansion coefficient for water (default= -3.4x10 <sup>-40</sup> C <sup>-1</sup> )
	$\gamma_{\rho L20}$	Solute variation (default=0.6923)
	$P_{L20}$	Reference pressure (default=0.1 MPa)
<b>Water retention curve for micro-structural level</b>	$(P_{T0})_1$	Measured air entry pressure (MPa)
	$\sigma_{T0}$	Surface tension at temperature in which $(P_{T0})_1$ was measured (Usually 0.072 N/m at 20°C)
	$(\lambda_o)_1$	Shape function
	$(S_r)_{L1}$	Residual saturation
	$(S_m)_{L1}$	Maximum saturation
	$(P_d)_1$	Pressure related with suction at zero degree of saturation
	$(\lambda_d)_1$	Model parameter
<b>Water retention curve for Macro-structural level</b>	$(P_{T0})_2$	Measured air entry pressure (MPa)
	$\sigma_{T0}$	Surface tension at temperature in which $(P_{T0})_2$ was measured (Usually 0.072 N/m at 20°C)
	$(\lambda_o)_2$	Shape function
	$(S_r)_{L2}$	Residual saturation
	$(S_m)_{L2}$	Maximum saturation
	$(P_d)_2$	Pressure related with suction at zero degree of saturation

	$(\lambda_d)_2$	Model parameter
<b>Intrinsic permeability for the double-structure medium</b>	$(k_o)_{11}$	Intrinsic permeability, 1 <sup>st</sup> principal direction ( $m^2$ )
	$(k_o)_{22}$	Intrinsic permeability, 2 <sup>nd</sup> principal direction ( $m^2$ )
	$(k_o)_{33}$	Intrinsic permeability, 3 <sup>rd</sup> principal direction ( $m^2$ )
	$(\phi_o)_2$	Reference porosity for read intrinsic permeability
	$(\phi_{min})_2$	Minimum porosity
<b>Relative permeability for the double-structure medium</b>	A	Constant
	b	Power
<b>Solid phase</b>	$\rho_s$	Solid density ( $kg/m^3$ )
<b>Initial conditions</b>	$P_o^*$	Isotropic yield stress at saturated state (MPa)
	$\phi$	Initial value of total porosity
	$\bar{\phi}_1$	Initial value of micro pore volume fraction
	$P_{L1}$	Initial value of liquid pressure at micro-structural level (MPa)
	$P_g$	Initial value of gas pressure (MPa)

### 3.7 Partial performance

The constitutive model described above has been implemented in the numerical code CODE\_BRIGHT (Olivella *et al.*, 1996). So far, the first objective is the description of some qualitative features. In this way, the capabilities and limitations of this formulation can be more readily assessed. The most natural way is to run the constitutive model on some suggested stress path (single element test) using credible set of input parameters. The solution of complex boundary value problems can be considered as a future goal.

The parameters used in this single element testing was obtained from the bentonite mixture (50% Powder/50% Pellets) reported by Gens *et al.*, (2011). They executed a detailed characterization, laboratory testing and microstructural visualization; indicating the homogenization process of this kind of material under hydro-mechanical (HM) actions. The input parameter calibration is done through the numerical modelling, as simple boundary value problem, of an oedometer swelling test (Figure 3-7) of this mixture at dry density of  $1.60 \text{ g/cm}^3$ .

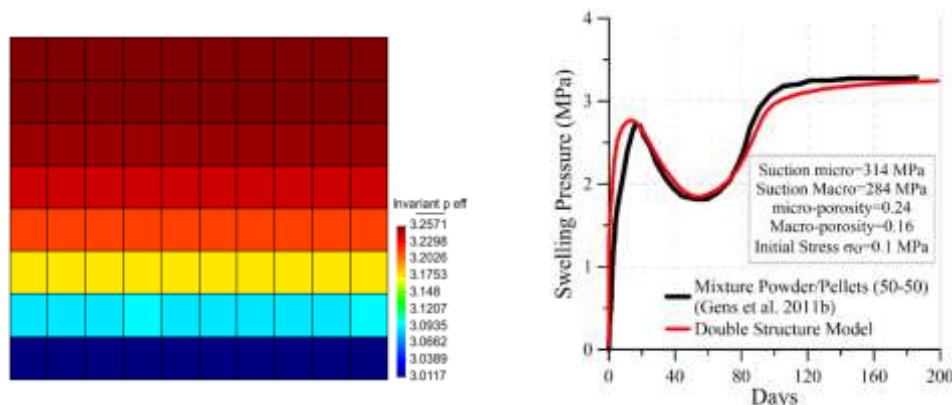


Figure 3-7. Numerical modelling of laboratory oedometer swelling pressure tests with the double structure model.

The initial conditions are determined by the experimental data reported in the Table 3-4 and the initial suction values obtained from the water retention curves (WRC) of each structural level (Figure 3-8).

Table 3-4. Main characteristic of swelling pressure test (from Gens *et al.*, 2011).

Sample height (mm)	Diameter (mm)	Void ratio of sample	Dry density of sample (g/cm <sup>3</sup> )	Initial water content of sample (%)	Dry density of pellets (g/cm <sup>3</sup> )	Initial water content of pellets (%)	Dry density of powder (g/cm <sup>3</sup> )	Initial water content of powder (%)
100	120	0.67	1.60	4.78	1.89	4.49	1.39	5.07

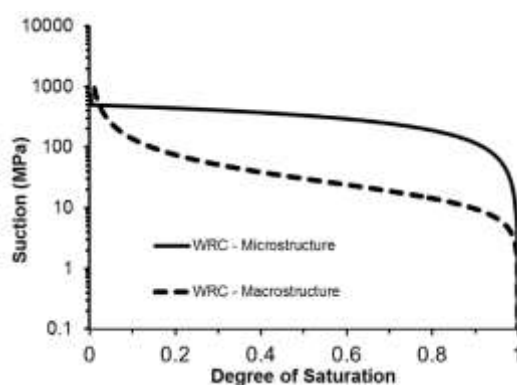


Figure 3-8. Water retention curves (WRC) for macro- and micro-structure of the powder-pellets mixture (from Gens *et al.*, 2011).

In the following items, several key features are explored in order to define some possible actions on the ongoing modelling work. Finally, the partial performance of the model is summarized in the Table 3-5.

### 3.7.1 Dependence of swelling strain on applied stress at the same dry density

As pointed Alonso, Pinyol and Gens, (2013); the development of elasto-plastic constitutive models provides an alternative way to characterise the initial state of compacted soils by associating model parameters and variables with the pair dry unit weight and water content ( $\gamma_d$ ,  $w$ ), which defines the ‘as-compacted’ condition. For instance, the dry density achieved by compaction can be related to the position of the initial yield surface after compaction. Water content, on the other hand, is controlled mainly by the current suction,  $s$ , and to a lesser extent by the void ratio. In the context of the simple elasto-plastic BBM model (Alonso, Gens and Josa, 1990), the yield surface is essentially defined by the isotropic yield stress for saturated conditions,  $P_0^*$ : Therefore, as a starting point, the pair ( $P_0^*$ ,  $s$ ) may provide equivalent information to ( $\gamma_d$ ,  $w$ ), with one added advantage: they supply fundamental information for constitutive modelling.

Under constant hydration rate (Figure 3-9), three swelling tests are performed under constant isotropic net stress (0.5, 1.0 and 1.5 MPa). The initial loading-collapse curve LC is determined by the initial conditions (Figure 3-7 and Table 3-4). A clear dependence of

swelling strains on applied stress at the same dry density is proven (Figure 3-10). This effect is produced by the location of the stress path respect to the LC curve. Macro-structural collapse are generated when we cross this yield limit. After the macro-structural collapse the strain response indicate a progressive swelling due to the subsequent micro-structural evolution. The mass transfer mechanism between macro- and micro-structural levels is always activated.

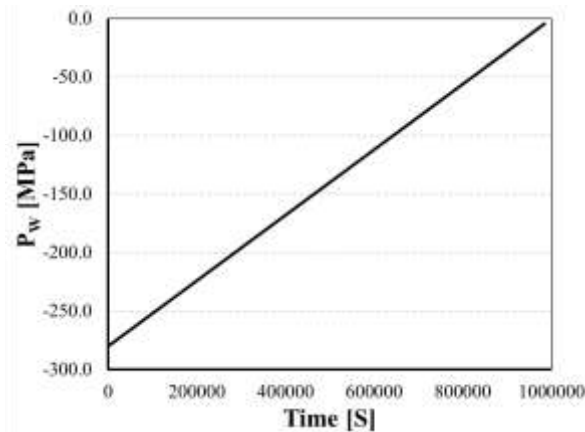


Figure 3-9. Hydration rate for swelling test at constant isotropic stress.

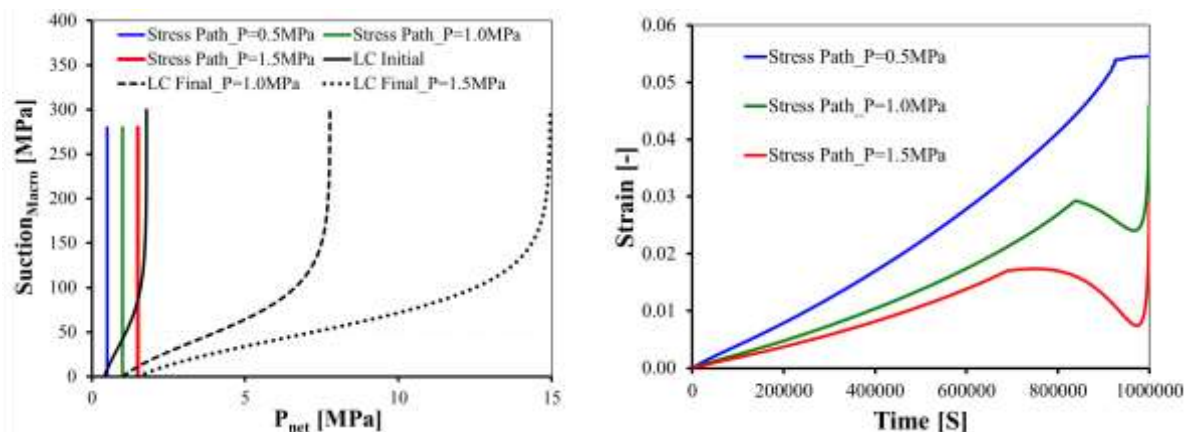


Figure 3-10. Wetting paths under constant isotropic net stress at the same dry density.

### 3.7.2 Dependence of swelling pressure on dry density

Now, the variation of the dry density generates different location of LC curves. Values of 0.40, 1.0 and 1.5 MPa are selected by for the isotropic yield stress at saturated state  $P_0^*$ .

The swelling pressure tests are conducted starting from the same initial stress state and preventing any deformation. Using the imposed hydration rate of the above case, different values and kinetic evolution of swelling pressure are observed (Figure 3-11). An initial swelling pressure increase is followed by the macro-structure collapse. Again, the evolution of the micro-structural level continues after macro-structural rearrangement.

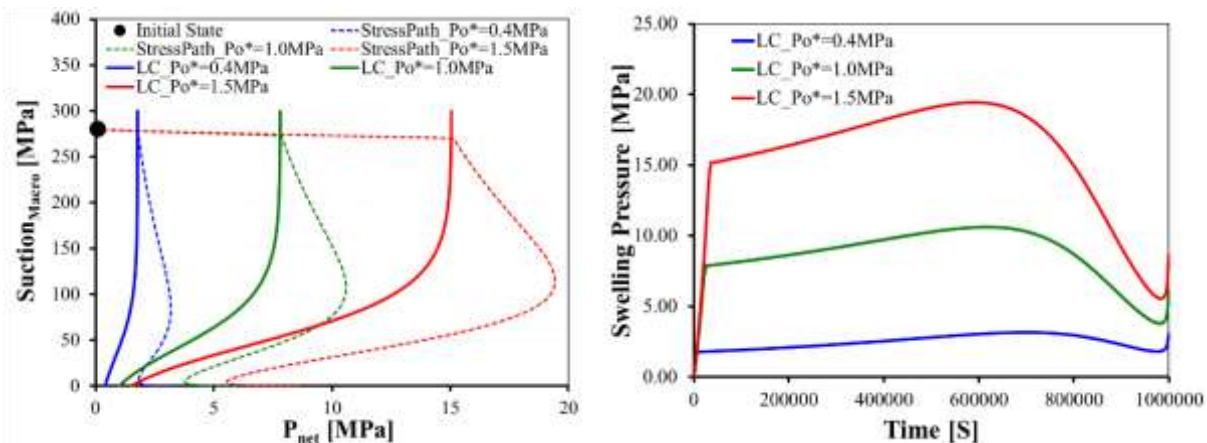


Figure 3-11. Suction stress paths in swelling pressure test.

### 3.7.3 Irreversibility of strains in wetting/drying cycles

The final test consider a wetting/drying cycle at constant stress isotropic stress. The wetting-drying rates indicated in the Figure 3-12 are performed at mean net stress of 0.3 MPa and 1.5 MPa (Figure 3-13). The strain irreversibility is clearly obtained (Figure 3-14). The suction path done at mean stress of 0.3 MPa shows a noteworthy response. It generates a small plastic deformation; despite it does not cross the initial LC curve. This happens thanks to the structural interaction mechanism; at some point the suction path touches the evolving LC curve.

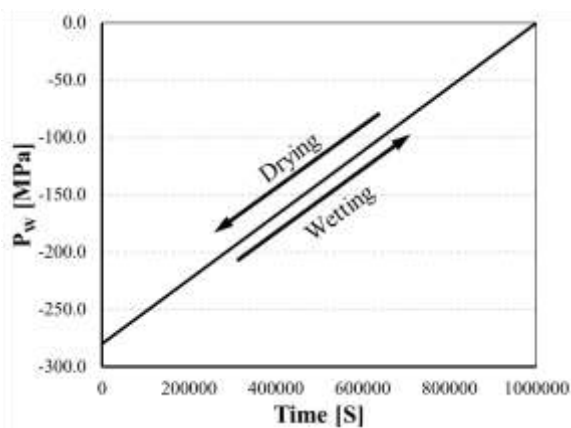


Figure 3-12. Hydration rate for wetting and drying cycle.

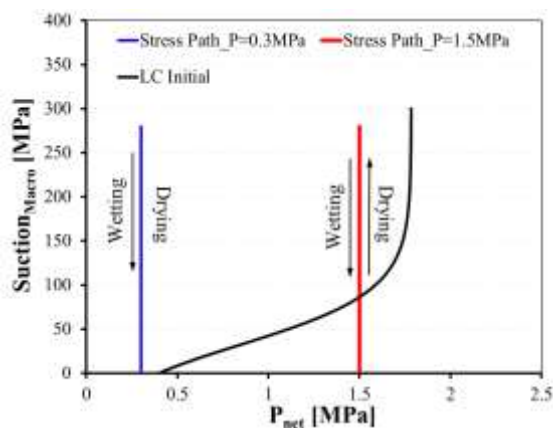


Figure 3-13. Wetting/Drying test at constant isotropic net stress.

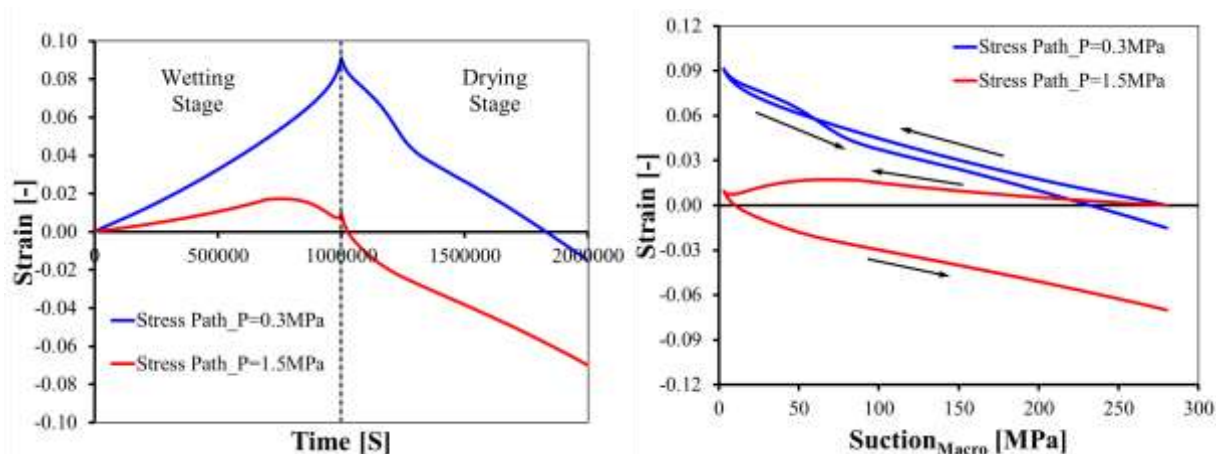


Figure 3-14. Strain irreversibility after one wetting-drying cycle

Table 3-5. Summary of the partial performance of the model (UPC team)

Name of the constitutive law: <b>Double Structure Model (UPC team)</b>			
Behaviour feature	YES	NO	Remarks
<b>Mechanical behaviour</b>			
Dependence of swelling strain on applied stress (at the same dry density) (Figure 3-10)	X		The location of the stress state respect to the LC curve generates this dependence. See Section 3.7.1.
Dependence of swelling stress on dry density (at the same stress)	---	---	The analysis performed at section 3.7.1. does not reflect this dependence in a single element test. The imposition of the stress state avoids the evolution of swelling stress. The better way to check this dependency is through swelling pressure test (Section 3.7.2)
Irreversibility of strains in wetting/drying cycles (Figure 3-14)	X		The irreversible strains are generated in wetting/drying paths that cross the LC curve. See Section 3.7.3.
Dependence of swelling pressure on dry density (Figure 3-11)	X		At the same initial conditions, stress state and suction, different values of the isotropic yield stress for saturated conditions $P_o^*$ (dry density) generate different kinetics and final values of swelling pressure. See Section 3.7.2.
Stress path dependence from an unsaturated to a saturated state	X		This feature comes from the hydro-mechanical (HM) constitutive formulation. Numerical testing requires an additional effort related to the numerical implementation. The transition of saturated to unsaturated (or vice versa) is not trivial issue with the net stress as stress variable.
Stress path dependence from a saturated to an unsaturated state	X		

Double structure/porosity considered?	X		The expansive clay is considered as a multiphase porous media composed by the arrangement of clay aggregates and micro- and macro-pores
Are temperature effects considered in the model?		X	The formulation presented here is Hydro-Mechanical (HM). This team is working (in parallel way) on the Thermo-Hydro-Mechanical (THM) coupling.
Dependence of strains developed in a temperature cycle (increase/decrease) on OCR (or stress)		X	---
<b>Hydraulic behaviour (retention curve)</b>			
Hysteresis		X	---
Dependence on void ratio		X	Ongoing work.
Double structure/porosity considered?	X		Macro- and micro-structural levels are associated to different water retention curve (WRC). The evolution of these WRC depends on the successful development of the above feature.

## 4 Concluding remarks and future developments

This report contains the coupled hydro-mechanical modelling of unsaturated expansive clays generated by the UPC team as part of the European research project BEACON —Bentonite mechanical evolution.

The main physical feature of expansive clays is the existence of a two pore structures. Strain irreversibility and stress path dependency are attributed to the effects of microstructural (particle level) deformation on the macrostructure.

The expansive clay has been considered as an unsaturated double-structure porous media. The internal structure and its evolution are the main responsible of the hydro-mechanical response.

Consistent governing equations and constitutive relations have been stated. New features are taking into account in this hydro-mechanical formulation:

- Unsaturated micro-structure
- Hydraulic non-equilibrium condition between macro- and micro-structure

Partial model performance proven the good reproduction of key features of the hydro-mechanical behaviour of the expansive clays.

Some specific issues (i.e. transition from unsaturated to saturated state) requires a more detailed analysis.

## 5 References

- Alonso, E. E., Gens, A. and Josa, A. (1990) 'A constitutive model for partially saturated soils', *Géotechnique*, 40(3), pp. 405–430.
- Alonso, E. E., Pinyol, N. M. and Gens, A. (2013) 'Compacted soil behaviour: initial state, structure and constitutive modelling', *Géotechnique*, 63(6), pp. 463–478.
- Alonso, E. E., Vaunat, J. and Gens, A. (1999) 'Modelling the mechanical behaviour of expansive clays', *Engineering Geology*, 54, pp. 173–183.
- de Boer, R. (2005) *Trends in continuum mechanics of porous media*. Netherlands: Springer.
- Borja, R. I. and Choo, J. (2016) 'Cam-Clay plasticity, Part VIII: A constitutive framework for porous materials with evolving internal structure', *Computer Methods in Applied Mechanics and Engineering*, 309, pp. 653–679.
- Borja, R. I. and Koliji, A. (2009) 'On the effective stress in unsaturated porous continua with double porosity', *Journal of the Mechanics and Physics of Solids*. Elsevier, 57(8), pp. 1182–1193.
- Brackley, I. J. (1975) 'Swell under load.', in *Proc. 6th Reg. Conf. for Africa on SMFE. DURBAN*, pp. 65–70.
- Burland, J. B. (1990) 'On the compressibility and shear strength of natural clays', *Géotechnique*, 40(3), pp. 329–378.
- Chandler, R. J. (2010) 'Stiff sedimentary clays: geological origins and engineering properties', *Géotechnique*, 60(12), pp. 891–902.
- Chapman, N. A. and Mc Kinley, I. G. (1987) *The geological disposal of nuclear waste*. Chichester:John Wiley.
- Collins, K. and McGown, A. (1974) 'The form and function of microfabric features', *Géotechnique*, 24(2), pp. 223–254.
- Coussy, O. (2004) *Poromechanics*. West Sussex:John Wiley & Sons Ltd.
- Gens, A. (2009) 'On the hydromechanical behaviour of argillaceous hard soils-weak rocks', in Al., A. A. et (ed.) *Proc. 15th European Conference on Soil Mechanics and Geotechnical Engineering – Geotechnics of Hard Soils – Weak Rocks (Part 4)*, Amsterdam: IOS Press; 2013, pp. 71–118.
- Gens, A. (2010) 'Soil–environment interactions in geotechnical engineering', *Géotechnique*, 60(1), pp. 3–74.
- Gens, A. *et al.* (2011) 'Hydromechanical behaviour of a heterogeneous compacted soil: experimental observations and modelling', *Géotechnique*, 61(5), pp. 367–386.
- Gens, A. and Alonso, E. E. (1992) 'A framework for the behaviour of unsaturated expansive clays', *Canadian Geotechnical Journal*, 29(6), pp. 1013–1032.
- Guimaraes, L. D. N. (2002) *Análisis multi-componente no isoterma en medio poroso deformable no saturado (in spanish)*. PhD Thesis, Universitat Politècnica de Catalunya,

Spain.

Guimaraes, L. D. N. *et al.* (2013) ‘A chemo-mechanical constitutive model accounting for cation exchange in expansive clays’, *Geotechnique*, 63(3), pp. 221–234.

Hueckel, T., Loret, B. and Gajo, A. (2001) ‘Expansive clays as two-phase, deformable, reactive continua: concepts and modelling options’, in Maio, C. D., Hueckel, T., and Loret, B. (eds) *Proc. of the Workshop on Chemo-Mechanical Coupling in Clays: From Nano-Scale to Engineering Applications. Maratea, Italy.*, pp. 105–120.

Jacinto, A. C., Villar, M. V. and Ledesma, A. (2012) ‘Influence of water density on the water-retention curve of expansive clays’, *Géotechnique*, 62(8), pp. 657–667.

Leroueil, S. and Vaughan, P. R. (1990) ‘The general and congruent effects of structure in natural soils and weak rocks’, *Géotechnique*, 40(3), pp. 467–488.

Lewis, R. W. and Schrefler, B. A. (1998) *The finite element method in the static and dynamic deformation and consolidation of porous media*. John Wiley and Sons, Ltd.

Lloret, A. *et al.* (2003) ‘Mechanical behaviour of heavily compacted bentonite under high suction changes’, *Géotechnique*, 53(1), pp. 27–40.

Mitchell, J. K. (1976) *Fundamentals of Soil Behavior. 1st ed.* New York: Wiley.

Murad, M. and Cushman, J. (2000) ‘Thermomechanical theories for swelling porous media with microstructure’, *International Journal of Engineering Science*, 38(5), pp. 517–564.

Musso, G., Romero, E. and Della Vecchia, G. (2013a) ‘Double-structure effects on the chemo-hydro-mechanical behaviour of a compacted active clay’, *Géotechnique*, 63(3), pp. 206–220.

Musso, G., Romero, E. and Della Vecchia, G. (2013b) ‘Double-structure effects on the chemo-hydro-mechanical behaviour of a compacted active clay’, *Géotechnique*, 63(3), pp. 206–220.

Olivella, S. *et al.* (1994) ‘Non-isothermal multiphase flow of brine and gas through saline media’, *Transport in Porous Media*, 15(3), pp. 271–293.

Olivella, S. (1995) *Non-isothermal multiphase flow of brine and gas through saline media. PhD Thesis, Universitat Politècnica de Catalunya, Spain.*

Olivella, S. *et al.* (1996) ‘Numerical formulation for a simulator (CODE\_BRIGHT) for the coupled analysis of saline media’, *Engineering Computations*, 13(7), pp. 87–112.

Rizzi, E., Maier, G. and Willam, K. (1996) ‘On failure indicators in multidissipative materials’, *Int. J. Solids Structures*, 33(20–22), pp. 3187–3214.

Romero, E. (1999) *Thermo-hydro-mechanical behaviour of unsaturated Boom clay: an experimental study. PhD Thesis, Universitat Politècnica de Catalunya, Spain.*

Romero, E., Della Vecchia, G. and Jommi, C. (2011) ‘An insight into the water retention properties of compacted clayey soils’, *Géotechnique*, 61(4), pp. 313–328.

Ruiz, D. F. *et al.* (2017a) ‘Analysis of the hydration of an unsaturated seal’, in *Second Pan-American Conference on Unsaturated Soils, PanAm-UNSAT 2017. Dallas, USA.*, pp. 1–11.

- Ruiz, D. F. *et al.* (2017b) ‘Hydro-mechanical modelling of a gallery sealing over the entire life of a deep repository’, in *6th International Conference on Coupled THMC Processes in Geosystems, GeoProc 2017. París, France.*, pp. 120–121.
- Salimzadeh, S. and Khalili, N. (2016) ‘Three-Dimensional Numerical Model for Double-Porosity Media with Two Miscible Fluids Including Geomechanical Response’, *International Journal of Geomechanics*, 16(3), p. 4015065.
- Sánchez, M. (2004) *Thermo-Hydro-Mechanical coupled analysis in low permeability media. PhD Thesis, Universitat Politècnica de Catalunya, Spain.*
- Sánchez, M. *et al.* (2005) ‘A double structure generalized plasticity model for expansive materials’, *International Journal for Numerical and Analytical Methods in Geomechanics*, 29(8), pp. 751–787. doi: 10.1002/nag.434.
- Santamarina, J. C. *et al.* (2001) ‘Micro-scale aspects of chemical-mechanical coupling: Interparticle forces and fabric’, in Maio, C. D., Hueckel, T., and Loret, B. (eds) *Proc. of the Workshop on Chemo-Mechanical Coupling in Clays: From Nano-Scale to Engineering Applications. Maratea, Italy.*, pp. 47–64.
- Schmertmann, J. H. (1964) ‘Generalizing and measuring the Hvorslev effective components of shear resistance’, in *Symposium on Laboratory Shear Testing of Soils, Ottawa, Canada.* American Society for Testing and Materials, ASTM., pp. 147–162.
- Schrefler, B. (2002) ‘Mechanics and thermodynamics of saturated/unsaturated porous materials and quantitative solutions’, *Applied Mechanics Reviews*, 55(4), p. 351.
- Sridhara, A. (2001) ‘Engineering behaviour of clays: Influence of mineralogy’, in Maio, C. D., Hueckel, T., and Loret, B. (eds) *Proc. of the Workshop on Chemo-Mechanical Coupling in Clays: From Nano-Scale to Engineering Applications. Maratea, Italy.*, pp. 3–28.

# D3.1



## A numerical hydro-mechanical model for unsaturated soils

### DELIVERABLE (D3.1)

## ANNEX I

**Author(s): Gramegna L, Charier R.**

Reporting period: 01/06/17 – 30/11/18

Date of issue of this report: **05/03/18**

Start date of project: **01/06/17**

Duration: 48 Months

This project receives funding from the Euratom research and training programme 2014-2018 under grant agreement No 745 942

**Dissemination Level (confidential)**

**PU** Public

**REVIEW**

Name	Internal/Project/External	Comments

**DISTRIBUTION LIST**

Name	Number of copies	Comments
Athanasios Petridis (EC) Christophe Davies (EC)  Beacon partners		

## **Abstract**

The description of the numerical hydro-mechanical model implemented in LAGAMINE for expansive clay is given. After providing the input parameters, a number of simulations is run in order to obtain relevant information about model's performances.

The results are finally presented.

# Content

<b>1. Introduction.....</b>	<b>5</b>
<b>2. Hydraulic model.....</b>	<b>6</b>
2.1 Background .....	6
2.2 Mathematical formulation.....	9
2.2.1 Microstructural water retention domain .....	10
2.2.2 Macrostructural water retention domain: .....	11
2.2.3 Microstructure evolution .....	12
2.2.4 Water permeability evolution.....	12
<b>3. Mechanical model .....</b>	<b>13</b>
3.1 Background .....	13
3.2 Mathematical formulation.....	14
3.2.1 Isotropic stress states.....	15
3.2.2 Triaxial stress states.....	17
3.2.3 Three dimensional stress states.....	18
3.2.4 New formulation of BBM .....	20
<b>4. Input parameters.....</b>	<b>21</b>
4.1 Hydraulic parameters .....	21
4.2 Mechanical parameters .....	22
<b>5. Performance .....</b>	<b>23</b>
5.1 Dependence of swelling strain on applied stress and on dry density .....	23
5.1.1 Different confining pressures, same dry density .....	23
5.1.2 Same confining pressures, different dry densities .....	25
5.2 Irreversibility of strains in wetting/drying cycles.....	26
5.3 Behaviour during swelling stress test. Dependence of swelling pressure on dry density....	27
5.4 Stress path dependence from an unsaturated to a saturated state.....	28
<b>6. Conclusions.....</b>	<b>30</b>
<b>7. References .....</b>	<b>31</b>

## 1. Introduction

The BEACON project (bentonite mechanical evolution) promotes the development of a dense academic network for a better understanding concerning bentonite-based materials.

This highly sensitive clay has indeed been selected due to the development of high swelling capacity and swelling stress, low permeability and important retention capacities as component of engineered barriers for nuclear waste disposals.

In order to assess the safeness of such kind of sealing system, it becomes fundamental to predict the capabilities of the hydro-mechanical behaviour of bentonite buffers, seals and backfills for all radioactive waste management programs using bentonite.

Due to this, many European universities are involved in this project, which is divided in a number of work-packages ranging from the experimental practice of multiscale tests to the numerical descriptions of long-time-term behaviour of bentonite materials, but also to the creation of a database available to all the members and many other activities.

The University of Liège, well known for the development of the finite element code LAGAMINE, takes part to this project and, in the present report, aims to describe the current state of the used hydro-mechanical model.

The concept of bimodal pore size distribution for both water retention behaviour and water permeability's evolution has been recently introduced in LAGAMINE (Dieudonné, 2016). In addition, a threshold value has been postulated in order to simulate some mechanical features of bentonite upon full saturation.

This modelling strategy will be further explained in this report.

Additionally, the mechanical part of the model will be treated. It consists on the well-known Barcelona Basic Model (BBM), which will also be briefly described.

Provided the basic mathematical and physical description of the model, the input parameters will be presented.

Those parameters will be further adopted in order to test the efficiency of the finite element code LAGAMINE via a number of simple tests.

The performances of the model will be commented and a summary table will be given as conclusion.

## 2. Hydraulic model

### 2.1 Background

The role of bentonite is central in engineered barriers for geological disposal of radioactive waste.

Upon saturation, the swelling capacity of such kind of material has to guarantee the fill of technological gaps assuring a tight contact with the host rock in order to prevent the formation of preferred pathways to the biosphere for radionuclide. In this context, also its low permeability competes to the efficiency of engineered barriers.

Experimental observations from large-scale in situ tests have shown that the transient stage of the hydration process may lead to a non-homogeneous distribution of dry density within the bentonite buffer.

Due to this, a better understanding of the water retention properties of bentonite is required.

In this context, it is suspected that the microscale hydraulic phenomena play a major role in the macroscopic hydraulic behaviour.

Neglecting the description of the available experimental techniques, some empirical observations on the microstructure of unsaturated soils and their water retention domains are presented.

Experimental campaigns led through mercury intrusion porosimetry and micrographs (See Figure 2-1 and 2-2), by (Lloret, et al., 2003) showed a bimodal pore size distribution for Febex bentonite compacted to different dry densities.

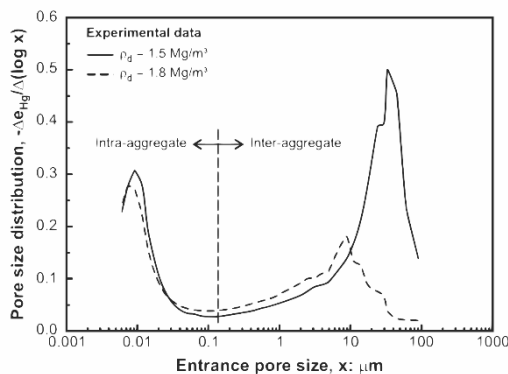


**Figure 2-1. Pore size distribution of Febex bentonite compacted at different dry densities,  $\rho_d = 1,5 \text{ Mg/m}^3$  and  $\rho_d = 1,8 \text{ Mg/m}^3$  (Lloret, et al., 2003).**

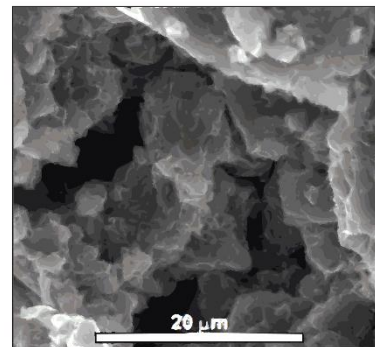


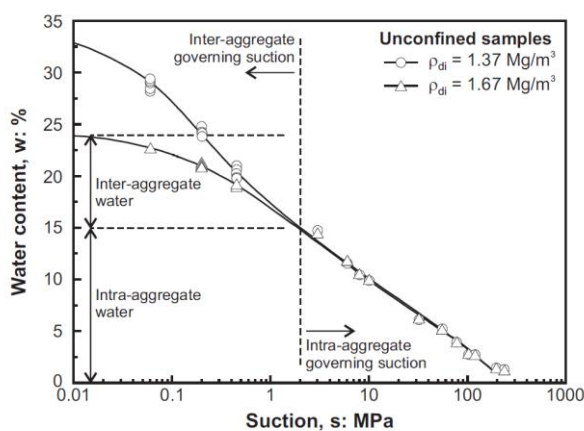
**Figure 2-2. Micrographs of Compacted Febex bentonite with dry density  $\rho_d = 1,72 \text{ Mg/m}^3$  and water content  $w = 13.7\%$  (Lloret, et al., 2003) obtained using scanning electron microscope.**

It can be observed that the macro-pores distribution is affected by the different compaction, whereas the micropores distribution remains quite constant.

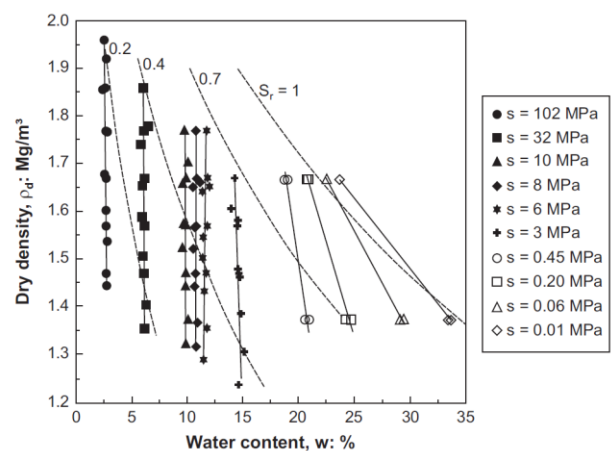
The bimodal pores distribution of bentonite is also supposed to be translated in the existence of two water retention domains.

One precursor of this concept was Romero (Romero, Gens, & Lloret, Water permeability, water retention and microstructure of unsaturated compacted Boom clay, 1999) publishing results of water retention curves of Boom clay compacted at different dry densities under unconfined conditions (see Figure 2-3 and 2-4).

Results showed that samples of Boom clay displayed bimodal pore size distributions upon compaction. Namely, for high suction values (above around 2 MPa), the water storage is controlled by the intra-aggregates domain (microstructural domain), whereas for lower suction values, the water content is sensitive to variations of the dry density (macrostructural domain). The independence of the water retention properties at high suction values may also be observed in the compaction plane in which the contours of equal suction are represented.



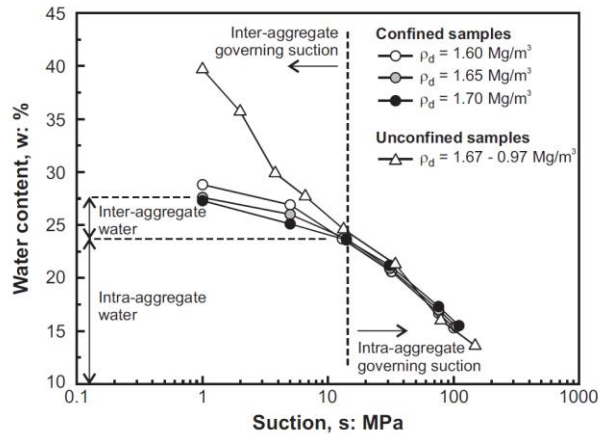
**Figure 2-3. Water retention curves of Boom clay compacted at two dry densities, obtained under unconfined conditions (Romero, Gens, & Lloret, Water permeability, water retention and microstructure of unsaturated compacted Boom clay, 1999).  $\rho_{di}$  denotes the initial dry density.**



**Figure 2-4. Static compaction curves of Boom clay with contours of equal suction (Romero, Gens, & Lloret, Water permeability, water retention and microstructure of unsaturated compacted Boom clay, 1999)**

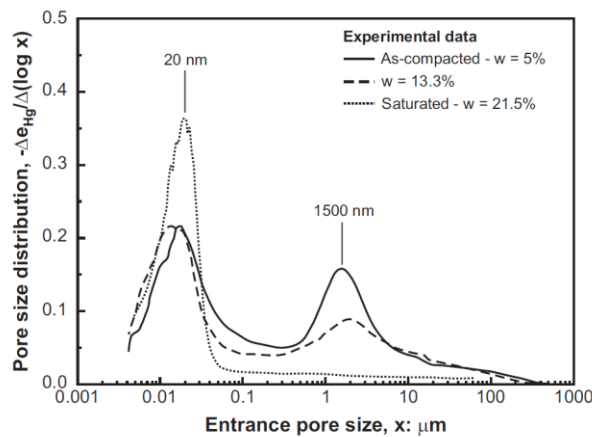
While these observations were made for a compacted clay with low activity, similar observations have been reported by Lloret (Lloret, et al., 2003) and Villar (Lloret & Villar, 2007) on Febex bentonite, among others.

Figure 2-5 presents the water retention curves of compacted Febex bentonite under both confined and unconfined conditions, obtained by Lloret (Lloret, et al., 2003). Samples of Febex bentonite were compacted to different dry densities and then wetted by controlling the surrounding relative humidity. Up to a suction of about 15 MPa, the water retention curve is independent from the dry density, while for lower values of suction, it becomes dry density dependent.



**Figure 2-5. Water retention curves of compacted Febex bentonite obtained under confined and unconfined conditions (Lloret, et al., 2003)**

It seems to be clear that the water storage and hydration mechanisms depend (among other features) on the double structure of bentonite. This double structure is characterized by two main domains: the macroscopic domain, affected by the initial dry density of the material (i.e. compaction), and the microscopic one, where adsorption mechanism takes place. However, it is worth to be noticed that, as a result of the sensitivity of clay minerals to water, the structure of compacted bentonites is significantly affected by changes in water content. In fact, an increase in the water content leads to the swelling of clay layers and particles, hence aggregates. Experimental observations (Seiphoori, Ferrari, & Laloui, 2014) show an increase of volume of the smaller pores and a progressive decrease of the inter-aggregate pore volume for MX-80 bentonite hydrated under constant volume conditions (see Figure 2.6).



**Figure 2-6. Influence of the water content on the pore size distribution of MX-80 bentonite compacted to a dry density  $\rho_d = 1,79 \text{ Mg/m}^3$  and hydrated under constant volume conditions (Seiphoori, Ferrari, & Laloui, 2014)**

Consequently, the structure of the material evolves from a bimodal pore size distribution (as-compacted material) towards a mono-modal distribution

under fully saturated conditions as a consequence of both multi-scale and multi-physical processes (Romero, 2013), having at the macroscale observation expansion and possible wetting collapses. Hence, the non-negligible distinction between micro and macro behaviour of bentonite is taken into account in the following mathematical implementation considering the water storage behaviour and the variation of water permeability.

## 2.2 Mathematical formulation

The unique relationship between suction and the degree of saturation or water content ( (Brooks & Corey, 1964); (van Genuchten, 1980)) does not suit the hydraulic behaviour of highly expansive soils such as bentonite. Indeed, in the case of compacted bentonites, the material swells significantly upon wetting, resulting in important changes in dry density. Consequently, the dependency of the water retention curve on the dry density of the material is a major issue.

Hence, a new model is proposed and implemented and it is currently adopted in Liège (Dieudonné, 2016).

Based on the abovementioned information, the model is formulated in terms of water ratio  $e_w$  reference, which is expressed as the superposition of a contribution from the water stored in the micropores  $e_{wm}$  and a second contribution from the water contained in the macropores  $e_{wM}$ :

$$e_w = e_{wm} + e_{wM} \quad (2.1)$$

This model takes into account the evidence of the different water retention mechanisms, namely adsorption in the microstructure (inter-layer porosity and inter-particle porosity) and capillary storage in the inter-aggregate porosity (see Figure 2-7).

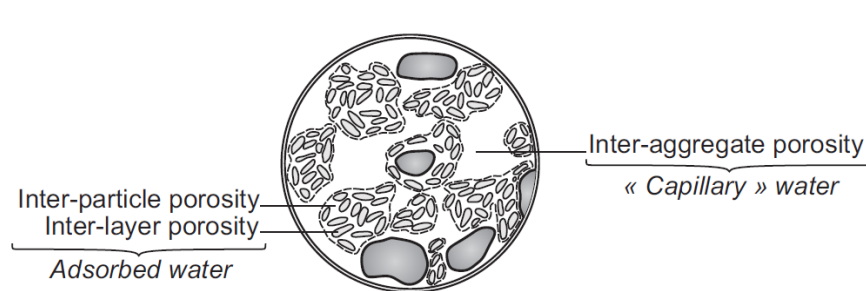


**Figure 2-7. Conceptual representation of the structure of compacted bentonite (in black) and the different water storage mechanisms (in blue) (modified after Gens & Alonso (Gens & Alonso, 1992); (Jacinto, Villar, & Ledesma, 2012).**

The degree of saturation  $S_r$  is then expressed as:

$$S_r = \frac{e_w}{e} = \frac{e_m}{e} S_{rm} + \frac{e_M}{e} S_{rM} \quad (2.2)$$

where  $e_m$  and  $e_M = e - e_m$  are respectively the microstructural and macrostructural void ratios, and  $S_{rm}$  and  $S_{rM}$  the microstructural and macrostructural degrees of saturation. The degrees of saturation are therefore not additive, as the global degree of saturation is obtained by the sum of the microstructural and macrostructural degrees of saturation, weighted by the corresponding volumetric fractions.

In the following, thermodynamic equilibrium between the microstructure and macrostructure is assumed. Accordingly, the current value of suction applies to both structural levels.

### 2.2.1 Microstructural water retention domain

Water in the microstructure is mainly stored by adsorption. Several adsorption isotherms have been proposed in the literature by the community of physicists. Dubinin's isotherm is adopted to describe the water retention behaviour of the microstructure. Its equation takes the following form:

$$\Omega_{wm} = \Omega_m \exp \left\{ - \left[ \frac{RT}{\beta_D E_0} \ln \left( \frac{u_v^0}{u_v} \right) \right]^{n_{ads}} \right\} \quad (2.3)$$

where  $\Omega_{wm}$  is the volume of water adsorbed in the micropores at temperature  $T$  and relative pressure  $u_v/u_v^0$ ,  $R$  is the universal gas constant ( $= 8:314 \text{ J/mol} \cdot \text{K}$ ), and  $\Omega_m$  is the total volume of the micropores,  $n_{ads}$  is a specific parameter of the system, called heterogeneity factor.  $\beta_D$  is termed similarity constant and  $E = DE_0$  is the characteristic adsorption energy for the given system.  $E_0$  is the characteristic energy of adsorption for a reference vapour for which  $\beta_D = 1$ .

By dividing both sides of equation 2.3 by the volume of solid particles  $\Omega_s$ , it yields:

$$e_{wm} = e_m \exp \left\{ - \left[ \frac{RT}{\beta_D E_0} \ln \left( \frac{u_v^0}{u_v} \right) \right]^{n_{ads}} \right\} \quad (2.4)$$

Moreover, assuming relative humidity  $RH$  being function of relative pressure  $u_v/u_v^0$ , in terms of suction  $s$ :

$$RH = \frac{u_v^0}{u_v} = \exp \left( \frac{-sM_w}{RT \rho_w} \right) \quad (2.5)$$

where  $M_w$  is the molecular mass of water ( $= 0:018 \text{ kg/mol}$ ) and  $\rho_w$  its density.

Gathering the constant parameters, the following expression is finally adopted for the microstructural water retention domain:

$$e_{wm}(s, e_m) = e_m \exp[-(C_{ads}s)^{n_{ads}}] \quad (2.6)$$

Where  $n_{ads}$  and  $C_{ads}$  are material parameters controlling respectively the curvature of the water retention curve in the high suction range and the dependency on the rate of desaturation of the soil.  $C_{ads}$  also reads:

$$C_{ads} = \frac{M_w}{\rho_w \beta_D E_0} \quad (2.7)$$

### 2.2.2 Macrostructural water retention domain:

The van Genuchten (van Genuchten, 1980) water retention model has been successfully used to model the water retention behaviour of a wide variety of soils. It is generally expressed as:

$$S_r(s) = \left[ 1 + \left( \frac{s}{\alpha} \right)^n \right]^{-m} \quad (2.8)$$

where  $m$  and  $n$  are material parameters, and  $\alpha$  is related to the air-entry value  $s_{AE}$ . Alternatively, the van Genuchten equation may be expressed in terms of water ratio  $e_w$ :

$$e_w(s, e) = e \left[ 1 + \left( \frac{s}{\alpha} \right)^n \right]^{-m} \quad (2.9)$$

In this model, the van Genuchten equation is selected to model the macrostructural water retention domain. Accordingly, the void ratio  $e$  is replaced by the macrostructural void ratio  $e_M = e - e_m$ , and the macrostructural water retention model reads:

$$e_{wM}(s, e) = (e - e_m) \left[ 1 + \left( \frac{s}{\alpha} \right)^n \right]^{-m} \quad (2.10)$$

In order to represent the influence of the bentonite structure on the air-entry value, the parameter  $\alpha$  is assumed to depend on the macrostructural void ratio. The following law is adopted:

$$\alpha = \frac{A}{e - e_m} \quad (2.11)$$

where  $A$  controls the dependence of the air-entry pressure on the macrostructural void ratio.

### 2.2.3 Microstructure evolution

In order to take into account the variation of microstructure due to saturation degree change, the following equation is written:

$$e_m = e_{m0} + \beta_0 e_w + \beta_1 e_w^2 \quad (2.12)$$

Where  $e_{m0}$  is the microstructural void ratio for the dry material ( $e_w = 0$ ) and  $\beta_0$  and  $\beta_1$  are parameters that quantify the swelling potential of the aggregates.

### 2.2.4 Water permeability evolution

Given the double structure of compacted bentonite, the water permeability evolution is modelled as follows:

$$K_w = K_{w0} \frac{e_M^N}{(1 - e_M^N)^M} \frac{(1 - e_{M0})^N}{e_{M0}} \quad (2.13)$$

where  $K_{w0}$  is a reference permeability measured on a material with a reference macroscopic void ratio  $e_{M0}$ .

By using equation 2.13, one implicitly assumes that water flow takes place essentially in the macropores of the material. Although this hypothesis cannot be directly checked using experimental techniques, some evidences tend to validate it.

Via this strategy, an additional hydro-mechanical and multi-scale coupling is added in the hydro-mechanical formulation of the model. Indeed, the saturated water permeability turns out to be affected by the mechanical deformation through the void ratio  $e$  and by microstructure evolution through  $e_m$ , since the macrostructural void ratio reads  $e_M = e - e_m$ .

### 3. Mechanical model

#### 3.1 Background

For the safety assessment of radioactive waste disposal, the swelling potential (i.e. the sealing of technological gaps) and the development of swelling pressure are two fundamental aspects that need to be accurately evaluated, represented and modelled.

The swelling potential  $\Delta H/H_i$  and the swelling pressure  $S_p$  are respectively the ratio between the change in sample height  $\Delta H$  (upon saturation under oedometer conditions) and its initial height  $H_i$  and the pressure required in order to prevent volume changes upon wetting.

Relatively simple laboratory tests such as swelling pressure tests, swell-consolidation tests and swell-under-load tests (path in Figure 3-1) were carried on by several authors in order to estimate these features.

All these experiments underlined the non-negligible path-dependency of the mechanical behaviour of bentonite.

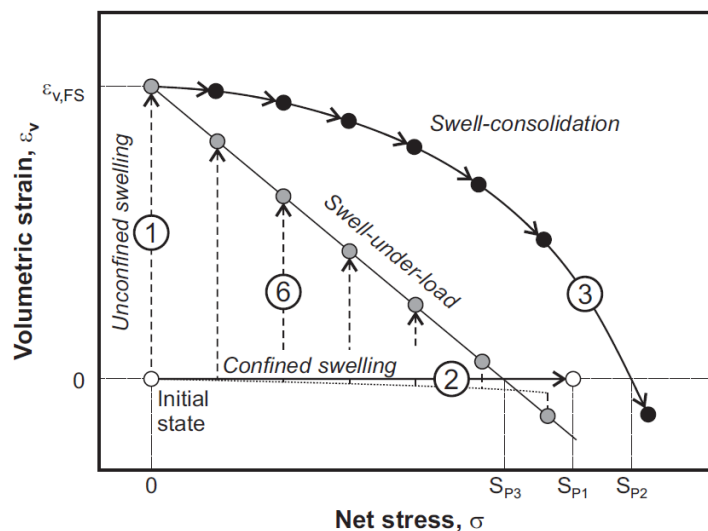


**Figure 3-1. Experimental techniques for the characterization of the swelling capacity of soils (after (Sridharan, Rao, & Sivapullaiah, 1986)).**

Since the use of bentonite for nuclear waste disposal is so that this material is classified as an unsaturated soil, the dependency on suction has to be also investigated.

Among other constitutive models for unsaturated soils, the work of Alonso (Alonso, Gens, & Josa, 1990) is chosen in order to study the mechanical behaviour of compacted bentonite-based materials. This approach is developed in the framework of elastoplasticity.

Experimental observations on laboratory tests performed along simple stress path in the space ( $p - q - s$ ) help to gain a comprehensive understanding of

the mechanical behaviour of saturated and partially saturated bentonites. The laboratory equipment used to carry out tests on unsaturated soils consists indeed in adapting classical techniques for saturated soils in order to control or measure suction.

The classically investigated stress paths (not described in this report) include mechanical loading under constant suction, hydraulic loading under constant stress and shearing path under constant suction. These tests demonstrate respectively that:

- the preconsolidation stress and the slope of the normal compression line  $\lambda$  are both suction dependent, with increasing yield stress and decreasing  $\lambda$  with increasing suction;
- Upon wetting under unconfined conditions, a gradual increase in volume, with a quasi-linear response in the  $(\ln s - e)$  plane with slope  $\kappa_s$  is found and  $\kappa_s$  increases with increasing dry density  $\rho_{di}$ . On the other hand, for wetting under stress, depending of the confining stress, the material exhibits swelling (for low stress) or it undergoes collapse (i.e. volumetric compression under high stress);
- The apparent shear strength (and accordingly the cohesion) increases with suction (Escario & Saez, 1986), while the slope of the critical state line (and so the friction angle) is not affected (Escario & Saez, 1986). Moreover, recently Romero (Romero, 2012) showed a linear increase of cohesion  $c(s)$  with suction  $s$  for Kunigel V1 bentonite compacted to a dry density of 1.36 Mg/m<sup>3</sup> (in the suction range from 0 to 140 kPa).

### 3.2 Mathematical formulation

The Barcelona Basic Model (BBM) was chosen for its well-known robustness and capacities. Its formulation in terms of net stress and suction allows an easier calibration than other models formulated using an effective stress. It was proposed by Alonso (Alonso, Gens, & Josa, 1990), who pioneered the development of mechanical constitutive models for partially saturated soils. Most of the existing models for unsaturated soils rely indeed on the concepts developed in the BBM. The idea behind the model is the extension of an existing model for saturated soils to unsaturated conditions.

Accordingly, the behaviour of unsaturated soils should be modelled consistently and full saturation considered as a limiting case. Therefore, the Barcelona Basic Model consists in the extension of the Modified Cam-Clay Model (Roscoe & Burland, 1968) to unsaturated conditions, by using suction as an additional stress variable. It is formulated adopting net stress  $\sigma$  and suction  $s$  as stress variables.

It is worth reminding the definition of net stress  $\sigma$ :

$$\sigma = \sigma_T - u_a I \quad (3.1)$$

With  $\sigma_T$  the total stress tensor,  $u_a$  the air pressure for  $s > 0$  and  $\mathbf{I}$  the identity tensor.

The model is first formulated for isotropic stress states and then it is progressively extended to triaxial and three-dimensional stress states.

### 3.2.1 Isotropic stress states

Under isotropic stress conditions ( $\sigma_1 = \sigma_2 = \sigma_3$ ), the mechanical stress state is described using the mean net stress  $p = \sigma_i$  and suction  $s$ .

Both changes in the mean net stress and in suction are assumed to be produced only by volumetric strains  $\varepsilon_v = \varepsilon_i$ . Accordingly, the space  $(p - s - \varepsilon_v)$  is relevant for the description of the model and yield limits should be defined in the plane  $(p - s)$ .

For saturated conditions, the Barcelona Basic Model coincides with the Modified Cam-Clay Model (Roscoe & Burland, 1968). The Modified Cam-Clay model belongs to the family of elastoplastic strain-hardening models.

Accordingly, the total strain increment can be decomposed into an elastic part and a plastic part. For isotropic stress states, the increment of total volumetric strain  $d\varepsilon_v$  is equal to the sum of the elastic  $d\varepsilon_v^e$  and plastic  $d\varepsilon_v^p$  components of the incremental volumetric strain:

$$d\varepsilon_v = d\varepsilon_v^e + d\varepsilon_v^p \quad (3.2)$$

In the elastic domain, the increment of volumetric strain associated to changes in mean net stress is given by:

$$d\varepsilon_v^e = \frac{\kappa}{1+e} \frac{dp}{p} = \frac{dp}{K} \quad (3.3)$$

where  $K$  is the slope of the unloading-reloading line and  $e$  is the void ratio. Elasticity in the Modified Cam-Clay Model is non-linear as the bulk modulus  $K$  is a function of both the void ratio and the mean net stress according to:

$$K = \frac{(1+e)p}{\kappa} \quad (3.4)$$

Once the mean net stress reaches the preconsolidation stress (yield limit)  $p_0^*$  plastic strain is generated. The evolution of the plastic strain is then governed by the hardening law:

$$d\varepsilon_v^p = \frac{\lambda(0) - \kappa}{1+e} \frac{dp_0^*}{p_0^*} \quad (3.5)$$

where  $\lambda(0)$  is the slope of saturated virgin consolidation line (see Figure 3-2).

However, since the suction dependency is un-negligible in unsaturated conditions, the slope of the virgin consolidation line  $\lambda(s)$  reads as follow:

$$\lambda(s) = \lambda(0)[(1 - r) \exp(-\omega s) + r] \quad (3.6)$$

where  $r$  and  $\omega$  are material parameters.  $r$  is related to the maximum stiffness of the soil (for an infinite suction) and  $\omega$  controls the rate of increase of the soil stiffness with suction.

On the other hand, the slope  $\kappa$  of the loading-unloading line is supposed to be constant.

The evolution of the preconsolidation pressure  $p_0(s)$  is modelled consistently with the concept of increasing the elastic domain with increasing suction:

$$p_0(s) = p_c \left( \frac{p_0^*}{p_c} \right)^{\frac{\lambda(0) - \kappa}{\lambda(s) - \kappa}} \quad (3.7)$$

where  $p_c$  is a reference net pressure. Equation 3.7 defines a yield curve in the  $(p - s)$  plane called the Loading-Collapse (LC) curve, which is fundamental for the Barcelona Basic Model.

Considering suction, the hardening law of the LC curve becomes:

$$d\varepsilon_v^p = \frac{\lambda(s) - \kappa}{1 + e} \frac{dp_0^*}{p_0^*} \quad (3.8)$$

And by substitution, it can be obtained:

$$d\varepsilon_v^p = \frac{\lambda(0) - \kappa}{1 + e} \frac{dp_0^*}{p_0^*} \quad (3.9)$$

Corresponding to the hardening law with no suction dependence.

Under these conditions, the suction change is supposed to affect only the volumetric part of the total strain, reading therefore:

$$d\varepsilon_v^e = d\varepsilon_{vp}^e + d\varepsilon_{vs}^e = \frac{\kappa}{1 + e} \frac{dp}{p} + \frac{\kappa_s}{1 + e} \frac{ds}{s + u_{atm}} = \frac{dp}{K} + \frac{ds}{K_s} \quad (3.10)$$

Where  $d\varepsilon_{vp}^e$  and  $d\varepsilon_{vs}^e$  represent respectively the elastic volumetric strain associated to the change in net stress and the one related to the change in suction. Then  $\kappa_s$  is the slope of the wetting-drying line in the space  $(e - s)$  and  $u_{atm}$  the atmospheric pressure. The bulk modulus for change in suction is expressed by the following equation:

$$K_s = \frac{(1 + e)(s + u_{atm})}{\kappa_s} \quad (3.11)$$

Finally, a second yield curve in the space  $(p - s)$  can be defined. It is called the Suction Increase curve and it defines, for a given drying path, irreversible plastic strain, after the threshold value of suction  $s_0$  (see Figure 3-3):

$$f_{SI} \equiv s = s_0 \quad (3.12)$$

The consequential value of plastic strain is given:

$$d\varepsilon_v^p = \frac{\lambda_s - \kappa_s}{1 + e} \frac{ds_0}{s_0 + u_{atm}} \quad (3.13)$$

Accordingly, irreversible strains control the position of the LC and SI yield surfaces and the hardening of both yield surfaces is coupled. Depending on the sign of the volumetric plastic strain, hardening or softening of the yield surface will take place.

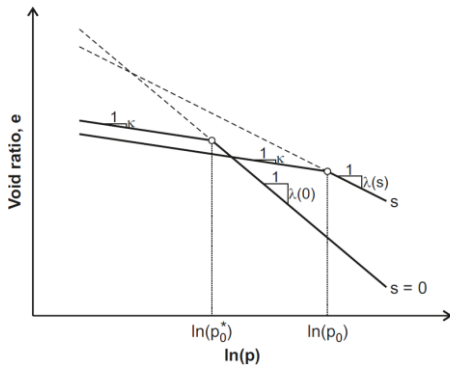


**Figure 3-2. Compression curves for saturated and unsaturated states (Alonso, Gens, & Josa, 1990).**

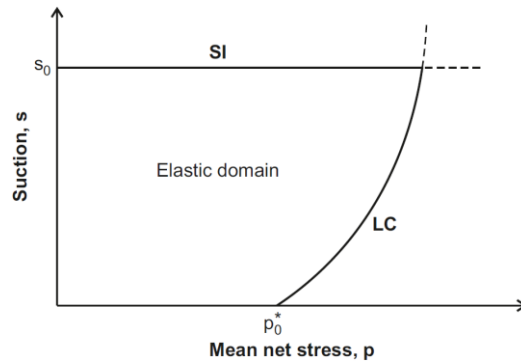


**Figure 3-3. Yield curves of the Barcelona Basic Model for isotropic stress states: Loading-Collapse (LC) and Suction Increase (SI) curves.**

### 3.2.2 Triaxial stress states

Under triaxial conditions  $(\sigma_1 \neq \sigma_2 = \sigma_3)$ , the mechanical stress state can be described by the mean net stress  $p$ , suction  $s$  and the deviatoric stress  $q = \sigma_1 - \sigma_3$  (see Figure 3-5).

In the elastic domain, the deviatoric deformation due to the deviatoric stress is given:

$$d\varepsilon_d^e = \frac{1}{3} G dq \quad (3.14)$$

where  $d\varepsilon_d^e$  is the elastic increment of deviatoric strain and  $G$  is the shear modulus. This modulus may be chosen as a constant or as a function of the bulk modulus  $K$  following:

$$G = \frac{3(1 - 2\nu)K}{2(1 + \nu)} \quad (3.15)$$

In the  $(p - q)$  plane, the yield surface is expressed (see Figure 3-4):

$$f_{LC} \equiv q^2 - M_\theta^2(p + p_s)(p_0 - p) = 0 \quad (3.16)$$

With  $M_\theta$  the slope of the critical state line,  $p_s$  the left intercept of yield surface and  $p_0$  the apparent preconsolidation pressure at a suction  $s$ .  $p_s$  increases with increasing cohesion, therefore it can be given as a function of suction:

$$p_s(s) = \frac{c(s)}{\tan\varphi} = \frac{c(0) + ks}{\tan\varphi} \quad (3.17)$$

where  $c(0)$  is the cohesion under saturated conditions and  $k$  is a parameter controlling the increase of cohesion.

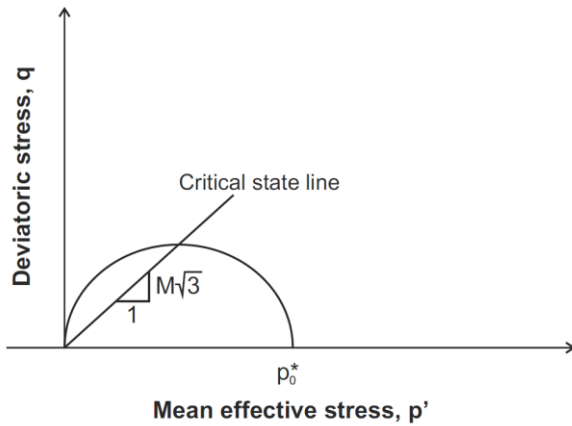


Figure 3-4. Modified Cam-Clay Model.

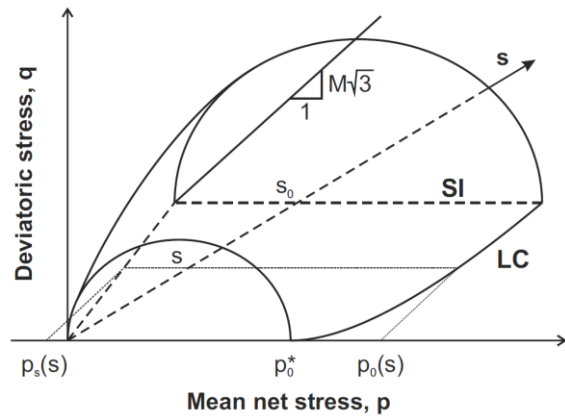


Figure 3-5. Barcelona Basic Model.

### 3.2.3 Three dimensional stress states

Finally, under three-dimensional conditions, the mechanical stress state is described by the mean net stress  $p$ , suction  $s$ , the second invariant of the deviatoric stress tensor  $J_2$  and the Lode's angle  $\theta$ , which are defined as follows:

$$J_2 = \sqrt{\frac{1}{2} \boldsymbol{\sigma} : \boldsymbol{\sigma}} \quad \theta = -\frac{1}{3} \sin^{-1} \left( \frac{3\sqrt{3} J_3}{2 J_2^2} \right) \quad J_3 = \frac{1}{3} \sigma_{ij} \sigma_{jk} \sigma_{ki} \quad (3.18)$$

where  $\boldsymbol{\sigma}$  is the deviatoric stress tensor given by  $\boldsymbol{\sigma} = \boldsymbol{\sigma}_T - p\mathbf{I}$ , the Lode's angle  $\theta$  gives the direction of the stress path in the deviatoric plane and  $J_3$  the third invariant of the deviatoric stress tensor.

In the elastic domain, the stress increment is related to the increments of

strains and suction through:

$$d\boldsymbol{\sigma} = \mathbf{D}^e : d\boldsymbol{\varepsilon}^e + \boldsymbol{\alpha}_s ds \quad (3.19)$$

where  $\mathbf{D}^e$  is the global elastic tensor and  $\boldsymbol{\alpha}_s$  is the elastic tensor for suction changes, given respectively by:

$$D_{ijkl}^e = 2G\delta_{ik}\delta_{jl} + \left(K + \frac{2}{3}G\right)\delta_{ik}\delta_{jl} \quad \boldsymbol{\alpha}_s = \frac{1}{K_s}\mathbf{D}^e : \mathbf{I} \quad (3.20)$$

Where  $K$ ,  $G$  and  $K_s$  have been already debated in the previous section. The elastic domain is bounded by the following yield surface:

$$f_{LC} \equiv 3J_2^2 - M_\theta^2(p + p_s)(p_0 - p) = 0 \quad (3.21)$$

where  $M_\theta$  is the slope of the critical state line,  $p_s$  considers the dependence of shear strength on suction and  $p_0$  is the apparent preconsolidation pressure at a suction  $s$ .

For three-dimensional stress states, the slope of the critical state line  $M_\theta$  is a function of the Lode angle  $\theta$  and determines the shape of the failure surface in the deviatoric plane. Among other authors, van Eekelen (van Eekelen, 1980) model is adopted in order to approximate the Mohr-Coulomb failure criterion. Therefore, the slope of the critical state line  $M_\theta$  is defined:

$$M_\theta = a(1 + b\sin 3\theta)^n \quad (3.22)$$

where the parameter  $n$  is a constant defining the convexity of the failure surface in the deviatoric plane and it is taken equal to -0.229 to ensure the convexity of the surface (van Eekelen, 1980), (Barnichon, 1998)) and  $a$  and  $b$  depend on the triaxial compression and extension friction angles as follows:

$$a = \frac{r_c}{(1 + b)^n} \quad b = \frac{\left(\frac{r_c}{r_E}\right)^{\frac{1}{n}} - 1}{\left(\frac{r_c}{r_E}\right)^{\frac{1}{n}} + 1} \quad (3.23)$$

$$r_c = \frac{2\sin\phi_c}{\sqrt{3}(3 - \sin\phi_c)} \quad r_E = \frac{2\sin\phi_E}{\sqrt{3}(3 + \sin\phi_E)}$$

where  $r_c$  and  $r_E$  are the reduced radii for axisymmetric triaxial stress paths of compression and extension.

The expression of the SI yield surface remains:

$$f_{SI} \equiv s = s_0 \quad (3.24)$$

**3.2.4 New formulation of BBM**

The following relation was introduced and implemented in LAGAMINE (Dieudonné, 2016):

$$\kappa_s = 0 \quad \text{if} \quad S_r > S_r^* \quad (3.25)$$

The main concept behind this relation is that bentonite-based materials are capable to sustain high value of suction without desaturating due to their important air-entry value.

Hence, saturation is obtained before reaching the suction zero value. As consequence, under confined conditions, the swelling stress, being generated by the saturation process, should not vary anymore as the few available experimental data show (Agus, Arifin, Tripathy, & Schanz, 2013) (see Figure 3-6).

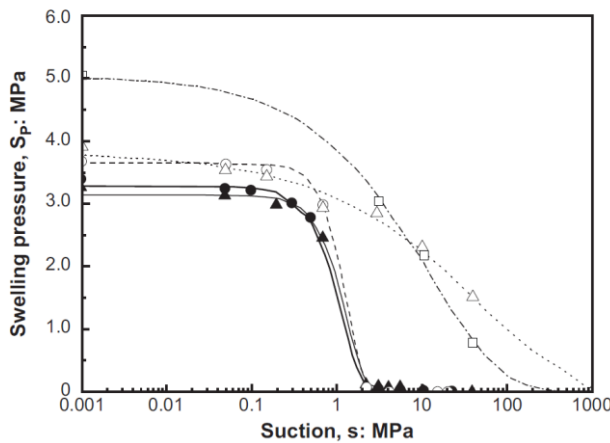


**Figure 3-6. Swelling pressure development upon suction decrease. Experimental data on a mixture of Calcigel bentonite and quartz sand with a respective proportion of 50/50 in dry mass, and on pure Calcigel bentonite (Agus, Arifin, Tripathy, & Schanz, 2013).**

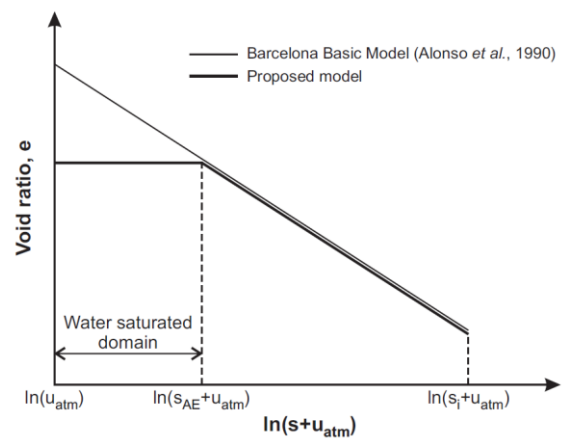


**Figure 3-7. Evolution of void ratio along a wetting path under constant mean net stress. Original formulation of the Barcelona Basic Model (Alonso, Gens, & Josa, 1990) and proposed model.**

On the other way, under free-swelling conditions, upon a threshold value of saturation (0.95 ÷ 0.98), corresponding to the air-entry value, no swelling strain occurs, being translated in equation 3.25 (see Figure 3-7).

For  $S_r^* = 1$  the original Barcelona Basic Model is recovered.

## 4. Input parameters

### 4.1 Hydraulic parameters

The proposed water retention model is validated against experimental data on wetting paths under unconfined conditions and for different dry densities for mixture of 70% MX-80 bentonite and 30% sand studied by Wang (Wang, et al., 2013) and Gatabin et al. (2016) (see Figure 4-1).

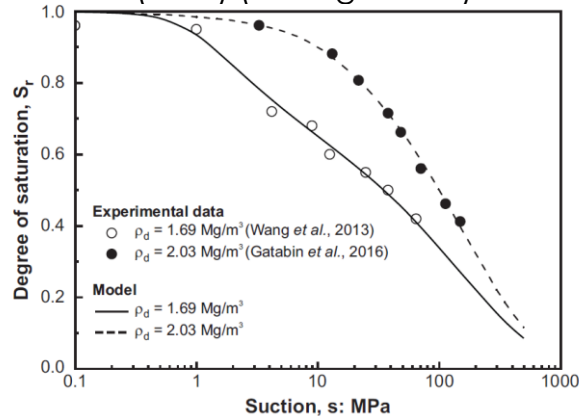


**Figure 4-1. Calibration of the water retention model against experimental data ( Wang, et al., 2013); Gatabin et al., 2016) on a MX-80 bentonite/sand mixture compacted at two different dry densities. Wetting path under confined conditions.**

The water permeability, and consequently the porosity, were selected in dependence of the initial dry density among the available experimental data (Gatabin, Touze, Billaud, Imbert, & Guillot, 2006) (see Figure 4-2 and 4-3 and Table 4-1).

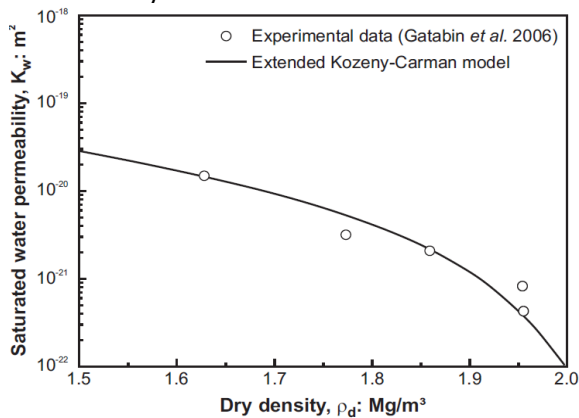


**Figure 4-2. Water permeability as a function of dry density. Experimental data on a mixture of MX-80 bentonite and sand (Gatabin, Touze, Billaud, Imbert, & Guillot, 2006) and model response.**

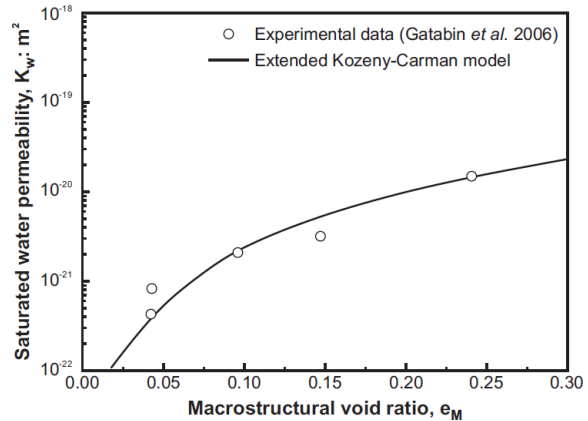


**Figure 4-3. Water permeability as a function of the macrostructural void ratio. Experimental data on a mixture of MX-80 bentonite and sand (Gatabin, Touze, Billaud, Imbert, & Guillot, 2006) and model response.**

**Table 4-1. Selected hydraulic parameters**

$\rho_{di}$ (Mg/m <sup>3</sup> )	$C_{ads}$ (MPa <sup>-1</sup> )	$n_{ads}$	$A$ (MPa)	$n$	$m$	$K_{w0}$ (m <sup>2</sup> )	$n$	$e_{m0}$	$\beta_0$	$\beta_1$
1.6	0.0053	0.79	0.2	2	0.2	2.0E-20	0.365	0.29	0.1	0.18
1.8	0.0053	0.79	0.2	2	0.2	4.0E-21	0.300	0.29	0.1	0.18
2.0	0.0053	0.79	0.2	2	0.2	1.0E-22	0.237	0.29	0.1	0.18

## 4.2 Mechanical parameters

The Barcelona Basic Model is validated against experimental data on bentonite-based materials from the literature.

The considered material is the MX-80 bentonite and sand with three different dry densities.

**Table 4-2. Selected mechanical parameters**

$\rho_{dt}$ ( $Mg/m^3$ )	$\kappa$	$\kappa_s$	$\lambda(0)$	$p_0^*$ ( $MPa$ )	$p_c$ ( $MPa$ )	$r$	$\omega$ ( $MPa^{-1}$ )
<b>1.6</b>	0.025	0.073	0.12	<b>0.68</b>	0.0036	0.8	0.09
<b>1.8</b>	0.025	0.073	0.12	<b>2.17</b>	0.0036	0.8	0.09
<b>2.0</b>	0.025	0.073	0.12	<b>5.665</b>	0.0036	0.8	0.09

The input parameters (see Table 4-2) were calibrated in order to best fit the experimental data presented by Wang (Wang, et al., 2013) on a compacted mixture of MX-80 bentonite and sand via suction-controlled oedometer tests (see Figure 4-4).

The preconsolidation pressure for saturated state  $p_0^*$  was selected by an iterative procedure in order to reproduce the results of swelling stress tests performed by Gatabin (Gatabin, Guillot, & Bernachy, 2016) (see Figure 4-5).

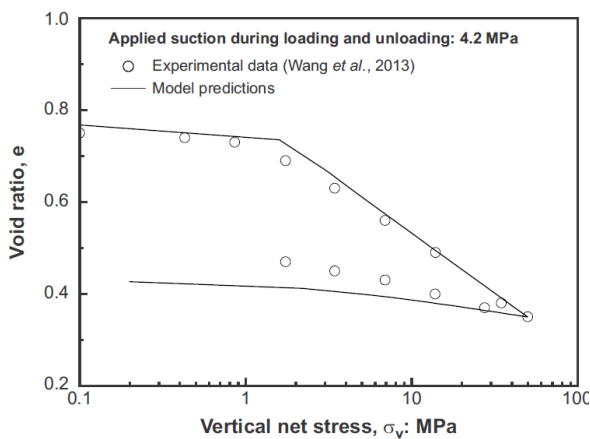


**Figure 4-4. Loading and unloading at a suction  $s = 4,2 MPa$  in a controlled-suction oedometer tests on a MX-80 bentonite/sand mixture compacted at a dry density  $\rho_d = 1,67 Mg/m^3$ . Comparison between experimental data (Wang, et al., 2013) and model responses.**

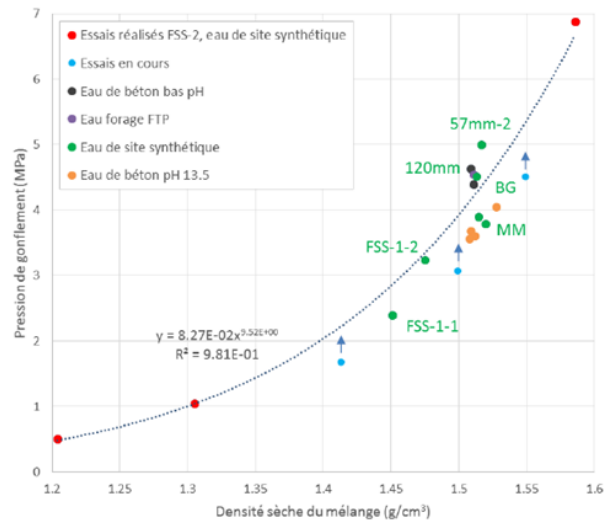


**Figure 4-5. Dry density VS Maximum swelling pressure in a swelling stress test (Gatabin, Guillot, & Bernachy, 2016)**

## 5. Performance

### 5.1 Dependence of swelling strain on applied stress and on dry density

In the following, a number of tests are modelled in order to assess the performance of the numerical hydro-mechanical model implemented in LAGAMINE.

Oedometer conditions are assumed (see Figure 5-1 and 5-2).

The soil sample consists in 1 eight-noded isoparametric element.

Despite the compaction process, the bentonite sample is assumed homogeneous.

The input parameters are presented in Table 4-1 and 4-2 of the previous section.

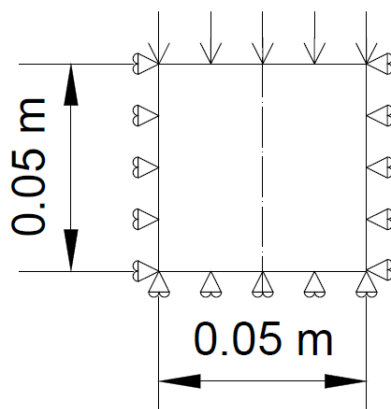


Figure 5-1. Soil sample for free swelling test

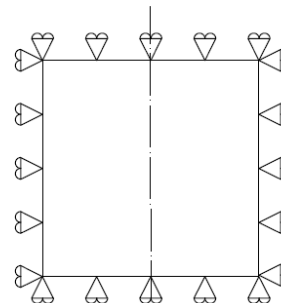


Figure 5-2. Soil sample for swelling stress test

#### 5.1.1 Different confining pressures, same dry density

A free swelling test is modelled (Figure 5-1) for a soil sample of dry density  $\rho_{ai} = 1.6 \text{ Mg/m}^3$ . Three different confining pressures are considered (see Table 5-1 and Figure 5-4):

Table 5-1. Considered confining pressures.

Confining Pressure	MPa
$\sigma_v^o$	0.515
$\sigma_v^o$	1.15
$\sigma_v^o$	1.51

A suction decrease is simultaneously applied to the whole sample (see Figure 5-3).

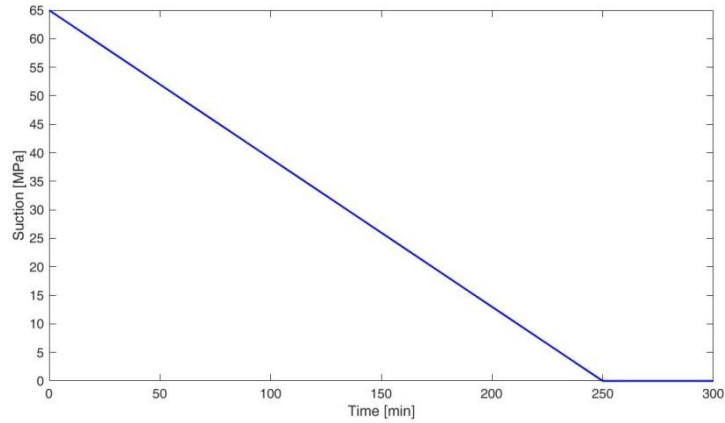


**Figure 5-3. Suction decrease function**

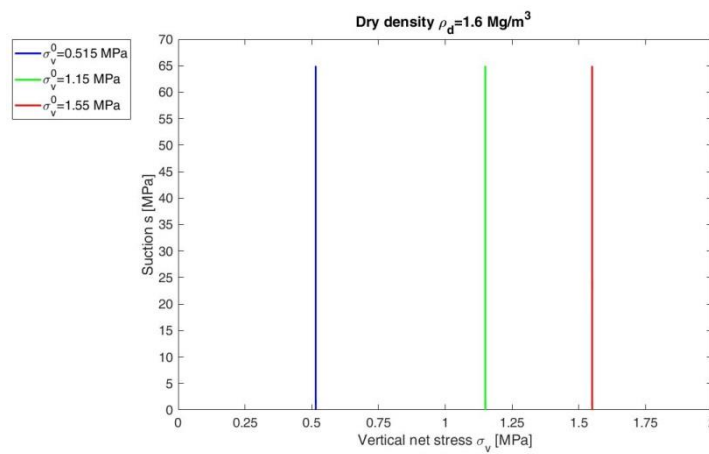


**Figure 5-4. Swelling tests at constant stress**

The obtained vertical displacements (see Figure 5-5) show different results for the three different cases highlighting a confining-pressure-dependency of the model.

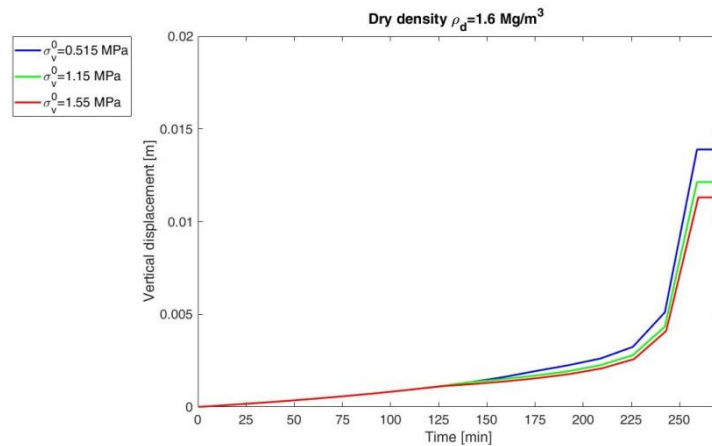


**Figure 5-5. Vertical displacement for swelling tests at different stresses**

**5.1.2 Same confining pressures, different dry densities**

Three soils sample with different initial dry densities but equal confining pressure (i.e.  $\sigma_v = 1.55 \text{ MPa}$ ) are considered in a free swelling test (see table 5-2).

**Table 5-2. Considered dry densities.**

Dry density	Mg/m <sup>3</sup>
$\rho_d$	1.6
$\rho_d$	1.8
$\rho_d$	2.0

The obtained vertical displacements and water retention behaviour curves (see Figure 5-6 and 5-7) show different results for the three different cases highlighting a dry-density-dependency of the model for both mechanical and hydraulic behaviour.

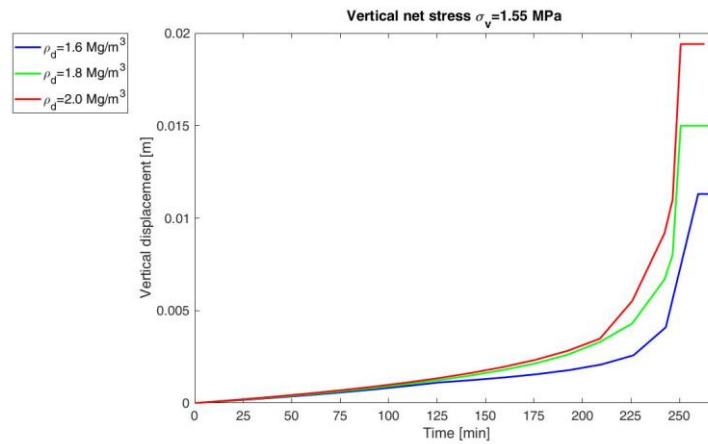


**Figure 5-6. Vertical displacement for swelling tests at different dry densities**

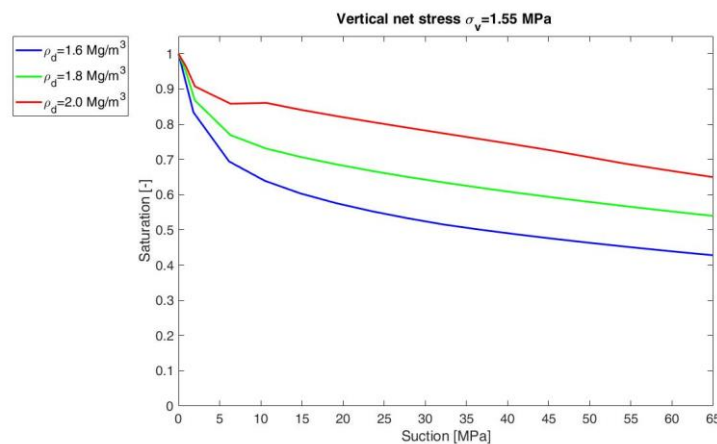


**Figure 5-7. Suction VS Saturation at different dry densities**

## 5.2 Irreversibility of strains in wetting/drying cycles

Three soils sample with different initial dry densities but equal confining pressure ( $\sigma_v = 1.55 \text{ MPa}$ ) are considered in a free swelling test (see Table 5-2). A suction decrease and a successive increase is simultaneously applied to the whole sample (see Figure 5-8).

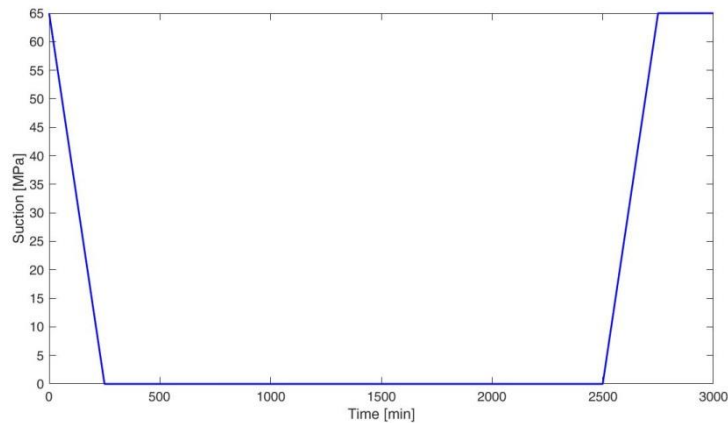


**Figure 5-8. Suction decrease and increase function**

The obtained vertical displacements (see Figure 5-9) show different results for the three different cases highlighting an initial-dry-density-dependency of the model and plastic strain. The water retention behaviour (see Figure 5-10) underlines hysteresis since the wetting and drying paths do not coincide.

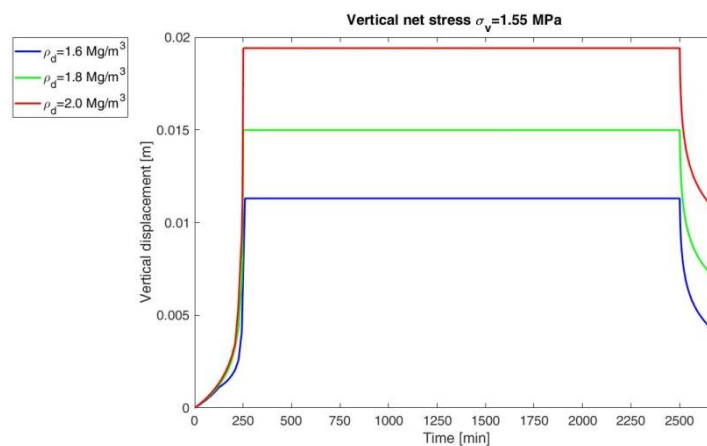


**Figure 5-9. Vertical displacement for swelling tests at different dry densities**

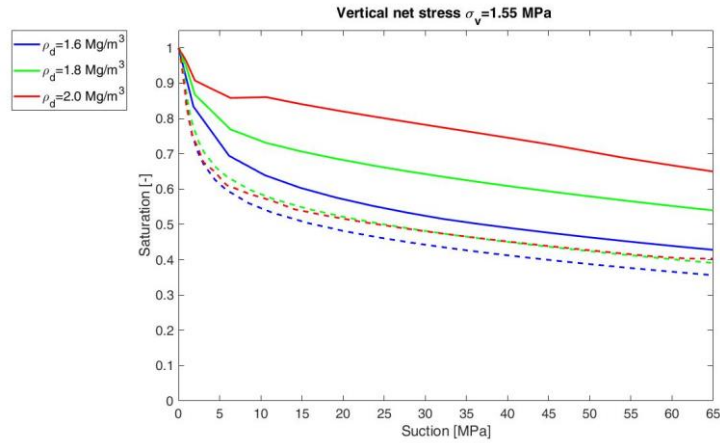


Figure 5-10. Suction VS Saturation at different dry densities. Continuous lines wetting path, dashed lines drying path.

### 5.3 Behaviour during swelling stress test. Dependence of swelling pressure on dry density.

A swelling stress test (i.e. wetting test in confined conditions) is simulated (see Figure 5-2) on three sample with different dry densities (see Table 5-2) at the same initial confining pressure ( $\sigma_v = 1.55 \text{ MPa}$ ).

A suction decrease is simultaneously applied to the whole samples (see Figure 5-3).

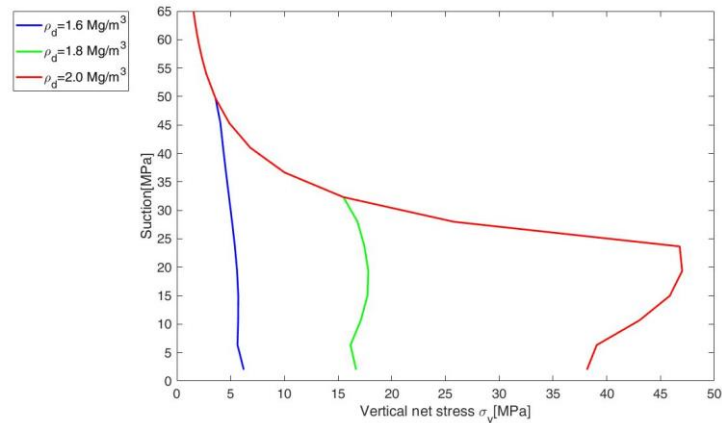
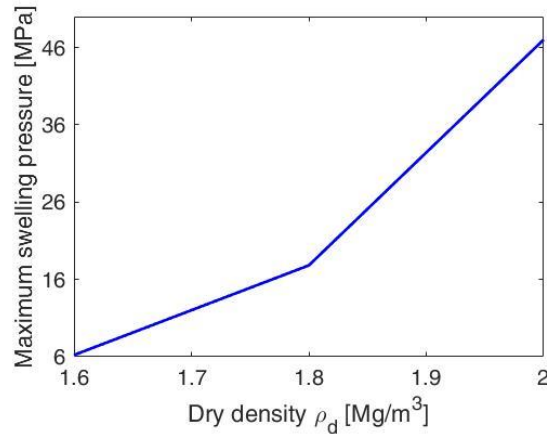


Figure 5-11. Suction-stress paths in swelling pressure tests at different dry densities



**Figure 5-12. Obtained maximum swelling stress VS dry density**

Results (see Figures 5-11 and 5-12) show a maximum-swelling-stress-dependency on the initial dry density.

#### 5.4 Stress path dependence from an unsaturated to a saturated state

In the following, three different loading cases test are considered for a sample with dry density  $\rho_d = 1.6 \text{ Mg/m}^3$  and initial confining pressure of 1.15 MPa:

1. Wetting in unconfined conditions, followed by a mechanical loading;
2. Mechanical loading, followed by wetting in unconfined conditions;
3. Swelling stress test, followed by mechanical loading.

The applied suction decrease is represented in Figure 5-3.

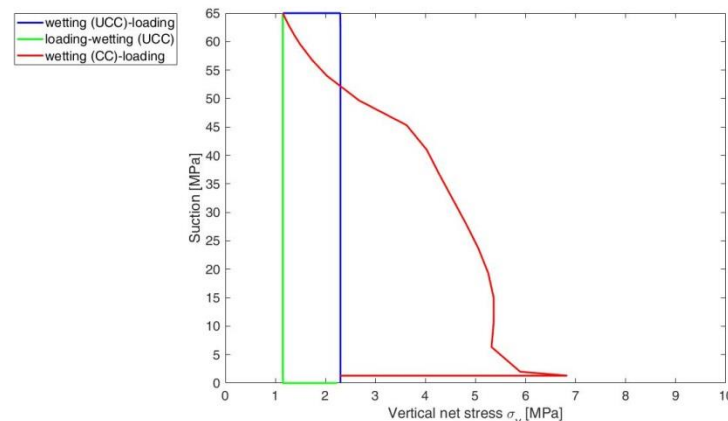


**Figure 5-13. Stress paths dependence from an unsaturated to a saturated state**

Results (see Figure 5-14 and 5-15) show stress-path dependency for both mechanical and hydraulic behaviour.

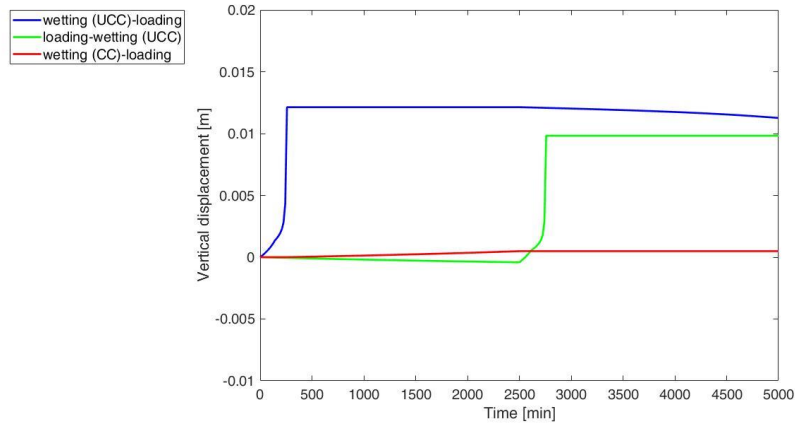


**Figure 5-14. Vertical displacement for different tests.**

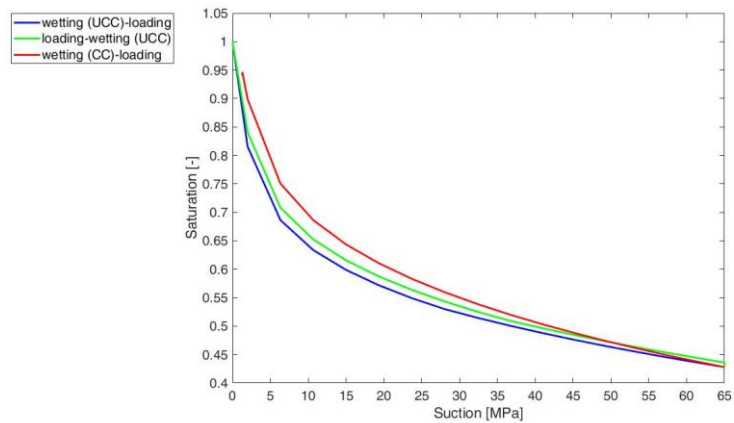


**Figure 5-15. Suction VS Saturation at different for different tests.**

## 6. Conclusions

The basic hypothesis of the hydro-mechanical model implemented in LAGAMINE were presented as well as the supporting experimental observations.

The mathematical description of the code was introduced in both mechanical and hydraulic formulation underlining the importance of the double structure concept.

After presenting the selected input parameters, a number of simple tests were simulated in order to assess the performances of this model.

The results of the numerical simulations are summarized in Table 6-1:

**Table 6-1. Summary table**

<b>Name of the constitutive law:</b>			
<b>Behaviour feature</b>	<b>YES</b>	<b>NO</b>	<b>Remarks</b>
<b>Mechanical behaviour</b>			
Dependence of swelling strain on applied stress (at the same dry density) (Figure 5-4 & 5-5)	√		
Dependence of swelling stress on dry density (at the same stress) (Figure 5-6 & 5-7)	√		
Irreversibility of strains in wetting/drying cycles (Figure 5-9 & 5-10)	√		
Dependence of swelling pressure on dry density (Figure 5-11 & 5-12)	√		
Stress path dependence from an unsaturated to a saturated state (Figure 5-14 & 5-15)	√		
Stress path dependence from a saturated to an unsaturated state			Not treated
Double structure/porosity considered?		√	
Are temperature effects considered in the model?		√	
Dependence of strains developed in a temperature cycle (increase/decrease) on OCR (or stress) (Figure 7)		√	
<b>Hydraulic behaviour (retention curve)</b>			
Hysteresis	√		
Dependence on void ratio	√		
Double structure/porosity considered?	√		

## 7. References

- Agus, S. S., Arifin, Y. F., Tripathy, S., & Schanz, T. (2013).** Swelling pressure – suction relationship of heavily compacted bentonite–sand mixtures. *Acta Geotechnica* 8, No. 2, 155–165.
- Alonso, E. E., Gens, A., & Josa, A. (1990).** A constitutive model for partially saturated soils. *Géotechnique* 40, No. 3, 405–430.
- Barnichon, J. D. (1998).** Finite element modelling in structural and petroleum geology. Ph.D. thesis, Université de Liège.
- Brooks, R. N., & Corey, A. T. (1964).** Hydraulic properties of porous media. Colorado State University Hydrology Paper No. 3.
- Dieudonné, A.-C. (2016).** Hydro-mechanical behaviour of compacted bentonite: from micro-scale analysis to macro-scale modelling. Liège: Université of Liège.
- Escarío, V., & Saez, J. (1986).** The shear strength of partly saturated soils. *Géotechnique* 36, No. 13, 453–456.
- Gatabin, C., Guillot, W., & Bernachy, F. (2016).** F.T. Caractérisation bentonite - Rapport final. Technical report, Commissariat à l'Energie Atomique (CEA).
- Gatabin, C., Touze, G., Billaud, P., Imbert, C., & Guillot, W. (2006).** ESDRED Project – Module 1. Selection and THM characterisation of the buffer material. Commissariat à l'Energie Atomique (CEA).
- Gens, A., & Alonso, E. E. (1992).** A framework for the behaviour of unsaturated expansive clays. *Canadian Geotechnical Journal* 29, No. 6, 1013–1032.
- Jacinto, A. C., Villar, M. V., & Ledesma, A. (2012).** Influence of water density on the water-retention curve of expansive clays. *Géotechnique* 62, No. 8, 657–667.
- Lloret, A., & Villar, M. V. (2007).** Advances on the knowledge of the thermo-hydromechanical behaviour of heavily compacted FEBEX bentonite. *Physics and Chemistry of the Earth* 32, No. 8–14, 701–715.
- Lloret, A., Villar, M. V., Sánchez, M., Gens, A., Pintado, X., & Alonso, E. E. (2003).** Mechanical behaviour of heavily compacted bentonite under high suction changes. *Géotechnique* 53, No. 1, 27–40.
- Romero, E. (2012).** Complementary triaxial compression and direct shear tests under high matric suctions on low-density Kunigel V1. report, Universitat Politècnica de Catalunya.
- Romero, E. (2013).** A microstructural insight into compacted clayey soils and their hydraulic properties. *Engineering Geology* 165, 3–19.
- Romero, E., Gens, A., & Lloret, A. (1999).** Water permeability, water retention and microstructure of unsaturated compacted Boom clay. *Engineering Geology* 54, No. 1–2, 117–127.
- Roscoe, K. H., & Burland, J. B. (1968).** On the generalized stress–strain behaviour of the "wet" clay. *Engineering plasticity* (Heyman, J. & Leckic, F., Eds.), pp. 535–609.
- Seiphoori, A., Ferrari, A., & Laloui, L. (2014).** Water retention behaviour and microstructural evolution of MX-80 bentonite during wetting and drying cycles. *Géotechnique* 64, No. 9, 721–734.
- Sridharan, A., Rao, A. S., & Sivapullaiah, P. V. (1986).** Swelling pressure of clays. *Geotechnical Testing Journal* 9, No. 1, 24–33.
- van Eekelen, H. M. (1980).** Isotropic yield surfaces in three dimensions for use in soil mechanics. *International Journal for Numerical and Analytical Methods in Geomechanics* 4, No. 1, 89–101.
- van Genuchten, M. T. (1980).** A closed-form equation for predicting the hydraulic

conductivity of unsaturated soils. Soil Science Society of America Journal 44, No. 5, 892–898.

**Wang, Q., Tang, A. M., Cui, Y. J., Delage, P., Barnichon, J. D., & Ye, W. M. (2013).** The effects of technological voids on the hydro-mechanical behaviour of compacted bentonite–sand mixture. *Soils and Foundations* 53, No. 2, 232–245.



## **DELIVERABLE (D3.1) GRS contribution**

### **ANNEX J**

#### **Content**

<b>1</b>	<b>GRS contribution .....</b>	<b>2</b>
1.1	Introduction.....	2
1.2	Approach.....	2
1.3	Basic hypotheses and scope .....	4
1.4	Mathematical description .....	6
1.4.1	General balance equation .....	6
1.4.2	Double-continuum approach .....	8
1.4.3	Balance equation for vapour in the pore space .....	9
1.4.4	Balance equation for the water in the interlamellar space .....	9
1.4.5	Coupling the balance equations .....	9
1.4.6	Final forms of the balance equation.....	10
1.4.7	Conditional equations.....	12
1.4.8	Boundary conditions.....	14
1.5	Input parameters and their sources.....	14
1.6	Performance.....	16
	<b>References.....</b>	<b>17</b>

# 1 GRS contribution

## 1.1 Introduction

Flow and transport in a bentonite pellet-based buffer will be influenced by the inhomogeneities of porosity and permeability that remain after full re-saturation. Especially granular bentonite buffer is inherently inhomogeneous when emplaced. With re-saturation a homogenization will take place, but, depending on parameters such as pellet size and size distribution, solution and wetting dynamics, density differences on pellet scale (between the previous granule cores and the outer parts) may remain. GRS intends to interpret the density distribution and variation range in terms of porosity/permeability distribution and relate these to the large-scale hydraulic behaviour, with the aim of confirming the adequacy of mean parameters or finding better suited substitute values. The aim is to take a step towards developing a conceptual model that helps to derive suitable hydraulic parameters for the saturated buffer from the conditions at emplacement, which will be useful for future flow and transport simulations. This will involve the interpretation of experiments (especially those performed by KIT in WP4) and orientating simulations.

In comparison to other approaches in Beacon, this is a more empirical view that disregards explicit modelling of the bentonite mechanical behaviour. The approach is explained in Section 1.2. Orientating simulations are performed using the hydraulic code VIPER, which is described in the Sections 1.3 and 1.4.

## 1.2 Approach

GRS investigations concentrate on the pellet buffer. The idea is to

- determine pellet-scale density distribution of the fully saturated buffer
- derive resulting porosity/permeability distribution
- relate these data to the overall hydraulic behaviour, checking adequacy of mean parameters and finding better suited substitute values, if applicable
- derive hydraulic parameters for the saturated buffer from the conditions at emplacement

This approach requires two steps of conceptual modelling, the first being linking the density distribution of a saturated granular bentonite buffer to the overall hydraulic properties after re-saturation and the second being relating the conditions at emplacement to the hydraulic parameters for the saturated buffer.

There is a wide variety of conditions and parameters relevant for the evolution of a granular buffer, including

- Host rock (clay or crystalline rock)
- Bentonite properties (bentonite composition, initial water content, pellet properties like pellet size distribution (single size, binary, spectrum) and geometry (sphere, drum, pillow, irregular))
- Solution composition
- Function/location of granular bentonite (thermal conditions, annulus between host rock and blocks?)
- Re-saturation conditions
  - Initial re-saturation by vapour
  - Solution injection – liquid supply
  - Injection sites (one or more sides)
  - Potential interaction with host rock

Obviously, not all possible conditions can be considered or experimentally investigated. As a first step, a reference case is defined, involving

- A clay host rock
- Far from waste canisters (isothermal)
- Na-bentonite (MX-80)
- One single pellet including appropriate free space
- Confined conditions
- Geometry: pillow
- Solution: Pearson water
- Re-saturation: First by vapour, then one-sided solution injection

The idea behind considering a single pellet is to characterize a “pellet-sized elementary cell” that includes the bentonite pellet and the surrounding (macro-) pore space, with a ratio representative for a pellet buffer.

Experiments on this reference case are performed by KIT. These will yield the spatially resolved density and/or water content after re-saturation and the spatially resolved evolution of swelling pressure, as well as the overall permeability. The next steps after investigating the single pellet system will involve measurements on clusters of a few pellets of identical size as well as of clusters with a pellet size distribution.

The simulation code used is VIPER, which was developed for confined conditions. It is planned to be extended to volume changing conditions and calibrated with the help of the planned experiments. Other WP4 experiments and existing experimental data collected in WP2 will be brought in as appropriate.

### 1.3 Basic hypotheses and scope

In order to concentrate on the hydraulic aspect of re-saturation the Extended Vapour Diffusion model (EVD) was developed under the premise of a fully bentonite-filled confined space which is a typical condition for the buffer in a repository. This allowed to drop mechanical calculations and thereby to accelerate modelling considerably. Simulation of heat transport is not incorporated in the model yet. At the present development stage predetermined or measured temperature data are used in case of non-isothermal conditions as input, instead.

The conceptual model for isothermal re-saturation of pre-compacted confined bentonite underlying VIPER was firstly formulated by Kröhn (2004b). It divides the process into at least two distinct stages that are described in the following in more detail. The illustrating figures for these two stages are exemplarily based on a characteristic experiment in which bentonite was compacted in a steel cylinder (providing confined conditions) and brought into contact with water at the open face side of the cylinder as shown in Fig. 1.1.

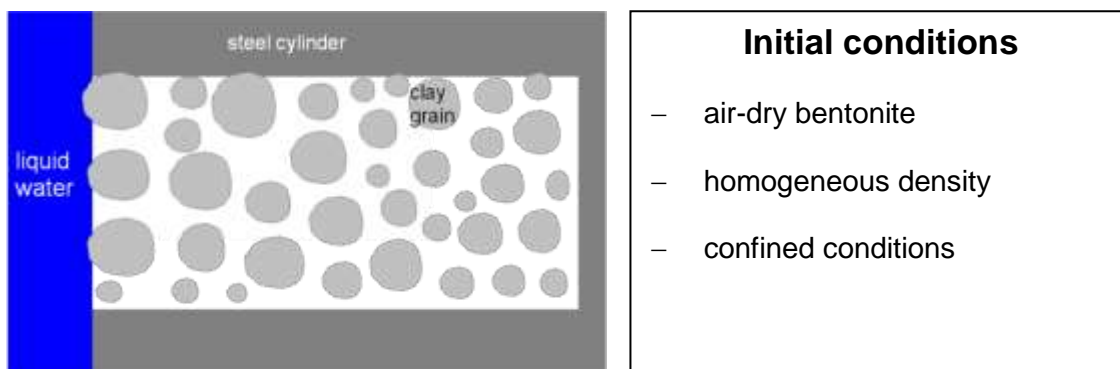


**Fig. 1.1. Initial conditions of an exemplary re-saturation situation**

**The first stage or pre-stage** begins with the first contact of water with the bentonite. In a rather short period of time water is sucked into the pore space rather fast, mainly by capillary forces. With the liquid water present in the pore space hydration kicks in. The reduction of pore space caused by the swelling of the minerals is accompanied by a dramatic reduction of permeability. Since uptake of liquid water by clay minerals is a fast process, too (e.g., Pusch & Young, 2003), only very little water penetrates into the bentonite before any further water inflow is hindered very effectively due to the low permeability. This view is supported by the experimental evidence of Kröhn (2004a) which shows exclusively for the immediate vicinity of the inlet an unproportionally high water content and a particularly low dry density indicating a local and comparatively high swelling. The end of stage 1 is illustrated in Fig. 1.2.

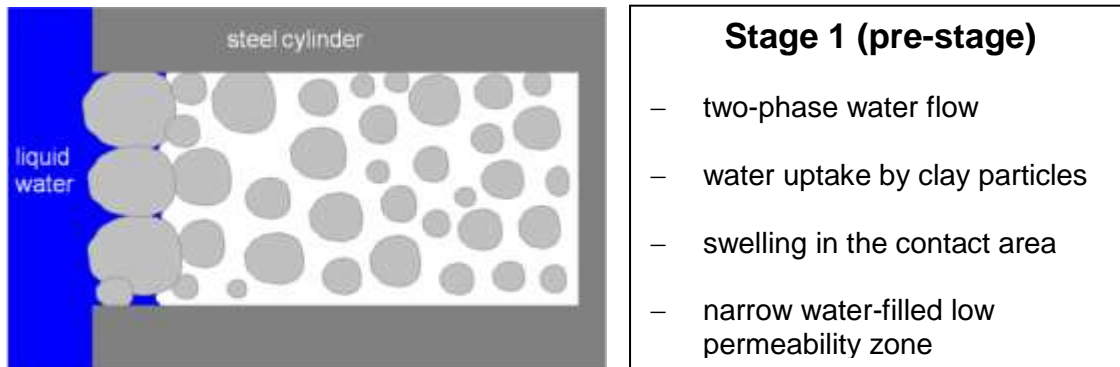
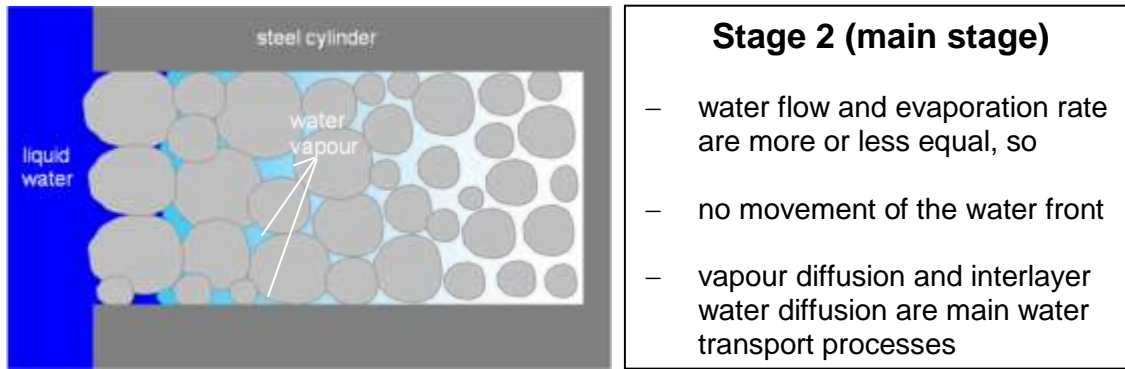


**Fig. 1.2. End of stage 1 in an exemplary re-saturation situation**

Parallel to the uptake of liquid water evaporation takes place in the pore space at the interface of the fluid and the gas phase. This becomes significant when the influx of liquid water is low after the end of stage 1 because progress of the water/air-interface in the pore space is slowed down even further by this process. A rough estimation of the flux densities at the end of the stage 1 shows that the supply of liquid water through the narrow, already saturated zone equals the following vapour flow further into the bentonite (Kröhn, 2004a). Thus the saturation with liquid water is temporarily limited to the wetted bentonite surface. The measurements of Push & Kasbohm (2001) indicate that the pre-stage of capillary water uptake takes times in the order of minutes rather than hours or even days.

**The second stage or main stage** is a stage in which all the water entering evaporates at the established interface between liquid water and air. Water transport further into the bentonite takes places only by means of vapour diffusion in the gas phase and of interlayer water diffusion. The low density of the vapour is here compensated by the high process velocity of the gas diffusion. The varying vapour density during stage 2 is indicated by different shades of light blue in Fig. 1.3.

During the main stage the vapour flux at the water/air-interface decreases as the gradient of the relative humidity decreases. Concurrently the water vapour increases the amount of hydrated water next to the interface. This reduces the suction and thus the liquid water flow through the thin saturated zone at the inlet. It is therefore quite probable that the water/air-interface moves very little for quite some time.



- Stage 2 (main stage)**
- water flow and evaporation rate are more or less equal, so
  - no movement of the water front
  - vapour diffusion and interlayer water diffusion are main water transport processes

Fig. 1.3. Stage 2 in an exemplary re-saturation situation

## 1.4 Mathematical description

### 1.4.1 General balance equation

The most general starting point for the derivation of a balance equation is the definition of a time-dependent state variable  $Z(t)$  in a moving domain  $B(t)$  (for nomenclature see tables 1.1 and 1.2):

$$Z(t) = \int_{B(t)} z(\mathbf{x}, t) dV \quad (1.1)$$

Allowing for a flux  $J$  of quantity  $Z$  across the moving surface of  $B$  and including a source  $r$  of quantity  $Z$  within  $B$  Reynolds' transport theorem yields for a fixed domain  $G$  (e.g., Görtner, 1987):

$$\int_G \left[ \frac{\partial z}{\partial t} + \nabla(\mathbf{v}z + \mathbf{J}) - r \right] dV = 0 \quad (1.2)$$

**Tab. 1.1. Nomenclature - symbols**

Symbol	Description	Dimension
$\mathcal{G}$	gravitational acceleration	[m s <sup>-2</sup> ]
$p$	pressure	[Pa]
$p_c$	capillary pressure/suction	[Pa]
$q$	production rate of a sink/source	[kg m <sup>-3</sup> s <sup>-1</sup> ]
$r$	sink/source of $Z$ in $G$	[<dim>/[m <sup>3</sup> s]]
$\tilde{r}$	source of vapour	[kg m <sup>-3</sup> s <sup>-1</sup> ]
$\bar{r}$	source of interlamellar water	[kg m <sup>-3</sup> s <sup>-1</sup> ]
$w$	gravimetric water content of the bentonite	[kg <sub>water</sub> kg <sub>solids</sub> <sup>-1</sup> ]
$t$	time	[s]
$\mathbf{v}$	advective flow velocity	[m/s]
$z$	density of $Z$	[<dim>/m <sup>3</sup> ]
$B$	time-dependent 3D-domain	[m <sup>3</sup> ]
$D_m$	coefficient of binary vapour diffusion in air	[m <sup>2</sup> s <sup>-1</sup> ]
$D'$	coefficient of diffusion of the interlamellar water	[m <sup>2</sup> s <sup>-1</sup> ]
$\tilde{D}$	"diffusion coefficient" for the empirical approach	[m <sup>2</sup> s <sup>-1</sup> ]
$\hat{D}$	"diffusion coefficient" derived from TPF-approach	[m <sup>2</sup> s <sup>-1</sup> ]
$\bar{D}$	"diffusion coefficient" derived from EVD-approach	[m <sup>2</sup> s <sup>-1</sup> ]
$G$	3D-domain fixed in space	[m <sup>3</sup> ]
$J$	non-advective flux of $Z$ across the surface of $G$	[<dim>/[m <sup>2</sup> s]]
$T$	temperature	[K]
$Z$	extensive state variable in $B$ with the dimension <dim>	[<dim>]
$\beta_p$	compressibility of water defined as $\beta_p = (1/\rho_i)(\partial\rho_i/\partial p_i)$	[Pa <sup>-1</sup> ]
$\beta_T$	volumetric coefficient of thermal expansion of water	[K <sup>-1</sup> ]
	defined as $\beta_T = (1/\rho_i)(\partial\rho_i/\partial T)$	
$\rho$	density	[kg m <sup>-3</sup> ]
$\tau$	tortuosity of the pore space	[-]
$\tau_{hyd}$	tortuosity of the interlamellar space	[-]
$\Delta$	Laplacian operator	[m <sup>-2</sup> ]
$\Phi$	porosity	[-]

**Tab. 1.2. Nomenclature - indices**

Index	Description
<i>a</i>	macroscopic, apparent
<i>d</i>	dry state of the bentonite
<i>ini</i>	initial state of the bentonite, i.e. partially saturated state
<i>max</i>	fully saturated state of the bentonite
<i>s</i>	solids
<i>w</i>	water
<i>v</i>	vapour
12	at completion of one hydrate layer
23	at completion of two hydrate layers
<i>hydi</i>	at forming the <i>i</i> <sup>th</sup> hydrate layer
<i>sat</i>	at vapour saturation

**1.4.2 Double-continuum approach**

The general balance equation ( 1.2 ) can apparently be used to describe mass conservation of water in the bentonite. In doing so, discrimination between vapour in the pore space and hydrated water in the interlamellar space appears to be advantageous. It allows to distinguish clearly between relative humidity in the pore space and water content, which are both easily measured as indicators of the actual status of re-saturation. The price to pay for this separation is that the two resulting continua have to be coupled.

This method of coupling two continua was already suggested in 1963 to describe flow in a fracture system and in the porous matrix simultaneously (Warren & Root, 1963). Fig. 1.4 illustrates the principle for a typical two-dimensional re-saturation situation. One continuum represents the pore space in which vapour diffusion takes place; the other continuum comprises the interlamellar space accommodating interlayer water. The coupling process is hydration which provides exchange of water between the two continua.

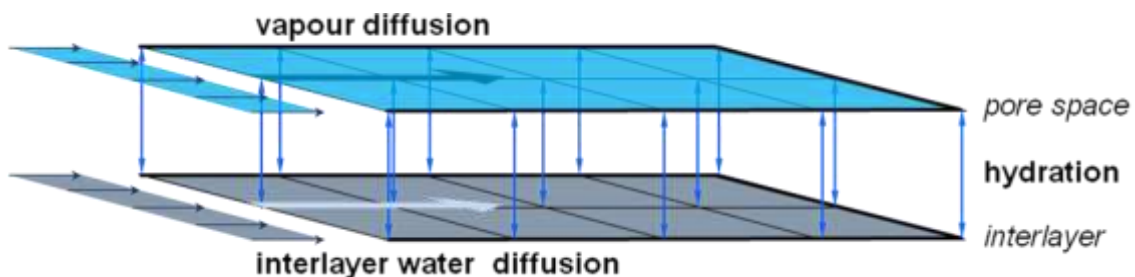


**Fig. 1.4. Double-continuum approach for re-saturating bentonite**

### 1.4.3 Balance equation for vapour in the pore space

In the domain describing the pore space of the bentonite  $Z$  represents the mass  $m_v$  of water vapour in the pore space. Also adopting straightforward assumptions (Kröhn, 2011) enables to specify the quantities in equation ( 1.2 ):

$$\begin{aligned} z &= \Phi \rho_v \\ \mathbf{v} &= \mathbf{0} \\ \mathbf{J} &= -\Phi \tau \mathbf{D}_m \cdot \nabla \rho_v \\ r &= r_{hyd} + r_{cond} \end{aligned} \quad (1.3)$$

Thus equation ( 1.2 ) is transformed into:

$$\int_G \left[ \frac{\partial(\Phi \rho_v)}{\partial t} - \nabla(\Phi \tau \mathbf{D}_m \cdot \nabla \rho_v) - r_{hyd} - r_{cond} \right] dV = 0 \quad (1.4)$$

Certain continuity conditions assured – for details see e.g. (Gärtner, 1987) – the integral form ( 1.4 ) of the balance equation can also be written as a partial differential equation:

$$\frac{\partial(\Phi \rho_v)}{\partial t} - \nabla(\Phi \tau \mathbf{D}_m \cdot \nabla \rho_v) - r_{hyd} - r_{cond} = 0 \quad (1.5)$$

### 1.4.4 Balance equation for the water in the interlamellar space

Analogously to the procedure in the previous section state variable  $Z$  can be chosen to represent the mass of water  $m_w$  in the interlamellar space of the clay minerals. Introducing Fickian diffusion of interlamellar water yields the balance equation

$$\int_G \left[ \frac{\partial(\Phi_{hyd} \rho_w)}{\partial t} - \nabla(\tau_{hyd} \mathbf{D}_{hyd} \cdot \nabla(\Phi_{hyd} \rho_w)) - \bar{r}_{hyd} \right] dV = 0 \quad (1.6)$$

Under some further assumptions (for details see Kröhn (2011)) equation ( 1.7 ) can be transformed into:

$$\rho_d \frac{\partial w}{\partial t} - \rho_d \nabla(\tau_{hyd} \mathbf{D}_{hyd} \cdot \nabla w) - \bar{r}_{hyd} = 0 \quad (1.7)$$

Note, that the local mass of water vapour is negligible compared to the local mass of hydrated water.

### 1.4.5 Coupling the balance equations

The two balance equations ( 1.5 ) and ( 1.7 ) describe water transport in two different continua that are coupled by exchange terms, formally the source terms  $r_{hyd}$  or  $\bar{r}_{hyd}$ , respectively. Since water is either present in the pore space as vapour or in the interlamellar space as hydrated water the process of hydration/dehydration decreases water in one continuum and adds the same amount of water in the other continuum:

$$r_{hyd} = -\bar{r}_{hyd} \quad (1.8)$$

By Kröhn (2004a) an exchange term was suggested that introduced the kinetics of hydration into the resulting balance equations<sup>1</sup>. Following this approach two independent variables – the partial vapour density in the pore space and the water content in the interlamellar space – remained to be calculated. The hydration kinetics appeared to play a minor role in the re-saturation process, though (Buhmann et al., 2004), which lead to the assumption that hydration occurs instantaneously meaning that the water content is always in equilibrium with the relative humidity in the pore space. Equations ( 1.5 ) and ( 1.7 ) can thus be added in such a way that the sink/source terms  $r_{hyd}$  and  $\bar{r}_{hyd}$  cancel out yielding eventually one partial differential equation with two independent variables, vapour density and water content:

$$\Phi \frac{\partial \rho_v}{\partial t} + \rho_d \left( 1 - \frac{\rho_v}{\rho_w} \right) \frac{\partial w}{\partial t} - \nabla \cdot (\Phi \tau D_m \cdot \nabla \rho_v) - \rho_d \nabla \cdot (\tau_{hyd} D_{hyd} \cdot \nabla w) - r_{cond} = 0 \quad (1.9)$$

#### 1.4.6 Final forms of the balance equation

Eq. ( 1.9 ) was further processed and further assumptions and simplifications were introduced leading eventually to the non-isothermal balance equation ( 1.10 ) (Kröhn, 2011).

Note that by eliminating the water content as a primary variable in the equation ( 1.10 ) the temperature has been introduced instead.

Note further that several terms in equation ( 1.10 ) are negligible or conditionally negligible (Kröhn, 2016).

---

<sup>1</sup>This approach led eventually to the code VAPMOD, the isothermal predecessor of VIPER.

$$\begin{aligned}
 & \rho_d \frac{\partial w}{\partial r_h} \frac{1}{\rho_{v \text{ sat}}} \frac{\partial \rho_v}{\partial t} \\
 & + \left\{ \rho_d \frac{\partial w}{\partial T} \right\} \frac{\partial T}{\partial t} \\
 & + \left\{ -D_a - \rho_d D'_a \frac{\partial w}{\partial r_h} \frac{1}{\rho_{v \text{ sat}}} \right\} \Delta \rho_v \\
 & + \left\{ \begin{aligned} & -\frac{\partial D_a}{\partial T} \nabla T \\ & -\rho_d D'_a \left[ \nabla \left( \frac{\partial w}{\partial r_h} \right) \right] \frac{1}{\rho_{v \text{ sat}}} - \rho_d D'_a \frac{\partial w}{\partial r_h} \left[ \nabla \left( \frac{1}{\rho_{v \text{ sat}}} \right) \right] - \rho_d \frac{\partial D'_a}{\partial T} \nabla T \frac{\partial w}{\partial r_h} \frac{1}{\rho_{v \text{ sat}}} \end{aligned} \right\} \cdot \nabla \rho_v \\
 & + \left\{ \begin{aligned} & -\rho_d \frac{\partial w}{\partial r_h} \frac{1}{(\rho_{v \text{ sat}})^2} \frac{\partial \rho_{v \text{ sat}}}{\partial T} \frac{\partial T}{\partial t} + \rho_d D'_a \left[ \nabla \left( \frac{\partial w}{\partial r_h} \right) \right] \frac{1}{(\rho_{v \text{ sat}})^2} \frac{\partial \rho_{v \text{ sat}}}{\partial T} \cdot \nabla T \\ & + \rho_d D'_a \frac{\partial w}{\partial r_h} \nabla \left( \frac{1}{(\rho_{v \text{ sat}})^2} \frac{\partial \rho_{v \text{ sat}}}{\partial T} \right) \cdot \nabla T + \rho_d \frac{\partial D'_a}{\partial T} \nabla T \frac{\partial w}{\partial r_h} \frac{1}{(\rho_{v \text{ sat}})^2} \frac{\partial \rho_{v \text{ sat}}}{\partial T} \cdot \nabla T \\ & + \rho_d D'_a \frac{\partial w}{\partial r_h} \frac{1}{(\rho_{v \text{ sat}})^2} \frac{\partial \rho_{v \text{ sat}}}{\partial T} \Delta T \end{aligned} \right\} \rho_v \quad (1.10) \\
 & + \left\{ -\rho_d D'_a \left[ \nabla \left( \frac{\partial w}{\partial T} \right) \right] - \rho_d \frac{\partial D'_a}{\partial T} \nabla T \frac{\partial w}{\partial T} \right\} \cdot \nabla T \\
 & + \left\{ -\rho_d D'_a \frac{\partial w}{\partial T} \right\} \Delta T \\
 & - r_{\text{cond}} = 0
 \end{aligned}$$

In case of isothermal conditions ( 1.10 ) simplifies to

$$\begin{aligned}
 & \rho_d \frac{\partial w}{\partial r_h} \frac{1}{\rho_{v \text{ sat}}} \frac{\partial \rho_v}{\partial t} - \left( D_a + \rho_d D'_a \frac{\partial w}{\partial r_h} \frac{\partial r_h}{\partial \rho_v} \right) \Delta \rho_v - \rho_d D'_a \frac{1}{\rho_{v \text{ sat}}} \nabla \left( \frac{\partial w}{\partial r_h} \right) \cdot \nabla \rho_v \quad (1.11) \\
 & = 0
 \end{aligned}$$

### 1.4.7 Conditional equations

Solving balance equation ( 1.10 ) requires the calculation of several secondary variables.

Fig. 1.5 illustrates the dependency of these secondary variables on the three primary variables vapour density, temperature, and pressure. Where possible the related conditional equations are listed in Tab. 1.3.

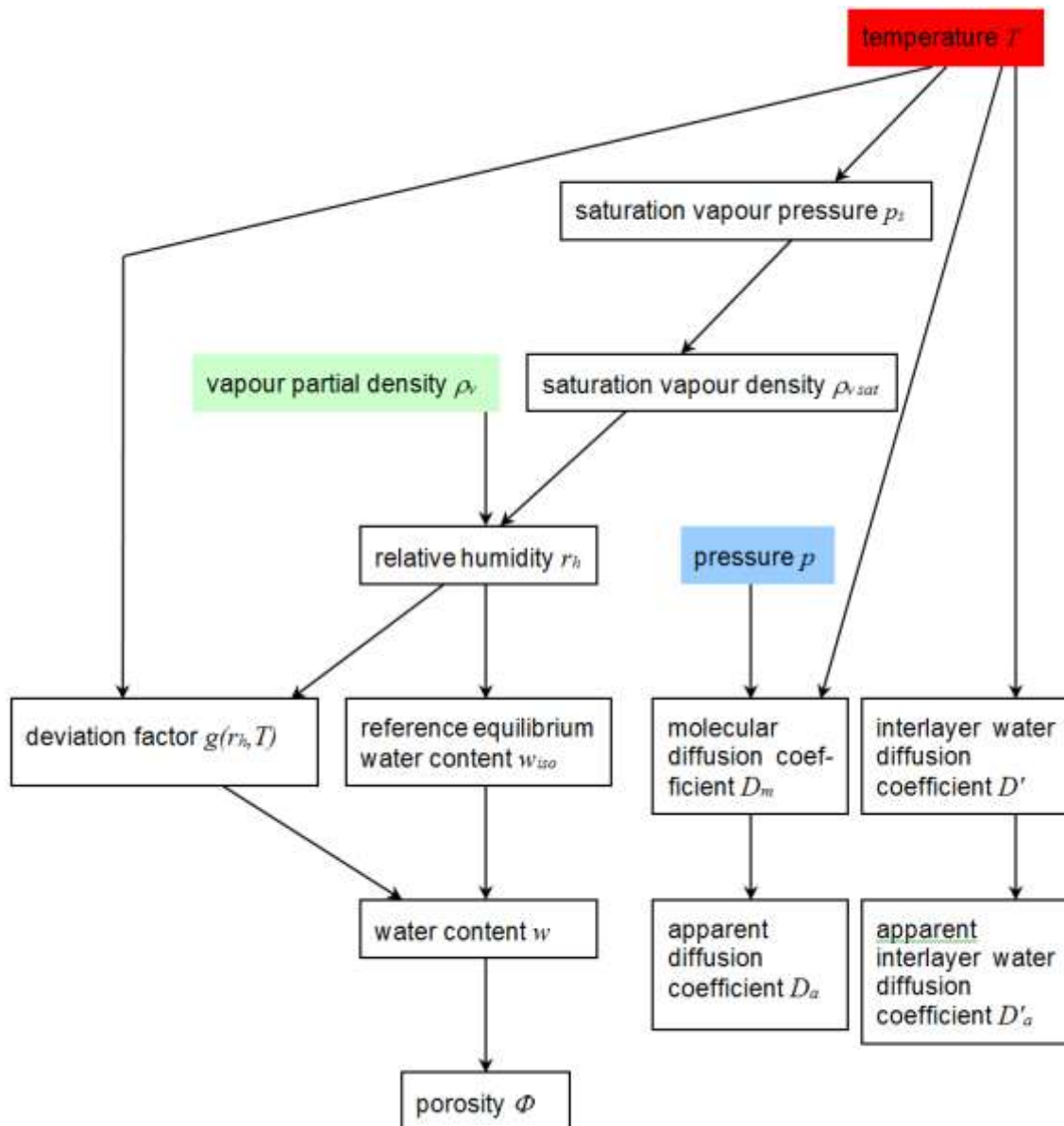


**Fig. 1.5. Dependency of secondary variables (white boxes) from the primary variables (coloured boxes); based on Kröhn (2008)**

**Tab. 1.3. Compilation of conditional equations**

quantity	unit	equation
saturation vapour pressure $p_s(T)$	[Pa]	calculated after IAPWS (1997)
saturation vapour density $\rho_{v\ sat}(p_s)$	[kg/m <sup>3</sup> ]	calculated after IAPWS (1997)
partial derivative $\partial\rho_{v\ sat}/\partial T(T)$	[-]	calculated numerically
relative humidity $r_h(\rho_v, \rho_{v\ sat})$	[-]	$r_h = \frac{\rho_v}{\rho_{v\ sat}} \quad (1.12)$
isotherm at reference temperature $w_{iso}(r_h, T_0)$	[-]	first approximation: $w_{iso} = w_e r_h \quad (1.13)$ alternatively data given in tabulated form as an analytical function using splines
deviation factor $g(r_h, T)$	[-]	product of temperature term and humidity term; present proposal: $g(r_h, T) = [1 - r_h(1 - r_h)]^{0.8} \frac{(T - 25)}{(98 - 25)0.6} \quad (1.14)$
water content $w(w_{iso}, g)$	[-]	$w = w_{iso} g(r_h, T) \quad (1.15)$
partial derivative $\partial w / \partial r_h(r_h, T)$	[-]	calculated numerically
partial derivative $\partial w / \partial T(r_h, T)$	[-]	calculated numerically
porosity $\Phi(w)$	[-]	$\Phi = 1 - \frac{\rho_d}{\rho_s} - \frac{\rho_d}{\rho_w} w \quad (1.16)$
molecular diffusion coefficient $D_m(p, T)$	[m <sup>2</sup> /s]	$D_m = D_{m0} \frac{p_{g0}}{p_g} \left( \frac{T}{T_0} \right)^\theta \quad (1.17)$ after Vargaftik et al. (1996)
macroscopic diffusion coefficient $D_a(D_m)$	[m <sup>2</sup> /s]	$D_a = \Phi_0 \tau_0 D_m \quad (1.18)$
partial derivative $\partial D_a / \partial T(p, T)$	[-]	calculated numerically
coefficient of interlayer water diffusion $D'(p, T)$	[m <sup>2</sup> /s]	$D' = \begin{cases} 0.5 - 4 \cdot 10^{-10} \text{ m}^2/\text{s} & \text{1 hydrate layer} \\ 10 \cdot 10^{-10} \text{ m}^2/\text{s} & \text{2 hydrate layers} \end{cases} \quad (1.19)$
macroscopic coefficient of interlayer water diffusion $D'_a(D')$	[m <sup>2</sup> /s]	$D'_a = \tau_{hyd} D' \quad (1.20)$
partial derivative $\partial D'_a / \partial T(p, T)$	[-]	calculated numerically

#### 1.4.8 Boundary conditions

In case of a Dirichlet boundary condition a specific value for the vapour density is assigned to a node. The equation referring to that node is not to be solved.

In case of a Neumann boundary condition, however, the referring equation must be solved. Usually, only the special case of a no-flow boundary is applied.

The only exception is the case of a limited flow rate at the inflow boundary. It is assumed that all the water coming from the rock is taken up by the bentonite but inflow is not sufficient to build up the narrow fully saturated zone as described in subsection **Fel! Hittar inte referenskälla..** Even if the bentonite hydrates immediately at the bentonite-water contact, the inflow is just sufficient to provide a partial water saturation. All water coming from the rock is transported away from the bentonite-water contact either by vapour flow in the pore space or by diffusion of hydrated water in the interlamellar space. The ratio of the two fluxes is not known beforehand, though. Instead, a Dirichlet boundary condition is substituted that is determined on the condition that the sum of both fluxes equals the prescribed flux from the rock (for details see Kröhn (2017)).

### 1.5 Input parameters and their sources

#### Geometry

- x-coordinate of left model boundary [m]
- x-coordinate of right model boundary [m]
- cross-section area [m<sup>2</sup>]

#### Discretization

- number of elements
- time step size [s]
- end of simulated time [s]

#### Parameters of the pore space

- tortuosity [-]
- pore air pressure [Pa]

#### Parameters of the pore space

- tortuosity [-]
- diffusion coefficient for first hydration layer [m<sup>2</sup>/s] (Skipper et al., 2006)
- diffusion coefficient for second and higher hydration layers [m<sup>2</sup>/s] (Skipper et al., 2006)
- water content related to switch between the two diffusion coefficients [-] (Kröhn 2011)

#### Initial conditions

- one of the following two
  - dry density [ $\text{kg}/\text{m}^3$ ]
  - density at emplacement [ $\text{kg}/\text{m}^3$ ]
- one of the following four
  - initial water content [-]
  - initial relative humidity [-]
  - initial dry porosity [-] (only if dry density is  $>0$ )
  - initial porosity [-] (only if density at emplacement is  $>0$ )

#### Final conditions

- one of the following two
  - final water content [-]
  - final porosity [-]

#### Boundary conditions on the left hand side

- time of beginning water uptake [s]
- water flux (optional) [ $\text{kg}/(\text{m}^2 \text{ s})$ ]

#### Boundary conditions on the right hand side

- time of beginning water uptake [s]
- water flux (optional) [ $\text{kg}/(\text{m}^2 \text{ s})$ ]

#### Temperature

- steady state temperature [ $^{\circ}\text{C}$ ]
- characterstring representing directory and file with temperature data

#### Other densities

- grain density [ $\text{kg}/\text{m}^3$ ]
- density of interlayer water [ $\text{kg}/\text{m}^3$ ]

#### Isotherm

- switch for linear, analytical or tabular data
- characterstring representing directory and file with isotherm data (if applicable)

#### Output

- number n of observation points providing breakthrough curves
- n x-coordinates [m]
- points in time for exporting physical and numerical data in TecPlot-files

## 1.6 Performance

The observation in the laboratory that water uptake dynamics using liquid water and water vapour as sources for re-saturation compared qualitatively well triggered the development of a vapour diffusion model and the referring code VAPMOD. It explained bentonite re-saturation by binary vapour diffusion in the pore space and by hydration only (Kröhn, 2005).

In order to explore the potential of this approach it was applied systematically to physically increasing complex conditions, namely increased hydraulic pressure at the inflow boundary (Kröhn, 2006) and non-isothermal conditions (Kröhn, 2010) as investigated in the laboratory.

For advancing the approach to non-isothermal conditions the code was re-written as VIPER (**V**apour transport **I**n **P**artially saturated bentonite as **E**ngineered barrier for **R**epositories) (Kröhn, 2011). Further investigations were performed with a view to in-situ experiment. They included non-isothermal conditions or involved bentonite-sand mixtures. During these works it became apparent that the model had to be supplemented by the diffusion of hydrated water in the interlamellar space (Kröhn, 2011) leading to the Extended Vapour Diffusion (EVD) model.

Supplementing in-situ investigations referring to the buffer-rock interaction in fractured rock indicated another unidentified deficiency. All the previously considered code qualifying experiments had been based on freely accessible and inexhaustible water supply for the bentonite. This, however, does not apply to the case of bentonite in contact with undisturbed granite where very low outflow rates from the rock can be expected. This was taken care of by theoretical considerations based on the EVD and an appropriate code extension (Kröhn, 2017).

## References

- Buhmann, D., Becker, D.-A., Keesmann, S., Kröhn, K.-P., Rübél, A., 2004.** Aktualisierung sicherheitsanalytischer Rechenprogramme für Teilsysteme eines Endlagers. Abschlussbericht des BMWA-Vorhabens 02 E 9178, GRS-report GRS-200. (In German)
- Gärtner, S., 1987.** Zur diskreten Approximation kontinuumsmechanischer Bilanzgleichungen. Bericht Nr. 24/1987, Institut für Strömungsmechanik und Elektronisches Rechnen im Bauwesen, Universität Hannover. (In German)
- International Association for Properties of Water and Steam (IAPWS), 1997.** Release on the IAPWS Industrial Formulation 1997 for the Thermodynamic Properties of Water and Steam. Homepage: <http://www.iapws.org>.
- Kröhn, K.-P., 2004a.** Modelling the re-saturation of bentonite in final repositories in crystalline rock. Final report, FKZ 02 E 9430 (BMWa), Gesellschaft für Anlagen- und Reaktorsicherheit (GRS) mbH, GRS-199, Köln.
- Kröhn, K.-P., 2004b.** Proposal of an alternative re-saturation model for bentonite buffers - the conceptual model, the numerical model and the data base. In: Pusch, R. and Svemar, Ch. (Eds.), Proceedings from Task Force-related meeting on buffer & backfill modelling, SKB International report IPR-04-23, Stockholm, pp. 95-101.
- Kröhn, K.-P., 2005.** New Evidence for the Dominance of Vapour Diffusion During the Re-saturation of Compacted Bentonite. Engineering Geology, Volume 82, Issue 2.
- Kröhn, K.-P., 2006.** About the role of vapour transport during bentonite re-saturation. FKZ 02 E 9954 (BMWa), Bericht GRS-222, GRS Braunschweig.
- Kröhn, K.-P., 2010.** Simulating water uptake of compacted bentonite under non-isothermal conditions, decoupled from the mechanics and without feedback of hydraulics to heat transport. Proceedings of the Workshop on "Long-term performance of smectitic clays embedding canisters with highly radioactive waste" held in Lund, 2007, Applied Clay Science, Vol. 47, pp. 28-35; Online: <http://dx.doi.org/10.1016/j.clay.2008.06.004>, 2008; printed version: 2010.
- Kröhn, K.-P., 2011.** Code VIPER - Theory and Current Status. Status report, FKZ 02 E 10548 (BMWa), Gesellschaft für Anlagen- und Reaktorsicherheit (GRS) mbH, GRS-269, Köln, 2011.
- Kröhn, K.-P., 2016.** Bentonite re-saturation: Different conceptual models – similar mathematical descriptions. FKZ 02 E 11284 (BMWa). In: Norris, S., Bruno, J., Van Geet, M. & Verhoef, E. (eds) Radioactive Waste Confinement: Clays in Natural and Engineered Barriers. Geological Society, London, Special Publications, 443, <http://doi.org/10.1144/SP443.12>, The Geological Society, Special Issue.
- Kröhn, K.-P., 2017.** Hydraulic Interaction of Engineered and Natural Barriers – Task 8b-8d,8f of SKB. Summary report, 02 E 10336, 02 E 10548, 02 E 10558, 02 E 11102, and 02 E 11213 (BMWa), Gesellschaft für Anlagen- und Reaktorsicherheit (GRS) mbH, GRS-430, Köln.
- Pusch, R., Kasbohm, J., 2001.** Can the Water Content of Highly Compacted Bentonite be Increased by Applying a High Water Pressure? SKB, Technical Report 01-33.
- Pusch, R., Yong, R., 2003.** Water saturation and retention of hydrophilic clay buffer – microstructural aspects. Applied Clay Science 23, 25-33.



**Skipper, N.T., Lock, P.A., Titiloye, J.O., Swenson, J., Mirza, Z.A., Howells, W.S., Fernandez-Alonso, F., 2006.** The structure and dynamics of 2-dimensional fluids in swelling clays. *Chemical Geology* 230, 182-196.

**Vargaffik, N.B., Vinogradov, Y.K., Yargin, V.S., 1996.** *Handbook of Physical Properties of Liquids and Gases, Pure Substances and Mixtures.* begell house, inc., New York, Wallingford (UK).

**Warren, J.E., Root, P.J., 1963.** The behaviour of naturally fractured reservoirs. *Soc. Petrol. Eng. J.*, 3,245-355.

# D3.1



## Description of models available at the start of the project at the Lithuanian Energy Institute and preliminary modelling results

### DELIVERABLE (D3.1)

### ANNEX K

Author(s): prof. P. Poskas  
dr. D. Justinavicius  
dr. A. Narkuniene

Reporting period: 01/07/17 – 30/11/18

Date of issue of this report: **28/02/18**

Start date of project: **01/06/17**

Duration: 48 Months

This project receives funding from the Euratom research and training programme 2014-2018 under grant agreement No 745 942	
<b>Dissemination Level</b>	
<b>PU</b>	Public

## Content

<b>1</b>	<b>Introduction.....</b>	<b>3</b>
<b>2</b>	<b>Basic hypotheses and scope.....</b>	<b>3</b>
<b>3</b>	<b>Mathematical description .....</b>	<b>4</b>
<b>4</b>	<b>Input parameters and their sources.....</b>	<b>6</b>
<b>5</b>	<b>Model performance on bentonite resaturation .....</b>	<b>7</b>
5.1	Modelling results using PETRASIM .....	7
5.2	Modelling results using COMSOL Multiphysics.....	11
<b>6</b>	<b>Conclusions.....</b>	<b>13</b>
	<b>Acknowledgements.....</b>	<b>14</b>
	<b>References.....</b>	<b>14</b>

# 1 Introduction

This report provides the description of current status of Lithuanian Energy Institute (LEI) work related to modelling of bentonite behaviour in repository conditions.

As a starting point in development of hydro-mechanical (HM) model, pure bentonite resaturation (H process) were analysed, taking into account Richard's or two-phase flow approaches. Both approaches were tested using two different modelling tools (PETRASIM and COMSOL Multiphysics) available at LEI. Specific exercise assessing bentonite resaturation in generic disposal system based on KBS-3 disposal concept as defined in (Dessirier et al., 2014) was studied and results were compared.

Mechanical processes are not included in the LEI model at this stage.

# 2 Basic hypotheses and scope

Prior to modelling of coupled HM processes, the efforts were put on the evaluation of capabilities of numerical tools to model processes separately. As a starting point the ability of numerical tools (PETRASIM and COMSOL Multiphysics) available at LEI to assess the bentonite resaturation process was studied for simplified generic disposal system based on KBS-3 concept in fractured rock as defined in (Dessirier et al., 2014).

Modelled system is presented in Figure 2-1. The system consists of open transportation tunnel, deposition hole filled with bentonite and intersecting fracture. Vertical deposition hole radius is 0.15 m, bottom located at 3 m below transportation tunnel. A horizontal rock fracture intersects the deposition hole at middle depth and is implemented as 10 cm thick vein with higher permeability and porosity as the rock matrix.

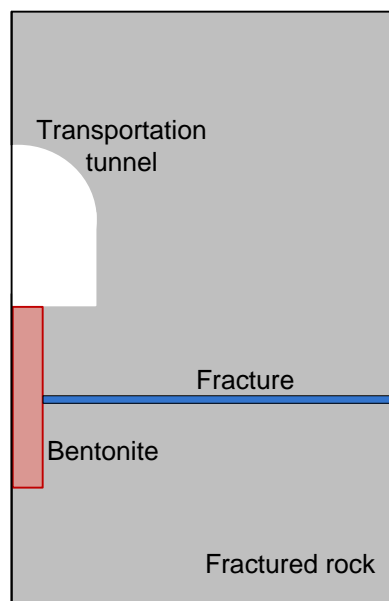


**Figure 2-1. Generic disposal system (not to scale) for analysis of capabilities of numerical tools for H process modelling**

### 3 Mathematical description

Approach of two-phase flow in porous media modelling and simplified formulation using Richard's equation could be considered for modelling of bentonite resaturation.

Modelling of material saturation using **Richard's approach** consists of solving the partial differential equations for liquid phase:

$$\rho \left( \frac{C_m}{\rho g} + S_e S \right) \frac{\partial p}{\partial t} + \nabla \cdot \rho \left( -\frac{k_s}{\mu} k_r (\nabla p + \rho g \nabla D) \right) = Q_m,$$

here  $p$  is the dependent variable (pressure of liquid phase),  $\rho$  is density of fluid,  $C_m$  is specific moisture capacity,  $g$  is acceleration of gravity,  $S_e$  is effective saturation,  $S$  is storage coefficient,  $k_s$  is absolute permeability at saturated conditions,  $k_r$  is relative permeability,  $\mu$  is dynamic viscosity of fluid,  $D$  represents elevation and  $Q_m$  is fluid source (positive) or sink (negative).

With variably saturated flow, hydraulic properties change as fluids move through the medium, filling some pores and draining others. It is assumed that the pore space not filled with liquid contains an immobile fluid (air) at atmospheric pressure.

The fluid velocity at Darcy scale is:

$$\mathbf{u} = -\frac{k_s}{\mu} k_r (\nabla p + \rho g \nabla D),$$

where  $\mathbf{u}$  is the flux vector (Darcy velocity). To characterize the average fluid velocity in the pores  $\mathbf{u}$  is divided by the volume liquid fraction  $\theta_s$ .

While modelling of resaturation of generic disposal system using **two-phase flow approach** it is assumed that their velocities can be expressed by the following extended form of the Darcy formula:

$$\mathbf{u}_\alpha = -\frac{k_s}{\mu_\alpha} k_{r_\alpha}(S_\alpha) (\nabla p + \rho_\alpha g \nabla D),$$

where  $k_{r_\alpha}(S_\alpha)$  is a relative permeability of  $\alpha$  phase (liquid, gas) as a function of phase saturation.

Continuum description of a multiphase porous medium at the Darcy scale implies that the relevant physical quantities defined at a given point  $x$  represent averages taken over a pore-scale representative elementary volume (REV) associated with that point. The volume fraction of phase  $\alpha$  is defined as the ratio of the volume of the part of the REV occupied by phase  $\alpha$  to the total volume of the REV:

$$\theta_\alpha = \frac{V_\alpha}{V}.$$

Porosity is defined as the volume fraction of pores, and it is equal to the sum

of the volume fractions of the two pore fluids:

$$n = \frac{V_{liq} + V_{gas}}{V} = \theta_{liq} + \theta_{gas}.$$

Saturation of each phase, which is equal to the fraction of the pore space occupied by a given fluid ( $S_\alpha$ ):

$$S_{liq} = \frac{\theta_{liq}}{n}, \quad S_{gas} = \frac{\theta_{gas}}{n},$$

$$S_{liq} + S_{gas} = 1.$$

Normalized (effective) saturation ( $S_e$ ) is defined as follows:

$$S_{e\alpha} = \frac{S_\alpha - S_\alpha^r}{S_\alpha^{max} - S_\alpha^r},$$

here  $S_\alpha^r$  is residual saturation of phase  $\alpha$  in porous media then there is no continuous flow of this phase,  $S_\alpha^{max}$  is a maximal saturation in analysed material.

The difference between the pressure potentials of gas and liquid in unsaturated conditions, caused by the action of capillary and adsorption forces, is called the capillary pressure:

$$p_{gas} - p_{liq} = p_c(S_{e\_liq}).$$

The capillary pressure at the Darcy scale is assumed to be a function of the liquid saturation. Among the most known dependencies of capillary pressure and relative permeability on effective saturation are those called van Genuchten (for capillary pressure) and Van Genuchten–Mualem (for relative permeability) as defined below (Szymkiewicz A, 2013):

$$p_c = p_0 \left( (S_{e\_liq})^{-\frac{1}{m}} - 1 \right)^{1/n},$$

$$S_{e\_liq} = \left( 1 + \left( \frac{p_c}{p_0} \right)^n \right)^{-\frac{1}{m}},$$

$$m = 1 - \frac{1}{n},$$

here  $p_0$  is a pressure scaling parameter (air entry pressure),  $n$  and  $m$  are Van Genuchten fitting parameters. Air entry pressure is related to the average size of the pores and its value approximately corresponds to the position of the inflection point at the capillary curve.

$$k_{r\_liq}(S_{e\_liq}) = S_{e\_liq}^l \left( 1 - \left( 1 - (S_{e\_liq})^{1/m} \right)^m \right)^2,$$

$$k_{r\_gas}(S_{e\_liq}) = (1 - S_{e\_liq})^l \left(1 - (S_{e\_liq})^{1/m}\right)^{2m},$$

here  $l$  is connectivity factor and can be treated as a fitting parameter of the dependency.

Integrated finite volume method as realized in PETRASIM (USA) and finite element method as realized in COMSOL Multiphysics (USA) are employed for the numerical analysis of the system resaturation.

## 4 Input parameters and their sources

Geometry of the model, material parameters and initial/boundary conditions were implemented as it is prescribed in (Dessirier et al., 2014). The material properties used in the analysis are summarized in Table 4-1.

**Table 4-1 Material properties of analysed system (Dessirier et al., 2014).**

<b>Material parameters</b>				
Material	$n$ (-)	$k_s$ (m <sup>2</sup> )	$m$ (-)	$p_0$ (MPa)
Bentonite	0.44	$6.4 \times 10^{-21}$	0.3	9.23
Rock matrix	$1 \times 10^{-5}$	$1 \times 10^{-19}$	0.6	1.74
Rock fracture	$1 \times 10^{-3}$	$5 \times 10^{-16}$	0.6	1.74

The water retention curves (capillary pressure  $p_c$  as a function of liquid saturation  $S_{e\_liq}$ ) of the bentonite, the rock matrix and the rock fracture follow a van Genuchten curve.

The relative permeability to liquid and gas in the bentonite were taken as functions of Fatt and Klikoff (1959):

$$k_{r\_liq} = (S_{e\_liq})^3,$$

$$k_{r\_gas} = (1 - S_{e\_liq})^3.$$

For the relative permeability to liquid and gas in the rock matrix and the rock fracture, a Van Genuchten parameterization was used:

$$k_{r\_liq} = S_{e\_liq}^{0.5} \left(1 - \left(1 - (S_{e\_liq})^{1/m}\right)^m\right)^2,$$

$$k_{r\_gas} = 1 - k_{r\_liq}.$$

Modelling was performed under isothermal 15 °C temperature conditions. Fixed boundary conditions were set at the borders other than the symmetry axis and in the cells forming the tunnel: liquid saturation with pressure equal to 2.0 MPa for the outer boundaries and gas saturation at atmospheric pressure (0.1 MPa) are assumed in the tunnel.

The initial conditions were set as the steady state determined by the given boundary conditions assuming that the deposition hole is open and filled with water but not yet filled with bentonite. The initial conditions (pressure field)

obtained by publication authors (Dessirier et al., 2014) using modelling tool TOUGH2 are shown in Figure 4-1. The initial liquid saturation is 0.36 in the bentonite and 1.0 in the rock matrix and the rock fracture.

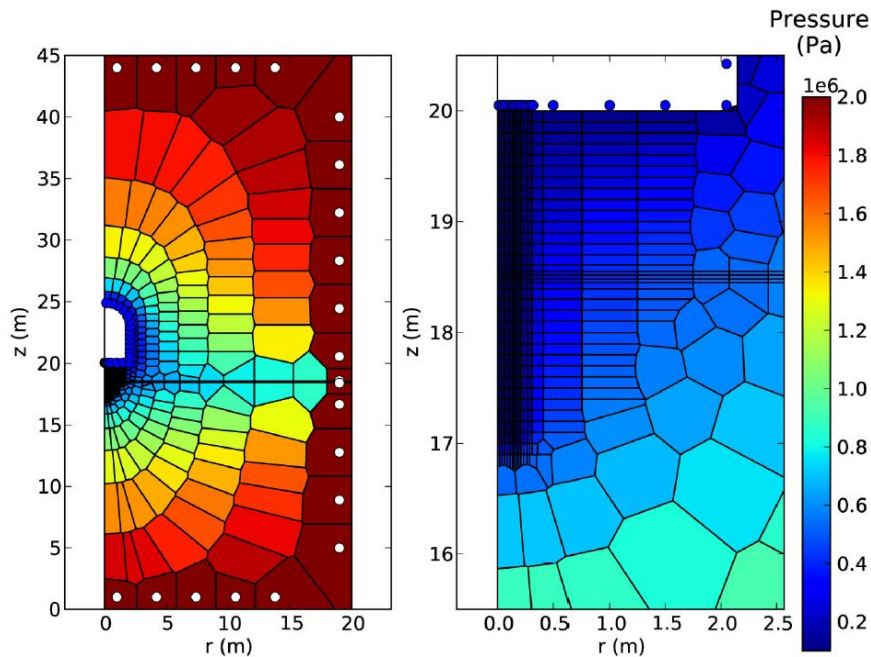


**Figure 4-1. Initial pressure field for bentonite resaturation modelling using TOUGH2 (Dessirier et al., 2014)**

## 5 Model performance on bentonite resaturation

Model performance on bentonite resaturation in generic disposal system based on KBS-3 disposal concept as defined in (Dessirier et al., 2014) was analysed, taking into account Richard's or two-phase flow approaches. Modelling tools PETRASIM (USA) and COMSOL Multiphysics (USA) were used for analysis. Qualitative comparison of modelling results obtained by LEI and results published in (Dessirier et al., 2014) is presented below.

### 5.1 Modelling results using PETRASIM

PETRASIM is a pre- and post-processor for TOUGH family of codes for simulating non-isothermal multiphase flow and transport in fractured and porous media. The idea to use PETRASIM for this exercise was to implement suggested model in very similar modelling tool used by the publication authors (TOUGH2) and repeat the results using Richard's and two-phase (air-water) flow approaches. The same equation-of-state modules (EOS9 for Richard's and EOS3 for two-phase flow) were used in PETRASIM and TOUGH2. The modelling domain in PETRASIM was meshed with 2.730 rectangular grid elements and was refined in and around the deposition hole as could be seen in Figure 5-1.

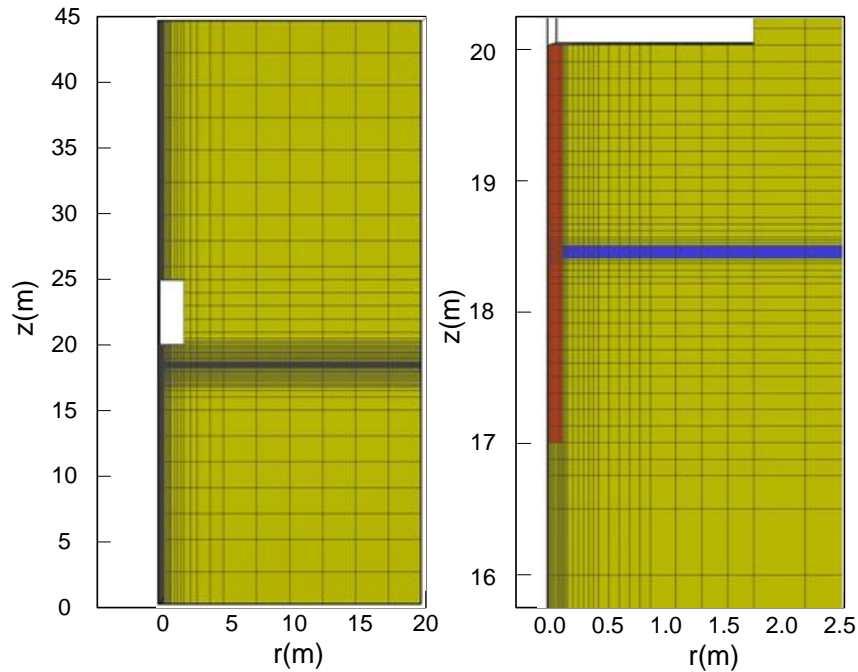


**Figure 5-1. Computational grid of PETRASIM model coloured by material type**

The initial conditions modelled by the given boundary conditions using PETRASIM are presented in Figure 5-2. The pressure field is very similar to the results obtained by publication authors using modelling tool TOUGH2 (see Figure 4-1).

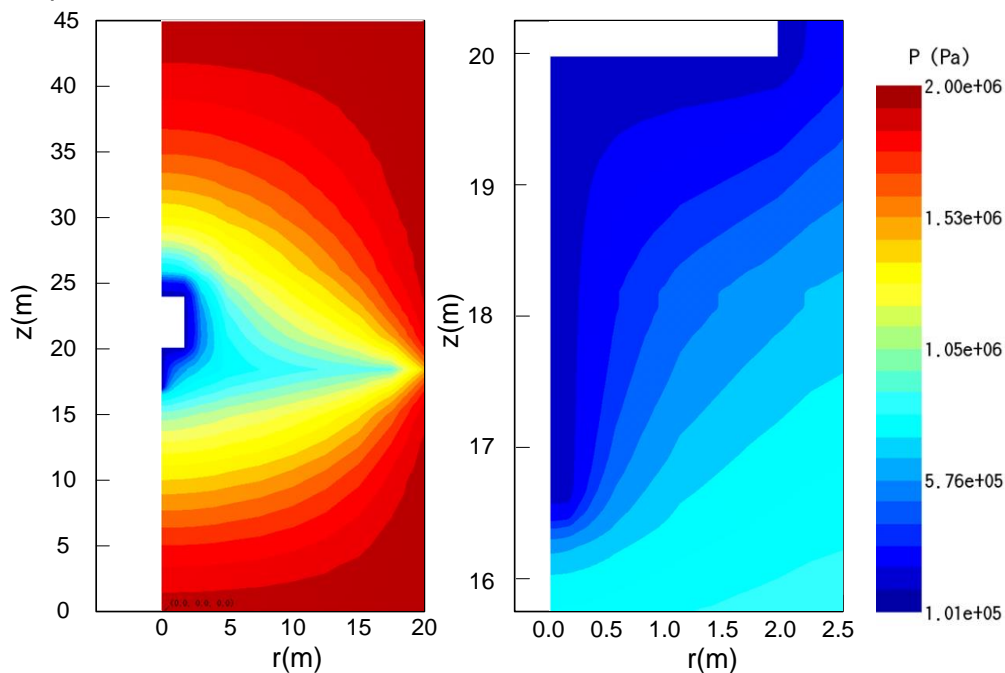


**Figure 5-2. Initial pressure field for bentonite resaturation modelling in PETRASIM model**

Figure 5-3 presents liquid saturation contours in the bentonite and in the close rock domain at different times for two-phase flow or Richard's approaches using PETRASIM.

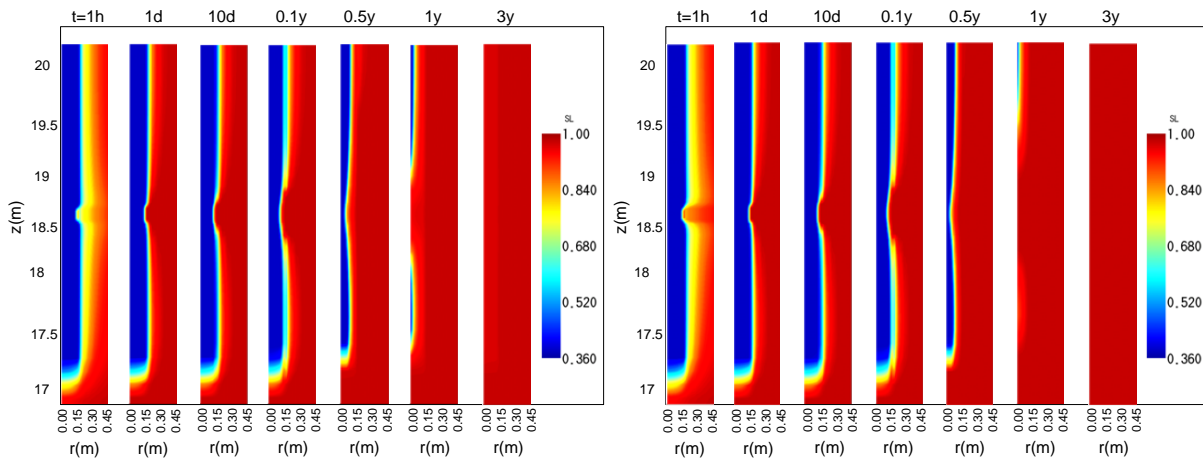


**Figure 5-3. Liquid saturation in the bentonite ( $r < 0.15$  m) and in the close rock domain ( $r > 0.15$  m) at different times for (a) the two-phase flow approach and (b) the Richard's approach (integrated finite volume method, PETRASIM)**

As it could be seen in Figure 5-3, very soon after emplacement of the unsaturated bentonite in the deposition hole, the sudden decrease of saturation in surrounding rock matrix and fracture was observed. Later on the water flow proceeded along the bentonite-rock, and bentonite-fracture interface with slightly advanced front of saturation in those bentonite regions close to the fracture. After 3 years the results of bentonite resaturation modelling indicated a fully saturated state.

The results were compared to that obtained using TOUGH2 and are published in (Dessirier et al., 2014, see Figure 5-4). While comparing the saturation profiles at all selected times, it was observed that modelling results obtained using PETRASIM code correlated well to the TOUGH2 profiles for two-phase flow and Richards's approaches.

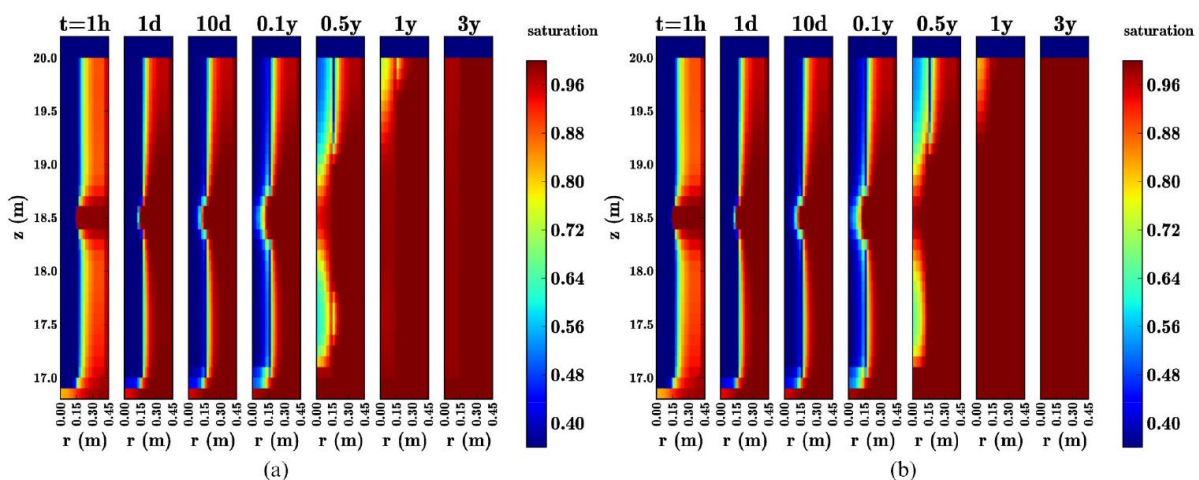


**Figure 5-4. Liquid saturation in the bentonite ( $r < 0.15$  m) and in the close rock domain ( $r > 0.15$  m) at different times for (a) the two-phase flow approach and (b) the Richard's approach (integrated finite volume method, TOUGH2, Dessirier et al., 2014)**

Figure 5-5 presents the modelling results on saturation variations over time

close to the bentonite-rock interface at two different depths for two-phase flow (EOS3) or Richard's (EOS9) approaches using PETRASIM. As it could be noticed from Figure 5-5, following the installation of bentonite in the deposition hole, desaturation of the closest region of the rock domain started. The saturation degrees in the rock matrix and fracture (Figure 5-5, dashed curves) became lower than in the bentonite itself (Figure 5-5, solid curves). High saturation degrees was reached faster close to the fracture-deposition hole intersection at  $z=18.5$  m (Figure 5-5, red curves) than away from it (Figure 5-5, blue curves), by about three orders of magnitude.

Comparing different approach's influence on saturation profiles at the same points, it could be noticed that global behaviour are very similar as reported in (Dessirier et al., 2014) – Richard's approach led to the shorter resaturation time and to the higher saturation degree at any given simulation time in materials compared to the two-phase flow approach.

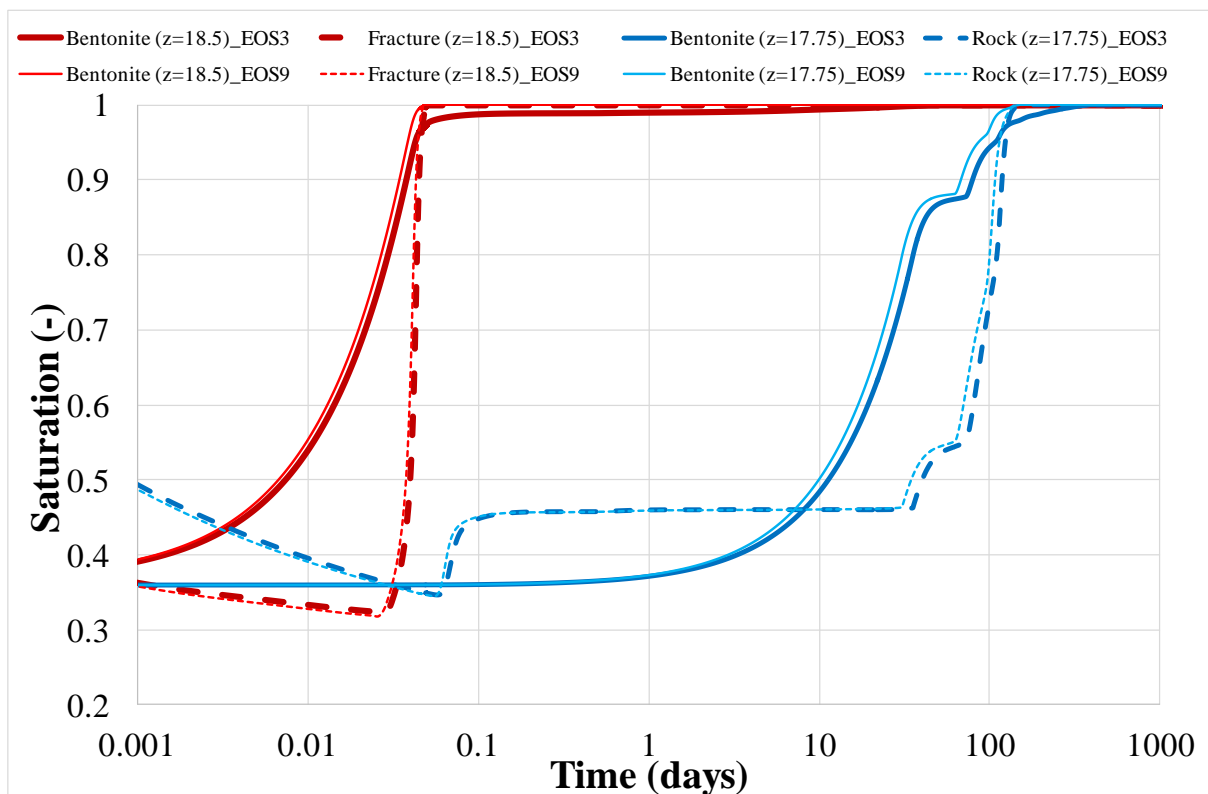


**Figure 5-5. Comparison of saturation at the bentonite-rock interface at two different depths for Richard's (EOS9) and the two-phase flow (EOS3) approaches (integrated finite volume method, PETRASIM).**

Comparison of the results for two-phase flow approach obtained using PETRASIM (see Figure 5-5, EOS3 curves) and TOUGH2 (see Figure 5-6) allowed concluding that saturation profiles and full resaturation times in bentonite (at both depths) and rock fracture were very similar. Slightly different profile was obtained for rock matrix at  $z=17.75$  m. Even the full resaturation times were similar (~200 days), the lowest liquid saturation are different: 0.2 was observed using TOUGH2 and 0.35 using PETRASIM.

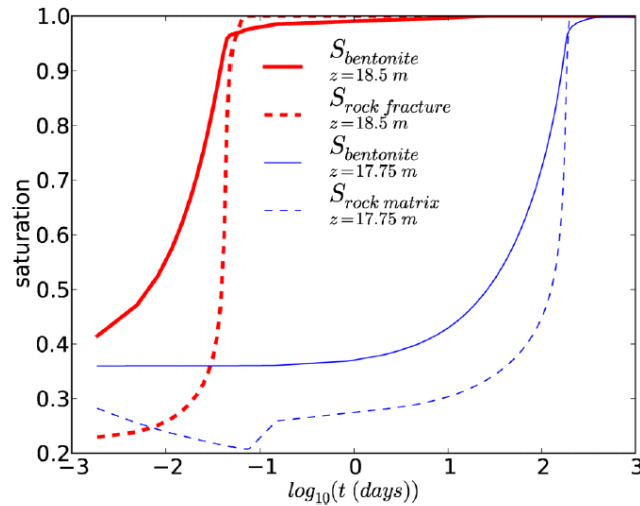


**Figure 5-6. Saturation at the bentonite-rock interface at two different depths for the two-phase flow approach using TOUGH2. Solid lines give saturation in the outermost layer of bentonite ( $r=0.14$  m), and dashed lines correspond to saturation in the rock domain just outside the deposition hole ( $r=0.16$  m). The thick red curves show the saturation at the fracture depth ( $z=18.5$  m), and the thin blue curves show the saturation below the fracture ( $z=17.75$  m), where the bentonite is in contact with the homogeneous rock matrix. (Dessirier et al., 2014)**

## 5.2 Modelling results using COMSOL Multiphysics

COMSOL Multiphysics is general-purpose platform software for modelling engineering applications. It allows conventional physics-based user interfaces and coupled systems of partial differential equations for simulation with finite element method.

Modelling domain was meshed with 23.705 triangular elements and was refined in and around the deposition hole as it could be seen in Figure 5-7.

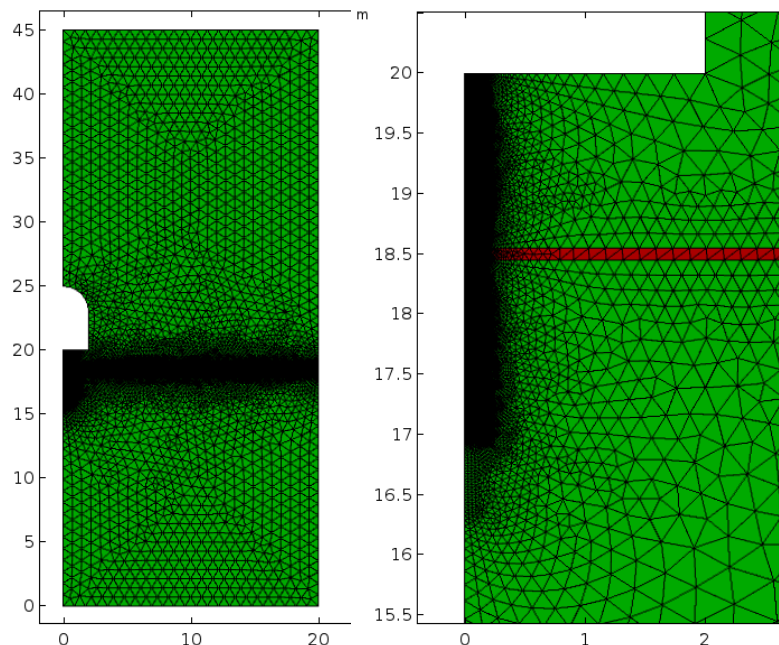


**Figure 5-7. Computational grid of COMSOL Multiphysics model coloured by material type**

Preliminary modelling results of bentonite resaturation under generic disposal conditions obtained using COMSOL Multiphysics are presented in Figure 5-8.

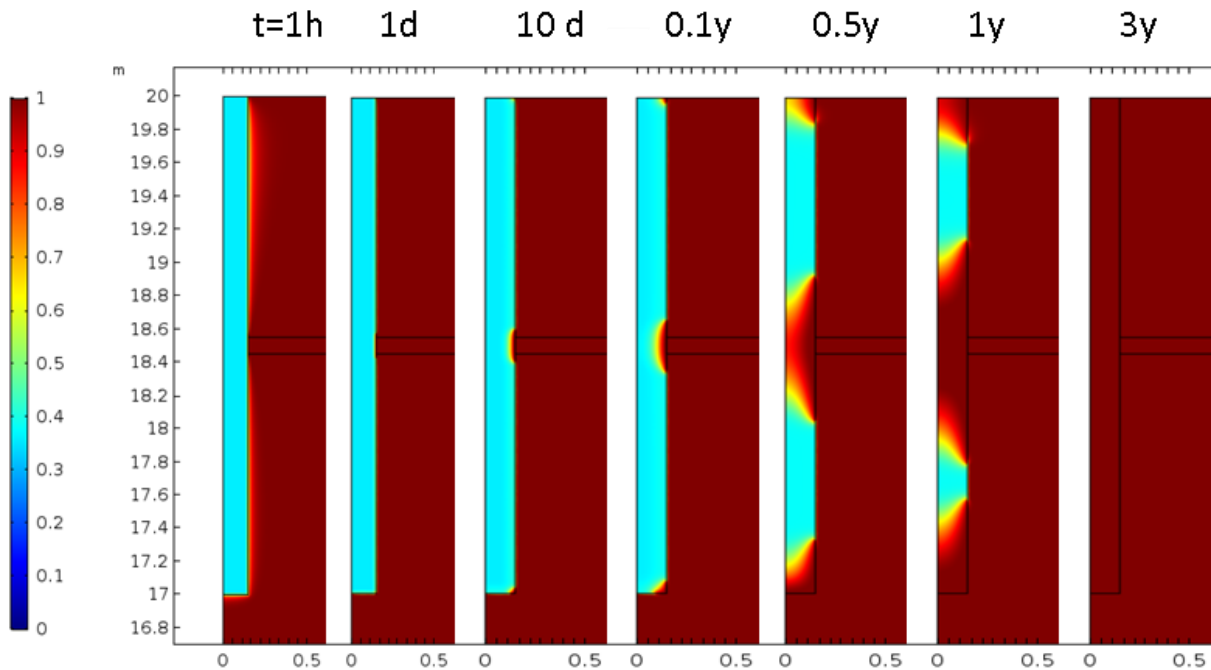


**Figure 5-8. Liquid saturation in the bentonite ( $r < 0.15$  m) and in the close rock domain ( $r > 0.15$  m) at different times (finite element method, COMSOL Multiphysics)**

Similarly to that was obtained in PETRASIM and (Dessirier et al., 2014), a sudden desaturation of rock surrounding deposition hole was also observed soon after bentonite emplacement ( $t=1$ h, see Figure 5-3 and Figure 5-4).

At later time's preferential saturation of bentonite close to the rock fracture was observed as well as close to the upper and bottom corners. However the saturation of bentonite at the middle parts of section above and below the rock fracture is somewhat delayed. The impact of interface between the materials with significantly variable properties was observed. An internal boundary layer of very low saturation was observed in rock close to the interface. Such a situation where the bentonite is more saturated than surrounding rock could also be noticed in the results of (Dessirier et al., 2014) in particular at times  $t=0.1$  y,  $t=0.5$  y, see Figure 5-4).

The comparison of saturation evolution at four predefined points is presented in Figure 5-9.

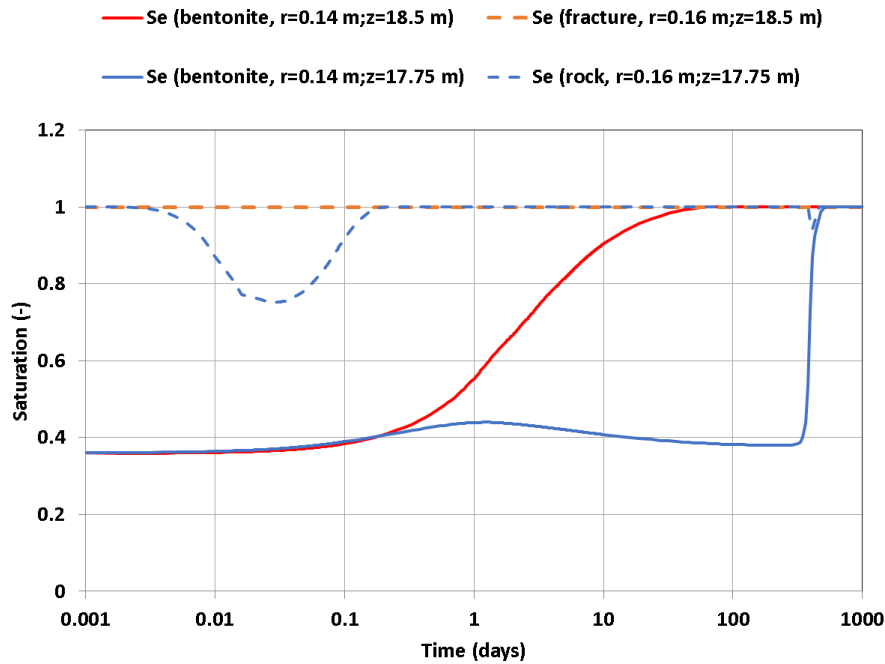


**Figure 5-9. Saturation at the bentonite-rock interface at two different depths for Richard's approach (finite element method, COMSOL Multiphysics)**

As it could be noticed from the figure above the results do not correlate well with results obtained using PETRASIM (see Figure 5-5) or TOUGH2 (see Figure 5-6). The point in the rock fracture remained saturated for all analysed period, and the rock matrix below the fracture experienced less significant decrease in saturation. Full saturation at points in bentonite was observed as delayed in comparison to the results obtained using PETRASIM and TOUGH2.

In general bentonite resaturation trends are similar to that obtained with PETRASIM and TOUGH2, where preferential saturation close to fracture was obtained and the bentonite was observed as fully saturated at  $t=3$  years from the beginning. The reasoning of differences observed is not clear and more detailed analysis of this aspect is needed.

## 6 Conclusions

Modelling saturated/unsaturated conditions in bentonite using numerical tools available at LEI was performed and preliminary results are presented. It was concluded that:

- Modelling results of bentonite resaturation under generic disposal conditions using PETRASIM showed a good agreement with published data for both Richard's and two-phase flow approaches.
- Bentonite resaturation modelling with other numerical tool based on finite element method (COMSOL Multiphysics) provided results different to some extent and more detailed analysis of this aspect is needed.
- Mechanical processes are not included in the models at this stage. Next step of LEI in the WP3 will be the coupling of unsaturated water flow in bentonite with mechanical behaviour.

**Table 6-1 Features table.**

<b>Name of the constitutive law:</b>		<b>Not implemented yet</b>	
<b>Behaviour feature</b>	<b>YES</b>	<b>NO</b>	<b>Remarks</b>
<b>Mechanical behaviour</b>			
Dependence of swelling strain on applied stress (at the same dry density)			Not implemented yet
Dependence of swelling stress on dry density (at the same stress)			Not implemented yet
Irreversibility of strains in wetting/drying cycles			Not implemented yet
Dependence of swelling pressure on dry density			Not implemented yet
Stress path dependence from an unsaturated to a saturated state			Not implemented yet
Stress path dependence from a saturated to an unsaturated state			Not implemented yet
Double structure/porosity considered?			Not implemented yet
Are temperature effects considered in the model?			Not implemented yet
Dependence of strains developed in a temperature cycle (increase/decrease) on OCR (or stress)			Not implemented yet
<b>Hydraulic behaviour (retention curve)</b>			
Hysteresis		x	
Dependence on void ratio		x	
Double structure/porosity considered?		x	

## Acknowledgements

This project receives funding from the Euratom research and training programme 2014-2018 under grant agreement No 745942.

## References

**Dessirier, B., Jarsjö, J., Frampton, A., 2014.** Modeling Two-Phase-Flow Interactions across a Bentonite Clay and Fractured Rock Interface, Nuclear Technology, 187:2, 147-157.

**Fatt, I. and Klikoff, W. A., 1959.** Effect of Fractional Wettability on Multiphase Flow Through Porous Media, AIIME Transactions, 216, 426-432.

**Szymkiewicz A, 2013.** Modelling Water Flow in Unsaturated Porous Media Accounting for Nonlinear Permeability and Material Heterogeneity, 238 p.